

A Blade-Resolved, Partitioned-Approach
Fluid-Structure Interaction Analysis
of a Ducted, High-Solidity Tidal Turbine
in Real Flow Conditions

Ph.D. Thesis

Mitchell Gareth Borg

B.Eng. (Hons.) (Melit.) || M.Sc. (Aberdeen)

Department of Naval Architecture, Ocean, and Marine Engineering

University of Strathclyde, Glasgow

United Kingdom

October 17, 2020

This thesis is the result of the author's original research. It has been composed by the author and has not been previously submitted for examination which has led to the award of a degree.

The copyright of this thesis belongs to the author under the terms of the United Kingdom Copyright Acts as qualified by University of Strathclyde Regulation 3.50. Due acknowledgement must always be made of the use of any material contained in, or derived from, this thesis.

Signed: Mitchell Gareth Borg

Date: October 17, 2020

Abstract

Harnessing the power of the ocean for sustainable energy generation is a compound, intricate task. In designing a tidal turbine rotor for long-term operation, a collation between high-efficiency hydrodynamic performance and robust structural integrity is imperative; this is more so when analysing the physics of an unconventional tidal turbine. This study investigates the hydrodynamic and structural performance of a full-scale, high-solidity, open-centre, ducted tidal turbine by implementing a numerical framework for a coupled fluid-structure interaction analysis.

The analysis primarily tackles the hydrodynamic performance of the tidal turbine by means of a temporal, blade-resolved computational fluid dynamic approach utilising Reynolds Stress turbulence modelling capacities. The model achieves similarity values of over 0.96 with three-bladed, horizontal-axis tidal turbine experimentation data in validation of three distinct parameters: power coefficient, thrust coefficient, and wake velocity profiles. Within aligned-flow conditions, the resultant hydrodynamic performance characteristics of the ducted turbine portrayed a peak power coefficient of 0.34, with a thrust coefficient of 0.97, at a nominal tip-speed ratio of 1.75; coefficient trend agreement was attained between the numerical model, experimentation data established in literature, and blade-element momentum theory.

In analysing the performance within yawed-flow conditions, increases in torque and mechanical rotational power were acknowledged within a limited angular range at distinct tip-speed ratio values. Through multiple yaw iterations, the peak attainment was found to fall at a bearing of 23.2° , resulting in a maximum power increase of 3.22%, together with an extension of power development to higher tip-speed ratios. Subsequently, by migrating the hydrodynamic outcomes into a finite-element model, the

rotor structural mechanics were investigated to acknowledge the most applicable blade design. The resultant axial deflections were found to be insubstantial, albeit inducing a significant maximum strain of 1.2%, where the reinforced blade design was established to be the most suitable.

Following a turbulence model evaluation for the turbine design, the analytical formulae established in ducted turbine theory were solved utilising the data acquired, presenting a novel formula derivation. In culmination, explicit vortices were numerically generated within the flow domain, upstream of the turbine, in effort of acknowledging performance disparity due to turbine-vortex interaction.

List of Publications

Journal Papers

M. G. Borg, Q. Xiao, S. Allsop, A. Incecik, and C. Peyrard, “A numerical performance analysis of a ducted, high-solidity tidal turbine,” *Renewable Energy*, vol. 159, pp. 663 - 682, 2020.

M. G. Borg, Q. Xiao, S. Allsop, A. Incecik, and C. Peyrard, “A numerical fluid-structure interaction analysis of a fibre-composite, ducted, high-solidity tidal turbine rotor in aligned and yawed flow conditions,” *Ocean Engineering*. Under Review.

M. G. Borg, Q. Xiao, S. Allsop, A. Incecik, and C. Peyrard, “A blade-resolved numerical analysis of a ducted, high-solidity tidal turbine in yawed flow,” *Applied Energy*. Under Review.

Research Awards

OCEANS '18 MTS/IEEE Kobe, Japan Conference, “Student Researcher Competition”, *1st Place (Offshore Renewable Energy Section) | 2nd Runner-Up (Overall)*, Kobe, Japan

Energy Transfer Protocol (ETP) Conference '18, “ETP Researcher Presentation Competition”, *1st Place (Marine Energy Division)*, Glasgow, Scotland, United Kingdom.

Conference Papers

M. G. Borg, Q. Xiao, A. Incecik, S. Allsop, and C. Peyrard, “Analysing Fibre Composite Designs for High-Solidity Ducted Tidal Turbine Blades” in *OCEANS '19 MTS/IEEE Marseille, (Marseille, France)*, IEEE, 2019.

M. G. Borg, Q. Xiao, A. Incecik, S. Allsop, and C. Peyrard, “An Actuator Disc Analysis of a Ducted High-Solidity Tidal Turbine in Yawed Flow,” in *ASME 2019, 38th International Conference on Ocean, Offshore, and Arctic Engineering, OMAE 2019*, (Glasgow, Scotland), ASME, 2019.

M. G. Borg, Q. Xiao, A. Incecik, S. Allsop, and C. Peyrard, “Blade-Explicit Fluid-Structure Interaction of a Ducted High-Solidity Tidal Turbine,” in *7th Oxford Tidal Energy Workshop (OTE2019)*, (Oxford, United Kingdom), University of Oxford, 2019.

M. G. Borg, Q. Xiao, A. Incecik, S. Allsop, and C. Peyrard, “Numerical Analysis of a Ducted High-Solidity Tidal Turbine,” in *OCEANS '18 MTS/IEEE Kobe, (Kobe, Japan)*, IEEE, 2018.

Acknowledgements

Primarily, I would like to thank my supervisors, Dr. Qing Xiao and Prof. Atilla Incecik for their aid throughout this thesis; their guidance had been invaluable throughout the pursuit of the PhD.

I would also like to thank my collaborators throughout the project, Mr. Christophe Peyrard and Dr. Steven Allsop. The research they had accumulated at EDF R&D, in relation to the ducted tidal turbine, was graciously forwarded to me upon the initial span of the degree; their aid continued to be of value even throughout its final stretch.

Furthermore, I would like to thank my mother and father, together with my siblings, grandparents, and (grand)aunts, for encouraging me to grasp any opportunity I deem worthy of pursuing (and for all the food I had eaten when I went back to Malta on holiday).

Every PhD student needs a good friend to go through the doctorate with; it's a linchpin to successfully complete it. I'd like to thank Alessandro for being this person, having beers with, going for pizza (or getting it ordered to the department), and offering to sleep on his couch when in between flats; always had my back. In extrapolation, I would need to thank the rest of the SB's (Bozo, Sotirios, Sefer, and Yiannis) for being an amazing group of friends to hang out with in and out of the department. Furthermore, Christos and Michail were always in the kitchenette with a flask full of coffee first thing in the morning, day in day out. Extremely grateful.

Finally, saving the best for last, I would like to thank my two best friends, Luke and Roberto, for their moral (and mental) support, not only for the three-and-a-half year duration of the doctorate, but throughout the past seventeen. I will forever be thankful for their friendship.

Table of Contents

List of Figures	i
List of Tables	x
List of Symbols	xi
List of Abbreviations	xiv
1 Introduction	1
1.1 Prelude	1
1.2 Aims & Objectives	3
1.3 Layout of the Thesis	4
1.4 Research Gap & Novelty of the Study	6
1.5 Contribution to Knowledge	8
1.6 Chapter Summary	9
2 Literature Review	10
2.1 Background Knowledge	10
2.1.1 Horizontal-Axis Turbine Blade Dynamics	11
2.1.2 Ducted Horizontal-Axis Turbine Dynamics	14
2.1.3 Turbine Dynamics in Yawed Flow Conditions	18
2.1.4 Turbine Dynamics in Vortex Flow Conditions	20
2.2 Commercial Applications of Ducted Tidal Turbines	22
2.2.1 Bi-directional Ducted Tidal Turbine Projects	22
2.2.2 Uni-directional Ducted Tidal Turbine Projects	26

2.3	State of the Art	26
2.3.1	Experimental Investigations of Ducted Turbines	26
2.3.2	Analytical Investigations of Ducted Turbines	36
2.3.3	Numerical Investigations of Ducted Turbines	40
2.3.4	State of the art Summary	47
2.3.5	Research Gap	47
2.4	Chapter Summary	49
3	Characterisation Modelling of a Ducted Tidal Turbine	50
3.1	Numerical Turbine Modelling Methodologies	50
3.1.1	Linear Momentum Theory	51
3.1.2	Rotor Disc Theory	56
3.1.3	Blade-Element Momentum Theory	57
3.1.4	Ducted Turbine Adaptation	59
3.1.5	Yawed Flow Adaptation	62
3.1.6	Disc Theory Correction Factors	64
3.1.7	Disc Theory Limitations	67
3.1.8	Computational Fluid Dynamics	68
3.2	Turbulent Flow	70
3.2.1	The Law of the Wall	71
3.2.2	Reynolds-Averaged Navier Stokes Turbulence Modelling	72
3.3	Physical Modelling	77
3.4	Chapter Summary	80
4	Methodology of the Fluid-Structure Interaction Analysis	82
4.1	Physical Setup of the Turbine Models	82
4.1.1	Three-Bladed Horizontal Axis Tidal Turbine	83
4.1.2	Ducted High-Solidity Tidal Turbine	83
4.2	Numerical Setup of the Turbine Model	90
4.2.1	Hydrodynamic Analysis	92
4.2.2	Structural Analysis	99

4.3	Chapter Summary	102
5	Numerical Validation of a Three-Bladed Horizontal-Axis Tidal Turbine	105
5.1	Power Coefficient	105
5.2	Thrust Coefficient	107
5.3	Wake Velocity Profiles	108
5.4	Chapter Summary	109
6	Hydrodynamic Performance of a Ducted High-Solidity Tidal Turbine in Aligned Flow Conditions	110
6.1	Power Coefficient	110
6.2	Thrust Coefficient	115
6.3	Static Pressure on Duct Ridges	120
6.4	Vortex Shedding	121
6.5	Blade Analysis	124
6.6	Wake Velocity Profiles	127
6.7	Chapter Summary	129
7	Hydrodynamic Performance of a Ducted High-Solidity Tidal Turbine in Yawed Flow Conditions	131
7.1	Power Coefficient	131
7.2	Thrust Coefficient	137
7.3	Linear Momentum Analysis	138
7.3.1	Axial Velocity & Volumetric Flow-Rate Coefficients	138
7.3.2	Static Pressure Coefficient	139
7.3.3	Total Pressure Coefficient	143
7.3.4	Linear Momentum Thrust Coefficient	144
7.4	Lateral Load Coefficient	145
7.5	Static Pressure Coefficient on Duct	146
7.6	Wake Profiles	147
7.7	Chapter Summary	149

8	Structural Analysis of Fibre-Reinforced High-Solidity Tidal Turbine Blades in Aligned and Yawed Flow Conditions	153
8.1	Geometric Analysis	153
8.2	Hydrostatic Analysis	154
8.3	Hydrodynamic Fracture Analysis	154
8.3.1	Blade Deflection	155
8.3.2	Normal Elastic Strain	157
8.3.3	Equivalent Elastic Strain	161
8.3.4	Shear Elastic Strain	164
8.4	Material Cost Analysis	165
8.5	Fatigue Analysis	168
8.5.1	Principal Elastic Strain	168
8.5.2	Strain-Life Analysis	169
8.6	Evaluation of the Structural Designs	172
8.7	Chapter Summary	173
9	Turbulence Modelling for a Ducted High-Solidity Tidal Turbine	174
9.1	Blade-Resolved CFD Analysis	175
9.1.1	Power & Torque Coefficient	175
9.1.2	Thrust Coefficient	176
9.1.3	Axial Velocity & Static Pressure Difference	178
9.1.4	Wake Velocity Profiles	179
9.2	Turbulence Modelling Review	181
9.3	Linear Momentum Rotor Properties under Highly-Loaded Conditions	184
9.3.1	Axial Induction Factor	184
9.3.2	Tangential Induction Factor	184
9.3.3	Ducted Turbine Properties	186
9.4	Chapter Summary	190
10	Vortex-Interaction Analysis of a Ducted High-Solidity Tidal Turbine	192
10.1	Power Coefficient	192

10.2 Thrust Coefficient	197
10.3 Wake Profiles	199
10.4 Chapter Summary	203
11 Conclusion	205
11.1 Summary of the Fluid-Structure Interaction Analysis	206
11.1.1 Aligned Flow Analysis	206
11.1.2 Yawed Flow Analysis	207
11.1.3 Structural Analysis	208
11.1.4 Turbulence Modelling Analysis	210
11.1.5 Vortex Flow Analysis	211
11.2 Evaluation of the Ducted High-Solidity Tidal Turbine	212
11.3 Future Work	213
11.4 Chapter Summary	216
References	217
A Characterisation Modelling of a Ducted Tidal Turbine	235
A.1 Law of the Wall	235
B Methodology of the Fluid-Structure Interaction	236
B.1 Mesh Independence Analysis	236
B.2 Concentrated Vortex Generation	238
B.2.1 Domain Model	238
B.2.2 User-Defined Function Macro	240
C Numerical Validation of a Three-Bladed Horizontal-Axis Tidal Turbine	243
D Hydrodynamic Performance of a Ducted High-Solidity Tidal Turbine in Aligned Flow Conditions	245

E Hydrodynamic Performance of a Ducted High-Solidity Tidal Turbine in Yawed Flow Conditions	248
F Structural Analysis of Fibre-Reinforced High-Solidity Tidal Turbine Blades	250
G Cost Analysis	253
H Ducted Turbine Outlet Pressure Equation Derivation	255

List of Figures

2.1	Local velocities at a blade element of a turbine rotor	11
2.2	Local forces at a blade element of a turbine rotor	13
2.3	Illustration of stream-tube boundary distinctions between bare turbines and ducted turbines	15
2.4	Schematic of the flow-field along a boundary-layer-control diffuser-augmented turbine configuration; depicts the additional momentum injection through auxiliary slots, preventing boundary layer separation within the duct . . .	16
2.5	Variation of maximum power coefficient as a function of yaw angle	19
2.6	Bi-directional ducted tidal turbine projects	24
2.7	The OpenHydro PS2 Ducted Turbine	25
2.8	Illustrative representation of a vacant shroud within a free-stream	27
2.9	Illustrative representation of a disc-embedded shroud	29
2.10	Illustrative representation of a rotor-embedded shroud	32
3.1	Illustrative representation of an actuator disc within a fluid stream-tube	51
3.2	Schematic of a ducted turbine incorporating the actuator disc bounded by a stream tube, with numbers corresponding to sections in which areas, pressures and velocities are taken, consisting of: 0 in-flow upstream; 1 - duct inlet; 2 - actuator disc upstream; 3 - actuator disc downstream; 4 - duct outlet; 5 - wake downstream; 6 - wake far downstream	60

3.3	Thrust coefficient against axial induction factor, showing comparisons against BEMT with experimental values and semi-empirical corrected values (left) and highly loaded corrected values with an arbitrary tip/hub loss of 0.8 applied (right)	66
4.1	Rendered three-dimensional CAD representation of the horizontal-axis tidal turbine utilised for the validation of the CFD model	84
4.2	Geometrical model of the ducted high-solidity tidal turbine utilised for the CFD analyses	85
4.3	Geometrical model of the ducted high-solidity tidal turbine utilised for the CFD analyses	89
4.4	Geometrical model of the ducted high-solidity tidal turbine utilised for the CFD analyses	91
4.5	Notation of incoming flow bearing in relation to rotor axis & positions of planar circular surfaces	93
4.6	Implementation of the one-way fluid-structure interaction technique; importing pressure distribution along the blade surface	101
4.7	Implementation of the one-way fluid-structure interaction technique; importing pressure distribution along the blade surface	103
5.1	Comparative evaluation of the current horizontal-axis tidal turbine CFD model with experimentation , and high-speed windmills	106
5.2	Comparative evaluation of the current horizontal-axis tidal turbine CFD model with experimentation for thrust coefficient (C_T) in relation to TSR	107
5.3	Comparative evaluation of the current horizontal-axis tidal turbine CFD model with experimentation for the wake velocity profiles at distinct downstream displacements ($x_{D_{tr}}^*$) in relation to TSR	108
6.1	Evaluation of the mean ducted turbine power coefficient (C_P) in relation to TSR	111

6.2	Evaluation of the ducted turbine mechanical power (P_{dvc}) in relation to free-stream velocity (U_∞) at distinct TSRs	114
6.3	Evaluation of the ducted turbine torque coefficient (C_Q) in relation to TSR	115
6.4	Representation of the transient power coefficient output at $U_\infty = 4.0$ m/s through turbine rotatory periods (T_ω)	116
6.5	Evaluation of the ducted turbine thrust coefficient (C_T) in relation to TSR	117
6.6	Illustrative top-view representation of the pressure coefficient (C_{Pr}) within the turbine domain at low, nominal, and high TSR at mean-average output; $U_\infty = 4$ m/s	118
6.7	Evaluation of the ducted turbine mass-flow rate coefficient ($C_{\dot{m}}$) in relation to TSR	119
6.8	Representation of the dynamics at the inner curved and outer straight geometry of the duct inlet; $U_\infty = 4$ m/s	120
6.9	Axial velocity coefficient (\bar{u}_z^*) illustration of the free shear layer at the duct outlet; $U_\infty = 4$ m/s, $TSR = 1.75$	122
6.10	Illustrative top-view representation of the axial velocity coefficient (\bar{u}_z^*) within the turbine domain at low, nominal, and high TSR ; $U_\infty = 4$ m/s	123
6.11	Evaluation of the vortex shedding frequency (f_v) in relation to free-stream velocity (U_∞) at distinct TSRs	124
6.12	Plots of pressure coefficient (C_{Pr}) along the blade chord ratio (x_{ch}/ch_{rtr}) at distinct rotor radius ratios (r_{rtr}/R_{rtr}) at $U_\infty = 4.0$ m/s, $TSR = 1.75$	126
6.13	Pressure coefficient (C_{Pr}) contour representation along the suction edge of the blade at rotation period $\frac{1}{4} T_\omega$ (left), $\frac{2}{4} T_\omega$ (mid-left), $\frac{3}{4} T_\omega$ (mid-right), and $\frac{4}{4} T_\omega$ (right) at $U_\infty = 1.00$ m/s at low (top) and nominal (bottom) TSR	127

6.14	Pressure coefficient (C_{Pr}) contour representation along the suction edge of the blade at rotation period $\frac{1}{4} T_\omega$ (left), $\frac{2}{4} T_\omega$ (mid-left), $\frac{3}{4} T_\omega$ (mid-right), and $\frac{4}{4} T_\omega$ (right) at $U_\infty = 4.00$ m/s at low (top) and nominal (bottom) TSR	128
6.15	Dimensionless axial velocity (\bar{u}_z^*) profiles within the ducted turbine wake at different rotor diameter displacements downstream – $U_\infty = 4$ m/s, $TSR = 1.75$	129
7.1	Evaluation of the mean ducted turbine power coefficient (C_P) at distinct flow bearings in relation to TSR	132
7.2	Evaluation of the true mean power at distinct $TSRs$ in relation to flow bearing (γ)	133
7.3	Evaluation of the instantaneous ducted turbine power coefficient (C_P) in relation to blade azimuth angle	135
7.4	Evaluation of the mean single-blade response (C_P) in relation to azimuth angle	136
7.5	Evaluation of the mean ducted turbine torque coefficient (C_Q) at distinct flow bearings in relation to TSR	137
7.6	Evaluation of the mean ducted turbine thrust coefficient (C_T) at distinct flow bearings in relation to TSR	138
7.7	Evaluation of the mean axial velocity coefficient ($C_{U,z}$) at distinct flow bearings in relation to TSR	139
7.8	Evaluation of the mean volumetric flow-rate coefficient ($C_{\dot{V}}$) at distinct flow bearings in relation to TSR	140
7.9	Evaluation of the mean static pressure difference coefficient ($C_{\Delta P,s}$) at distinct flow bearings in relation to TSR	141
7.10	Evaluation of the mean static pressure difference coefficient ($C_{\Delta P,s}$) at distinct $TSRs$ in relation to flow bearing (γ)	142
7.11	Evaluation of the mean static pressure coefficient ($C_{P,s}$) upstream at distinct flow bearings in relation to TSR	143

7.12	Evaluation of the mean static pressure coefficient ($C_{P,s}$) downstream at distinct flow bearings in relation to TSR	144
7.13	Evaluation of the mean total pressure coefficient difference ($\Delta C_{P,t}$) at distinct flow bearings in relation to TSR	145
7.14	Evaluation of the mean blade thrust coefficient (C_T) with the mean linear momentum thrust ($C_{T_{AD}}$) at distinct flow bearings in relation to TSR .	146
7.15	Evaluation of the mean lateral load coefficient ($C_{F,x}$) at distinct flow bearings in relation to TSR	147
7.16	Evaluations of static pressure coefficient ($C_{P,s}$) distribution along the duct inlet surfaces	148
7.17	Illustrative representation of the upstream stream-tube boundaries at the duct inlet	149
7.18	Illustrative top-view representation of the axial velocity coefficient ($C_{U,z}$) within the turbine domain at distinct flow bearings	150
7.19	Illustrative top-view representation of the axial velocity coefficient ($C_{U,z}$) at port-side duct, focusing on the induced re-circulation zone region . .	151
8.1	Structural response cross-section of the cored blade design under hydrostatic load	155
8.2	Axial deflection of the distinct blade designs within aligned flow conditions	156
8.3	Axial deflection of the distinct blade designs within yawed flow conditions	157
8.4	Global deflection of the distinct blade designs within aligned flow conditions	158
8.5	Axial deflection distribution along the ‘solid’ blade structural design at nominal flow (4 m.s^{-1}) and nominal rotational velocity (TSR 1.75) . . .	159
8.6	Mean values of the maximum normal radial strain of the distinct blade designs within aligned flow conditions	160
8.7	Mean values of the maximum normal radial strain of the distinct blade designs within yawed flow conditions	161
8.8	Radial strain distribution along the blade structural designs at nominal flow (4 m.s^{-1}) and nominal rotational velocity (TSR 1.75)	162

8.9	Mean values of the maximum normal tangential strain of the distinct blade designs within aligned flow conditions	163
8.10	Mean values of the maximum normal axial strain of the distinct blade designs within aligned flow conditions	164
8.11	Von Mises analysis of the distinct blade designs within aligned flow conditions	165
8.12	Shear strain of the distinct blade designs within aligned flow conditions	166
8.13	Shear strain distribution at the blade root at nominal flow (4 m.s^{-1}) and nominal rotational velocity (TSR 1.75)	167
8.14	Cyclic representation of maximum equivalent strain of the distinct blade designs within aligned and yawed flow conditions	168
8.15	Fatigue response of a ‘reinforced’ high-solidity tidal turbine rotor blade .	170
8.16	Fatigue response of a ‘solid’ high-solidity tidal turbine rotor blade . . .	171
9.1	Comparison of the ducted turbine power coefficient (C_P) utilising different turbulence models	176
9.2	Comparison of the ducted turbine torque coefficient (C_Q) utilising different turbulence models	177
9.3	Comparison of the ducted turbine thrust coefficient (C_T) upon the system area utilising different turbulence models	178
9.4	Comparison of the ducted turbine thrust coefficient (C_T) upon the component areas utilising different turbulence models	179
9.5	Comparison of the ducted turbine parameters utilising different turbulence models within a mean free-stream of 4 m.s^{-1}	180
9.6	Illustrative top-view representation of the axial velocity coefficient (\bar{u}_z^*) within the turbine domain at nominal TSR ; $U_\infty = 4 \text{ m/s}$	182
9.7	Evaluation of the ducted turbine rotor thrust coefficient (C_T) in relation to the axial induction factor (a_f)	185
9.8	Evaluation of the ducted turbine rotor torque coefficient (C_Q) in relation to the tangential induction factor (a'_f)	186

9.9	Evaluation of the tangential induction factor (a'_f) in relation to the axial induction factor (a_f)	187
9.10	Linear momentum properties of the ducted turbine at a nominal free-stream velocity (U_∞) of $4 \text{ m}\cdot\text{s}^{-1}$	188
9.11	Evaluation of the static pressure & axial velocity at the duct outlet with duct efficiency (η_{34})	190
10.1	Evaluation of the mean ducted turbine power coefficient (C_P) in relation to TSR	193
10.2	Evaluation of the instantaneous ducted turbine power coefficient (C_P) in relation to blade azimuth angle under distinct vortex length-scales at nominal TSR	194
10.3	Evaluation of the mean single-blade response (C_P) in relation to azimuth angle under distinct vortex length-scales at nominal TSR	195
10.4	Evaluation of the ducted turbine torque coefficient (C_Q) in relation to TSR	196
10.5	Evaluation of the mean single-blade response (C_P) in relation to azimuth angle under distinct vortex length-scales at nominal TSR	198
10.6	Illustrative top-view representation of the velocity coefficient within the turbine domain at nominal TSR and $l_s = 0.25 \cdot R_{tr}$; $U_\infty = 4 \text{ m/s}$. . .	200
10.7	Illustrative representation of the pressure coefficient (C_{Pr}) within the turbine domain at nominal TSR and $l_s = 0.25 \cdot R_{tr}$; $U_\infty = 4 \text{ m/s}$. . .	201
10.8	Illustrative representation of the vorticity within the turbine domain at nominal TSR and $l_s = 0.25 \cdot R_{tr}$; $U_\infty = 4 \text{ m/s}$	202
A.1	Typical velocity profile for a turbulent boundary layer	235
B.1	Vortex Domain Layout	239
B.2	Vortex Domain Mesh	239
B.3	Vortex Domain Example	240
D.1	Torque Coefficient Standard Deviation	246

D.2	Thrust Coefficient Standard Deviation	246
D.3	Illustrative top-view representation of the vorticity within the turbine domain at nominal TSR; $U_\infty = 4 \text{ m.s}^{-1}$	247
D.4	Illustrative angular representation of the vorticity within the turbine domain at nominal TSR; $U_\infty = 4 \text{ m.s}^{-1}$	247
E.1	Torque Coefficient Standard Deviation	249
E.2	Thrust Coefficient Standard Deviation	249
F.1	Structural response cross-section of the ‘solid’ blade design at 4 m.s^{-1} TSR 1.75	250
F.2	Standard deviation of the maximum normal radial strain of the distinct blade designs within aligned flow conditions	251
F.3	Standard deviation of the maximum normal radial strain of the distinct blade designs within aligned flow conditions	252

List of Tables

2.1	Summary of Rotor-Embedded Ducted Turbine Experimentation	47
2.2	Summary of Rotor-Embedded Ducted Turbine Simulation	48
3.1	Summary of Turbine Model Descriptions	52
3.2	The notation utilised in one-dimensional actuator disc theory for un- constrained flow in a duct, indicating velocities, areas and pressures at several cross sectional locations within the stream-tube	61
4.1	Summary of Turbine Model Descriptions	86
4.2	Detailed ducted turbine blade profile descriptions	87
4.3	Material properties adopted in the structural numerical model	89
4.4	Lay-up of the composite materials adopted in the structural numerical model	90
8.1	Geometric Properties of the High-Solidity Tidal Turbine Rotor	154
8.2	Total Material Costs (rounded to the nearest thousand) for the High- Solidity Tidal Turbine Rotor Designs	166
B.1	Mesh Independence analysis for the Validation Three-Bladed Tidal Turbine	236
B.2	Mesh Independence analysis for the Ducted, High-Solidity Tidal Turbine	237
B.3	Mesh Independence analysis for the Rotor Blade Structural Design . . .	237
G.1	Material Cost per unit mass for the High-Solidity Tidal Turbine Rotor Designs	253

G.2	Required Material Volume for the High-Solidity Tidal Turbine Rotor Designs	253
G.3	Total Material Costs (rounded to the nearest thousand) for the High-Solidity Tidal Turbine Rotor Designs	254

List of Symbols

Greek Symbols

α_{AoA}	Angle of attack	$^{\circ}$
γ	Yaw angular bearing	$^{\circ}$
ν	Poisson ratio	
Ω_{sys}	System rotational velocity	rad.s^{-1}
ω	Specific dissipation rate	s^{-1}
ρ	Volumetric mass density	kg.m^{-3}
σ	Standard deviation	
τ_{ij}	Reynolds stress	kg.m^{-1}
ε_E	Material strain	m.m^{-1}
ε	Turbulence dissipation rate	$\text{m}^2.\text{s}^{-3}$

Latin Symbols

A_{dvc}	Device area	m^2
A_{rtr}	Rotor area	m^2
$C_{\dot{m}}$	Mass-flow co-efficient	
C_F	Force co-efficient	

C_{Pr}	Pressure co-efficient	
C_P	Power co-efficient	
C_Q	Torque co-efficient	
c_{rtr}	Rotor blade chord length	m
C_T	Thrust co-efficient	
D_{rtr}	Rotor diameter	m
E	Material Young's modulus	$\text{kg}\cdot\text{m}^{-1}\cdot\text{s}^{-2}$
f_v	Vortex shedding frequency	Hz
G	Material shear modulus	
k	Turbulence kinetic energy	$\text{m}^2\cdot\text{s}^{-2}$
L_{dct}	Duct length	m
L_{hub}	Hub length	m
L_{St}	Strouhal characteristic length	m
l_s	Turbulent length-scale	m
P_s	Static pressure	$\text{kg}\cdot\text{m}^{-1}\cdot\text{s}^{-2}$
R^2	Co-efficient of determination	
R_{dvc}	Device radius	m
R_{rtr}	Rotor radius	m
r_{rtr}	Rotor radial co-ordinate	m
R_{trb}	Turbine radius	m
Re_∞	Radius-based Reynolds number	

Re_{ch}	Chord-based Reynolds number	
Re_L	Length-based Reynolds number	
S_{rtr}	Rotor solidity	
St	Strouhal number	
t	Elapsed time	s
T_ω	Rotary period	rev
t_{step}	Time-step	s
u_z^*	Axial velocity co-efficient	
U_∞	Free-stream velocity	m.s ⁻¹
x^*	Dimensionless x-coordinate	
y^*	Dimensionless y-coordinate	

Physical Constants

g	Gravitational acceleration	9.81 m.s ⁻²
-----	----------------------------	------------------------

List of Abbreviations

ADT	Actuator Disc Theory
AoA	Angle of Attack
BEMT	Blade-Element Momentum Theory
BSL	Baseline
CAD	Computer-Aided Drawing
CFD	Computational Fluid Dynamics
DB	Double-Biased
EDF	Electricité de France
FEA	Finite-Element Analysis
FEM	Finite-Element Method
FSI	Fluid-Structure Interaction
FVM	Finite-Volume Method
GFRP	Glass-Fibre Reinforced Polymer
HATT	Horizontal-Axis Tidal Turbine
LES	Large-Eddy Simulation
MRF	Multiple Reference Frame
NACA	National Advisory Committee for Aeronautics

NURBS	Non-Uniform Rational Basis Spline
PRESTO!	PREssure STaggering Option
R&D	Research and Development
RANS	Reynolds-Averaged Navier Stokes
RNG	Re-Normalisation Group
RSM	Reynolds-Stress Model
SIMPLE	Semi-Implicit Method for Pressure Linked Equations
SST	Shear-Stress Transport
SRF	Single Reference Frame
TI	Turbulence Intensity
TSR	Tip-Speed Ratio
TST	Tidal Stream Turbine
UD	Uni-Directional
UDF	User-Defined Function
VIV	Vortex-Induced Vibrations

Chapter 1

Introduction

In establishing the basis of the thesis, this chapter puts forward the premise of the motivations, objectives, and investigations tackled to holistically represent the research endeavours in evaluating the numerical blade-resolved fluid dynamics and structural mechanics of a ducted, high-solidity tidal turbine utilising a coupled fluid-structure interaction approach.

1.1 Prelude

Efforts to increase the efficacy of energy-generating turbines have been in constant development following their implementation in the global market. At the forefront of the pertinent research is the effort of increasing the mass-flow through the turbine, along with the constraint and alignment of the wake flow, to facilitate further turbine installations [1]. As a result of the research and development attained, a conventional classification of installations has been implemented around a turbine rotor: unidirectional ducts and bi-directional ducts. Both systems have been considered to enhance the performance of a turbine by increasing the flow velocity along the structure as a result of the induced physical phenomena. Albeit the potential improvements, the performance capacities of a rotor within a bi-directional duct under open-ocean conditional parameters are inadequately understood.

The physics governing the flow within a vacant duct, in contrast, are widely un-

derstood. In accordance to Bernoulli's principle, the energy state of an ideal fluid is a relationship between its kinetic and potential energy, hence a function of its pressure, density, and velocity, through a spatial discrepancy [2]. In consideration of a bidirectional duct with a constricted section, hence a decrease in internal cross-sectional area, a Venturi effect phenomenon is induced through the system. Through this effect, in concordance to the principle of mass continuity, the axial velocity of an incompressible fluid increases along the constriction, along with a decrease in static pressure. In this confine, the application is numerically simplistic if a finite section of a duct system is considered, as the parameters are largely consistent. Yet an open-ended duct succumb to variable conditional parameters of an external fluid domain, together with the implementation of a rotor, which, as a structure, will vary the pressure and velocity gradients through the duct, shall induce high degrees of complexity. Nonetheless, the potential increase in flow velocity through the turbine, as a result of the Venturi effect, is of particular interest.

Albeit a handful of recent research ventures have tackled the fluid dynamics of the implementation of a duct feature in a turbine system, they have had numerical forms of methodological limitations, such as analytically capturing mass and momentum continuity through the duct [3], or discretising the blade structure into elements [4], rather than portraying the true physicality. To overcome the limitations, this research puts forward a numerical analysis of the hydrodynamic and structural performance of a ducted, high-solidity tidal turbine, coupled within a one-way fluid-structure interaction approach. This methodology emphasises the presence of duct-rotor affiliation due to the implementation of blade-resolved computational fluid dynamic analysis. Coupling general continuity at both the domain and turbine, this feature allows the modelling of flow three-dimensionality at the rotor, together with induced turbulence effects, in further effort of numerically replicating the true performance of the tidal turbine.

1.2 Aims & Objectives

To accomplish the task at hand, the aims instigating the pursuit of this research were established:

- (i) To enhance the available knowledge regarding the performance of ducted tidal turbines in aligned, yawed, and vortex flow conditions; and
- (ii) To put forward a computationally-efficient, high-precision methodology in design selection / material selection of turbine blades.

In result, an itemisation of the objectives was established to discretise the efforts constituting this work:

- (i) To conduct a critical literature review focusing on current, state-of-the-art experimental, analytical, and numerical modelling investigations in relation to the performance outcomes of ducted turbines and induced flow phenomena when succumb to a dynamic fluid flow;
- (ii) To establish a one-way fluid-structure interaction model of a true-scale ducted, high-solidity tidal turbine within verified tidal flow conditions implementing fibre-reinforced material properties;
- (iii) To develop a validated blade-resolved numerical model, coupled with a high-order turbulence model, of a horizontal-axis tidal turbine in application of rotary blade analyses;
- (iv) To establish the hydrodynamic performance and wake profiles of a ducted, high-solidity, open-centred tidal turbine, within verified tidal conditions, when succumb to flow vectors both aligned and misaligned to the turbine axis;
- (v) To analyse the structural response of a high-solidity turbine rotor when succumb to aligned and yawed hydrodynamic flow conditions, and propose an appropriate internal blade design;

- (vi) To acknowledge the most appropriate Reynolds-Averaged Navier-Stokes turbulence model for the numerical hydrodynamic analysis of a full-scale ducted turbine; and
- (vii) To establish the impact of discrete vortices upon the hydrodynamic properties of a ducted tidal turbine when present within the incoming flow.

1.3 Layout of the Thesis

This thesis undertakes a one-way (partitioned-approach) fluid-structure interaction (FSI) analysis of a ducted, high-solidity tidal turbine, where the numerical modelling schemes simulating the hydrodynamic flow, and the induced structural response, were resolved separately utilising two distinct, yet coupled, solvers. The hydrodynamic investigations within the domain, undertaken by means of finite-volume computational fluid dynamics (CFD), were primarily carried out to analyse the performance of the power-generating structure, and subsequently utilised as boundary conditions to establish the degree of structural discrepancy by means of the finite-element method (FEM). This thesis consists of eleven discrete chapters.

The second chapter presents a description of the underlying physics governing aerofoil theory and its utilisation in establishing the efficiency of power-generating horizontal-axis turbines. In compliment, supplementary adaptations into ducted turbine configurations, together with rotor characterisation in yawed flow and vortex flow conditions, are expounded. Furthermore, commercial applications implementing ducted tidal turbine technology are discussed, in addition to a detailed review of the recent, state-of-the-art ducted turbine experimental, analytical, and numerical investigations.

The third chapter provides a detailed elaboration into the background concepts of fundamental turbine theory and their numerical modelling capacities in specification to linear momentum (actuator disc) theory, blade element theory, and their coupled approach, whilst elaborating ducted turbine and yawed flow adaptations. In addition, the governing continuity equations, together with the turbulence models required to numerically describe a turbulent regime, are expanded as resolved by the computational

fluid dynamics technique. Furthermore, the physical characterisation of the numerical model, where the formulae utilised in relation to the physical parameters of the tidal turbine and in analysis of the fluid continuum, are specified.

The fourth chapter depicts the methodological procedures with which the one-way fluid-structure interaction analysis was performed. Describing the geometrical models, hydrodynamic parameters, and structural properties utilised within the turbine setup, a characterisation of the numerical framework, in reference to the techniques implemented within the computational fluid dynamic and finite element solvers, is presented.

The fifth chapter describes the validation outcomes of a blade-resolved computational fluid dynamic model whilst coupled with a high-order Reynolds-Averaged Navier-Stokes turbulence model, employed for rotary blade analyses, attaining good comparison with experimentation analysis of a bare horizontal-axis tidal turbine.

The sixth chapter describes the hydrodynamic performance analysis concerning a true-scale, ducted, high-solidity tidal turbine in axially aligned flow utilising the validated blade-resolved computational fluid dynamic model, elaborating the induced flow physics.

The seventh chapter describes the hydrodynamic performance analysis concerning a true-scale, ducted, high-solidity tidal turbine in yawed flow conditions utilising the validated blade-resolved computational fluid dynamic model, detailing the augmentation in rotor performance.

The eighth chapter elaborates a one-way fluid-structure interaction numerical model utilised in investigating the structural mechanics of the rotor blades comprising the ducted, high-solidity tidal turbine. Coupling the hydrodynamic outcomes as boundary conditions in effort of acknowledging the most applicable setup, three distinct designs are investigated: solid blades, cored blades, and reinforced blades, utilising fibre-reinforced composite material properties, analysed within criteria related to blade axial deformation, induced radial strains, and rotor specific mass.

The ninth chapter depicts an evaluation between the three most applicable ‘specific dissipation rate’ Reynolds-Averaged Navier-Stokes turbulence models for rotating bladed structures. By distinguishing the performance outcomes, an assessment is put

forward, evaluating the numerical terminology variation most effective in attaining a more representative simulation: the Wilcox assumption, the Menter assumption, or the Boussinesq-Menter assumption.

The tenth chapter describes the hydrodynamic performance analysis concerning a true-scale, ducted, high-solidity tidal turbine in vortex flow conditions by inducing a fixed vortex along a cell-zone within the domain, upstream of the rotor. Varying the diameter of the induced vortex stream in impact with the turbine, the deficiencies in rotor performance are elaborated.

The eleventh and final chapter presents a general description of the investigations carried out throughout the thesis, with concluding remarks and a closing summary, together with an outline for future work.

1.4 Research Gap & Novelty of the Study

Having established a comprehensive literature review in relation to the hydrodynamic and structural analysis of a ducted, high-solidity tidal turbine, four main factors were identified:

- (i) what is the blade-resolved performance in real-ocean conditions;
- (ii) what is the performance variation in yawed flow conditions, and its causation;
- (iii) what is the ideal interior structural design of the rotor blades under the acknowledged conditions; and
- (iv) what is the performance variation in vortex flow conditions.

In an effort to tackle the research questions and fulfil the research gap within the work presented, each chapter has a degree of novelty in its analysis to tackle the issues raised. Notably, this consisted of the implementation of computationally-intensive turbulence models, flow condition variations in evaluating the ducted turbine performance, comparison of numerical model assumptions, and manipulation of the domain to induce flow phenomena, where:

The fifth chapter provides an implementation of the Standard ‘specific dissipation rate’ Reynolds-Averaged Navier Stokes turbulence model in numerically simulating a blade-resolved, three-bladed tidal turbine to acquire hydrodynamic rotor performance validation, together with wake velocity profile development downstream of the turbine.

The sixth and seventh chapter evaluate the hydrodynamic performance of a blade-resolved numerical representation of the ducted tidal turbine within aligned and yawed flow conditions, utilising the Standard Reynolds-Stress turbulence model. The blade-integrated performance results were elaborated and verified by means of experimentation, blade-element momentum theory, and linear momentum theory in effort of acknowledging the variation in the hydrodynamic performance.

The eighth chapter tackles a three-dimensional, solid-body, finite-element analysis of a high-solidity rotor blade for a ducted turbine. The static pressure and wall shear-stress distribution loads were imported from the hydrodynamic solver onto the fibre-composite blades in the structural solver as boundary conditions, establishing a one-way fluid-structure interaction in the investigation of appropriate interior structural designs.

The ninth chapter puts forward the implementation of two supplementary ‘specific dissipation rate’ turbulence models in analysing the performance of the ducted, high-solidity tidal turbine in variations of the Standard Reynolds-Stress model, Baseline Reynolds-Stress model, and Shear-Stress Transport eddy-viscosity model. Further to the evaluation, the analytical formulae established through ducted turbine theory were solved utilising the data gained through the numerical simulations to establish a calibration effort for analytical models. A novel formula was then derived utilising one-dimensional momentum continuity, in concurrence to the theory, specifically for the static pressure and axial velocity at the turbine outlet.

The tenth chapter provides a manipulation of the geometrical domain by segregating a cylindrical partition. By coupling a physics code to the cell-zone, fixed vortices are introduced within the domain in the direction of the turbine. This permits vortex interaction with the rotor, investigating the discrepancy in the performance due to the induced hydrodynamic phenomenon.

1.5 Contribution to Knowledge

In recognition of providing to the state of the art, the following achievements were attained:

Journal Papers

M. G. Borg, Q. Xiao, S. Allsop, A. Incecik, and C. Peyrard, “A numerical performance analysis of a ducted, high-solidity tidal turbine,” *Renewable Energy*. Accepted - 2020.

M. G. Borg, Q. Xiao, S. Allsop, A. Incecik, and C. Peyrard, “A numerical fluid-structure interaction analysis of a fibre-composite, ducted, high-solidity tidal turbine rotor in aligned and yawed flow conditions,” *Ocean Engineering*. Under Review.

M. G. Borg, Q. Xiao, S. Allsop, A. Incecik, and C. Peyrard, “A blade-resolved numerical analysis of a ducted, high-solidity tidal turbine in yawed flow,” *Applied Energy*. Under Review.

Research Awards

OCEANS '18 MTS/IEEE Kobe, Japan Conference, “Student Researcher Competition”, *1st Place (Offshore Renewable Energy Section) | 2nd Runner-Up (Overall)*, Kobe, Japan

Energy Transfer Protocol (ETP) Conference '18, “ETP Researcher Presentation Competition”, *1st Place (Marine Energy Division)*, Glasgow, Scotland, United Kingdom.

Conference Papers

M. G. Borg, Q. Xiao, A. Incecik, S. Allsop, and C. Peyrard, “Analysing Fibre Composite Designs for High-Solidity Ducted Tidal Turbine Blades” in *OCEANS '19 MTS/IEEE Marseille, (Marseille, France)*, IEEE, 2019.

M. G. Borg, Q. Xiao, A. Incecik, S. Allsop, and C. Peyrard, “An Actuator Disc Analysis of a Ducted High-Solidity Tidal Turbine in Yawed Flow,” in *ASME 2019, 38th International Conference on Ocean, Offshore, and Arctic Engineering, OMAE 2019*, (Glasgow, Scotland), ASME, 2019.

M. G. Borg, Q. Xiao, A. Incecik, S. Allsop, and C. Peyrard, “Blade-Explicit Fluid-

Structure Interaction of a Ducted High-Solidity Tidal Turbine,” in *7th Oxford Tidal Energy Workshop (OTE2019), (Oxford, United Kingdom)*, University of Oxford, 2019.

M. G. Borg, Q. Xiao, A. Incecik, S. Allsop, and C. Peyrard, “Numerical Analysis of a Ducted High-Solidity Tidal Turbine,” in *OCEANS '18 MTS/IEEE Kobe, (Kobe, Japan)*, IEEE, 2018.

1.6 Chapter Summary

This chapter consisted of an introduction to the thesis, putting forward the premise of the motivations, objectives, and investigations tackled, holistically representing the research endeavours implemented in evaluating the blade-resolved fluid dynamics and structural mechanics of a ducted, high-solidity tidal turbine.

Chapter 2

Literature Review

This chapter presents a general elaboration of the physical concepts tackled throughout this work in investigating the response of a ducted, high-solidity tidal turbine. Primarily, the fundamental aerofoil theory governing the efficacy of power-generating horizontal-axis turbines is detailed, together with adaptations into ducted turbine configurations, in addition to output variations in differing environmental flow conditions. In compliment, commercial applications of the adoption of ducted turbines for large-scale projects in the tidal industry are acknowledged, accompanied by a detailed review of the recent, state-of-the-art ducted turbine experimental, analytical, and numerical investigations portrayed in respect of the current work.

2.1 Background Knowledge

In representation of the concept of ducted, high-solidity, horizontal-axis tidal turbines, a description of fundamental aerofoil blade theory is primarily put forward with regard to the forces and torques induced by the pressure distribution, and its augmentation due to a shroud installation, whilst succumb to aligned, yawed, and vortex flows.

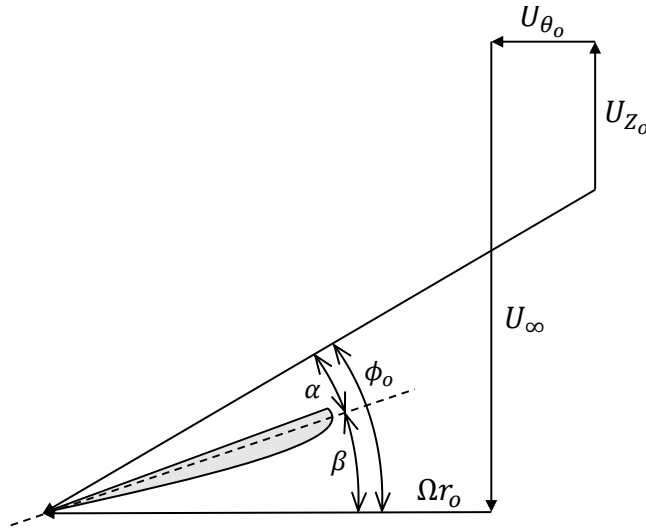


Figure 2.1: Local velocities at a blade element of a turbine rotor

2.1.1 Horizontal-Axis Turbine Blade Dynamics

A horizontal-axis turbine describes an energy-extracting system comprising of lift-generating bladed surfaces, positioned radially about a shaft, aligned characteristically with the direction of the domain free-stream flow. In consequence of the revolving motion, the distinct cross-sections along the blade are subjected to a relative velocity (V_{rel}) as a function of the free-stream velocity (U_∞) and the rotational velocity (Ωr_o), illustrated in Figure 2.1, together with the induced wake velocities, in the axial (U_{Z_o}) and the tangential (U_{θ_o}) directions relative to the rotor, due to the disturbance of the fluid by the rotor [5]:

$$V_{rel} = \sqrt{(U_\infty - U_{Z_o})^2 + (\Omega r_o + U_{\theta_o})^2} \quad (2.1)$$

In accordance to the relative velocity, its angle with the rotor plane, the in-flow angle (ϕ_o), may hence be established in relation to the velocity components:

$$\tan \phi_o = \frac{U_\infty - U_{Z_o}}{\Omega r_o + U_{\theta_o}} \quad (2.2)$$

where the in-flow angle is equivalent to the summation of the angle of attack (α) and

the geometric blade angle (β):

$$\phi_o = \alpha + \beta \quad (2.3)$$

The fundamental expressions for the forces developed within dynamic flow conditions upon a structure may be expressed as perpendicular components of the resultant force, drag (F_D) and lift (F_L) forces, in-line and normal to the relative velocity, induced by the fluid-structure interaction. Composed of pressure forces and frictional viscous forces, perpendicular and parallel to the structure surface, respectively, net drag and lift are established by means of their summation:

$$dF_D = (p - p_\infty)(\hat{\mathbf{n}} \cdot \hat{\mathbf{i}}) dS + \tau_w(\hat{\mathbf{t}} \cdot \hat{\mathbf{i}}) dS \quad (2.4)$$

$$dF_L = (p - p_\infty)(\hat{\mathbf{n}} \cdot \hat{\mathbf{k}}) dS + \tau_w(\hat{\mathbf{t}} \cdot \hat{\mathbf{k}}) dS \quad (2.5)$$

where p is the static pressure at the surface with surface area dS , p_∞ is the atmospheric pressure, $\hat{\mathbf{n}}$ is the vector normal to the surface dS , $\hat{\mathbf{i}}$ is the unit vector parallel to the direction of the relative velocity, τ_w is the shear stress acting on the surface dS , $\hat{\mathbf{t}}$ is the vector tangent to the surface dS , and $\hat{\mathbf{k}}$ is the unit vector perpendicular to the direction of the relative velocity.

In the case that pre-established processed data has been developed for a specific aerofoil, the induced forces may be analytically attained in relation to the properties of a dynamic rotor within a free-stream:

$$dF_D = \frac{1}{2}\rho c V_{rel}^2 C_D dr \quad (2.6)$$

$$dF_L = \frac{1}{2}\rho c V_{rel}^2 C_L dr \quad (2.7)$$

where ρ is the fluid density, c is the aerofoil chord length, C_L and C_D are the lift and drag coefficients, and r is the length of the blade cross-section.

In continuation, the resultant thrust (T) and torque (Q) developed as a result of the

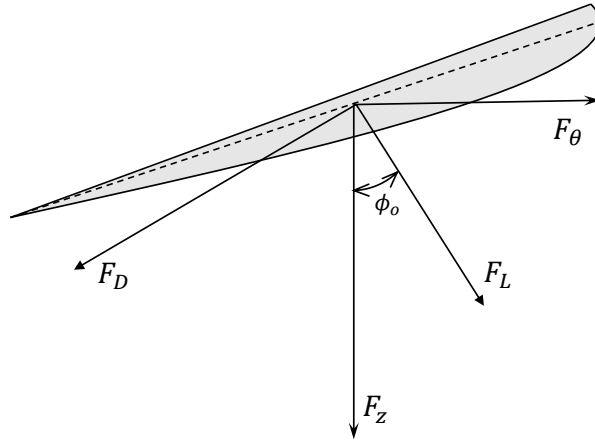


Figure 2.2: Local forces at a blade element of a turbine rotor

lift and drag forces upon the bladed surfaces, illustrated in Figure 2.2, may be deduced:

$$dT = dF_z = dF_L \cos \phi_o + dF_D \sin \phi_o \quad (2.8)$$

$$dQ = r \cdot dF_\theta = r \cdot [dF_L \sin \phi_o - dF_D \cos \phi_o] \quad (2.9)$$

which further establishes a coefficient classification of the resultant factors in relation to the properties of a dynamic rotor within a free-stream:

$$dT = \frac{1}{2} \rho c V_{rel}^2 C_T dr \quad (2.10)$$

$$dQ = \frac{1}{2} \rho c V_{rel}^2 C_Q r dr \quad (2.11)$$

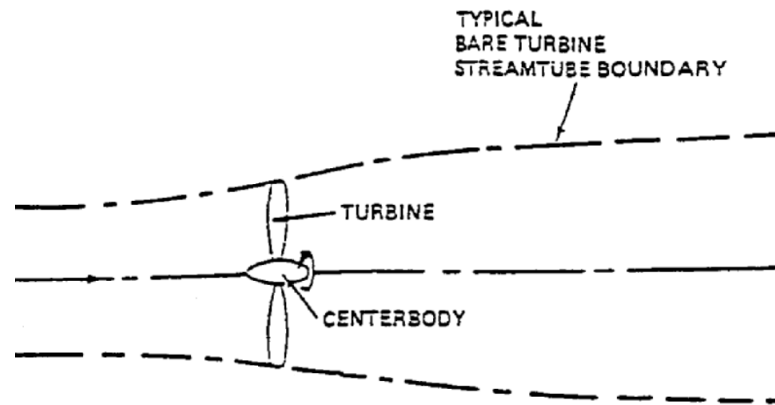
where C_T and C_Q are the thrust and torque coefficients.

In essence, therefore, as a flow-stream interacts with a turbine rotor, the kinetic energy is extracted from the incoming free-stream velocity as the fluid induces a pressure upon the surface of the blades, instigating a force distribution upon an array of blade cross-sections, consequently initiating a torque about the rotor centre of rotation; a theoretical limit of 16/27 (or 59.3%) was found to be the maximum degree of kinetic energy that may be extracted by an ideal rotor, as derived by Betz [6], with 16/25 (or 64%) being the limit for two rotors in tandem, as derived by Newman [7].

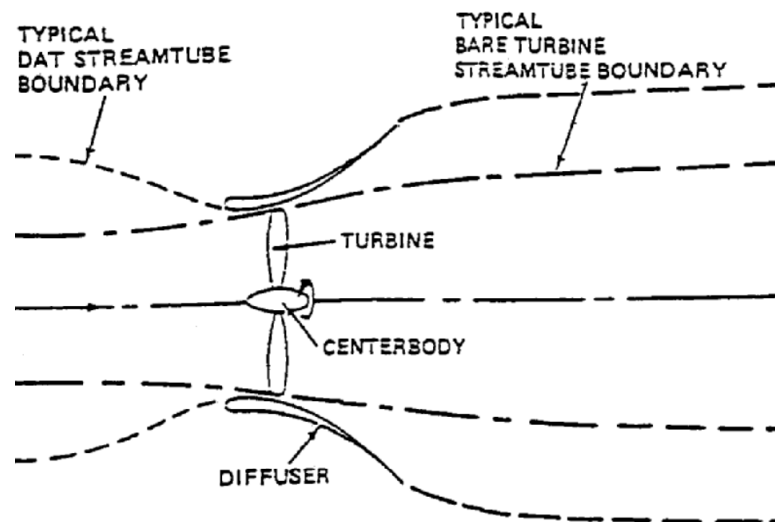
2.1.2 Ducted Horizontal-Axis Turbine Dynamics

Diffuser-augmented turbines, also referred to as ducted turbines, have been proposed as a fluid-flow energy conversion approach to potentially improve the economics of converting kinetic energy from a free-stream into useful mechanical power. In consideration of sustainable fluid-flow energy extracting systems, amongst the detrimental aspects of their implementation is the relatively low energy density and periodic, intermittent nature, of a flow-stream. In an effort to rectify this, the premise of the ducted turbine concept puts forward the installation of a static shroud, encompassing the rotor, to increase mass-flow and, hence, the fluid-energy density through the turbine as an alternative to constructing large rotating structures to capture large quantities of fluid.

Physically, once a ducted turbine is succumb by a free-stream, the interaction with the diffuser results in a greatly diminished region of pressure downstream of the rotor, compared with a bare turbine, dependent on the layout of the installation. As a result of the augmented pressure drop, an enhancement in mass-flow is induced through the rotor; the incoming velocity, together with the resultant relative velocity, exhibit an increase in magnitude, establishing a higher angle-of-attack, and, therefore, dependent on the pitch and geometric configuration of the aerofoil, a variation in the generated lift, torque, and resultant power is produced. Ducted turbines have been theoretically established to attain a peak power coefficient of $49/25$ (or 196%), equivalent to a 3.3 augmentation factor magnitude higher than the Betz limit, as derived by Riegler [8], due to the degree of flow drawn in from a greater area upstream than that interacted with by a similarly sized rotor in open flow, as illustrated in Figure 2.3. This considerable reduction in downstream pressure, however, may induce very strong adverse pressure gradients within the diffuser as the flow attempts to exit, resulting in the de-energisation of the boundary layer along the inner duct wall, diminishing boundary layer momentum, and increasing the probability of boundary layer separation. In recognition, auxiliary slots, illustrated in Figure 2.4, are fabricated for boundary-layer control to re-energise the boundary layer, and sustain the diffuser efficiency through the pressure difference and mass-flow along the duct [9].



(a) Representation of a bare turbine and its stream-tube boundaries



(b) Representation of a ducted turbine and its stream-tube boundaries

Figure 2.3: Illustration of stream-tube boundary distinctions between bare turbines and ducted turbines [8]

For the reason that rotor power is relative to the flow-rate and pressure drop of the flow-field, as described by linear momentum theory, the resultant performance of a rotor within a free-stream may be potentially improved by a significant degree. Yet, albeit the advantages, for the shrouded turbine concept to be commercially viable, the structural costs of the diffuser installation must be firmly offset by the improved annual energy production as a result of the enhanced power generation; a compromise between diffusers with large outlet-to-inlet area ratios and structural expenditure is therefore required [11]. In essence, this classification of energy conversion systems may

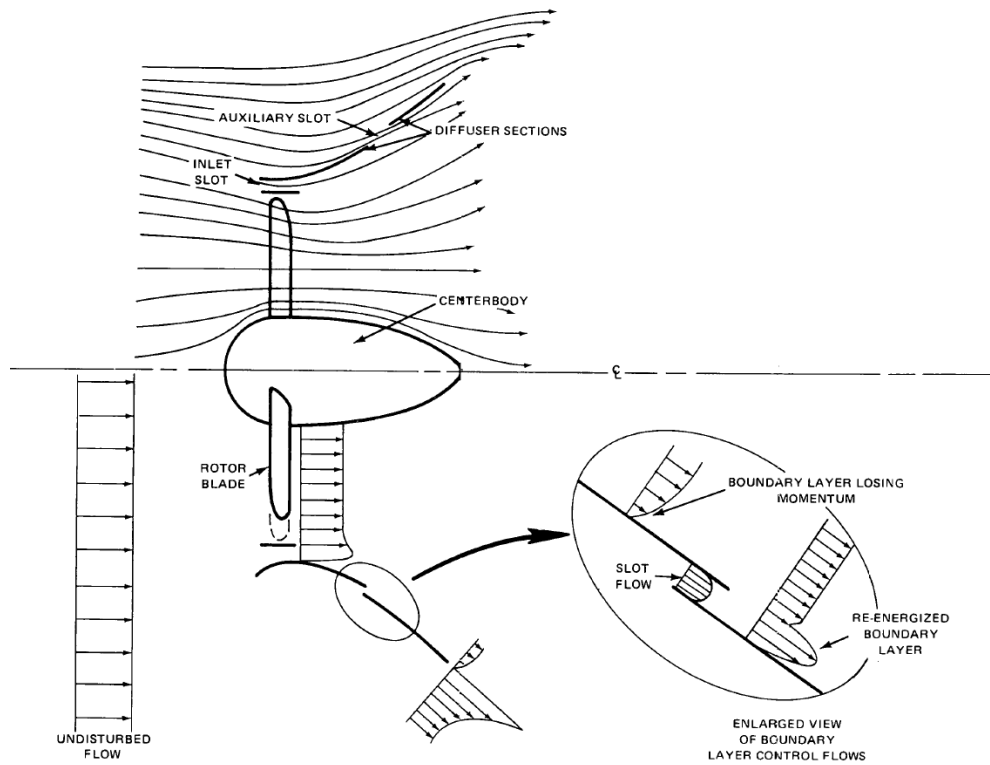


Figure 2.4: Schematic of the flow-field along a boundary-layer-control diffuser-augmented turbine configuration; depicts the additional momentum injection through auxiliary slots, preventing boundary layer separation within the duct [10]

be considered to potentially provide a significant contribution to the global energy requirements, moreover in site-specific cases with lower mean flows, if established to be cost-competitive with alternative energy-generating systems. In concisely elaborating the advantages of the implementation of a turbine equipped with a duct, established by means of theoretical analysis, field experiments, and numerical simulations, the following aspects have been put forward:

1. Improved rotor efficiency – As elaborated, the installation of a diffuser generates a high pressure difference fore and aft of the rotor and, together with a Venturi converging-diverging profile at the throat of the duct, the incoming velocity of the tidal stream is accelerated toward the rotor, resulting in a concentration of mass-flow through the turbine. This augmentation of flux induces an output power increase factor of approximately four to five times that of conventional

turbines [12]; this, however, is solely applicable to the dynamics of a diffuser (uni-directional duct) turbine. The power output of a ducted turbine with a cylindrical (bi-directional) external duct profile is theoretically correspondent to that of an unshrouded rotor possessing an identical rotor-disc area as the duct inlet and exit areas, whilst attaining an equivalent pressure drop, of the ducted arrangement [13]. As comparable power generation capacities may be attained, smaller rotor blades may therefore be utilised within a ducted turbine arrangement, thereby keeping costs of manufacture and maintenance down.

2. Consistent output at both tidal directions (bi-directional duct) – A bi-directional turbine unit incorporates a symmetrical duct & rotor system in which the blades are designed to attain equivalent performance in either tide direction. In this respect, there is no need to rotate the entire unit or vary the pitch of the blades when the tide turns, reducing capital and operational costs.
3. Limitation of wake expansion – Downstream of a single bare rotor, flow continuity through the stream-tube is sustained as the volume of the flow expands due to the comparatively lower static pressure, increasing the possibility of wake-interaction with neighbouring turbine units. With a duct installation, the flow boundaries immediately downstream of the rotor are physically defined, hence limiting the wake expansion from interacting with turbines in the vicinity [9].
4. Reduction in turbine noise – The vortices generated from the blade tips that create acoustic pulsations are suppressed by the interference of the boundary layer within the diffuser shroud; correspondingly, the noise is reduced definitively [14].
5. Shallow water implementable – Within sites where large, cumbersome turbines are not suitable, smaller, shrouded turbines may be seabed-mounted, permitting safe navigation of the water ways [15].
6. Eco-benign & bio-fouling resistant – As the blades are concealed, shrouded rotors are unexposed to the environment installed within, hence presenting little to no visual impact. Additionally, bio-fouling is potentially reduced due to the shroud

presence, diminishing natural light exposed upon the blades, while the increased velocities through the turbine flushes the shroud throat and rotor, disallowing organisms to attach at the increased velocities [16].

7. Improved safety – The turbine blades, rotating at high rotational velocities, are shrouded from impacts with foreign objects [12].
8. Performance sustainability under yawed and unsteady conditions – In the case of a fixed turbine succumb to yawed flow, the local flow at the throat, instigated by the pressure drop, largely converges to a vector normal to the aperture plane, and hence the rotor plane, due to the variation in cross-sectional area within the duct. Considering that the yaw angle is not substantial, the induced outcome is adequate in aligning the intake flow velocity to be perpendicular to the rotor; as a result, any variations in tidal stream direction offset from the axis of the rotor will be counteracted and balanced by the flow phenomena [17]. In addition, due to the convergence region ahead of the rotor, the static pressure build-up reduces the unsteadiness of the flow across the turbine, improving the uniformity of the performance output [13].
9. Flange-based yaw control – In the case of a non-fixed turbine, the flange along the outlet of its diffuser enables uni-directional ducted turbines to rotate with the incoming flow, given a variation in flow direction, to face the free-stream, acting as a passive yaw mechanism [12].

2.1.3 Turbine Dynamics in Yawed Flow Conditions

Yawed flow conditions describe a fluid domain in which the free-stream acts at a vector non-perpendicular to the rotor plane of a power-generating turbine. A bare turbine operating in yawed conditions typically brings about diminished energy conversion efficiency, as depicted in Figure 2.5, due to the lessened exposed rotor area, altering both the resultant axial velocity through, and pressure difference fore and aft of, the rotor, indifferent of the rotor solidity [18, 19]. Succumb to the angular flow direction, the rotating blades additionally experience a variation in relative velocity, and hence

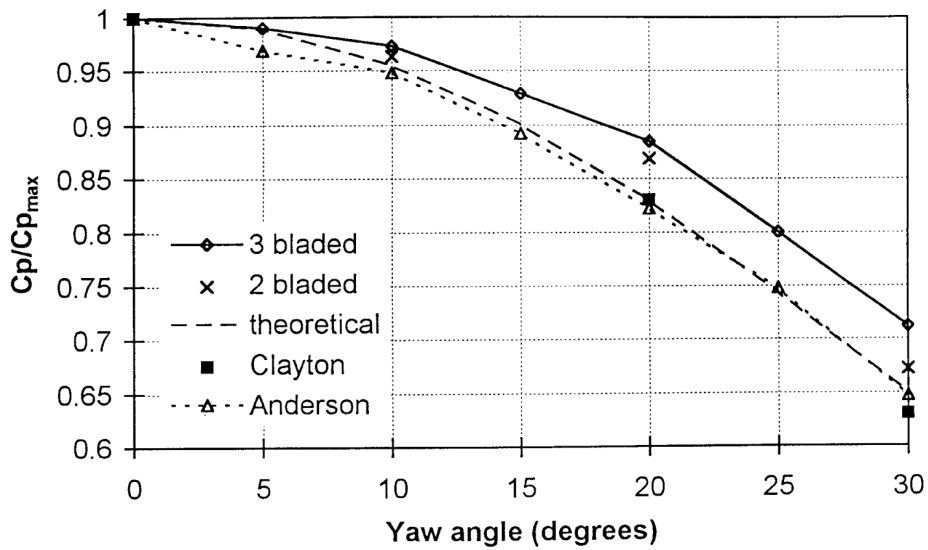


Figure 2.5: Variation of maximum power coefficient as a function of yaw angle [21]

angle-of-attack with azimuthal blade position, inducing unsteady fluid load variations and relevant structural responses along rotational periods [20].

Oceanographic studies have tackled the variance in the instantaneous direction of a tidal current, establishing a non-linear relationship with both water depth and peak tidal velocity [22]. Albeit the acknowledgement of the periodic, cyclic characteristics of the mean velocity of tidal currents [23], further analyses have been performed on band-passed time series of barotropic and baroclinic velocity components that retain a semidiurnal frequency band tidal species [24]. The principal axis analysis of barotropic band-passed currents demonstrated the polarisation of semidiurnal tidal ellipses in the cross-isobath direction. In contrast, baroclinic tidal currents were found to be less polarised; towards the surface, at 10 m depth, the principal axes were consistently oriented to the cross-isobath direction, yet the tidal ellipses were found to be less elongated in comparison to barotropic currents. The polarisation of baroclinic tidal ellipses dissipated further along the near-bottom layer, at which the principal axes ceased orientation in the cross-isobath direction. Estimating the spectral amplitudes of baroclinic velocity components at layer depths farther than 10 m, the phase differences were acknowledged to delineate the vertical structure of the semi-diurnal frequency band tidal species, resulting in the near-surface and near-bottom flows to attain an

approximately opposite (180°) phase difference. Furthermore, Pham and Martin [25] and Pham and Pinte [26] conducted numerical models to simulate the tidal cycle at the Paimpol-Bréhat site. Acknowledging an asymmetric velocity in both magnitude and direction at flood and ebb, higher maximum velocity magnitudes were attained within the prior, with two prevailing bearings being identified along the bi-directional flow, 120° and 320° clockwise from North during flood and ebb, respectively, establishing an average-depth angular discrepancy of 20° .

Albeit modern turbine designs are configured with yaw mechanisms to align the rotor to the free-stream, a number of tidal turbines currently in operation are either installed upon the seabed by means of a gravity base framework [27], or just below the waterline secured to a vessel [28]. As a result, the response to an abrupt variation in flow direction is either slow-moving or non-existent and, hence, in consequence, is present within yawed conditions for a substantial period of its operational lifetime.

Nonetheless, rotors operating within turbine farm conditions may, alternatively, be subject to efficiency increases as a result of the yawed flow circumstances; a downstream rotor, succumb to axial flow within a turbine farm, may attain efficiency ratings of solely 40% to that of a standalone rotor due to the reduced energy within the wake of upstream turbines, dependent on the mean velocity magnitude and turbulence intensity conditions of the free-stream [29]. Upon being subject to yawed flow conditions, therefore, a turbine farm may collectively generate a higher degree of power due to lesser interactions between rotors and the induced wakes. For this reason, in consideration of a turbine system that sustains efficiency through an angular flow bearing, further power output may potentially be generated within a farm when succumb to yawed flow at an optimal bearing; yawed flow investigations are therefore imperative in acknowledging the variation in power conversion efficiency of a turbine rotor.

2.1.4 Turbine Dynamics in Vortex Flow Conditions

In consideration that the analysed ducted tidal turbine may be installed within a tidal turbine farm site that potentially constitutes a turbulent, vortical domain, the resultant hydrodynamic effects upon the structure may induce a substantial variation

in response performance, and, hence, encumber the operational capacity of the tidal installation. Classifying the induced physics dependent on the length-scale size of the eddy currents present within the flow, Clark [30] described the effects imposed in relation to the fluid-structure interaction.

Upon blade rotation, the helical wake sheets shed from the trailing edge influence the flow parameters upstream of a neighbouring turbine rotor. The sheets are distorted by large (l_{lrg}) to middle (l_{mid}) scale vortices, and diffused by small (l_{sml}) scale vortices, non-linearly manipulating the in-flow velocity interacting with the downstream rotor blades; the distortion and dissipation of the vortices present within the turbine wake vary the mean mass-flux and velocity profiles of the flow, altering mean and periodic loads, as the wake interacts with downstream rotors.

In reference to the fluid-structure interaction, flow fluctuations having a characteristic length scale smaller than the blade chord length, $l_{sml} < c_{rtr}$, influence the boundary layer properties at the blade surface, notably skin friction and transition location, varying the mean drag-and-lift coefficients of a blade section. The hydrodynamic performance of a device is therefore affected without physically exerting a load, as the scale is significantly smaller than the structure itself, and hence any direct loading disperses over the surface; this occurrence alters dynamic stall and cavitation susceptibility, transpiring periodically within the rotor cycle. Mid-scale eddies have a characteristic length scale that is larger than l_{sml} , yet not of considerable size to be misinterpreted for a variation in the mean flow. As a turbine wake is considered to physically represent a dynamic variation of the mean fluid-flow, the upper limit of the mid-length scale range is taken to be the turbine disc diameter, $c_{rtr} \leq l_{mid} \leq 2R_{rtr}$. Mid-scale vorticial motions exert bouts of snap (un)loading as blades pass through the eddy formations, inducing a variation in the local angle-of-attack, affecting blade bending modes and amplitudes. Similar to smaller scales, local extreme variations in angle-of-attack caused by mid-scale vortices may induce dynamic stall and/or cavitation. Large-scale eddies, having a characteristic length-scale larger than the turbine disc diameter, $l_{lrg} > 2R_{rtr}$, exert uniform parameters once evaluated over an area as large as a turbine disc, yet encompass intermittency and fluctuations on a larger scale

of the domain; the eddies hence induce a variation in accordance to the mean flow within the entire domain, yet the parameters induced upon the turbine structure are largely consistent due to the physical magnitude.

2.2 Commercial Applications of Ducted Tidal Turbines

Tidal stream turbine (TST) technology has been in its primal, developmental phase for the past decade with substantial potential, yet has not taken off as rapidly as had been predicted. This outcome has been argued to be largely due to engineering challenges in designing for extreme operating conditions, in combination with political and environmental factors, which has limited the rate of industry maturity [1]. Albeit the drawbacks observed in the tidal industry, European, North American, and Asian states have largely invested in the deployment of full-scale tidal turbine arrays, with a wide range of the European investment being installed within territorial waters of France and the United Kingdom [31].

In specification to ducted turbine configurations, interest had been notably enticed due to the potential increase in power extraction as a result of the enhancement of mass-flow through the rotor. A number of commercial endeavours have attempted to adopt ducted turbine technology in attaining economical prospects, yet a substantial quantity of the investments have ensued in insolvency and cessation to the point that, as of late 2019, the pursued tidal projects have been either largely abandoned or are currently ambivalent [31, 32]. Consequently, despite the milestones, the imminent commercial instability of the development of ducted turbines may potentially falter the perception of this technology.

2.2.1 Bi-directional Ducted Tidal Turbine Projects

Bi-directional turbine units describe a symmetrical duct & rotor system with a converging-diverging aperture. Inducing a Venturi effect at the throat, the blades are designed to attain equivalent performance in either tide direction, rendering yaw mechanisms unessential, hence advantageous in limiting the quantity of moving components

in the system, and, therefore, capital and operational cost of the installation.

Lunar Energy Ltd.

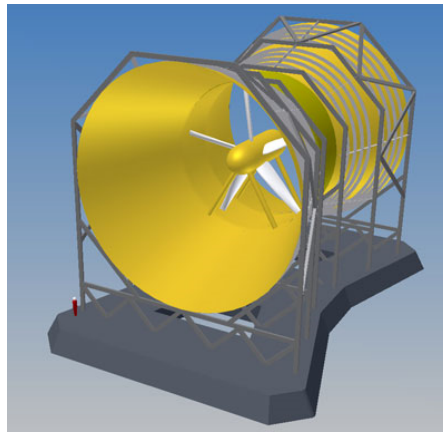
The Rotech tidal turbine, a robust five-bladed structure developed by Lunar Energy Limited in collaboration with Rotech Fabrication Limited, was conceptually designed to generate a peak device power of 1.5 MW at a rated flow-speed of 3.1 m.s^{-1} [33]. The 27 m long, 1200 tonne turbine, with inner and outer diameters of 16 m and 21 m, respectively, therefore attained a power coefficient of 0.32; a prior, three-bladed version, 19.2 m long with a 15 m external diameter, was deemed to generate a rated power of 1 MW [34]. The turbine body, supported by a heavy-duty bracket, as illustrated in Figure 2.6a, was designed to sink through the site seabed by means of gravity, reducing the anchoring cost; the rotor was constructed to be separable from the bracket and shroud to facilitate maintenance. Experimentation had been undertaken in 2007, with site development in British waters proposed in 2011, yet the project was not further developed.

Clean Current Power Systems Inc.

The Clean Current CC035B turbine, a four-bladed structure with a 20 m-diameter rotor, illustrated in Figure 2.6b, was designed in collaboration with Alstom SA to generate a peak device power of 2.2 MW and 3.5 MW at rated flow speeds of 3.0 m.s^{-1} and 3.5 m.s^{-1} , respectively [34, 38]. Tested within Canadian waters prior to project abandonment in 2015, the turbine was arranged to anchor to the seabed by a single pile or gravity base. The turbine boasted a simple design with generator magnets embedded into the rotor blades, and windings in the stationary shroud, hence making a nacelle redundant and consigning an aperture in replacement; the direct-drive, variable-speed, permanent magnet generator permitted the capacity to produce both alternating and direct current [33].

Atlantis Resources Corporation Pte Ltd.

The Solon (AS) tidal turbine, a six-bladed, 20 tonne, 8 m-long structure with rotor and duct diameters of 5 m and 7 m, respectively, illustrated in Figure 2.6c, had undergone offshore tow-testing along the coast of Singapore in 2008, producing in excess of 500kW in 4.1 m.s^{-1} flow; a 0.1, 0.5, 1, and 2 MW turbine series was made avail-



(a) Lunar Energy [35]



(b) Clean Current Power Systems [36]



(c) Atlantis Resources Corporation [37]

Figure 2.6: Bi-directional ducted tidal turbine projects

able [34]. Further development led to the AK series in 2011, a twin-rotor set with fixed pitch blades, with a power generation capacity of 1 and 2 MW at a rated flow of $2.6 \text{ m}\cdot\text{s}^{-1}$; the projects have since been abandoned [33,41].

OpenHydro Group Ltd.

Amongst the ventures, OpenHydro Ltd. had, disputably, attained quasi-sustainable grid implementation with an open-centre ducted design approach, in which an aperture is employed at the centre of the turbine in replacement of a turbine nose cone hub [42, 43]. Due to this approach, the setup not only utilised the duct as a flow modifier, but also as a unit in which the power generating system may be housed. DCNS/OpenHydro Ltd. had successfully installed a 21 m tall, 16 m diameter wide [34], 850 tonne [44], 2 MW turbine in the Bay of Fundy, Canada, illustrated in Figure 2.7a, at 35 m depth [45],



(a) 2 MW-rated turbine for the Cape Sharp project [39]



(b) 500 kW-rated turbine at the Paimpol Bréhal site in Northern France [40]

Figure 2.7: The OpenHydro PS2 Ducted Turbine

together with a pair of 500 kW rated capacity turbines, illustrated in Figure 2.7b, as a demonstration array in Paimpol-Bréhat, Northern France, in collaboration with EDF France. The latter turbine solely attained a peak device power coefficient of 0.16 at a rated flow speed of $2.5 \text{ m}\cdot\text{s}^{-1}$, hence notably falling within the lower sectors of the overall turbine performance ratings. Albeit, due to the distinction in the rotor and device diameters, 5 m and 7 m, respectively, the rotor power coefficient increases by a factor of 2.0, hence resulting in an adequate performance value of 0.32 [33]. Project development had ceased in mid-2018.

2.2.2 Uni-directional Ducted Tidal Turbine Projects

Uni-directional turbine units describe a non-symmetrical duct & rotor system in which the blades are designed to attain performance in a singular tide direction. Due to its non-symmetric features, a uni-directional tidal turbine exhibits superiority if installed within river basins or an ocean current system, as the flow acts in a singular direction, yet requires a passive yawing mechanism design to attain rotor alignment once installed within a tidal stream. Albeit not many large-scale projects have been proposed, the more prominent uni-directional tidal turbines, which had had considerable investment into their development, include Blustream by Guinard Energies [46], EET SeaUrchin by Elemental Energy Technologies Ltd. [47], G-TT by Green-Tide Turbines Ltd. [47], and Underwater Electric Kite by UEK Corporation [48].

2.3 State of the Art

A detailed review of preceding analyses, regarding state-of-the-art experimental, analytical, and numerical investigations, conducted in relation to the performance outcomes of ducted turbines, is portrayed and associated to the current work.

2.3.1 Experimental Investigations of Ducted Turbines

In establishing amongst the earliest developments in ducted turbine research, experimentation analyses, initially conducted several decades ago, has consisted of analysing rotor-embedded shrouds, describing an operational rotor within a duct, disc-embedded shrouds, describing a porous disc in representation of the rotor, together with vacant shrouds, describing an empty duct, to acknowledge the variations in flow-field parameters due to the performance-enhancing installation.

2.3.1.1 Vacant Shrouds

In investigating the influence of the presence of a shroud along the rotor perimeter, initial studies describe the experimentation of a shroud, vacant, within a free-stream, as illustrated in Figure 2.8. These analyses have established the axial velocity and static

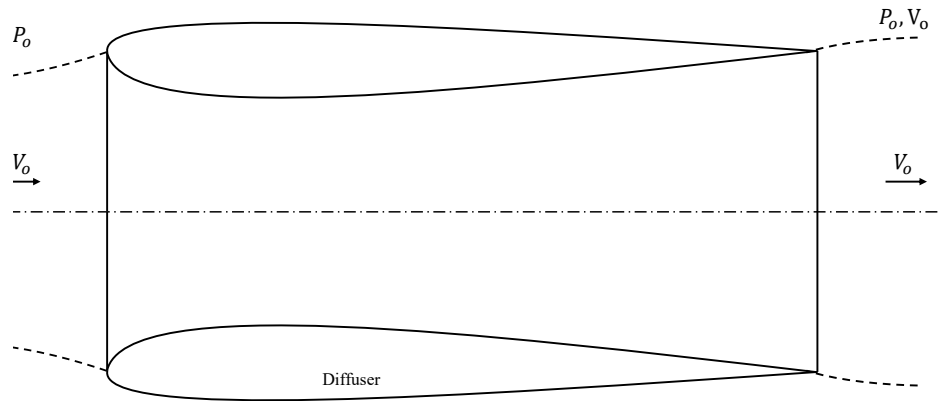


Figure 2.8: Illustrative representation of a vacant shroud within a free-stream

pressure of the mass-flow through, variation in static pressure distribution along the interior and exterior upstream surfaces of, geometrical optimisation of, together with the inclusion of performance-enhancing components within, a diffuser when succumb to aligned and yawed flows.

Within a fluid domain, an enhanced mass-flow is instigated through a diffuser; Kogan and Seginer [49] describe the driving factors for this phenomenon to be: (i) the production of a low-pressure region downstream of the structure due to flow deviation away from the diffuser outlet, hence segregating the outlet region from the energised free-stream, and drawing in a larger amount of fluid, together with (ii) a flow acceleration induced by an areal contraction of the shroud inner orifice, in accordance to Bernoulli's principle. Ohya et al. [12] evaluated three distinct duct structures: a nozzle, cylindrical, and diffuser form types. The cylindrical duct was found to sustain an axial velocity relatively equivalent to the free-stream throughout its length, whereas the diffuser-type accelerated the flow by a magnitude of ≈ 1.8 as a result of the negative static pressure induced, a factor of ≈ -1.9 the atmospheric pressure; the nozzle-type attained a general diminished mass-flow through. In continuation, performance-enhancing components, namely an inlet rim and an outlet ring-type flange, were incorporated to the ducts to investigate the resultant performance augmentation. Their combination, rather than their independent installation, attained the highest flow rate, where, with a variation in diffuser length to establish the optimal geometrical parameters, a maximum flow

acceleration magnitude of ≈ 2.3 was attained at the highest duct length. Masukume et al. [50, 51] similarly discussed the enhanced mass-flow relevant to the variation in length-to-throat-diameter ratio and expansion angle of the diffuser in establishing the optimum geometrical shape parameters for maximum duct flow rate. On average, a maxima magnitude of ≈ 1.5 the free-stream velocity was attained through the diffuser at all combinations of length ratios and diffuser expansion angles.

In specification of a tidal current application, Setoguchi et al. [52] developed three geometrical variations for a two-way, symmetrical, bi-directional diffuser: a shell-type for unmodified-control comparison, a straight-type describing a solid diffuser with an outer duct surface parallel to the centre axis, and a bulge-type describing a solid diffuser with an outer duct surface mirroring the inner duct surface. Comparing the increase in axial velocity through the duct orifice, the highest performance was attained by the straight-type bi-directional diffuser with a vertical rim (brim) at the outlet to induce a higher pressure drop, accelerating the flow within the duct by a magnitude of 1.3, whilst limiting the region of flow separation along the outer surface of the duct. Ponta and Jacovkis [53] designed and constructed channelling devices to be installed on a seabed for the purpose of accelerating the flow through a rotor. Albeit not designed to be directly attached to a rotor, the structures resembled an extruded lateral cross-section of a duct; the designs consisted of a diffuser-type layout, with widened edges downstream of the flow accelerator, and straight-type, with external edges parallel to the turbine axis. Specifically designed for low-current tidal regions, the flow accelerators increased the velocity through the vacant throat by $\approx 42\%$ to $\approx 82\%$, dependent on the geometrical layout of the structures.

Analysing the static pressure distribution along the leading edge of a vacant diffuser within aligned and yawed flow conditions, Cresswell et al. [17] acknowledged a pressure increase at both the internal and external surfaces of the diffuser with an increase in yaw bearing, eventually inducing flow separation within the shroud at high flow bearings, instituting diffuser stall. This occurrence was found to be a result of the angle-of-attack between the external flow and the diffuser internal wall, which increases proportional to the yaw angle. In accordance, greater degrees of flow separation are induced within

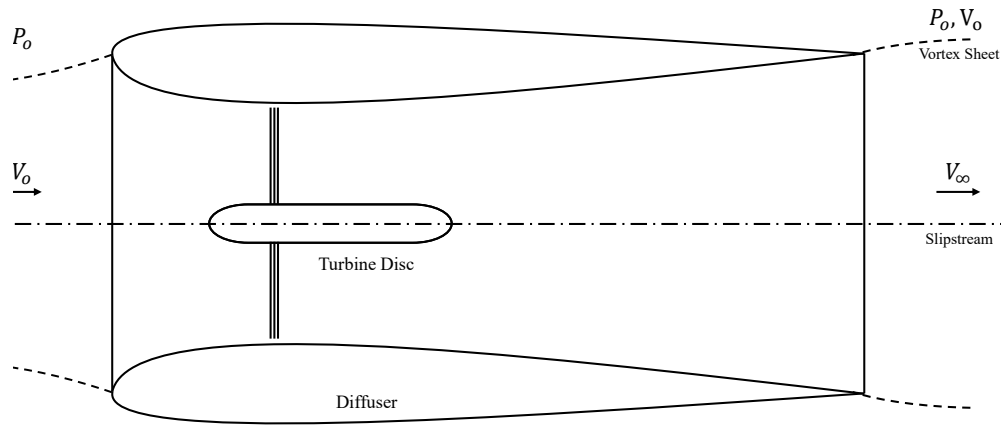


Figure 2.9: Illustrative representation of a disc-embedded shroud

the internal upstream section of the diffuser, leading to an adverse pressure gradient and a reduction in the flow velocity. With the reduced velocity, insufficient boundary layer momentum was sustained for the flow to retain attachment to the downstream section of the diffuser.

2.3.1.2 Disc-Embedded Shrouds

Secondary analyses include an identical experimentation methodology, yet introducing a meshed screen disc within the shroud in an effort to induce a pressure discrepancy and, hence, simulate the presence of an embedded rotor, as illustrated in Figure 2.9. This approach introduces a number of limitations, namely an absence of turbine wake tangential exit-swirl and radially-divergent flux, yet it has been acknowledged to obtain sufficiently accurate performance trends of the disc-loading (thrust) coefficient at low financial expense. These analyses have established the axial velocity of the mass flow through, geometrical optimisation of, and the inclusion of performance-enhancing components within, the diffuser when succumb to aligned and yawed flow. In addition, blunt comparisons of the fluid dynamic properties of bare discs to shrouded discs were put forward.

Conducting small-scale model experiments in a low-speed, low-turbulence, free-jet tunnel facility, Foreman et al. [54] investigated unconventional, very short, cost-effective diffuser configurations in preventing separation of the internal boundary layer within

the diffuser by means of two designs: the primary allowed the introduction of the external energetic fluid through boundary-layer-control auxiliary slots, whilst the secondary utilised flapped-ring wings formed from high-lift aerofoil contours in representation of the diffuser wall shape. Both designs successfully increased the resultant power by a factor, yet, the prior design, with a 30° diffuser angle, was deemed to be the more effective, attaining a 1.9 magnitude factor over the original performance at a load coefficient of 0.6, compared to 1.6, attained by the latter, at a load coefficient of 1.1.

Within the same facility, Gilbert et al. [55] simulated a number of ducted turbines, within which a 0.045 m diameter screen was placed precisely at the boundary-layer-controlled diffuser inlet. Distinct diffuser orientation angles were utilised, varying from 40° to 90° , hence establishing a range of diffuser-exit-to-screen-area ratios, from 1.28 to 4.94, with and without centre-bodies, at a diffuser-exit-based Reynolds number of 6×10^4 . The screens simulated turbine loading coefficients of 0.37 to 0.93, where, from the designs tested, one was selected as a cost-effective candidate baseline configuration for further testing. The referred design consisted of a 60° angle conical diffuser with a disc-loading coefficient of 0.63. By means of the experimentation, the maximum performance attained was a magnitude of 1.9 above the ideal conventional rotor, in agreement with values deduced by linear momentum theory, concluding that the optimum configuration is a trade-off between expenditure and benefit of additional auxiliary slots for boundary-layer control. Further to this, in an approach to reduce tower and structural costs, the simulated turbine experimentation was carried out within close proximity to the ground to examine the system performance. With the trailing edge of the diffuser directly on the ground plane, the upper portion of the diffuser exhibited a very slight increase in mass-flow when compared to the same diffuser configuration away from the ground plane. The lower section of the rotor also exhibited improvement, albeit nearer to the ground, with the flow-rate increasing by 10 to 14%. This increase was deduced to be a result of the distortion of the exit plane static-pressure profile, yet no evidence of this was apparent from the exit plane static-pressure surveys. In speculation, however, this increase in flow-rate may have been induced due to the increase in blockage ratio at the horizontal ground plane, hence resulting in more fluid to enter the diffuser due to

a pressure build-up between the structure and the ground plane.

Advancing into large-scale experimentation, Gilbert and Foreman [56] fabricated a 0.45 m diameter screen within a boundary-layer-controlled diffuser, ten times larger than the prior tests, with disc-loading coefficients of 0.390, 0.465, and 0.565, at higher flow-stream velocities, to attain a diffuser-exit-based Reynolds number of 2×10^6 , in replication of a real-scale turbine configuration. The large-scale models induced a higher degree of mass-flow, therefore attaining a higher power coefficient than the smaller models at an identical local loading. This outcome, however, was primarily a Reynolds number effect; larger models with higher Reynolds numbers have relatively diminished frictional loss, and hence, both the diffuser and the injection slots attain better performance. Due to the Reynolds number effects, however, the screens selected were unable to exceed the predicted optimum loading coefficient; by extending the experimentation results by means of axial momentum theory, it was projected that the maximum augmentation was to be ≈ 2.57 at an average free-stream disc-loading coefficient of ≈ 1.22 . The empirical prediction of the large-scale loading coefficient was found to be in better agreement with the ideal one-dimensional momentum theoretical value in comparison to the values established by means of the small-scale models, largely due to the lessened frictional effects.

In acknowledging performance-enhancing parameters for a shroud, Igra [57] made use of a number of NACA 4412 shroud profiles incorporated with supply holes and discharge holes along the inlet and outlet of the duct, respectively, to vary the pressures at both ends of the screen; a NACA 4412-profiled ring flap was additionally installed downstream of the duct to induce a more substantial pressure drop. Flow was regulated through the supply and discharge holes to prevent boundary-layer separation due to the rapid cross-sectional area divergence within the shroud downstream of the screen; the bleeding effect increased the efficiency of the duct, permitting higher mass-flow through the shroud in addition to the flow induced by the pressure drop at the NACA-profiled ring flap. Through the experimentation, it was acknowledged that, for a shroud with comparatively small diffuser-area ratios, the flow appeared to aptly adhere to the internal shroud wall and, hence, no exchange in flow is required. For shrouds analysed

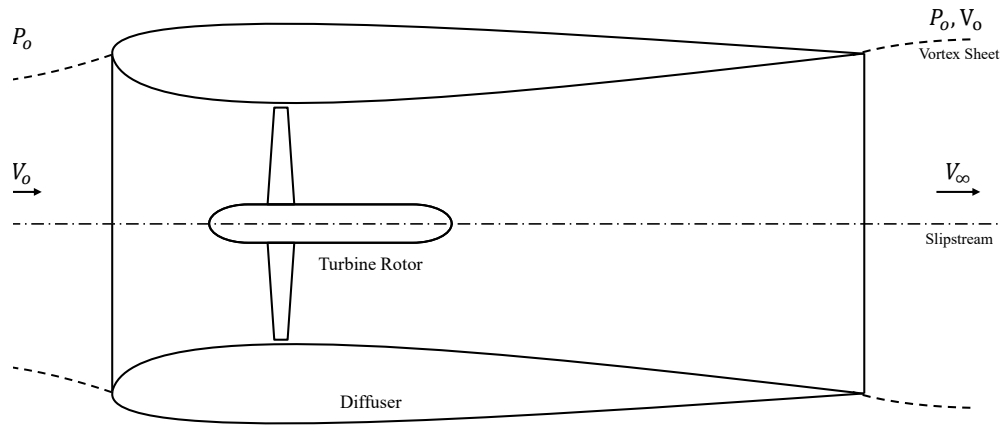


Figure 2.10: Illustrative representation of a rotor-embedded shroud

with increasing diffuser-area ratios, however, boundary-layer separation was present, requiring the use of the supply and discharge holes to divert the outside flow towards the internal shroud wall and sustain the efficiency of the shroud. Further investigations included establishing the resultant power output when the ducted turbine was succumb to yawed flow conditions. Varying the incoming free-stream within an angular bearing range of $-30^\circ < \gamma < 30^\circ$, whilst utilising the ring flaps and supply and discharge holes, the performance was found to vary dependent on the boundary-layer control parameters of the shroud, where a maximum power coefficient augmentation ratio of ≈ 2.69 was attained at a yaw of 15° , with a largely symmetrical response along the bearing range.

2.3.1.3 Rotor-Embedded Shrouds

Tertiary analyses include an identical experimentation methodology, yet introduce a turbine rotor within the shroud in an effort to attain the true fluid dynamic performance of an embedded rotor within a turbine shroud, as illustrated in Figure 2.10. These analyses have established the axial velocity and static pressure of the mass flow through, variation in static pressure distribution along the interior and exterior upstream surfaces of, geometrical optimisation of, rotor blade variation of, and the inclusion of performance-enhancing components within, the diffuser when succumb to aligned and yawed flow. Collectively, the majority of the works underlined describe blunt comparisons of the fluid dynamic properties of bare rotors to shrouded rotors.

In analysing the static pressure along the surface of a rotor-embedded shroud, Cresswell et al. [17] acknowledged a variation in the values attained to that of a vacant structure. Upon the introduction of a rotor, the leading external section of the diffuser encounters a degree of negative pressure when succumb to aligned flow, described to be due to the induction of fluid build-up within the shroud upon the introduction of the rotor, disallowing an equivalent flow-rate to pass through the shroud, resulting in a degree of flow spillage from the inlet, instigating flow separation; the pressure region then increases with an increase in yaw bearing. Luquet et al. [58] tested a 1/16th-scale model of a ducted current turbine unit; comparing a two-bladed to a four-bladed rotor, the prior was acknowledged to generate a higher degree of power, whereas the latter attained the higher degree of torque, within the water current-speed range investigated. As a result of this outcome, further analysis in varying the pitch of the rotor blades was undertaken, acknowledging a 5° pitch to be the optimal blade parameter for the ducted rotor, increasing its performance by a factor of 1.5. Goltenbott et al. [59] analysed the variation in ducted turbine performance within a linear turbine farm layout configuration at close vicinity, oriented normal to a uniform flow. Varying the displacement between a linear array of three turbines, an enhanced power output was attained, peaking at 9%, within a spacing of up to half a turbine diameter between each turbine.

Amongst the advantages of a ducted turbine is the capacity of increasing the rotor performance when compared to a bare identical rotor; undertaken within an aerodynamic domain, Igra [60] elaborated upon this outcome when comparing a bare contra-rotor turbine, hence a rotor and a stator rotating in opposite orientations, to a shrouded contra-rotor turbine, attaining a factor increase of ≈ 1.7 by means of the installation of the diffuser. By advancing from a screen to a rotor, Gilbert and Foreman [9, 56] analysed a fixed pitch, constant chord and section turbine with a NACA63(420)-422 blade profile, acknowledging a ≈ 5.75 increase factor in the rotor efficiency over its bare equivalent, along with a ≈ 1.5 increase factor in blade loading; the pitch of the blades, however, were dissimilar between the two distinctive experimentation, hence skewing the true power increase under identical conditions.

Similarly, Abe et al. [14] established the performance of a shrouded rotor to aug-

ment the power output of an identical bare rotor by a mean magnitude of ≈ 4.0 . Yet, albeit the increase, when normalised against the local mean velocity in the near-wake, immediately downstream of the turbine blades, the performance of both the bare and the shrouded wind turbine was found to be quasi-identical. Ohya et al. [12, 61] and Grassmann et al. [62] carried out an on-site prototype field test, attaining a ≈ 5.5 and ≈ 1.5 magnitude increase, respectively, over a bare turbine. Analysing a ducted turbine developed by the then-active Vortec Energy, Phillips [63] investigated the optimised shape of a diffuser, together with the pitch angle of the blades integrated, establishing a 7° blade pitch within a multi-slotted profile, for boundary layer re-energisation, fitted with a NACA-0024 centrebody to attain a ≈ 1.5 factor increase over the Betz limit. Visser [64] introduced a uniquely shaped diffuser to roughly double the power generated by a rotor within identical conditions, and deduced the increase to be a result of the tip-loss reduction, improving the efficiency by $\approx 8 - 10\%$, together with the enhancement of the mass-flow through the rotor. Further to this, Moeller and Visser [65] analysed a high-solidity, low tip-speed ratio ducted turbine with a twisted flat-plate rotor. Attaining a power coefficient of ≈ 0.4 when bare, the performance was found to increase to ≈ 0.6 once combined with the diffuser.

In establishing optimised geometrical parameters for a uni-directional duct for tidal applications, Reinecke et al. [66] compared two identical rotors, with and without the constructed diffuser. Attaining a power coefficient increase factor of ≈ 4.0 when compared to the bare turbine, the duct successfully sustained boundary layer attachment to the rotor at higher rotational velocities, attaining higher power outputs. Albeit the advantageous outcome, the blockage ratio of the experimental setup differs significantly between the bare turbine and ducted turbine cases, being rather substantial with the latter, hence potentially skewing the true performance representation of the turbine. Similarly, Sun and Kyojuka [67] also carried out a comparative analysis between a bare and a ducted rotor; utilising a short, flanged uni-directional duct, a power coefficient increase factor of ≈ 2.5 was attained when compared to the bare rotor. Likewise, Lokocz et al. [68] investigated a rotor within a NACA 4412-profiled diffuser; directly comparing the power output to that of a bare rotor at two distinct Reynolds numbers, the

installation of the diffuser induced a slight depreciation in performance within nominal rotational velocity values at low and high Reynolds numbers, yet attained an increase in power at higher rotational parameters at high Reynolds number, acknowledging a shift in nominal rotational velocity. Further, Shi [69] analysed an optimised diffuser installed upon a rotor; implementing the ducted turbine as a power source for an autonomous underwater vehicle, a power coefficient increase factor of ≈ 2.0 was attained when compared to the bare rotor.

Albeit the favourable outcomes in power augmentation via the installation of a diffuser, the elaborated experimentation studies exhibit significant blockage bias within the laboratory circumstances, yet fail to mention any analytical corrections to account for this skewness, hence pertaining a potential artificial induction in the energy generated. Appropriately detailing the blockage effect within the comparison analysis, Cresswell et al. [17] established the efficiency discrepancy due to the implementation of a uni-directional duct; the performance increase was found to be a factor of ≈ 2.4 for two distinct blade pitches, 0° and -5° , when compared to the bare rotor representation. Similarly, Munes et al. [70] implemented bias correction when associating a rotor within a lens-flanged diffuser and a rotor within a SELIG-1223 aerofoil-profile diffuser to a bare hydrokinetic rotor; the power coefficient was found to increase by factors of ≈ 1.8 and ≈ 1.5 , respectfully, when compared to the bare rotor.

An additional advantage of a ducted turbine is the capacity of sustaining rotor performance when succumb to yawed flow. Igra [60, 71] elaborated upon this outcome when comparing the outcomes of a shrouded contra-rotor turbine in aligned flow to those within yawed flow of up to $\pm 30^\circ$ in iterations of 5° . Acknowledging the augmentation in rotor efficiency in proportion to the yaw angle, a maximum increase of ≈ 1.30 at a bearing of 25° , it was deduced that, within limited yawed conditions, the flow-rate through the turbine was higher than that at aligned flow and, as a result, the power available for the turbine increased. Analysing a micro shrouded wind turbine, Kosasih and Tondelli [72] established a sustained power output within a yaw bearing variation of 0° to 5° . Cresswell et al. [17] discussed the concept by comparing the performance of a shrouded rotor to that of a bare rotor in yawed flow conditions; in the case of the bare

turbine, the rotor efficiency decreases in proportion to an increase in flow bearing, where the greater the yaw angle, the more substantial the power coefficient reduction. This was acknowledged to occur as the yaw angle alters the local relative flow-angle distribution along the rotor, shifting the blade angle-of-attack and diminishing power capture. This development differs as a shroud is installed; the relative velocity is largely consistent for a limited flow bearing, hence sustaining the performance of the rotor within an angular range, after which a depreciation in power efficiency is established.

2.3.2 Analytical Investigations of Ducted Turbines

Preceding experimentation analyses, analytical developments have established the dynamic characteristics of ducted turbines under ideal conditions. Primarily conducted in the mid-fifties, the rotor is portrayed as an infinitely thin, porous disc with properties of a momentum sink, where the duct is represented as a set of distinct boundary conditions within the slipstream.

2.3.2.1 Linear Momentum Theory

By means of linear momentum theory, Lilley and Rainbird [13] analysed the optimum theoretical performance of ducted rotors designed at a diffuser expansion ratio (duct outlet against throat cross-sectional area) range of 2.0 – 5.0, with a total internal head-loss coefficient range of 0.0 – 0.25, for values within a duct exit pressure coefficient range of -0.3 – 0.0. Under the assumption that the entry head-loss coefficient is null throughout, as is the value in well-designed duct systems, the results were compared to the optimum performance of an unshrouded rotor, attaining a maximum theoretical power increase of 85% over a bare turbine with use of a diffuser expansion ratio of 5.0, and a 65% increase for an expansion ratio of 3.5; disc loading within these parameters was found to be reduced by 58%. The parameter values required to attain enhanced performance, in comparison to a bare turbine, were found to be: an expansion ratio of ≥ 1.54 , an outlet pressure coefficient of ≤ 0.0 , and an internal head loss coefficient of ≤ 0.15 . Thus, when neglecting internal losses, the gain in power attained by the ducted rotor was deduced to be proportional to the diffuser expansion ratio, with the

disc loading being inversely proportional to the square of the diffuser expansion ratio. Nonetheless, albeit the advantageous performance increase, such expansion ratios result in a duct outlet diameter range equivalent to a $\sqrt{3.5}$ to $\sqrt{5.0}$ factor of the rotor diameter, and, as a result, the cost of the installation may be unjustifiable for the power increase. In addition to disc comparison analysis, the effect of the clearance between the blades and the duct upon the reduction of mass-flow through the rotor, and the power output, was investigated, establishing that, at moderate tip clearance ratios, the loss in power is less than 1%, hence neglecting tip clearance within linear momentum calculations is justifiable.

In empirically deriving relevant theoretical coefficients, Igra [73] similarly determined measures to attain maximum augmentation. It was established that: (i) the shroud exit pressure is to be low, having a substantially large negative value, (ii) the duct outlet-to-throat cross-sectional area ratio should be large, and (iii) the diffuser recovery factor is to be large, practically sustained by means of boundary-layer-control techniques. Shives and Crawford [74] established diffuser efficiency coefficients for a variety of diffuser geometries for implementation in linear momentum modelling. Riegler [8] derived the theoretical maximum power coefficient for a diffuser-augmented turbine, based on turbine area variation, to be 1.96, a magnitude of 3.3 higher than the Betz limit. This increase was attained due to the degree of flow drawn in from a greater area upstream than that potentially interacted by a similarly sized bare turbine in open flow. Lewis et al. [75] presented an adaptation to linear momentum theory relating the parameters of a ducted turbine, such as duct length, diffusion angle, diffuser area ratio, speed of rotation, and thrust ratio to calculate the output shaft power. Lawn [76] analysed the performance of a shrouded turbine by considering the duct geometrical variations, upstream and downstream of the turbine, as contractions and expansions of the fluid, sustaining specified diffusion efficiencies. Van Bussel [11] put forward the significance of the back pressure at the duct outlet, in relation to the duct expansion ratio, on the power generated by a rotor, whereas Jamieson [77] established a holistic shroud efficiency terminology. Werle and Presz [78] argued that the majority of ducted turbine linear momentum studies were based on an incomplete formulation of the prob-

lem, enacting incorrect limits in establishing the predicted potential performance gain over the bare rotor counterparts, and hence, a corrected formulation proposal was put forward.

Bontempo and Manna [79,80] presented an extension to non-uniform heavy loading and variable radial distribution in actuator disc theory by introducing the influence of a shroud upon the rotor. The ducted turbine performance analysis was carried out by means of a non-linear, semi-analytical actuator disc model, establishing an implicit formulation by analytically superpositioning ring vortices along the duct surface and the wake region in relation to duct shapes, wake rotation, and rotors, characterised by radially varying load distributions. Accounting for the non-linear mutual interaction between the duct and rotor, and the divergence of the slipstream, a ducted turbine was established to sustain a higher mass-flow rate when compared to an open turbine with an equivalent rotor load; consequently, the ducted turbine attains higher performance. In continuation, further analyses [81], accounting for wake rotation and divergence, and the mutual interaction between the rotor and shroud, identified the relationship between the thrust parameters of the duct and the augmentation of the rotor performance in terms of mass flow-rate and power extraction, acknowledging a proportional relationship. Additionally, characterising the load upon a shrouded disc by means of radial distributions within linear, triangular, trapezoidal, and polynomial functions [82], the thrust and power coefficients were established in terms of shape parameters and the load magnitude.

2.3.2.2 Blade-Element Momentum Theory

In investigating the performance of a diffuser-augmented rotor, Fletcher [83,84] implemented a blade-element analysis by considering the local fluid dynamic properties of each element on the blade profile implemented, together with wake rotation, when coupling the parameters of the free-stream. The resultant validated outcomes indicated the detriment of utilising screens to simulate shrouded turbines; as the true drag on the blades is variant along the rotor span, the implementation of a screen was found to overestimate the axial force by $\approx 8\%$ due to the assumption of a consistent load

distribution, together with an underestimation of power of $\approx 30\%$ due to the incomprehension of wake rotation behind the turbine, decreasing the actual diffuser efficiency. Further analyses demonstrated the capacity of a diffuser-augmented turbine in generating a magnitude of two to four times the performance of a bare turbine of equivalent area, dependent on the diffuser efficiency and outlet pressure coefficient. Tavares Dias do Rio Vaz et al. [85] utilised the blade-element approach to provide an extension to the highly-loaded Glauert correction, attaining agreement between the estimated diffuser-velocity enhancement ratio and experimentation data. Laurens et al. [86] compared the outcomes from blade element momentum theory to panel method, establishing the detriments of a duct installation.

Utilising blade-element momentum coupling to predict the hydrodynamic load upon a duct fabricated from glass-fibre-reinforced polymer composite materials, Nachtane et al. [87] imported the outcomes into a finite-element code, utilising an interpolation mapping procedure, to employ the hydrodynamic pressures as boundary conditions, and predict the structural behaviour and mechanical performance under normal conditions. Having attained a validated blade-element model against a HATT, Allsop et al. [3, 88] developed an analytical model to characterise the effects of flow through a ducted rotor as a function of the inlet efficiency, diffuser efficiency, and outlet pressure coefficient. In relating the outcomes to those found in literature, quasi-identical correlations were attained for rotor velocities up to the optimal operating condition, yet presented discrepancies of up to 25% higher power and 13% higher thrust at higher speeds. Albeit the sufficient accuracy attained, the over-predictions were acknowledged to be due to the local flow velocity derived at the elements in the vicinity of the hub, deduced to be due to the indefinite modelling of the flow around the hub and through the open centre, deemed to be beyond the capability of the blade-element method to capture. Further investigations [89] relate the induced hydrodynamic outputs as boundary conditions within a structural solver to undertake structural analyses in an effort to model the resultant blade stress distribution profiles, detailing concentration zones and cyclic values for use in fatigue analyses of high-solidity tidal turbine blades.

2.3.3 Numerical Investigations of Ducted Turbines

In more recent years, with improvements in computer processing power and programming literacy, numerical endeavours have been the prevalent source of ducted turbine fluid dynamic analyses, predominantly directed by finite-volume methodologies. In direct representation of experimentation, simulation modelling has been utilised to investigate the flow properties of vacant shrouds, disc-embedded shrouds, and rotor-embedded shrouds.

2.3.3.1 Vacant Shrouds

In numerically investigating the physics about a vacant flanged duct, Kardous et al. [90] implemented a three-dimensional axi-symmetric computational fluid dynamic analysis, utilising periodic boundary conditions, to establish the variations in flow velocity and static pressure within the structure. Varying the height of a straight rim at the outlet plane of a diffuser in relation to the throat diameter, a critical height ratio of 0.1 was found to attain the highest increase in throat velocity, equivalent to a magnitude of ≈ 1.6 to ≈ 1.7 over the free-stream velocity. Investigating the variation in flow velocity within differing flanged diffuser geometrical profiles, Kannan [91] utilised a two-dimensional straight-body diffuser cone with a 16° aperture, coupled with a 0.5 m long, 4° centre-body cone, establishing a 61.25% increase in axial velocity over the free-stream. Mansour and Meskinkhoda [92] utilised an axi-symmetric model, applying both the Spalart-Allmaras and the RNG $k-\varepsilon$ turbulence model, to acknowledge the static pressure and axial velocity variations through a simple diffuser incorporated with a straight, vertical rim. Similarly implementing an axi-symmetric model of a flanged diffuser, yet utilising the SST $k-\omega$ turbulence model, Khamlaj and Rumpfkeil [93] acknowledged the generation of two static vortices downstream of the flange, inducing further low-pressure at the region immediately downstream of the structure, permitting an augmented flow acceleration through the throat. Kesby et al. [94] investigated a 10° axi-symmetric vacant duct to identify the efficiency coefficients of the structure for implementation within blade-element analysis. In continuation, El-Zahaby et al. [95] analysed a two-dimensional axi-symmetric model of a flanged diffuser designed

for micro-turbines by establishing the variation in duct inlet velocity relative to the aperture angle of the installed body, ranging from -25° to $+25^\circ$ with the vertical axis; the diffuser length, entrance diameter, exit diameter, and flange height were kept constant. Indicating good agreement with published experimental work, the optimum angle, a flange angle of $+15^\circ$, accelerated the flow at the diffuser entrance by 5% due to the developed vortices immediately downstream of the flange. Tampier et al. [96] numerically investigated the axial induction factor, average velocities at the turbine plane, and diffuser thrust coefficient along a three-dimensional shroud in accordance to a variation in free-stream velocity. The resultant induction factors were found to be consistent inasmuch as flow separation was not present along the NACA-profiled cross-section diffuser, which was found to occur at an angle-of-attack of 15° .

2.3.3.2 Disc-Embedded Shrouds

In an effort to couple actuator disc theory within a computational fluid dynamic domain for ducted turbine analyses, a rotor-representative plane is introduced within the throat of a shroud, explicitly defined as a momentum sink by mathematically instituting thrust momentum equations. This setup simulates the presence of a rotor, permitting the reproduction of the stream-wise thrust, yet does not reproduce its swirl, radial flux distribution, or additional turbulence generation.

Implementing the methodology, Fleming and Willden [97] investigated the relative performance of two-dimensional, axi-symmetric bi-directional ducted tidal turbines in confined flow. Analysing five duct profiles of differing curvature gradients and thickness, the resultant outcomes were compared to those of two bare turbines of differing sizes. The fundamental effects of the duct profile upon a rotor, as well as the secondary effects due to duct camber and thickness, were identified by varying the loss factor of the momentum sink, in proportion to the rotor solidity, analysing the width of the stream-tube along the domain and the stream-wise velocity and pressure distributions. Maximum power extraction was attained by the system with the highest internal duct curvature, found to be a result of the mass-flow increase due to the Venturi effect at the throat. Further investigations into flow domain effects, by altering the loss factor

within the duct of highest curvature, depicted the formation of a re-circulation zone along the exterior of the high rotor-solidity representative shrouds. Utilising a duct with an Eppler-423 geometrical cross-section due to its high lift coefficient, Venters et al. [98] incorporated an actuator disc with the Standard $k-\varepsilon$ turbulence model to establish the optimal rotor placement and duct aperture angle in attaining the highest rotor-disc thrust coefficient. By means of the investigation, the optimal coefficient of thrust was found to be similar to that of a bare rotor, indifferent of the augmented local flow velocity through the duct, yet attained a 66% greater power output. In addition, the established optimal duct-profile stall angle was found to be substantially larger than the stall limit of the aerofoil in a free-stream; flow separation was not induced due to the expansion at the rotor-disc sustaining flow attachment.

Bontempo and Manna [80,99] utilised a two-dimensional disc CFD analysis implementing a “fan” boundary condition at the thin disc; this approach permitted a direct radial distribution of the pressure jump across the disc, simulating the effect of the turbine energy extraction in a more accurate manner than an area-averaged actuator disc, yet not as accurate as a blade-element representation. By means of this method, a high degree of similarity was achieved when comparing the radial and axial velocity profiles and duct wall pressure outcomes of the computational fluid dynamic model to that attained by means of prior-derived semi-analytical outcomes; the analytical implementation was noted to be more practical, as the CFD analysis required a higher computational demand. Via the outcomes, it was acknowledged that, due to the non-linear mutual interaction between the duct and rotor, together with the downstream divergence of the slipstream, a suitably-designed ducted turbine sustains a higher mass-flow rate than a bare turbine with an equivalent rotor load, consequently attaining a higher value of extracted power.

Phillips et al. [100] utilised the momentum sink methodology, implementing site data, to cost-effectively establish improvements for the Vortec-7 turbine. Hansen et al. [101] utilised the SST $k-\omega$ turbulence model to attain validation by comparing a CFD computation of a bare turbine with the theoretical expression; by subsequently incorporating a diffuser, the Betz limit was exceeded by a ratio corresponding to the

relative increase in mass-flow through the rotor, which was acknowledged to vary inversely proportional to the rotor thrust coefficient. Dighe et al. [102] utilised the “fan” boundary condition within a two-dimensional axi-symmetric model to analyse ducted turbines in yawed conditions, identifying a limited increase in performance enhancement. Gaden and Bibeau [103] conducted simulations varying the diffuser rim height, establishing a power output augmentation factor of 3.1, together with a thrust augmentation factor of 3.9. Validated by means of a comparison with outcomes from a far-wake, swirl-corrected blade-element momentum model, together with horizontal-axis wind turbine experimentation results, Hjort and Larsen [104] employed a swirled actuator disk CFD code to analyse the performance of a ducted turbine. Utilising a similarly validated modelling approach, Shives and Crawford [74] simulated several duct designs, utilising an actuator disc representation of the rotor, providing insight into distinct factors influencing the performance-enhancement properties constituted by the implementation of a diffuser, notably viscous losses, flow separation, and base pressure at both ends of the diffuser. Viscous losses were deemed to be negligible, yet flow separation at either location induced a significant performance degradation and concurrent diffuser efficiency reduction, established to be correspondent to diffuser outlet expansion ratios, inlet contraction ratios, and diffuser exit angles. However, as larger expansion ratios and larger outlet angles within a duct design provide increased base pressure, the maximum performance factor was attained via an optimisation between the performance gain from increasing the expansion/contraction ratios, to that lost from diminished efficiency.

In sustaining higher accuracy when simulating the rotor blades as a disc, blade-element theory may be coupled within the computational fluid dynamic domain, capturing the radial geometrical variation of the structure, and reproducing swirl in accordance to a more definitive radial load distribution. Belloni et al. [4, 105] implemented the methodology to resolve the performance, together with the velocity profiles within the wake, of three distinct real-scale turbines: a bare turbine, a ducted turbine, and an open-centred ducted turbine. When comparing the devices at their respective design points, the performance outcomes attained by the RANS-BEM model were found to

be 8 – 15% lower than those attained by actuator disc simulations. This reduction in performance is largely due to the blade loading distribution captured by the segmented blade elements, which is not modelled by the actuator disc. At a rated flow-speed of 2.5 m/s, the bare, ducted, and open-centred turbines were acknowledged to produce an output of 0.97 MW, 0.61 MW, and 0.53 MW, respectively, while the thrust loading was found to be 0.64 MN, 0.52 MN, and 0.41 MN, respectively. In continuation, yawed flow analysis [106] was undertaken comparing bare and ducted turbine performance, observing that, whilst the bare turbine performance decreased in yawed flow, the ducted turbine performance increased, speculated to be due to a flow straightening effect, together with an increase in effective blockage, as ducts present greater projected frontal area when approached non-axially.

2.3.3.3 Rotor-Embedded Shrouds

In an effort to overcome the numerical shortcomings of disc theory when coupled to a computational fluid dynamic domain for ducted turbine analyses, both the shroud and the rotor blades may be explicitly resolved, induced with a rotational velocity, to replicate the true fluid-structure interaction of the subsea structure in open-water.

Luquet et al. [58] utilised a steady-state blade-resolved RANS-CFD methodology incorporating the multiple reference frame (MRF) momentum model, whilst excluding a turbulence model, to simulate half of the rotor in an axi-symmetric approach to design a rotor within a uni-directional duct, accounting for the admissible structural loading and relevant cavitation constrains. Designing for several rotor geometries to attain a structure with optimum parameters, the set-up had been developed to simulate the turbine at model-scale to attain validation in comparison to an experimentally-analysed ducted turbine within a towing tank. Aranake et al. [107] similarly utilised half the domain for an axi-symmetric MRF model, yet incorporating the Spalart-Allmaras model, evaluating distinct flow separation patterns along the inner surfaces of the duct. Ghassemi et al. [108] spatially discretised the turbine domain in a hexahedral manner within an identical momentum and turbulence approach acknowledging an increase in turbine performance. Tampier et al. [96] employed a transient blade-resolved RANS

methodology, incorporating a variation of the SST $k-\omega$ turbulence model together with a moving (rotating) mesh momentum model, simulating the full rotor, to obtain the performance, thrust, and average flow speeds of a three-bladed rotor within a comparison between a bare rotor and a diffuser-augmented rotor. Upon validating the bare turbine outcomes to experimentation, axial induction factors were attained in terms of the average speeds along the turbine plane for their implementation in disc approaches.

Wang and Chen [109] investigated the effects of differing blade numbers upon the performance of a ducted turbine utilising the Standard $k-\varepsilon$ turbulence model, simulating one-eighth of the rotor in an axi-symmetric MRF approach with periodic boundary conditions to permit rotating flow. Variations in the blade geometry, stagger pitch angle, and the number of blades were found to induce differing duct blockage effects, affecting the turbine performance; increasing the number of blades induced a higher starting-torque, yet reduced cut-in speed due to the high blade-area upon which energy is transferred, together with resulting in a higher degree of blockage and lower blade entrance velocity, hence reducing the resultant power coefficient. Hadya and Pailla [110] utilised this method to simulate a rotor within an omni-directional duct, acknowledging an appropriate flow diversion and acceleration to axially interact with the rotor. Wang et al. [111] evaluated the response of a unique rotor, fabricated from angled plates in an octagram configuration, within a diffuser, acknowledging a quintuple magnitude power increase over a bare rotor. Prakash et al. [112] investigated a full rotor within a convergent-divergent and divergent-convergent duct distinctively, acknowledging the higher torque induced within the prior, whilst Venkatesan et al. [113] investigated the performance of a rotor within a flanged diffuser. Similarly utilising the MRF approach, yet coupling the Realizable $k-\varepsilon$ model, Alpman [114] analysed a full rotor, acknowledging the augmentation of the power production with an extension of the tip-speed ratio range in which the rotor produces positive torque, in accordance to an increase in thrust; comparing a six-bladed rotor to a four-bladed structure, a higher flow-rate was induced in the prior, yet more power was produced in the latter. Evaluating the response of a rotor within a shroud with a lobed ejector for low-velocity free-streams,

Han et al. [115] acknowledged a power coefficient range of 0.39 - 0.43 at free-stream velocities ranging from 2 to 6 m.s^{-1} by utilising a partitioned MRF segment of the turbine domain with periodic boundary conditions and the Standard $k-\varepsilon$ turbulence model.

Implementing the large-eddy simulation (LES) turbulence methodology within the MRF momentum approach, Takahashi et al. [116] simulated one-third of the three-dimensional turbine domain of a rotor within a flanged diffuser for the purpose of accurately simulating the flow separation and dissipative flow eddies induced by the blade-tip vortices along the gap between the rotor blade-tip and the diffuser. The generated blade-tip vortices further induce an array of contra-rotating vortices between the blade tips and the inner surface of the diffuser, qualitatively consistent with findings observed in flow tunnel experimentation. Designing a bi-directional ducted rotor system for its implementation upon a vessel for energy-generation, Zefreh [117] utilised the Standard $k-\varepsilon$ turbulence model in accompaniment to the moving (rotating) mesh technique, segregating the shroud and general domain from the rotor, allowing physical rotational motion. In an effort to accurately represent the fluid dynamics of a high-solidity open-centre rotor within a bi-directional duct, Borg et al. [118,119] analysed the full domain by means of a moving mesh momentum technique, explicitly resolving the blades, whilst implementing the use of the high-order Stress- ω RANS turbulence model. Primarily tackling the performance of the turbine within axial flow, a peak power coefficient of 0.34 was attained at a nominal TSR of 1.75, with a thrust coefficient of 0.97. Investigating the variation in turbine performance due to the vectorial divergence of the free-stream [120,121], an increase in performance factors were acknowledged at higher rotational velocities for a limited angular range within the yawed flow conditions. In further analysis [122,123], a one-way fluid-structure interaction was established by exporting pressure values from the cell nodes within the hydrodynamic solver and imported into the structural solver, evaluating the structural response of distinct designs of fibre-composite rotor blades comprising a ducted, high-solidity tidal turbine.

2.3.4 State of the art Summary

In summary of the reviewed state of the art, Tables 2.1 and 2.2 were established for rotor-embedded experimentation and numerical literature, respectively. From this comparison, it was clear that no bidirectional ducted turbine experimentation cases, with a singular high-solidity turbine scenario, had been carried out. In addition, solely one blade-resolved bidirectional ducted turbine numerical analysis had been put forward, yet having incorporated a low-solidity rotor.

Author	Domain	Solidity	Duct Type	Yawed
Cresswell et al. [17]	Hydro	Low	Unidirectional	Yes
Luquet et al. [58]	Hydro (check)	Low	Unidirectional	No
Goltenbott et al. [59]	Hydro	Low	Unidirectional	No
Igra [60]	Aero	Low	Unidirectional	Yes
Gilbert and Foreman [55]	Aero	Low	Unidirectional	No
Abe et al. [14]	Aero	Low	Unidirectional	No
Phillips [100]	Aero	Low	Unidirectional	No
Visser [124]	Aero	Low	Unidirectional	No
Moeller and Visser [65]	Aero	High	Unidirectional	No
Reinecke et al. [66]	Hydro	Low	Unidirectional	No
Sun and Kyojuka [67]	Hydro	Low	Unidirectional	No
Lokocz et al. [68]	Hydro	Low	Unidirectional	No
Shi [69]	Hydro	Low	Unidirectional	No
Kosasih and Tondelli [72]	Aero	Low	Unidirectional	Yes

Table 2.1: Summary of Rotor-Embedded Ducted Turbine Experimentation

2.3.5 Research Gap

From reviewing the literature, it was perceived that the experimentation and numerical research ventures that have tackled the analysis of a rotor-embedded ducted turbine were largely based upon low-solidity rotors with a unidirectional duct. As a result, the rotor-embedded analysis of a high-solidity, open-centred rotor within a bidirectional duct has not been tackled.

Specifically elaborating the general numerical literature of the duct feature implementation in a turbine system, numerical forms of methodological limitations were acknowledged. Predominantly, this consisted of analytically capturing mass and mo-

Author	Phys. Model	Turb. Model	Solidity	Duct Type
Luquet et al. [58]	Axi-symmetric	Laminar	Low	Unidirectional
Aranake et al. [107]	Axi-symmetric	Spal-Allma	Low	Unidirectional
Ghassemi et al. [108]	Axi-symmetric	Spal-Allma	Low	Unidirectional
Tampier et al. [96]	Full rotor	SST $k - \omega$	Low	Unidirectional
Wang and Chen [109]	Axi-symmetric	SST $k - \omega$	Medium	Unidirectional
Hadya and Pailla [110]	Axi-symmetric	SST $k - \omega$	Low	Omnidirectional
Wang et al. [111]	Full rotor	SST $k - \omega$	Medium	Unidirectional
Prakash et al. [112]	Full rotor	SST $k - \omega$	Low	Unidirectional
Venkatesan et al. [113]	Full rotor	SST $k - \omega$	Low	Unidirectional
Alpman [114]	Full rotor	RSB $k - \varepsilon$	Medium	Unidirectional
Han et al. [115]	Axi-symmetric	STD $k - \varepsilon$	Low	Unidirectional
Takahashi et al. [116]	Axi-symmetric	LES	Low	Unidirectional
Zefreh [117]	Full rotor	STD $k - \varepsilon$	Low	Bidirectional
Borg et al. [119]	Full rotor	STD $\tau - \omega$	High	Bidirectional

Table 2.2: Summary of Rotor-Embedded Ducted Turbine Simulation

mentum continuity through the duct, or representing the blade structure by means of disc-planes or disc-elements, rather than portraying its true, blade-resolved physicality. Arguably, this had been put forward due to the difficulty in computationally modelling the fluid flow through the limited disparity between the rotor tip and the duct surface. Accurately attaining an analytical/numerical representation would require either substantial experimentation testing to establish a formulaic analogy or a substantially dense mesh; being financially/computationally costly and time consuming. Additionally, flow conditions such as establishing the causation of performance discrepancies under yawed flow conditions, acknowledging the structural response of the ducted rotor blades under real flow conditions, and accurately capturing explicit flow phenomena in relation to turbulence length-scales within the free-stream flow, have not been carried out.

For this reason, this research strives to overcome that gap of knowledge by implementing a coupled finite-volume computational fluid dynamic and finite-element analysis with blade-explicit actuality, with general continuity at both the domain and turbine. This feature allows the aspect of modelling flow three-dimensionality at the turbine, together with induced turbulence effects, in effort of numerically replicating

the true performance of a ducted, high-solidity tidal turbine rotor.

As a result of this implementation, the outcomes shall consist of an accurate performance analysis of a ducted, high-solidity tidal turbine in aligned and yawed flow conditions. Furthermore, the hydrodynamic solver shall be coupled to the structural solver to analyse the solid mechanical properties of the rotor blades. In culmination, explicit vortical flow phenomena shall be introduced within the domain to establish the performance of the ducted tidal turbine within vortex flow conditions. Due to the aims of this research venture, a numerical implementation was imperatively required, particularly due to the interest of full-scale analysis, and, hence, the computational fluid dynamic and finite-element methodologies were deemed to be the most instrumental.

2.4 Chapter Summary

This chapter presented an elaboration of the underlying physics governing aerofoil theory and its utilisation in establishing the efficiency of power-generating horizontal-axis turbines. In compliment, supplementary adaptations into ducted turbine configurations, together with yawed flow and vortex flow conditions, were expounded. Further to this, commercial applications of the adoption of ducted turbines for large-scale projects in the tidal industry were acknowledged, in addition to a detailed review of the recent, state-of-the-art ducted turbine experimental, analytical, and numerical investigations was portrayed in association to the current work.

Chapter 3

Characterisation Modelling of a Ducted Tidal Turbine

This chapter provides a detailed elaboration into the fundamental methodologies utilised to model turbine hydrodynamics, in specification to linear momentum theory, blade element theory, and their coupled approach, whilst expounding into ducted turbine and yawed flow adaptations. In addition, the governing continuity equations, together with the turbulence models required to numerically describe a turbulent regime, are expanded as resolved by the computational fluid dynamics technique. Furthermore, the characterisation of the numerical model, where the formulae utilised in relation to the physical parameters of the tidal turbine within the flow continuum, are specified.

3.1 Numerical Turbine Modelling Methodologies

In consideration of the distinct approaches with which the performance analysis of a turbine may be carried out, the techniques that are utilised within this work, notably blade-element momentum theory in Chapter 6 & 9, linear momentum theory with ducted, highly-loaded adaptations in Chapter 7 & 9, and computational fluid dynamics in Chapters 5 - 10, are described sequential to the numerical complexity.

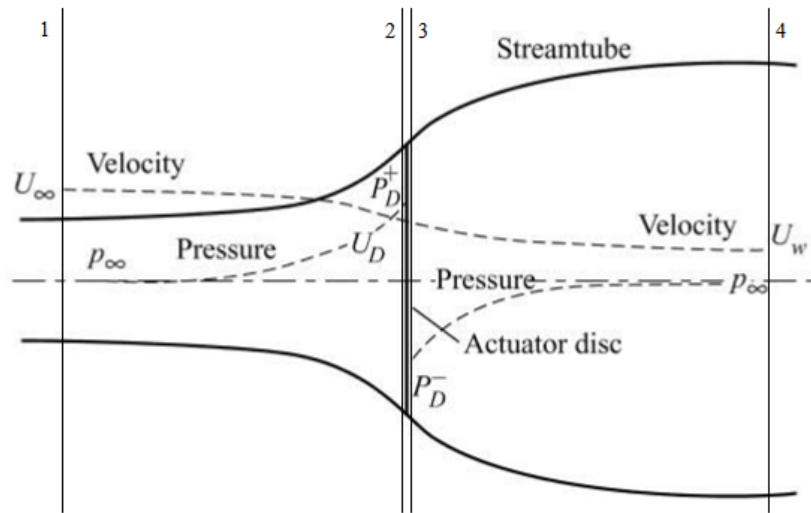


Figure 3.1: Illustrative representation of an actuator disc within a fluid stream-tube [125]

3.1.1 Linear Momentum Theory

By means of a principal numerical technique, a turbine rotor is associated with a thin, planar, porous disc in establishing the dynamics of an ideal turbine succumb to axial flow. Linear (one-dimensional) axial momentum theory, also known as actuator disc theory, assumes a homogeneous, incompressible, inviscid, steady-state fluid flow interacting with uniformly-projected static blades of a frictionless rotor around the turbine axis, inducing a consistent loading distribution over the disc [125]. The assumptions hence constitute a fluid stream-tube where, due to the fluid interaction at the static disc, a discontinuity in pressure, with a variance in velocity, is induced with a non-rotating (swirl-void) wake, at which the static pressure distantly upstream and downstream of the rotor is equivalent to the ambient static pressure, illustrated in Figure 3.1; Table 3.1 details the notation utilised in explanation of the schematic figure.

3.1.1.1 Mass Continuity

In application of the premise that the rate of fluid flow is continuous throughout the stream-tube, the mass-flow rate is assumed to be equivalent at all regions in the

Region	1	2	3	4
Velocity	$U_1 = U_\infty$	$U_2 = U_D$	$U_3 = U_D$	$U_4 = U_W$
Area	A_1	$A_2 = A_D$	$A_3 = A_D$	A_4
Pressure	$p_1 = p_\infty$	$p_2 = p_D^+$	$p_3 = p_D^-$	$p_4 = p_\infty$

Table 3.1: Summary of Turbine Model Descriptions

domain:

$$\dot{m}_1 = \dot{m}_D = \dot{m}_4 \quad (3.1)$$

$$\rho A_1 U_\infty = \rho A_D U_D = \rho A_4 U_4 \quad (3.2)$$

where \dot{m} is the mass-flow rate, ρ is the fluid density, A is the cross-sectional area of the stream-tube through which the fluid passes, and U is the velocity magnitude of fluid flow.

3.1.1.2 Axial Momentum Continuity

As the actuator disc extracts energy from the fluid flow, the flow velocity through the stream-tube is, inherently, diminished. This reduction in velocity gives rise to a rate of change in axial momentum, defined as the product of the mass flow-rate and variance in velocity, which is equivalent to the axial force, or thrust, exerted onto the disc, given that no energy losses occur:

$$\frac{\delta M}{\delta t} = \dot{m} \Delta U \quad (3.3)$$

$$T = F_{ax} = \rho A_D U_D (U_\infty - U_4) \quad (3.4)$$

where $\frac{\delta M}{\delta t}$ is the axial momentum flux, F_{ax} is the axial loading, and T is the induced thrust.

3.1.1.3 Bernoulli's Principle

When considering a system within which no work done is imposed on the fluid, Bernoulli's principle states that the energy density throughout the system, comprising

of kinetic energy, static pressure potential energy, and gravitational potential energy is constant:

$$\frac{1}{2}\rho U_n^2 + p_n + \rho g h_f = c_f \quad (3.5)$$

where p is the static pressure, g is the gravitational acceleration, h_f is the liquid column height, and c_f is a constant relating the terms within the function.

At the distinct stations within the stream-tube, the function alters to:

$$\frac{1}{2}\rho U_1^2 + p_1 = \frac{1}{2}\rho U_2^2 + p_2 \quad \Rightarrow \quad \frac{1}{2}\rho U_\infty^2 + p_\infty = \frac{1}{2}\rho U_D^2 + p_D^+ \quad (3.6)$$

$$\frac{1}{2}\rho U_3^2 + p_3 = \frac{1}{2}\rho U_4^2 + p_4 \quad \Rightarrow \quad \frac{1}{2}\rho U_D^2 + p_D^- = \frac{1}{2}\rho U_4^2 + p_\infty \quad (3.7)$$

In implementation of the Bernoulli function, the difference in pressure, upstream and downstream of the disc, may therefore be established:

$$\Delta p_D = p_2 - p_3 = p_D^+ - p_D^- = \frac{1}{2}\rho(U_\infty^2 - U_4^2) \quad (3.8)$$

The thrust induced as a result of the reduction in kinetic energy, relative to the pressure drop, therefore becomes:

$$T = F_{ax} = \frac{1}{2}\rho A_D(U_\infty^2 - U_4^2) = \Delta p_D A_D \quad (3.9)$$

3.1.1.4 Axial Induction Factor

As two expressions are established for the thrust induced, via the axial momentum flux and Bernoulli principle functions, they may hence be equated to establish an expression for the velocity at the disc:

$$\begin{aligned} \frac{1}{2}\rho A_D(U_\infty^2 - U_4^2) &= \rho A_D U_\infty (U_\infty - U_4) \\ U_D &= \frac{U_\infty + U_4}{2} \end{aligned} \quad (3.10)$$

Thus, the fluid velocity at the rotor plane, in accordance to the model, is the mean average of the upstream and downstream flow speeds. In continuation, by re-arranging Equation 3.10, the ratio between the free-stream and the disc-plane velocity may be established as an axial induction factor (a_f):

$$1 - \frac{U_D}{U_\infty} = \frac{1}{2} - \frac{U_4}{2U_\infty}$$

$$a_f = 1 - \frac{U_D}{U_\infty} \quad (3.11)$$

$$a_f = \frac{1}{2} - \frac{U_4}{2U_\infty} \quad (3.12)$$

By means of the above equations, the axial induction factor may be substituted within the axial loading function (Equation 3.9) to achieve:

$$T = F_{ax} = 2\rho A_D U_\infty^2 a_f (1 - a_f) \quad (3.13)$$

3.1.1.5 Rotor Disc Power

The generated power by a rotor may be defined as the product of the axial loading force upon, and the axial velocity of the flow through, the disc:

$$P = F_{ax} U_D \quad (3.14)$$

where P is the generated power.

By incorporating the previously derived terms into Equation 3.14, the generated power may be established in relation to the variations in pressure and velocity:

$$\begin{aligned} P &= \rho A_D U_D^2 (U_\infty - U_4) \\ &= \frac{1}{2} \rho A_D (U_\infty^2 - U_4^2) \end{aligned} \quad (3.15)$$

$$\begin{aligned}
 P &= \Delta p_D A_D U_D \\
 &= (p_D^+ - p_D^-) A_D U_D
 \end{aligned} \tag{3.16}$$

$$P = 2\rho A_D U_\infty^2 a_f (1 - a_f^2) \tag{3.17}$$

3.1.1.6 Thrust & Power Coefficients

In establishing non-dimensional performance terms, the thrust and power parameters are correlated to properties within the flow domain. The coefficient of thrust (C_T) may be expressed by:

$$\begin{aligned}
 C_T &= \frac{F_{ax}}{\frac{1}{2}\rho A_D U_\infty^2} \\
 &= \frac{2\rho A_D U_\infty^2 a_f (1 - a_f)}{\frac{1}{2}\rho A_D U_\infty^2} \\
 &= 4a_f (1 - a_f)
 \end{aligned} \tag{3.18}$$

The coefficient of power (C_P) may be expressed by:

$$\begin{aligned}
 C_P &= \frac{P}{\frac{1}{2}\rho A_D U_\infty^3} \\
 &= \frac{2\rho A_D U_\infty^3 a_f (1 - a_f)^2}{\frac{1}{2}\rho A_D U_\infty^3} \\
 &= 4a_f (1 - a_f)^2
 \end{aligned} \tag{3.19}$$

3.1.1.7 The Betz Limit

By means of the derived equations, the nominal axial induction factor ($a_{f,nom}$), at which the maximum power coefficient ($C_{P,max}$) is attained, may be deduced when the performance derivative $\frac{dC_P}{da_f} = 0$, developed at $a_f = \frac{1}{3}$. This point attains a peak power coefficient of $C_{P,max} = \frac{16}{27} = 0.5926$, known as the Betz limit [6]. Utilising Equation 3.11, maximum power extraction is hence attained when:

$$U_D = \frac{2}{3}U_\infty$$

In continuation, the maximum thrust coefficient ($C_{T,max} = 1$) occurs when the performance derivative $\frac{dC_T}{da_f} = 0$, developed at $a_f = \frac{1}{2}$. Upon exceeding this axial induction value, the far downstream velocity (U_4) negates, as per Equation 3.12. This implies a reversal of the flow within the far wake, which is physically unrealistic, and is hence a limitation within the methodology. In this consideration, axial momentum theory is unsatisfactory in modelling highly-loaded turbines, such as ducted, high-solidity rotors. An extension to this theory has been proposed by applying empirical correction factors to the derivation when in the highly-loaded state, elaborated in Section 3.1.6.2.

3.1.2 Rotor Disc Theory

The energy exchange due to the fluid-structure interaction with a rotating turbine in a fluid domain is not limited to a variation in axial momentum, yet additionally induces a variation in angular momentum, in relation to the rotation of the rotor. The angular momentum flux is therefore associated with the angular forces induced upon a rotating semi-permeable disc, generating a torque about a pivot.

The flow-stream within the domain is considered to be acting at a vector perpendicular to the rotor disc plane, with null rotational motion. As the fluid exerts a moment upon a rotating disc, the torque induced upon the disc may be defined as the rate of change of angular momentum:

$$Q = \frac{dL}{dt} \quad (3.20)$$

where L is the angular momentum and is equivalent to $I\omega$; I is the moment of inertia of the structure, equivalent to mr^2 , ω is the wake mean rotational velocity, m is the disc mass, and r is the radius of the disc. The function may be expanded into:

$$\begin{aligned} Q &= \frac{\delta(mr^2\omega)}{\delta t} \\ &= \frac{\delta m}{\delta t} r^2 \omega \end{aligned} \quad (3.21)$$

where $\frac{\delta m}{\delta t} = \dot{m}$ is the mass-flow rate, and therefore:

$$\begin{aligned} Q &= \dot{m}r^2\omega \\ &= \rho A_D U_D r^2 \omega \end{aligned} \quad (3.22)$$

By incorporating the axial induction factor within the function:

$$Q = \rho A_D U_\infty (1 - a_f) r^2 \omega \quad (3.23)$$

The torque coefficient may be therefore deduced:

$$\begin{aligned} C_Q &= \frac{\rho A_D U_\infty (1 - a_f) r^2 \omega}{\frac{1}{2} \rho A_D U_\infty^2 r} \\ &= 2(1 - a_f) \frac{r\omega}{U_\infty} \\ &= 4a'_f(1 - a_f) \frac{r\Omega}{U_\infty} \end{aligned} \quad (3.24)$$

where a tangential induction factor (a'_f) relating the rotational velocity of the disc (Ω) to the rotational velocity of its wake is introduced:

$$a'_f = \frac{\omega}{2\Omega} \quad (3.25)$$

3.1.3 Blade-Element Momentum Theory

Through the analytical formulae implemented for axial and angular momentum conservation, the expressions of the thrust, torque, and power are derived in terms of axial and tangential induction factors. The formulae, however, solely consider the area-averaged pressure and velocity along the stream-tube; a single value of the properties at the rotor is therefore attained, both upstream and downstream, which is largely inaccurate specifically due to the variation of pressure along a blade surface. In substitute, the hydrodynamic lift and drag forces upon the distinct, local foil cross-sections along the blade length, in relation to the relative flow, may be evaluated to establish the global-induced thrust and power ratings of the rotor.

3.1.3.1 Blade-Element Theory

Portraying an improved representation of the turbine in comparison to linear momentum theory, the blade is partitioned into a number of discrete hydrofoil elements to represent the actual geometrical properties of the blade. As each element along the blade is individually considered, the resultant velocity, as a function of axial and in-plane velocities, and the developed hydrodynamic forces induced, as elaborated in Section 2.1.1, are established at each cross-section.

3.1.3.2 Coupling of Linear Momentum and Blade-Element Theories

With use of momentum theory, the thrust (T_{AD}) and torque (Q_{AD}) are specified in relation to axial and tangential induction factors. By means of blade-element theory, the thrust (T_{BE}) and torque (Q_{BE}) are defined as a function of the flow parameters by incorporating the in-flow angle and lift-and-drag coefficients. Due to the relationship of the variables present within both techniques, the theories may be coupled to acquire the induction factors at which the forces and moments are resolved and balanced. Yet the combination of the theories requires the assumption that the momentum flux through the annular area swept by the discrete element is induced solely by the fluid dynamic force-exchange upon the element. Each annular ring must therefore be of equivalent radius (r) and width (dr) as the size of the blade elements.

In coupling the two theories, the thrust computed by axial momentum theory (T_{AD}) from Equation 3.13 may be equated to that derived by blade element theory (T_{BE}) from Equation 2.10, therefore establishing:

$$\begin{aligned} dT_{AD} &= dT_{BE} \\ 4\pi\rho U_{\infty}^2 a_f(1-a_f)r \, dr &= \frac{1}{2}\rho c V_{rel}^2 N_b C_T \, dr \end{aligned} \quad (3.26)$$

where N_b is the number of blades. The equation may be re-arranged to solve for the axial induction factor:

$$\frac{a_f}{(1-a_f)} = \frac{\sigma_r C_T}{4 \sin^2 \phi_o} \quad (3.27)$$

where σ_r is the local blade solidity: $\sigma_r = \frac{N_b c}{2\pi r}$

In a similar manner, the torque attained by means of angular momentum theory (Q_{AD}) from Equation 3.24 may be equated to that derived by blade element theory (Q_{BE}) from Equation 2.11, therefore establishing:

$$\begin{aligned} dQ_{AD} &= dQ_{BE} \\ 4\pi\rho\Omega U_\infty a'_f(1-a_f)r^3 dr &= \frac{1}{2}\rho c V_{rel}^2 N_b C_Q r dr \end{aligned} \quad (3.28)$$

The equation may be re-arranged to solve for the axial induction factor:

$$\frac{a'_f}{(1+a'_f)} = \frac{\sigma_r C_Q}{4 \sin \phi_o \cos \phi_o} \quad (3.29)$$

With use of these functions, the torque and axial force at each element is therefore calculated and integrated along the rotor area to attain the overall values; numerically, the non-linear equations are arranged in a form to solve the flow induction factors by means of an iterative process. Ultimately, the overall turbine thrust (C_T) and power (C_P) coefficients are defined by:

$$C_T = \frac{\sum_{n=r_h}^R dT}{\frac{1}{2}\rho A U_\infty^2} \quad (3.30)$$

$$C_P = \frac{\sum_{n=r_h}^R dQ \cdot \Omega}{\frac{1}{2}\rho A U_\infty^3} \quad (3.31)$$

where r_h is the radius of the element at the hub, R is the radius of the element at the tip, and A is the system reference area.

3.1.4 Ducted Turbine Adaptation

The implementation of a shroud along the circumference of a rotor is carried out to improve the hydrodynamic performance of the turbine system. The addition of the convergent-divergent external structure directs a higher degree of mass flux through the rotor, hence increasing the available momentum exchange. The convergence at

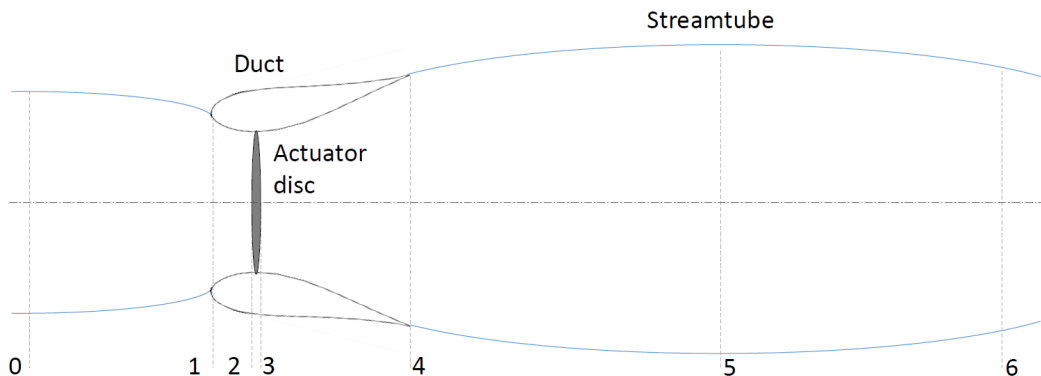


Figure 3.2: Schematic of a ducted turbine incorporating the actuator disc bounded by a stream tube, with numbers corresponding to sections in which areas, pressures and velocities are taken, consisting of: 0 in-flow upstream; 1 - duct inlet; 2 - actuator disc upstream; 3 - actuator disc downstream; 4 - duct outlet; 5 - wake downstream; 6 - wake far downstream [3]

the inlet increases the velocity of the fluid at the throat, with divergence towards the outlet, inducing flow expansion, reducing the pressure downstream, further augmenting the flux through the duct.

In relation to linear momentum theory, the presence of the duct varies the flow profile through the actuator disc, altering the momentum flux conditions of the streamtube, illustrated in Figure 3.2, formulating a new expression for the rate of change of axial momentum. Table 3.2 details the notation utilised in the ducted momentum equations, where the far downstream pressure is assumed to return to that of the free-stream; in the case of a symmetrical bi-directional duct, the areal values at the inlet and outlet are equivalent, hence $A_1 = A_4$. This variation in notation then introduces efficiency terms and additional pressure coefficients in an effort to couple the continuity at distinct regions of the stream-tube, differing from that of a bare turbine [126].

Albeit the variation for the case of a ducted turbine, the coefficient of thrust retains its appropriation to the pressures fore and aft of the disc, equivalent to Equation 3.18, hence:

$$C_T = \frac{p_2 - p_3}{\frac{1}{2}\rho U_\infty^2}$$

Region	0	1	2	3	4	5	6
Velocity	$U_0 = U_\infty$	U_1	$U_2 = U_D$	$U_3 = U_D$	U_4	U_5	$U_6 = U_W$
Area	A_0	A_1	$A_2 = A_D$	$A_3 = A_D$	A_4	A_5	A_6
Pressure	$p_0 = p_\infty$	p_1	p_2	p_3	p_4	p_5	$p_6 = p_\infty$

Table 3.2: The notation utilised in one-dimensional actuator disc theory for unconstrained flow in a duct, indicating velocities, areas and pressures at several cross sectional locations within the stream-tube

Within the stream-tube, the flow converges from position 0 to position 2 at the duct throat where the disc is located; the variation in velocity may be related by means of Bernoulli's principle:

$$C_{p02} = \frac{p_2 - p_\infty}{\frac{1}{2}\rho U_\infty^2} \quad (3.32)$$

which may be parametrised utilising an efficiency term, such that:

$$C_{p02} = \eta_{02} \left(1 - \frac{U_D^2}{U_\infty^2} \right) \quad (3.33)$$

where η_{02} is the efficiency term parametrising the viscous losses in the inlet; due to the convention used, the efficiency is greater than unity for contracting flow.

The pressure variation in the diffuser, downstream of the rotor, may similarly be expressed by incorporating an efficiency term, noting the comparison to the velocity at the disc [76], together with the incompressible continuity expression ($U_D A_D = U_4 A_4$):

$$C_{p34} = \frac{p_4 - p_3}{\frac{1}{2}\rho U_D^2} \quad (3.34)$$

$$\begin{aligned} &= \eta_{34} \left(1 - \frac{U_4^2}{U_D^2} \right) \\ &= \eta_{34} \left(1 - \frac{A_D^2}{A_4^2} \right) \end{aligned} \quad (3.35)$$

where η_{34} is the diffuser efficiency term. The pressure difference between the diffuser outlet and far downstream may be parametrised by the base pressure coefficient:

$$C_{pb} = \frac{p_\infty - p_4}{\frac{1}{2}\rho U_\infty^2} \quad (3.36)$$

By means of the summation of the individual pressure differences from far upstream and far downstream, and equating to zero, yields:

$$C_T - C_{p02} - C_{p34} \cdot \left(\frac{U_D}{U_\infty}\right)^2 - C_{pb} = 0 \quad (3.37)$$

where the velocity ratio $\left(\frac{U_D}{U_\infty}\right)$ is the measure of the mass-flow rate through the turbine, also known as the swallowing capacity. This may be re-arranged to solve for the thrust coefficient in terms of the axial induction factor:

$$C_T = \eta_{02} + C_{pb} - (\eta_{02} - C_{p34})(1 - a_f)^2 \quad (3.38)$$

Albeit the equations are not utilised to attain the thrust coefficient when employing the computational fluid dynamic technique, it may be implemented to acquire analytical parameters distinctive to the duct and rotor configuration. Specifically, the thrust coefficient, axial induction factor, and the pressures upstream and downstream of the rotor (p_2 & p_3) are easily attainable through the technique, yet the pressure at the outlet (p_4) may be less straightforward due to the significant flow property fluctuations in the turbulent wake. In this premise, two related variables are unknown, η_{34} and p_4 , where the prior may be approximated by:

$$\eta_{34} = a_1 + b_1 \cdot \left(\frac{A_D}{A_4}\right) + c_1 \theta_{in} + d_1 \cdot \left(\frac{A_1}{A_D}\right) \quad (3.39)$$

where θ_{in} is the inner diffuser angle, and the constants and coefficients $a_1 = 0.8867$, $b_1 = 0.5212$, $c_1 = -0.0108$, and $d_1 = -0.1313$ are implemented as within prior analyses [3].

3.1.5 Yawed Flow Adaptation

When succumb to flow bearing domain conditions, the free-stream and inflow velocities relative to the rotating turbine blades vary in relation to the blade position along the turbine rotation:

$$U_{z,\gamma} = U_\infty \cos \gamma - U_{Z_o} \quad (3.40)$$

$$U_{\theta,\gamma} = r\Omega + U_{\theta_o} - U_{\infty} \sin \gamma \cos \psi \quad (3.41)$$

where $U_{z,\gamma}$ is the resultant axial velocity in yawed conditions, $U_{\theta,\gamma}$ is the resultant tangential velocity in yawed conditions, and ψ is the rotor azimuth angle.

In modifying linear momentum theory to acknowledge variations in flow bearing, Glauert [5] argued that the fluid flow component normal to the rotor plane ($U_{\infty} \cos \gamma$) is the sole component affected by the presence of an actuator disc in recognising the balance of linear and rotational velocities [127]. The velocity component is altered by a uniform induced velocity (u_{ind}) to $U_{\infty} \cos \gamma - u_{ind}$ at the disc, hence altering the resultant flow velocity in yaw ($V_{rel,\gamma}$) to:

$$V_{rel,\gamma} = \sqrt{U_{\infty}^2 \sin^2 \gamma + (U_{\infty} \cos \gamma - u_{ind})^2} \quad (3.42)$$

In continuation, a variation in the axial momentum equation is introduced, establishing the axial thrust (T) upon the rotor:

$$T = 2\rho AV_{rel,\gamma}u_{ind} \quad (3.43)$$

$$C_T = 4a_f \sqrt{1 - a_f(2 \cos \gamma - a_f)} \quad (3.44)$$

By means of this assumption, however, the inherent non-uniform distribution of the induced velocity through the rotor is not sustained. In relation, the distinct velocity components were derived to contribute to the induced thrust at a normal to the rotor: the mean induced uniformly-distributed velocity through the rotor (u_0), established by Equation 3.43, the normal uniformly-distributed component of the free-stream ($U_{\infty} \cos \gamma$), both as previously elaborated, and, a non-uniform velocity component (u_1) inducing non-linearity within the output relative to the rotor radius and azimuth angle, of similar magnitude to u_0 .

$$u_1(r, \psi) = u_1 \frac{r}{R} \sin \psi \quad (3.45)$$

$$|u_1| = |u_0|$$

$$u_{ind} = u_0 \left(1 + K_{\chi} \frac{r}{R} \sin \psi\right) \quad (3.46)$$

where K_χ is the coefficient dependent on the yaw angle.

In establishing a value for the yaw-dependent coefficient, a number of models have been put forward:

Coleman et al. [128]

$$K_\chi = \tan\left(\frac{\chi}{2}\right) \quad (3.47)$$

White and Blake [129]

$$K_\chi = \sqrt{2} \sin(\chi) \quad (3.48)$$

Pitts and Peters [130]

$$K_\chi = \frac{15\pi}{32} \tan\left(\frac{\chi}{2}\right) \quad (3.49)$$

Howlett [131]

$$K_\chi = \sin^2(\chi) \quad (3.50)$$

where χ is the angle of skew between the mean wake flow and rotor axis, which is defined as:

$$\tan \chi = \frac{U_\infty \sin \gamma}{U_\infty \cos \gamma - U_D} \quad (3.51)$$

3.1.6 Disc Theory Correction Factors

3.1.6.1 Tip/Hub Loss Correction

As momentum theory resolves forces over an entire disc, or distinct annular sectors of a disc, rather than simulating the flow around the individual blades in motion, the methodology assumes that the fluid within the entire annular segment interacts with the blade section containing an infinite number of blades. To overcome this numerical limitation, the effects of individual blades may be approximated by considering the flow at the outer and inner boundaries of the blade; the tip and hub. These analytical approaches are utilised within the momentum equations to correct for the effects.

As vortex shedding occurs at the blade edges due to flow separation, resultant helical rotary flow structures are present within the rotor wake. Prandtl conceptualised the helical sheet surfaces as a succession of discs travelling at a constant wake velocity of $U_\infty(1 - a_f)$ with separation distances equivalent to the mean average length be-

tween the vortex sheets. In relation, Prandtl proposed the loss factor as an arithmetic representation of the flow fluctuations:

$$F_{tip} = \left(\frac{2}{\pi}\right) \cos^{-1} e^{-f_{tip}} \quad (3.52)$$

$$f_{tip} = \frac{N_b}{2} \left(\frac{R-r}{r}\right) \frac{1}{\sin \phi} \quad (3.53)$$

$$F_{hub} = \left(\frac{2}{\pi}\right) \cos^{-1} e^{-f_{hub}} \quad (3.54)$$

$$f_{hub} = \frac{N_b}{2} \left(\frac{r-r_h}{r_h}\right) \frac{1}{\sin \phi} \quad (3.55)$$

$$F_{losses} = F_{tip}F_{hub} \quad (3.56)$$

where f_{tip} and f_{hub} are the Betz-Prandtl approach with the Glauert adjustment ratio, assuming an inviscid non-swirl flow, N_b is the number of blades, R is the blade radius, r_h is the hub radius, r is a radius along the blade length, ϕ is the angle between the vortex sheets, and F_{losses} is the total loss ratio due to the tip & hub effects.

3.1.6.2 Highly-Loaded Conditions

In numerically representing a rotor as a thin disc, the downstream velocity in the wake is expressed as a function of the free-stream velocity and the axial induction factor: $U_4 = U_\infty(1 - 2a_f)$. As previously elaborated, when the rotor succumb to highly-loaded conditions, where $a_f > 0.5$, the model predicts a negative downstream velocity, hence portraying flow reversal within the wake; being physically unrealistic, this property is a significant limitation of disc modelling.

The permeability of the representative disc reduces proportionally to an increase in tip-speed ratio and/or rotor solidity (a function of blade area and number of blades) to the point where the axial induction factor approaches the value of 1.0; at this parameter, the disc effectively acts as a solid plate. Towards the limit of rotor permeability, a restricted degree of fluid is successfully transferred through the disc, resulting in secondary radial fluid transportation along the rotor until the tip of the structure, at which the fluid accelerates due to the sudden variation in geometry, inducing an ad-

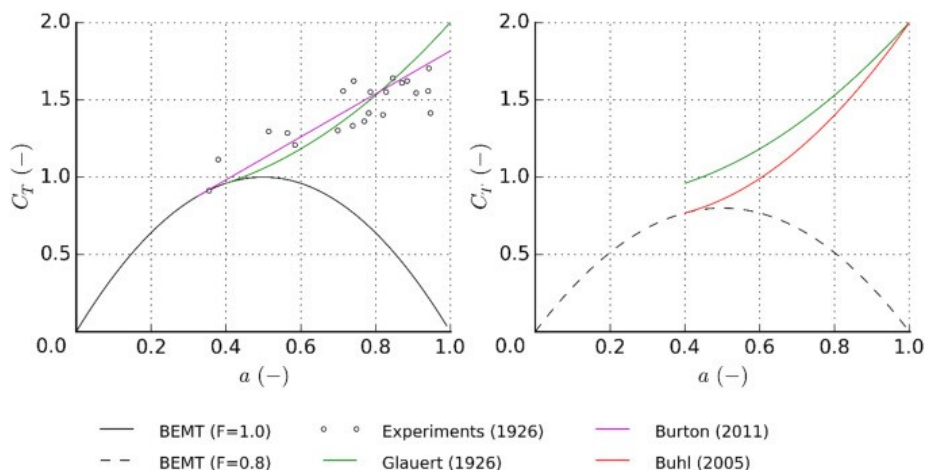


Figure 3.3: Thrust coefficient against axial induction factor, showing comparisons against BEMT with experimental values and semi-empirical corrected values (left) and highly loaded corrected values with an arbitrary tip/hub loss of 0.8 applied (right) [3]

verse pressure gradient, separating at the tip. As a result, the fluid induces a significant degree of static pressure at the fluid stagnation region upstream of the rotor, together with a region of suction downstream, both proportional to the tip-speed ratio. The significantly large pressure drop, due to the high static pressure upstream with low static pressure downstream, brings about the increased thrust.

In experimentally investigating the pressure induced upon flat circular plates, considerably higher axial forces were observed to that deduced by disc theory [127]; experimentation upon rotors [132] has shown further variance due to a thicker rotating boundary layer inducing greater suction downstream. A comparison of the experimentation points with disc theory and supplementary correction functions, illustrating the numerical distinction, is depicted in Figure 3.3.

Semi-empirical approximations have been put forward in acknowledging highly-loaded conditions to account for the considerable thrust induced upon the rotor. Linear [127] and polynomial [132,133] functions coupled to the momentum theory parabola at a transition point (a_T) have provided a numerical extension to actuator disc theory by employing a function subsequent to a_T (when $a_f \geq a_T$):

$$C_T = C_{T1} - 4\sqrt{(C_{T1} - 1)(1 - a_f)} \quad (3.57)$$

where $C_{T1} = 4(1 - a_T)^2$. The value of C_{T1} is variant within the literature when linear regression-analysing data; Burton et al. [127] put forward $C_{T1} = 1.816$ when $a_T = 0.326$ as a best-fit for data established by Glauert [132], whereas Wilson and Lissaman [134] suggested $C_{T1} = 1.60$ when $a_T = 0.368$. Distinctively, Glauert employed a parabolic function in establishing the thrust coefficient subsequent to a_T (when $a_f \geq a_T$), where $a_T = 0.4$:

$$C_T = 0.889 - \frac{(0.0203 - (a_f - 0.143)^2)}{0.6427} \quad (3.58)$$

3.1.6.3 Coupling Highly-Loaded Conditions with Tip/Hub Loss Correction

The tip/hub factor may be incorporated directly with the standard thrust equation, varying the gradient of the quadratic function: $C_T = 4F_{loss}a_f(1 - a_f)$. Yet, once implemented to the Glauert parabolic highly-loaded function, a discrepancy is present between the two models at specific loss ratios. In recognition, Eggelston and Stoddard proposed a modification:

$$C_T = 0.889 - \frac{(0.0203 - (a_f F_{loss} - 0.143)^2)}{0.6427} \quad (3.59)$$

which, albeit reducing the discrepancy, a discontinuation is still present. Buhl therefore suggested an alternative form of the equation by implementing the correction parabola as a quadratic function with relevant boundary conditions:

$$C_T = \frac{8}{9} + \left(4F_{loss} - \frac{40}{9}\right) a_f + \left(\frac{50}{9} - 4F_{loss}\right) a_f^2 \quad (3.60)$$

This adaptation accommodates the mathematical coupling of the standard thrust curve with the highly-loaded correction and tip/hub losses, where the upper limit ($a_f = 1$) is analogous to flow upon a solid plate.

3.1.7 Disc Theory Limitations

In numerically representing a rotor as a thin disc, the above methodology and its variants are implemented to approximate the force exerted on a rotor under the assumption of a singular body acting in a uniform, single-phase flow-stream. This introduces

numerical approximations upon the overall rotor performance in extrapolation from thrust and power for constant free-streams. Albeit useful in industrial applications, such as regional scale models of turbine farm arrays where individual turbine representation is superfluous, this fundamental approach does not consider temporal variations in thrust along the turbine frontal area or, in the case of a ducted turbine, the specific effect of the diffuser along the radial extremities of the system, which is imperative when assessing the performance of a single rotor.

3.1.8 Computational Fluid Dynamics

The various models previously described have been developed in disc-analysing a turbine, yet an array of limitations have been acknowledged to accompany their implementation. Amongst the key limitations of the technique is the inability of capturing transient flow phenomena within the domain and its effect upon the rotor response; when considering a true-scale, ducted, high-solidity tidal turbine, the relevant flow parameters are likely to be significant, particularly within the vicinity of the blades, and along the near-wake region immediately downstream of the turbine. In addition, the disc technique is incapable of resolving turbulence effects induced by the rotor and duct upon the flow in result of the fluid-structure interaction. For these reasons, in analysing the temporal fluid dynamic response of a geometrically-complex structure within an anisotropic, high Reynolds number flow-field, alternative high-fidelity modelling approaches are required.

Distinctively, computational fluid dynamics is a largely applicable methodology for such an analysis due to the spatial discretisation of the domain and structure in applying the finite-volume method to couple higher degrees of flow physics. The classification of computational fluid dynamics utilised in this piece of work solves the flow-field within the high Reynolds number ranges by Reynolds-averaging the fluctuations of the flow properties. The mean derivatives of the continuity and Navier-Stokes equations are, therefore, utilised to model these flow properties, where the quantities are expressed as a vectorial summation of their mean and fluctuating terms, the latter of which, in turn, are equated by means of turbulence models to achieve mathematical closure.

3.1.8.1 Mass Conservation Modelling

Within three-dimensional Cartesian space, the conservation of mass is represented as:

$$\frac{\partial \bar{\rho}}{\partial t} + \frac{\partial}{\partial x_i}(\bar{\rho}\tilde{u}_i) + \frac{\partial}{\partial x_j}(\bar{\rho}\tilde{u}_j) + \frac{\partial}{\partial x_k}(\bar{\rho}\tilde{u}_k) = 0 \quad (3.61)$$

where $\bar{\rho}$ is the Reynolds-averaged density, x_i is the Cartesian coordinate, t is the elapsed time, and \tilde{u}_i is the mass-averaged velocity [135, 136].

Assuming the fluid is incompressible, single-phase, and isotropic, due to the physicality of the hydrodynamic domain, within a Reynolds-averaged, indicial notation form, the mass continuity equation takes the form of:

$$\frac{\partial U_i}{\partial x_i} + \frac{\partial U_j}{\partial x_j} + \frac{\partial U_k}{\partial x_k} = 0 \quad (3.62)$$

where U_i is the Reynolds-averaged velocity.

3.1.8.2 Momentum Conservation Modelling

In continuation, the conservation of momentum within three-dimensional, tensor notation is represented as:

$$\frac{\partial(\bar{\rho}\tilde{u}_i)}{\partial t} + \frac{\partial}{\partial x_j}(\bar{\rho}\tilde{u}_i\tilde{u}_j - \bar{\sigma}_{ij}) = 0 \quad (3.63)$$

where $\bar{\sigma}_{ij}$ is the total stress tensor. The above equation, in Reynolds-averaged format, then becomes:

$$\rho \frac{\partial U_i}{\partial t} + \rho \frac{\partial}{\partial x_j}(U_i U_j + \overline{u'_j u'_i}) - \frac{\partial}{\partial x_j}(\sigma_{ij}) = 0 \quad (3.64)$$

where ρ is the Reynolds-averaged density, U_i is the Reynolds-averaged velocity, u'_i is the fluctuating velocity component, and σ_{ij} is the Reynolds-averaged total stress tensor, which, for incompressible flows, under the absence of volume dilation (or elastic stress), is specified as the tensor summation of the static pressure and viscous stress tensor:

$$\sigma_{ij} = -\delta_{ij}P_s + \mu\left(\frac{\partial U_i}{\partial x_j} + \frac{\partial U_j}{\partial x_i}\right) \quad (3.65)$$

where δ_{ij} is the Kronecker delta (or unit tensor), P_s is the static pressure, and μ is the dynamic viscosity. The momentum equation, therefore, may be presented as:

$$\rho \frac{\partial U_i}{\partial t} + \rho U_j \frac{\partial U_i}{\partial x_j} = -\frac{\partial P_s}{\partial x_i} + \frac{\partial}{\partial x_j} \left(\mu \left(\frac{\partial U_i}{\partial x_j} + \frac{\partial U_j}{\partial x_i} \right) - \rho \overline{u'_j u'_i} \right) \quad (3.66)$$

where $-\rho \overline{u'_j u'_i} = \rho \tau_{ij}$, and is known as the Reynolds-stress tensor, with $\tau_{ij} = -\overline{u'_j u'_i}$ being the specific Reynolds-stress tensor.

3.2 Turbulent Flow

When considering flow domains at comparatively low velocities and minute length-scales, depicting low Reynolds number values, the equations of motion for a viscous fluid present a development of steady conditions. Representing the laminar nature of a fluid flow, this regime is largely governed by the viscous diffusion of kinetic energy present as vorticity and momentum. Yet, as the kinetic energy within the flow increases, the specific inertia overcomes the viscous stresses, inducing rapid spatial and temporal fluctuations of velocity and pressure, resulting in an unstable regime characterising three-dimensional, non-linear, unsteady motion, describing the transition to a turbulent domain [137].

As turbulence is characterised by random flow property fluctuations, statistical methodologies are utilised in its analysis; to account for its effect within a flow-field, the equations of fluid motion are then modified and amended by the statistical approach. To acquire the response, the Reynolds-Averaged approach may be utilised, where the flow properties are integrated over time to extract their time-averaged outcomes:

$$f_{fl} = \bar{f}_{fl} + f'_{fl} \quad (3.67)$$

$$\bar{f}_{fl} = \frac{1}{\Delta t} \int_{t_0}^{t_0+\Delta t} f_{fl} dt \quad (3.68)$$

$$\bar{f}'_{fl} = \frac{1}{\Delta t} \int_{t_0}^{t_0+\Delta t} f'_{fl} dt = 0 \quad (3.69)$$

where f_{fl} is the instantaneous flow quantity, \bar{f}_{fl} is the summation of the mean component, and f'_{fl} is the time-dependent fluctuating component [138].

In specification of flows along a structure, viscous forces act in regions adjacent to the surface, restricting the flow velocity, and inducing a boundary layer. Primarily initiated within a streamline laminar response, where the presence of eddy current mixing occurs at a microscopic scale, the geometrical and physical properties of the domain may substantiate the degree of flow mixing, hence increasing the quantity and magnitude of the eddy currents to a macroscopic scale, transitioning the flow into a turbulent regime [138].

Within a marine environment, the induced shear profile of the current along the seabed comprises of turbulence generation and wall normal mixing, where, due to the substantial height of the region, design loading is affected at all scales. Therefore, as turbulence is inherently aperiodic/chaotic, its influence upon the performance of an engineering system may be acknowledged to be periodic, aperiodic, or steady-state, establishing the requirement for a high-fidelity analysis, distinctively within the investigation of fluid-structure interaction [30].

3.2.1 The Law of the Wall

The principle of the law of the wall elaborates a dynamic fluid response describing the stream-wise velocity of a fluid particle within the turbulent region of a boundary layer to be proportional to the logarithmic distance of the particle from the wall [139]. As an incompressible fluid flows along a smooth structure, unsuccumb to an external pressure gradient, three distinct regions are discernible within the turbulent boundary layer: the viscous sublayer, buffer zone, and turbulent log layer; these layers have been mathematically characterised in describing the velocity profiles in relation to the distance from the surface:

$$u^+ = y^+ \tag{3.70}$$

$$u^+ = \frac{1}{\kappa} \ln y^+ + C \tag{3.71}$$

where u^+ is the dimensionless velocity, y^+ is the dimensionless distance from the surface, κ is the Kármán's constant, C is a dimensionless integration constant; the graphical constitutions of the dimensionless variables are illustrated in Appendix A.1 Figure A.1.

3.2.2 Reynolds-Averaged Navier Stokes Turbulence Modelling

In introducing mathematical capacities to model the specific Reynolds-stress tensor, and hence, model turbulence within the computational domain, measures are implemented to regard parametric effects of flow history transience, together with the development of convection, production, and body-force terms, in response to physical disparities in strain rate, and the resultant diffusion, redistribution, and dissipation [137].

3.2.2.1 Standard Stress- ω (STD τ - ω)

In an effort to introduce the aspects of turbulence, the Wilcox Stress- ω turbulence model was primarily utilised in this CFD model, in which the specific Reynolds-stress tensor (τ_{ij}), in tensor notation, is established by:

$$\rho \frac{\partial \tau_{ij}}{\partial t} + \rho U_k \frac{\partial \tau_{ij}}{\partial x_k} = D_{T,ij}^T + D_{L,ij}^T + P_{ij}^T + G_{ij}^T + \Pi_{ij}^T - \varepsilon_{ij}^T + F_{ij}^T \quad (3.72)$$

where $\rho \frac{\partial \tau_{ij}}{\partial t}$ is the local time derivative term, $\rho U_k \frac{\partial \tau_{ij}}{\partial x_k}$ is the convection term, $D_{T,ij}^T$ is the turbulent diffusion term, $D_{L,ij}^T$ is the molecular diffusion term, P_{ij}^T is the stress production term, G_{ij}^T is the buoyancy production term (null when utilising RSM- ω model), Π_{ij}^T is the pressure strain term, ε_{ij}^T is the dissipation term, F_{ij}^T is the production by system rotation term. In elaboration of the terms, the equation becomes:

$$\rho \frac{\partial \tau_{ij}}{\partial t} + \rho U_k \frac{\partial \tau_{ij}}{\partial x_k} = \frac{\partial}{\partial x_k} \left(\frac{\mu_T}{\sigma_k} \frac{\partial \tau_{ij}}{\partial x_k} \right) + \frac{\partial}{\partial x_k} \left(\mu \frac{\partial \tau_{ij}}{\partial x_k} \right) - \rho P_{ij} - \rho \Pi_{ij} + \frac{2}{3} \beta^* \rho \omega k \delta_{ij} - 2 \rho \omega_k (\tau_{jm} \epsilon_{ikm} + \tau_{im} \epsilon_{jkm}) \quad (3.73)$$

$$\rho \frac{\partial \tau_{ij}}{\partial t} + \rho U_k \frac{\partial \tau_{ij}}{\partial x_k} = \frac{\partial}{\partial x_k} \left[\left(\mu + \frac{\mu_T}{\sigma_k} \right) \frac{\partial \tau_{ij}}{\partial x_k} \right] - \rho P_{ij} - \rho \Pi_{ij} + \frac{2}{3} \beta^* \rho \omega k \delta_{ij} - 2 \rho \omega_k (\tau_{jm} \epsilon_{ikm} + \tau_{im} \epsilon_{jkm}) \quad (3.74)$$

where P_{ij} is the Reynolds stress production tensor, k is the kinetic energy of turbulent fluctuations per unit mass (or turbulence kinetic energy), ω is the specific dissipation rate, σ_k is the turbulent Prandtl constant, δ_{ij} is the Kronecker delta, Π_{ij} is the pressure-strain correlation tensor, μ is the dynamic viscosity, μ_T is the eddy viscosity / turbulent viscosity, ω_k is the rotation vector, and ϵ_{ijk} is the Levi-Civita pseudotensor.

$$\epsilon_{ijk} = \begin{cases} +1 & \text{if } (i, j, k) \text{ is } (1, 2, 3), (2, 3, 1), \text{ or } (3, 1, 2), \\ -1 & \text{if } (i, j, k) \text{ is } (3, 2, 1), (1, 3, 2), \text{ or } (2, 1, 3), \\ 0 & \text{if } i = j, \text{ or } j = k, \text{ or } k = i \end{cases} \quad (3.75)$$

In continuation, the specific dissipation rate (ω) is defined by:

$$\rho \frac{\partial \omega}{\partial t} + \rho U_j \frac{\partial \omega}{\partial x_j} = \frac{\partial}{\partial x_j} (\Gamma_\omega \frac{\partial \omega}{\partial x_j}) + G_\omega - Y_\omega + S_\omega \quad (3.76)$$

where Γ_ω is the effective diffusivity, G_ω is the production, Y_ω is the dissipation, and S_ω is the user-defined source terms. In elaboration of the terms, the equation becomes:

$$\rho \frac{\partial \omega}{\partial t} + \rho U_j \frac{\partial \omega}{\partial x_j} = \frac{\partial}{\partial x_j} [(\mu + \frac{\mu_T}{\sigma_k}) \frac{\partial \omega}{\partial x_j}] + \alpha \frac{\rho \omega}{k} \tau_{ij} \frac{\partial U_i}{\partial x_j} - \beta_o f_\beta \rho \omega^2 \quad (3.77)$$

where β is a variable utilised to implement the mean rotation tensor (Ω_{ij}); α , σ_d , and σ are closure coefficients. The pressure-strain correlation tensor (Π_{ij}) is defined by:

$$\Pi_{ij} = \beta^* C_1 \omega (\tau_{ij} + \frac{2}{3} k \delta_{ij}) - \hat{\alpha} (P_{ij} - \frac{1}{3} P_{kk} \delta_{ij}) - \hat{\beta} (D_{ij} - \frac{1}{3} P_{kk} \delta_{ij}) - \hat{\gamma} k (S_{ij} - \frac{1}{3} S_{kk} \delta_{ij}) \quad (3.78)$$

where S_{ij} is the mean strain-rate tensor and D_{ij} is the rotation production tensor; C_1 , $\hat{\alpha}$, $\hat{\beta}$, and $\hat{\gamma}$ are closure coefficients. The turbulence kinetic energy (k) is defined by:

$$k = \frac{1}{2} \overline{u'_i u'_i} \quad (3.79)$$

The eddy viscosity / turbulent viscosity (μ_T) is defined by:

$$\mu_T = \alpha^* \rho \frac{k}{\omega} = \alpha^* \rho k^{\frac{1}{2}} l_s \quad (3.80)$$

where l_s is the turbulent length scale. Low Reynolds number corrections are not implemented within this analysis, hence $\alpha^* = 1$. The mean strain-rate tensor (S_{ij}) is defined by:

$$S_{ij} = \frac{1}{2} \left(\frac{\partial U_i}{\partial x_j} + \frac{\partial U_j}{\partial x_i} \right) \quad (3.81)$$

The mean rotation tensor (Ω_{ij}) is defined by:

$$\Omega_{ij} = \frac{1}{2} \left(\frac{\partial U_i}{\partial x_j} - \frac{\partial U_j}{\partial x_i} \right) \quad (3.82)$$

The Reynolds stress production tensor (P_{ij}) is defined by:

$$P_{ij} = \tau_{im} \frac{\partial U_j}{\partial x_m} + \tau_{jm} \frac{\partial U_i}{\partial x_m} \quad (3.83)$$

The rotation production tensor (D_{ij}) is defined by:

$$D_{ij} = \tau_{im} \frac{\partial U_m}{\partial x_j} + \tau_{jm} \frac{\partial U_m}{\partial x_i} \quad (3.84)$$

The vortex-stretching function (f_β) is defined by:

$$f_\beta = \frac{1 + 85\chi_\omega}{1 + 100\chi_\omega} \quad (3.85)$$

The dimensionless vortex-stretching parameter (χ_ω) is defined by:

$$\chi_\omega = \left| \frac{\Omega_{ij} \Omega_{jk} S_{ki}}{(\beta^* \omega)^3} \right| \quad (3.86)$$

The rotation production tensor (D_{ij}) is defined by:

$$S_{ki} = S_{ki} - \frac{1}{2} \frac{\partial U_m}{\partial x_m} \delta_{ki} \quad (3.87)$$

Specificities with regard to tensor definitions, and closure coefficients and derivatives may be further established in the referenced literature [135,137].

3.2.2.2 Baseline Stress- ω (BSL τ - ω)

The BSL Stress- ω model was developed to effectively blend the robust and accurate formulation of the ω - model in the near-wall region, with the free-stream independence of the ε -model in the far field; to achieve this, the ω model is converted into an ε formulation by utilising a mathematical blending function. The BSL Stress- ω model is similar to the Standard Stress- ω model, yet includes the following refinements:

- The ω model and the transformed ε model are multiplied by a blending function, with both models in summation. The blending function is designed to produce unity (1) in the near-wall region, activating the ω model, and null (0) away from the surface, initiating the transformed ε model.
- The BSL model incorporates a damped cross-diffusion derivative term in the equation.
- The modeling constants are different.

The specific Reynolds-stress tensor (τ_{ij}) is established by a quasi-equivalent function as the Standard τ - ω , yet implements a blending function at the molecular diffusion term:

$$\rho \frac{\partial \tau_{ij}}{\partial t} + \rho U_k \frac{\partial \tau_{ij}}{\partial x_k} = \frac{\partial}{\partial x_k} \left[\left(\mu + \frac{\mu_T}{(F_1)\sigma_{k,1} + (1 - F_1)\sigma_{k,2}} \right) \frac{\partial \tau_{ij}}{\partial x_k} \right] - \rho P_{ij} - \rho \Pi_{ij} + \frac{2}{3} \beta^* \rho \omega k \delta_{ij} - 2 \rho \omega_k (\tau_{jm} \epsilon_{ikm} + \tau_{im} \epsilon_{jkm}) \quad (3.88)$$

where F_1 is a blending function, equivalent to $\tanh(\phi_1^4)$, which considers the distance of the fluid from a surface in relation to distinct fluid properties.

In turn, the specific dissipation rate (ω) is defined by a quasi-equivalent function as the Standard τ - ω , yet incorporates a cross-diffusion modification term (D_ω) in addition

to implementing a blending function at the remaining terms:

$$\rho \frac{\partial \omega}{\partial t} + \rho U_j \frac{\partial \omega}{\partial x_j} = \frac{\partial}{\partial x_j} (\Gamma_\omega \frac{\partial \omega}{\partial x_j}) + G_\omega - Y_\omega + D_\omega \quad (3.89)$$

$$\begin{aligned} \bar{\rho} \frac{\partial \omega}{\partial t} + \bar{\rho} U_j \frac{\partial \omega}{\partial x_j} &= \frac{\partial}{\partial x_j} \left[\left(\mu + \frac{\mu_T}{\frac{F_1}{\sigma_{\omega,1}} + \frac{1-F_1}{\sigma_{\omega,2}}} \right) \frac{\partial \omega}{\partial x_j} \right] + \\ \alpha \frac{\rho \omega}{k} \tau_{ij} \frac{\partial U_i}{\partial x_j} - [F_1 \beta_{i,1} + (1-F_1) \beta_{i,2}] \rho \omega^2 &+ \frac{2(1-F_1)}{\sigma_{\omega,2}} \frac{\bar{\rho}}{\omega} \frac{\partial \tau_{ij}}{\partial x_j} \frac{\partial \omega}{\partial x_j} \end{aligned} \quad (3.90)$$

3.2.2.3 Shear-Stress Transport $k - \omega$ (SST $k - \omega$)

Implementing the methodology defined by the Boussinesq eddy-viscosity approximation, the two-equation model computes the Reynolds' stress tensor as the product of the eddy viscosity and the mean strain-rate tensor:

$$\rho \tau_{ij} = -\overline{\rho u'_j u'_i} = 2\mu_T S_{ij} - \frac{2}{3} \rho k \delta_{ij} \quad (3.91)$$

Due to this assumption, the transport of the turbulence kinetic energy (k) is then required, and is defined by:

$$\rho \frac{\partial k}{\partial t} + \rho U_i \frac{\partial k}{\partial x_i} = \frac{\partial}{\partial x_j} (\Gamma_k \frac{\partial k}{\partial x_j}) + G_k - Y_k + S_k \quad (3.92)$$

where, with regard to turbulence kinetic energy, Γ_k is the effective diffusivity, G_k is the production, Y_k is the dissipation, and S_k are user-defined source terms. In turn, whilst implementing a blending function, the general function elaborates into:

$$\bar{\rho} \frac{\partial k}{\partial t} + \bar{\rho} U_j \frac{\partial k}{\partial x_j} = \frac{\partial}{\partial x_j} \left[\left(\mu + \frac{\mu_T}{\frac{F_1}{\sigma_{k,1}} + \frac{1-F_1}{\sigma_{k,2}}} \right) \frac{\partial k}{\partial x_j} \right] + \mu_T |S_{ij}|^2 - \rho \beta_i^* f_{\beta^*} k \omega \quad (3.93)$$

where F_1 is a blending function and is equal to $\tanh(\phi_1^4)$ is a variable utilised to implement the mean rotation tensor (Ω_{ij}); α , σ_d , and σ are closure coefficients.

The transport of specific dissipation rate (ω) is defined by a quasi-equivalent function as the BSL τ - ω , yet incorporates turbulence kinetic energy terms, rather than the

Reynolds' stress tensor:

$$\begin{aligned} \bar{\rho} \frac{\partial \omega}{\partial t} + \bar{\rho} U_j \frac{\partial \omega}{\partial x_j} = \frac{\partial}{\partial x_j} \left[\left(\mu + \frac{\mu_T}{\frac{F_1}{\sigma_{\omega,1}} + \frac{1-F_1}{\sigma_{\omega,2}}} \right) \frac{\partial \omega}{\partial x_j} \right] + \\ \alpha \rho |S_{ij}|^2 - [F_1 \beta_{i,1} + (1-F_1) \beta_{i,2}] \rho \omega^2 + \frac{2(1-F_1) \bar{\rho}}{\sigma_{\omega,2}} \frac{\partial k}{\omega} \frac{\partial \omega}{\partial x_j} \end{aligned} \quad (3.94)$$

where β is a variable utilised to implement the mean rotation tensor (Ω_{ij}); α , σ_d , and σ are closure coefficients.

The eddy viscosity / turbulent viscosity (μ_T) is defined by:

$$\mu_T = \rho \frac{k}{\omega} \frac{1}{\max\left[\frac{1}{\alpha^*}, \frac{SF_2}{\alpha_1 \omega}\right]} \quad (3.95)$$

where F_2 is a blending function, equivalent to $\tanh(\phi_2^4)$, which considers the distance of the fluid from a surface in relation to distinct fluid properties.

3.3 Physical Modelling

In consideration of the analysis of a physical turbine, notable definitions concerning the resultant performance outcomes, in terms of the boundary conditions employed, are identified. Utilised to attain quasi-real-ocean conditions, the blockage ratio (α_{bl}) is defined as a correlation between the device reference area (A_{dvc}) and the domain sectional area (A_{dmn}):

$$\alpha_{bl} = \frac{A_{dvc}}{A_{dmn}} = \frac{\pi R_{dvc}^2}{L_{dmn}^2} \quad (3.96)$$

where R_{dvc} is the device radius, and L_{dmn} is the length of the quadratic cross-sectional area of the computational domain.

The tip-speed ratio (TSR) is established as an equivalence between the linear blade-tip velocity and the free-stream velocity:

$$TSR = \frac{|\Omega_{sys}| R_{rtr}}{U_\infty} = \frac{|\Omega_x| R_{rtr}}{U_\infty} \quad (3.97)$$

where Ω_{sys} is the system rotational speed, hence Ω_x being the axial angular velocity,

and R_{rtr} is the rotor radius. A distinction must be made between the device radius and the rotor radius when modelling ducted turbines. In the case of a ducted turbine, $R_{dvc} \neq R_{rtr}$, but $R_{dvc} = R_{dct}$, contrary to a non-ducted turbine, where $R_{dvc} = R_{rtr}$.

The rotor solidity (σ_r) of a turbine is applied to establish a ratio between the projected area of the static rotor in the axial direction (A_{bld-z}) and the total area of the rotor rotation (A_{rtr}):

$$\sigma_r = \frac{A_{bld-z}}{A_{rtr}} = \frac{A_{bld-z}}{\pi R_{rtr}^2} \quad (3.98)$$

The radius-based Reynolds number (Re_∞) is utilised to acquire a dimensionless representation of the fluid-structure interaction by considering the fluid inertial and viscous forces as a blunt body:

$$Re_\infty = \frac{\rho U_\infty R_{dvc}}{\mu} \quad (3.99)$$

where ρ is the fluid density, U_∞ is the free-stream velocity, and μ is the fluid dynamic viscosity.

The length-based Reynolds number (Re_L) is utilised to acquire a dimensionless representation of the fluid-structure interaction by considering the fluid inertial and viscous forces along the length of the structure:

$$Re_L = \frac{\rho U_\infty L_{dvc}}{\mu} \quad (3.100)$$

where L_{dvc} is the device length, and hence is equal either to the hub length (L_{hub}) for the HATT, or the duct length (L_{dct}) for the ducted turbine.

In continuation, the chord-based Reynolds number (Re_{ch}) is utilised to acquire a dimensionless representation of the fluid-structure interaction in terms of the resultant velocity at 75% of the radius of the rotating device blades:

$$Re_{ch} = \frac{\rho c_{75\%} \sqrt{(U_\infty)^2 + (\Omega_x R_{75\%})^2}}{\mu} \quad (3.101)$$

where $c_{75\%}$ is the chord length at 75% of the blade radius ($R_{75\%}$).

To determine the turbine capacity in converting the fluid free-stream energy into

rotational energy, the power coefficient (C_P) is established. This considers the mechanical rotational power attained by the device (P_{dvc}) as a ratio of the maximum rotational power potentially acquired in the device area (P_∞):

$$C_P = \frac{P_{dvc}}{P_\infty} = \frac{M_x \Omega_x}{\frac{1}{2} \rho A_{dvc} U_\infty^3} = \frac{M_x \Omega_x}{\frac{1}{2} \rho \pi R_{dvc}^2 U_\infty^3} \quad (3.102)$$

where M_x is the axial moment, also referred to as the rotor torque.

In relation to the power generated, the torque coefficient (C_Q) evaluates the mechanical torque attained by the device (Q_{dvc}) as a ratio of the maximum torque potentially acquired in the device area (Q_∞):

$$C_Q = \frac{Q_{dvc}}{Q_\infty} = \frac{M_x}{\frac{1}{2} \rho A_{dvc} R_{rtr} U_\infty^2} = \frac{M_x}{\frac{1}{2} \rho \pi R_{dvc}^2 R_{rtr} U_\infty^2} \quad (3.103)$$

In relation to the power generated, the mass flow-rate coefficient ($C_{\dot{m}}$) evaluates the mass flow-rate through the rotor (\dot{m}_{rtr}) as a ratio of the maximum mass flow-rate which may be potentially attained within the duct:

$$C_{\dot{m}} = \frac{\dot{m}_{rtr}}{\rho A_{rtr} U_\infty} = \frac{\dot{m}_{rtr}}{\rho \pi R_{rtr}^2 U_\infty} \quad (3.104)$$

In continuation, the resultant thrust on the device induced in a direction parallel to the turbine axis contributes to the fluid-structure phenomenon. The thrust coefficient ($C_{T,dvc}$) quantifies this as a function of the device thrust (T_{dvc}) and the maximum thrust potentially induced upon the device area (T_∞):

$$C_{T,dvc} = \frac{T_{dvc}}{T_\infty} = \frac{F_x}{\frac{1}{2} \rho A_{dvc} U_\infty^2} = \frac{F_x}{\frac{1}{2} \rho \pi R_{dvc}^2 U_\infty^2} \quad (3.105)$$

where F_x is the stream-wise axial force on the device.

In analysing the transient sinusoidal fluctuations in the performance outcomes, Strouhal's law was utilised in evaluating its relationship with the Reynolds number of the domain:

$$St = \frac{f_v L_{St}}{U_\infty} \quad (3.106)$$

where St is the Strouhal number, f_v is the vortex-shedding frequency, and L_{St} is the Strouhal characteristic length.

In establishing the fatigue life of the materials constituting the blades, the strain-life method was utilised to relate the temporal structural response:

$$\frac{\Delta\varepsilon_e}{2} = \frac{\sigma'_f}{E} \cdot (2N_f)^b \quad (3.107)$$

where $\Delta\varepsilon_e$ is the total strain amplitude, σ'_f is the fatigue strength parameter, E is the Young's modulus, N_f is the number of cycles to failure, and b is the fatigue strength exponent (Basquin's exponent).

In putting forward a statistical measure of the modelling prediction aptitude to the real data points, the coefficient of determination (R^2) was utilised:

$$\bar{y}_n = \frac{1}{n} \sum_{i=1}^n y_i \quad (3.108)$$

$$SS_{tot} = \sum_i (y_i - \bar{y})^2 \quad (3.109)$$

$$SS_{res} = \sum_i (y_i - f_i)^2 \quad (3.110)$$

$$R^2 = 1 - \frac{SS_{res}}{SS_{tot}} \quad (3.111)$$

where y_i is the observed data, \bar{y}_n is the mean of the observed data, SS_{tot} is the total sum of squares, SS_{res} is the sum of squares of residuals, and f_i is the predicted data.

3.4 Chapter Summary

This chapter provided a detailed elaboration into the fundamental methodologies utilised within this thesis to model turbine hydrodynamics, in specification to linear momentum theory, blade element theory, and their coupled approach, whilst expounding into ducted turbine and yawed flow adaptations. In addition, the governing continuity equations, together with the turbulence models required to numerically describe a turbulent regime, were expanded as resolved by the computational fluid dynamics

technique. Furthermore, the characterisation of the numerical model, where the formulae utilised in relation to the physical parameters of the tidal turbine, within the flow continuum, were specified.

Chapter 4

Methodology of the Fluid-Structure Interaction Analysis

This chapter provides an elaboration on the procedures with which the one-way fluid-structure interaction analysis was performed. In describing the geometrical models, hydrodynamic parameters, and structural properties utilised within the turbine setup, a characterisation of the numerical framework, in reference to the computational fluid dynamic and finite element solvers, is presented.

4.1 Physical Setup of the Turbine Models

In an effort to establish an accurate blade-resolved fluid-structure interaction framework, a three-dimensional geometrical representation of a three-bladed horizontal-axis tidal turbine (HATT) was primarily modelled from literature to be employed in attaining a validated hydrodynamic finite-volume computational model. Subsequently, the geometrical representation of the ducted high-solidity tidal turbine was implemented within the validated CFD model library setup to acquire its hydrodynamic performance and rotor structural response within aligned, yawed, and vortex flow conditions.

4.1.1 Three-Bladed Horizontal Axis Tidal Turbine

For the purpose of attaining a validated computational fluid dynamic model for tidal turbine analyses applications, simulations were established to numerically replicate the experimentation undertaken by Mycek et al. [140]. Identical blade, nacelle, and mast geometry were utilised within the model domain, where the main dimensions of the turbine include a rotor diameter (D_{rtr}) of 0.7 m, a nacelle length of 2.5 m, and a mast length of 1 m, as illustrated in Figure 4.1; supplementary descriptions may be attained within the literature. A distinction is present, however, between the physical aspects of the experimentation and the numerical model. In the prior, the nacelle mast protruded through the free-surface to connect to the above support, whereas, in the latter, solely the submerged length of the mast was considered, with a hemisphere at the tip to avoid tip-induced vortices. A physical assumption is hence present within which the drag forces upon the mast are solely considered to be due to the current, rather than any additional wave & wind factors. Albeit, due to the fact that waves were not induced in the experimentation, and that the setup was in a closed, controlled environment, the assumption that free-surface and topside effects were insignificant, when considering the induced physics of the turbine, was held. In addition, within the experimentation rig, fairings were installed along the submerged section of the mast to avoid vortex-induced vibrations (VIVs). The geometry of the installation, however, was not elucidated, and hence, was not included in the numerical model. The parameters of the turbine rotational velocity and fluid-flow were instated from the literature, with a constant incoming free-stream velocity of 0.8 m/s, a tip-speed ratio (TSR) range of 1.00 - 8.26, an inlet turbulence intensity of 3%, and a turbulent length scale of 1 m.

4.1.2 Ducted High-Solidity Tidal Turbine

Upon attaining validation, the model libraries were implemented for the analysis of a ducted eight-bladed tidal turbine, similar to the design of the OpenHydro PS2 device. The general dimensions of the turbine were provided by EDF R&D, which describe a rotor diameter of 12 m, a duct diameter of 15 m, and a duct length of 10 m, as illustrated in Figure 4.2, with a solidity factor of 0.614; supplementary descriptions

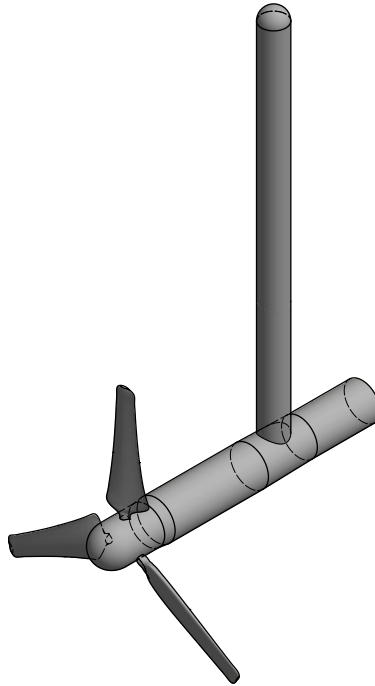
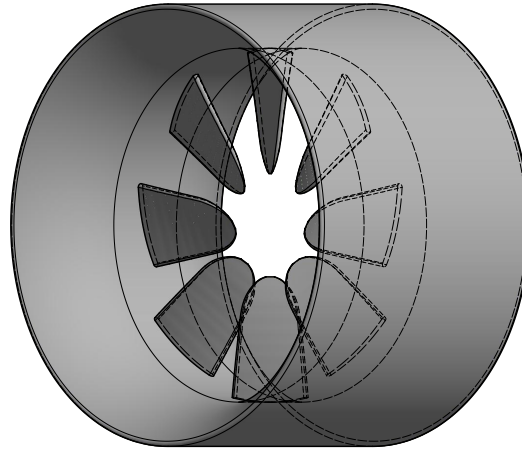


Figure 4.1: Rendered three-dimensional CAD representation of the horizontal-axis tidal turbine [140] utilised for the validation of the CFD model

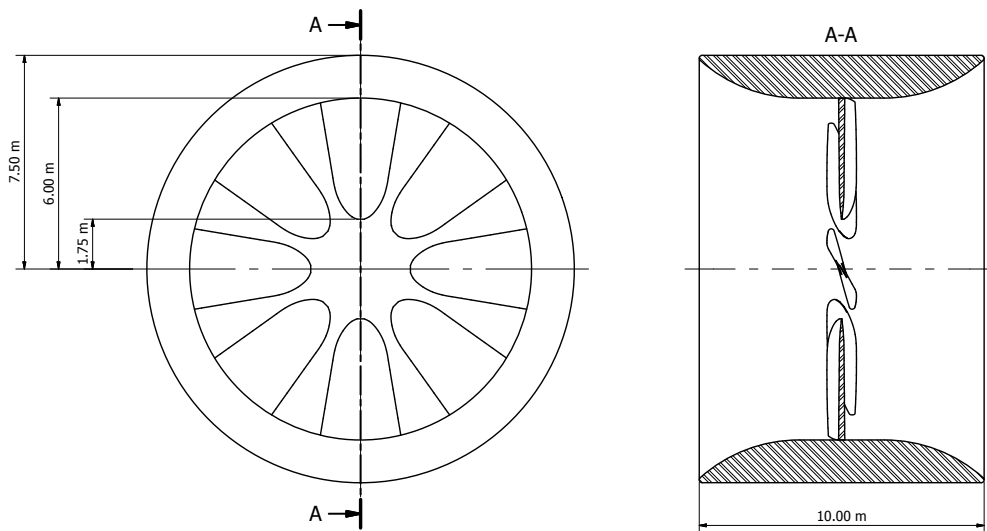
are available in Table 4.1. The hydrofoil sections comprising the rotor blades consisted of a flat-plate design with rounded edges, where the geometry is quasi-identical to Allsop et al. [3], being slightly adapted to attain a more homogeneous blade surface, as described in Table 4.2.

4.1.2.1 Hydrodynamic Analysis

The parameters of the turbine and fluid flow were instated from real-world data, recommended by EDF R&D, as reported in Neill et al. [141] and Bahaj and Myers [142], with maximum acquired spring tide velocities of 4.0 m.s^{-1} , and surface velocities of 5.0 m.s^{-1} . For this reason, the initiated free-stream velocity range within the CFD model varied between 1 m.s^{-1} and 7 m.s^{-1} , in iterations of 1.5 m.s^{-1} , with an inlet turbulence intensity of 3% and an inlet turbulent length scale of 1 m, to acquire a definitive performance spectrum of the turbine. Within this free-stream velocity variation, a turbine TSR range of 1 - 2.5 was considered as the nominal region, both due to high-



(a) Rendered three-dimensional CAD representation



(b) First-angle sectioned projection

Figure 4.2: Geometrical model of the ducted high-solidity tidal turbine utilised for the CFD analyses

solidity predictions specified by Betz [143], and analysis by Allsop et al. [88].

In continuation, furthering the ducted tidal turbine performance investigation from aligned flow response, yawed flow analysis was subsequently pursued. The parameters of the turbine and fluid flow were, again, instated from real-world data, recommended by EDF R&D, as reported in Pham and Martin [25] and Pham and Pinte [26] when numerically simulating the tidal cycle at the Paimpol-Bréhat site, acknowledging

Description	Validation Turbine [140]	Ducted Turbine
Blade Profile	NACA 63418	Round-Edged Flat Plate
Rotor Radius (R_{rtr})	0.35 m	6.00 m
Hub Radius (R_{hub})	0.046 m	1.75 m
Duct Radius (R_{dct})	N/A	7.50 m
Hub Length (L_{hub})	0.72 m	N/A
Duct Length (L_{dct})	N/A	10.00 m
Linear Velocity (U_∞)	0.8 m.s ⁻¹	1 m.s ⁻¹ - 7 m.s ⁻¹
Angular Bearing (ϕ_∞)	0°	0° - 45°
Tip-Speed Ratio (TSR)	1.00 - 8.26	1.00 - 2.50
Rotor Solidity (S_{rtr})	0.132	0.614
Rotational Orientation	counter-clockwise	clockwise
Reynolds Number (Re_∞)	$0.279 \cdot 10^6$	$[5.97 - 41.80] \cdot 10^6$
Reynolds Number (Re_L)	$0.573 \cdot 10^6$	$[9.95 - 69.67] \cdot 10^6$
Reynolds Number (Re_{ch})	$[0.049 - 0.245] \cdot 10^6$	$[3.15 - 37.49] \cdot 10^6$

Table 4.1: Summary of Turbine Model Descriptions

an asymmetric velocity, in both magnitude and direction, at ebb and flood, with an average-depth angular discrepancy of 20°. For this reason, a free-stream velocity of 4 m.s⁻¹ was solely utilised, yet induced within an angular bearing range of 0° to 45°, in iterations of 15°, together with a bearing of 23.2°, equivalent to the geometrical angle of the inner duct profile curvature, to acquire a definitive performance spectrum of the turbine.

Supplementary to current flow analysis, numerical investigations [144] relevant to the resultant production of vortical flow structures along potential tidal turbine sites, in consequence of tidal-current interaction with bathymetric features, has put forward a probabilistic spectrum of properties within the induced flow along the English Channel. By means of the analysis, the range of vorticity, vortex length scale, and turbulence intensity had been acquired, with values of $\leq 0.3 \text{ s}^{-1}$, $\leq 25 \text{ m}$, and 7% (15 m above the seabed) - 20% (seabed), respectively. In relation to the study, as the tidal turbine was designed to be in operation between 5 m to 30 m above the seabed, the possibility of the rotor being succumb to significant, performance-affecting, highly-turbulent flow structures, such as discrete vortices, from the incoming flow is substantial.

In interest of the performance discrepancy brought about by site conditions, an

r_{rtr}/R_{rtr}	c_{rtr}/R_{rtr}	Pitch ($^{\circ}$)	t_{rtr}/c_{rtr} (%)
0.2917	0.0500	32.00	6.67
0.3067	0.1208	31.66	4.14
0.3350	0.1908	30.98	5.24
0.3633	0.2383	30.30	6.29
0.3917	0.2750	29.62	6.67
0.4200	0.3025	28.94	7.16
0.4483	0.3233	28.26	7.22
0.4767	0.3383	27.58	6.90
0.5050	0.3500	26.90	7.14
0.5333	0.3583	26.22	6.98
0.5617	0.3667	25.54	6.82
0.5900	0.3750	24.86	7.11
0.6183	0.3833	24.18	6.96
0.6467	0.3917	23.50	6.81
0.6750	0.4000	22.82	7.08
0.7033	0.4083	22.14	6.94
0.7317	0.4167	21.46	7.20
0.7600	0.4250	20.78	7.06
0.7883	0.4333	20.10	6.92
0.8167	0.4417	19.42	7.17
0.8450	0.4500	18.74	7.04
0.8733	0.4583	18.06	6.91
0.9017	0.4667	17.38	7.14
0.9300	0.4750	16.70	7.02
0.9583	0.4833	16.02	6.90
0.9867	0.4917	15.34	7.12
1.0000	0.5000	15.00	7.00

Table 4.2: Detailed ducted turbine blade profile descriptions

artificially-induced explicit vortex, known as a forced vortex or flywheel vortex, was generated within the computational fluid dynamic domain, upstream of the turbine, to replicate the unsteady flow phenomena established within the literature. Imposed with parameters relative to the findings, vortex conditions were represented by a constant vorticity range of 0.3 s^{-1} , together with three distinct length scales analogous to the rotor radius: $0 \cdot r_{rtr}$, $0.25 \cdot r_{rtr}$, and $0.5 \cdot r_{rtr}$, to acknowledge the effect of differing vortical structure scale upon the properties at the rotor blades.

4.1.2.2 Structural Analysis

In an effort to establish a one-way fluid-structure interaction (FSI) model, the hydrodynamic solver was coupled with the structural solver by implementing the outcomes attained from the prior model into the latter. In consideration of this technique, each of the rotor blades, disassociated from the duct, was individually modelled within the finite-element solver utilising the ducted turbine blade geometrical profiles employed within the fluid dynamic solver. A one-way FSI analysis was favoured due to three factors: (i) the internal blade structure was required to be altered, hence varying the response properties of the structure, (ii) the non-slender physicality of the high-solidity blades may exhibit high structural stiffness, and (iii) as the extremities of the blades are fixed at the duct, where the highest dynamics are induced, the structural response may not be significant. Due to the incorporation of a one-way approach, the loading data was therefore identical for each blade design upon implementation.

In consideration of the round-edged, flat-plate blade profile constituting the ducted rotor to acquire bi-directional turbine properties, an investigation into the most appropriate internal blade structure design was instated due to its substantial chord-to-thickness aspect ratio, hence potentially requiring unique structural configurations when compared to conventional slender blade designs. For this reason, in an effort to acquire an efficacious internal blade design in terms of specific mass, material cost, and structural response of the rotor blades, three design variations were investigated in replication of turbine blade designs elaborated in Krstulovic et al. [145]: (a) a solid blade consisting of a single material throughout its volume, (b) a cored blade consisting of a thick shell with a foam core, and (c) a reinforced blade consisting of a thick shell with webbing reinforcements, oriented perpendicular to the blade chord, in a void core, which is water-flooded upon installation, along the entire blade length, as illustrated in Figure 4.3. The implemented shell and reinforcement thicknesses of the two latter blade designs were instituted to be one-fourth of the blade profile thickness down the entire blade, as a proximate median value from rotor composite cross-section evaluations by Grogan et al. [146]. In addition, the distance between each spar reinforcement

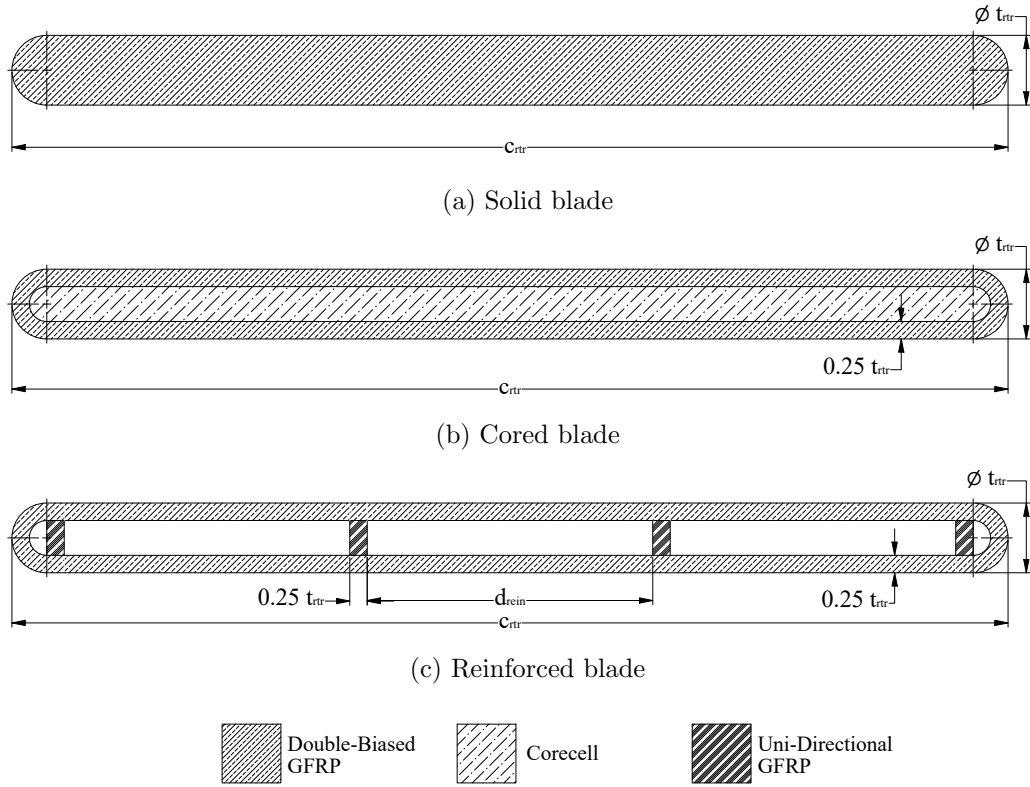


Figure 4.3: Geometrical model of the ducted high-solidity tidal turbine utilised for the CFD analyses

Table 4.3: Material properties adopted in the structural numerical model [146]

Material	E_1 (GPa)	E_2 (GPa)	G_{12} (GPa)	ν_{12}	Density (kg.m^{-3})	Design
DB GFRP	22.0	22.0	2.7	0.30	1850	a, b, c
Corecell	0.044	0.044	0.020	0.30	65	b
UD GFRP	38.8	10.0	2.7	0.28	1950	c

was acquired by means of:

$$d_{rein} = \frac{c_{tr} - 2t_{tr}}{3} \quad (4.1)$$

The materials considered for the structural analysis comprised of composite materials commonly utilised in the tidal turbine industry, specifically for three-bladed rotor applications [146]: (i) double-biased (DB) orthotropic glass-fibre reinforced polymers (GFRP), employed for the solid body (design (a)) and shell segments in the cored (de-

Table 4.4: Lay-up of the composite materials adopted in the structural numerical model [146]

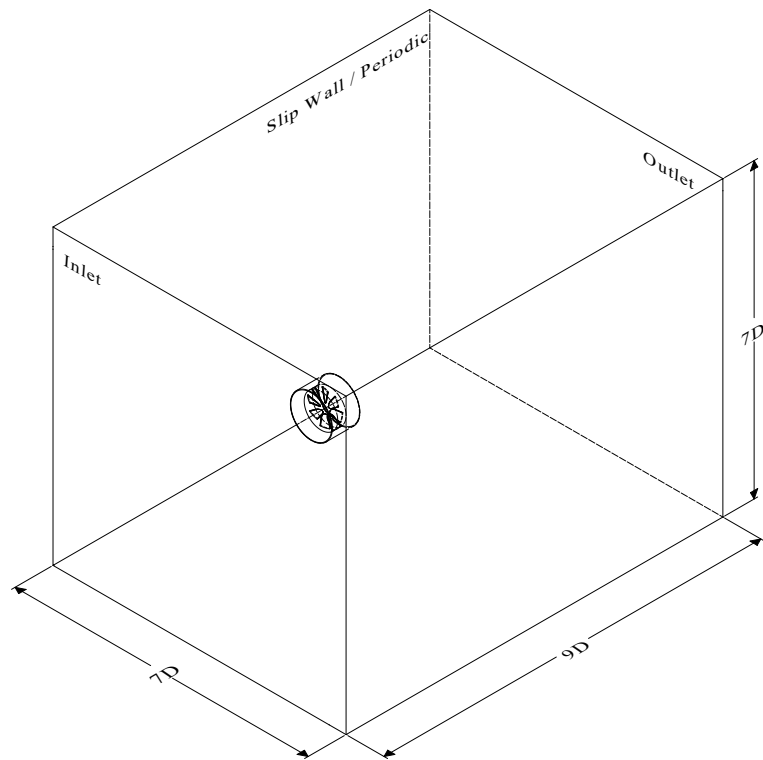
Material	Composite Lay-Up
DB GFRP	[45/-45/0/90/90/0/-45/45]
UD GFRP	[45/-45/0/-45/45]

sign (b)) & reinforced (design (c)) blade designs, (ii) uni-directional (UD) anisotropic glass-fibre reinforced polymers, employed for the spar reinforcement segments in the reinforced (design (c)) blade design, and (iii) corecell structural foam for the interior of the cored (design (b)) blade design; the properties of the listed materials are presented in Table 4.3, with the composite lay-up orientation presented in Table 4.4.

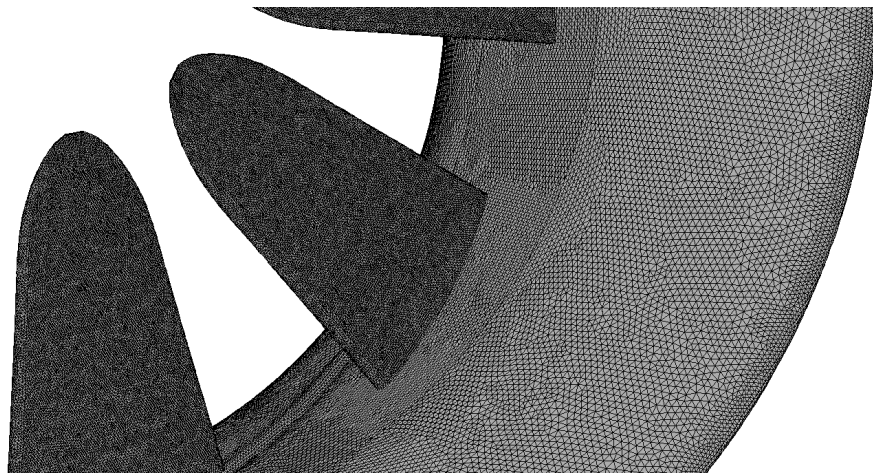
A select range of hydrodynamic conditions was considered for the analysis, specifically low, mean, and extreme currents (1 m.s^{-1} , 4 m.s^{-1} , and 7 m.s^{-1}) within aligned flow conditions, together with the bearing range (γ) of 0° , 15° , 23.2° , 30° within yawed flow conditions, both of which at low, nominal, and high rotational velocities (TSR 1.00, 1.75, and 2.50). At these conditions, a variety of criteria were acknowledged in assessing the elaborated rotor designs: the blade (i) global deformation, (ii) axial deformation, (iii) induced equivalent Von Mises strain, (iv) normal radial compressive and tensile strain, (v) the summation of the tangential and axial normal strains, (vi) shear strain at the blade root plane, (vii) rotor specific mass, and (viii) rotor moment-of-inertia to establish a definitive blade design selection for effective implementation for tidal turbine operation.

4.2 Numerical Setup of the Turbine Model

In establishing the hydrodynamic and structural numerical models required to carry out the one-way fluid-structure interaction analysis, a description of the mathematical environments and libraries utilised is presented.



(a) Layout of the ducted turbine domain



(b) Geometric tessellation of the mesh on the duct and rotor blades

Figure 4.4: Geometrical model of the ducted high-solidity tidal turbine utilised for the CFD analyses

4.2.1 Hydrodynamic Analysis

Inferred as fully submerged systems within a constant fluid flow, the numerical models were founded under the premise that no far-stream effects are in interaction with the turbines, hence unaffected by the implications of the free-surface and the seabed; this was purposely implemented to acknowledge the performance of the turbines under ideal, consistent temporal conditions.

4.2.1.1 Domain Setup

To establish the numerical environment within which the turbine was analysed, the developed physical models were designed to consist of a cuboidal external domain layout, imposed with relevant boundary conditions, with use of the commercial solver ANSYS Fluent 19.2. The computational fluid dynamic solver was utilised in computing Reynolds-averaged representations of the continuity and Navier-Stokes equations, which govern the three-dimensional, unsteady, incompressible fluid flow, together with a Reynolds-Averaged Navier-Stokes (RANS) turbulence model applied in mathematical closure to represent flow property fluctuation. For both the three-bladed and ducted turbine models, the domain encompassing the turbine rotor was segregated from the global domain in an effort to induce a moving-mesh scheme with rotation at the turbine rotor, relative to a stationary outer domain, with interfaces between the two domains; a tetrahedral mesh was imprinted along the entire domain volume. No-slip wall conditions were instated at the rotor, mast and nacelle, and duct structures, whereas slip conditions and coupled conditions were instated at the boundaries of the domain parallel to the axis of the turbine for aligned flow analysis and yawed flow analysis, respectively; velocity-inlet and pressure-outlet conditions were instated to the remainder perpendicular boundaries, as illustrated in Figure 4.4a. In addition, two pairs of numerical planar surfaces were introduced equidistant on either side of the rotor; one with a circular surface of diameter D_{rtr} , the other of an annular surface of inner and outer diameters D_{hub} and D_{rtr} , both situated within the CFD model at a distance $0.125D_{rtr}$ fore and aft of the rotor, as illustrated in Figure 4.5. The prior plane pair represent the cross-section of the duct throat, whereas the latter represent the rotor

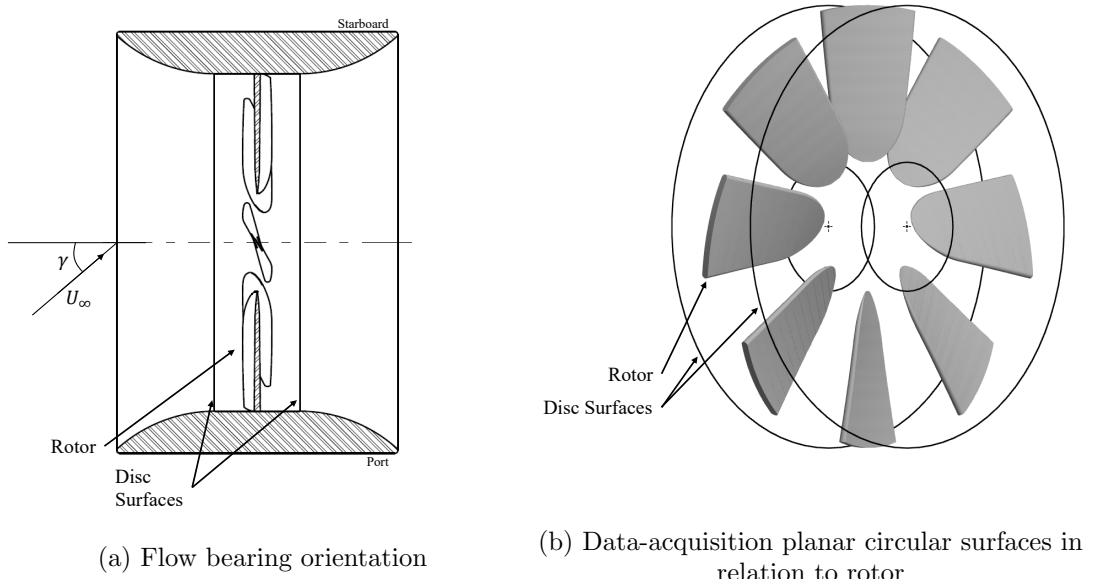


Figure 4.5: Notation of incoming flow bearing in relation to rotor axis & positions of planar circular surfaces

with an open-centre; this constitutes a disc representation, albeit quite thick. The surfaces were utilised as data acquisition hubs to attain area-averaged values of axial velocity and static pressure in an effort to establish a relationship between the flow properties with rotational velocity and flow bearing.

In a similar layout employed by Mason-Jones et al. [147], the dimensions of the computational domain were contrived to attain a numerical blockage ratio (α_{bl}) of less than 2% to the turbine to ascertain the absence of far-field effects, replicating quasi-real-ocean conditions. This corresponded to a cross-sectional domain dimension of $7D_{sys}$ along the edges of the quadratic face, with the rotor cylindrical domain positioned at the centre of the plane. In consideration of wake analysis, a domain length of $9D_{sys}$ was instituted, where the inlet and outlet planes were situated at a distance $3D_{sys}$ upstream and $6D_{sys}$ downstream of the turbine, respectively.

4.2.1.2 Time-Step Convergence

The time-step considered was assigned in relation to the tip-speed ratio of the rotor, where each transient iteration is temporally equivalent to one-half of a degree of

a turbine revolution, therefore attained by:

$$\Delta t_{step} = \frac{1}{2} \times \frac{2\pi}{360 \times \Omega_{sys}} \quad (4.2)$$

where Δt_{step} is the time-step and Ω_{sys} is the rotational velocity of the system. Having undertaken a time-step independence analysis, this was found to suffice both in sustaining stability in the model, and in achieving a sufficient Courant number at regions of interest throughout the domain.

4.2.1.3 Mesh Convergence

A mesh independence procedure was primarily carried out on the three-bladed HATT by considering the parameter with the highest degree of dynamics; the highest TSR condition. Subsequent to the procedure, the final average surface mesh count utilised was marginally above 87,000 cell faces per blade, with dense volumetric cells around the turbine and within the wake, to achieve a total mesh count of 13.5 million for the three-bladed HATT, over 8 million of which within the turbine rotating region. The mesh independence analysis is elaborated in Appendix B.1 Table B.1. An identical procedure was undertaken for the ducted turbine, attaining an average surface mesh of slightly above 94,000 cell faces per blade, illustrated in Figure 4.4b, with more than 18.5 million volumetric cells within the entire domain, over 10 million of which within the turbine rotating region. The mesh was implemented with an appropriate prism layer size to achieve a y^+ value of $60 \leq y^+ \leq 500$ across the blades and duct. This range was considered due to the high Reynolds number ($> 10^6$) of the system, hence modelling the viscous sublayer was abdicated to reduce computation time. The mesh independence analysis is elaborated in Appendix B.1 Table B.2.

4.2.1.4 Turbulence Modelling

In implementing a turbulence model for mathematical closure of the Navier-Stokes momentum conservation equation, an imperative characteristic behind the investigations tackled throughout this work was the selection of a model that supported

anisotropic stress analysis. Due to the significant scale/size of the rotor, the induced turbulence effects in result of the presence of the shroud-rotor interaction were perceived to be substantial, hence requiring a high-order turbulence model to fully capture the phenomena. Furthermore, the technique implemented would additionally be required to be computationally sustainable due to the finite time-frame within which the analyses may be undertaken. For these reasons, Reynolds-Averaged Navier Stokes (RANS) turbulence models were opted for, due to their comparatively lower computational expense, yet, to solve for the Reynolds stresses within a three-dimensional fluid flow, solely a selective number of models, the Reynolds-Stress Model (RSM) turbulence models, were deemed appropriate.

Ensuing the classification of RANS turbulence models, subsidiary approaches include the turbulence dissipation rate (ε) and specific dissipation rate (ω) variations. The latter implementation was opted for two distinctive reasons: i) as a variable, the specific dissipation rate (ω) is superior to the turbulence dissipation rate (ε) in establishing the turbulent length scale as a result of its capacity in modelling all degrees of production, redistribution, and dissipation of turbulent kinetic energy within the flow [137], and ii) mathematically, ω does not require the implementation of near-wall treatment equations to model the boundary layer at non-slip surfaces, as the function is able to be integrated to the wall, sustaining higher accuracy within the log-linear range of the law-of-the-wall y^+ spectrum.

In accordance, as a result of incorporating the specific dissipation rate variation of the Reynolds-Stress Model into the CFD model, all Reynolds stresses in three-dimensional space are analysed due to its non-implementation of the Boussinesq approximation/assumption, prompting superiority in analysing anisotropic flows, such as flows over curved surfaces, flows in rotating fluids, and flows in ducts with secondary (rotational) motion [137]. In addition, as the effects of streamline curvature, swirl, rotation, and rapid changes in strain rate are considered in a more effective manner than one-equation or two-equation models, the RSM model, hence, has greater potential in attaining accurate predictions when resolving the complex flow field identified in ducted turbine analyses. Correspondingly, mathematical closure was attained by means of the

Reynolds-Stress ‘Stress-Omega’ ($\tau - \omega$) Model turbulence model.

In continuation, as elaborated in Section 3.4, two variations of the $\tau - \omega$ model have been developed, the Standard (STD) and Baseline (BSL) $\tau - \omega$ RSM models, explicating their mathematical difference, where the BSL model effectively blends the robust and accurate formulation of the ω -model in the near-wall region, with the free-stream independence characteristics of the ε -model in the far-field, hence converting the ω model into an ε formulation along the boundary-layer height, encompassing features of the BSL $k - \omega$ turbulence model. The latter, theoretically more accurate, model was inopportunely unavailable within the commercial software when the main tasks described by this written work were initiated; the Standard $\tau - \omega$ was therefore utilised when tackling the primary three aims of the investigations in analysing the three-bladed HATT to attain validation, together with the performance of the ducted turbine in aligned and yawed flow conditions. Yet, albeit the advantages of the Standard $\tau - \omega$ turbulence model, specifically in wall-bounded flows, a significant drawback it presents is the potential oversensitivity in shear flow at high Reynolds numbers, similarly to the Standard $k - \omega$ turbulence model, hence potentially portraying unphysically higher performance outcomes, under exaggerated physics, within the fluid-structure interaction phenomena. Therefore, for the reason of attaining appropriate flow phenomena scaling along the duct and within the wake, once the BSL $\tau - \omega$ was available for implementation, it was utilised under identical circumstances of the aligned flow task to analyse the flow physics of the tidal turbine bereft of the adverse aspects analogous to the prior turbulence model.

Nonetheless, albeit the superior applicability of RSM turbulence modelling, the fidelity of accurately predicting the true Reynolds stress distribution within a finite volume is ultimately limited by the numerical assumptions employed to model the various terms within the Reynolds-Stress transport equations. The modelling of the pressure-strain and dissipation-rate terms is particularly complex, and may be responsible for compromising the accuracy of the RSM predictions [137]. In addition, RSM models rely on scale equations when considering the dissipation rate schemes, and hence inherit deficiencies from the underlying assumptions innate to the equations. In consequence,

RSM modelling might not yield results that are clearly superior to the less complex models in all classes of flows to justify the additional computational expense. On that premise, an overt comparison of the physical representation between two high-order (7-equation) and a two-equation turbulence model was undertaken to pinpoint the performance output distinction between the Menter assumption (BSL $\tau - \omega$), the Wilcox assumption (Standard $\tau - \omega$), and the Boussinesq-Menter assumption (SST $k - \omega$), when analysing a ducted tidal turbine.

In accompaniment to the ω models, the mathematical libraries utilised include the SIMPLE pressure-velocity coupling scheme setting, the Green-Gauss Node Based gradient, Pressure Staggering Option (PRESTO!) pressure, Second Order Upwind momentum, Second Order Upwind specific dissipation rate, Second Order Upwind turbulent kinetic energy, and Second Order Upwind Reynolds stresses spatial discretisation settings, and the Bounded Second Order Implicit transient formulation setting were utilised as the solution methodologies. The implementation of the specific schemes were imperative for reason of second-order accuracy, in addition to the gradient scheme discretising flow separation more accurately, and the pressure scheme integrating the pressure distribution along rotating surfaces more appropriately. It should be stated that the dissipation rate was altered to Second Order from First Order settings once the resultant parameter outputs were periodic in time, as initially running with the more accurate setting would result in the simulation to fail within the first few time-steps. Furthermore, the pressure setting was altered from Second Order to PRESTO! once the resultant parameter outputs were periodic in time as the prior setting greatly underestimates the parameters if retained. In addition, for the successful use of the Stress- ω turbulence model with these settings, a quality mesh is required. Through empirical methods, it was acknowledged that a mesh with skewness higher than 0.79 resulted in the divergence of the continuity residual, highlighting the limited robustness of the turbulence model; other mesh qualimetrics had no such an effect.

The CFD computations were performed using the ARCHIE-WeSt cluster facility at the University of Strathclyde by running two Intel Xeon Gold 6138 2.00 GHz computational nodes, with 40 cores and up to 192 GB of RAM per node per simulation.

The ducted turbine simulations were completed within roughly 75 wall-clock hours, equivalent to 3,000 core-hours, hence resulting in an average of 5 wall-clock hours per turbine rotation.

4.2.1.5 Concentrated Vortex Generation

A concentrated vortex is described as a region of fluid circulating within a closed path about an axis [148]. At a subsea site, within a turbulent, hydrodynamic domain in result of flow interaction with bathymetric variations, the generation of explicit, sole tubular flow structures is largely improbable as turbulence forms through an array of distorted vortices intervalled by sheets of minor flow structures [144]. In an effort to analyse vortex interaction with the ducted, high-solidity tidal turbine, a premise was put forward, where the induced flow phenomena was assumed to be temporally steady when approaching the rotor, hence replicating a consistent stream of vortices.

To attain the steady vortex-representation phenomenon within the computational grid, concentrated vortices were required to be generated within the domain, upstream of the structure, to be propelled by the free-stream towards the rotor plane, resulting in an elongated flow region with a velocity variance. A sub-domain of cylindrical form, replicating the form of a concentrated vortex, was hence physically created, as illustrated in Appendix B.2.1 Figures B.1 and B.2, to house a cell-zone of numerically-induced rotating flow, whose flow properties may be adapted to undergo parametric analysis.

Primarily, the segregated cell zone was numerically induced with rotation by means of the multiple reference frame (MRF) technique. This implementation, however, solely induces rotation at the boundaries of the cell zone, at the interface with the global domain, rather than throughout its entirety. For this reason, a user-defined function (UDF) was utilised to induce the cell zone with rotational velocity at each of the cell centroids by means of a parallelised “Define_Profile” function. By implementing the UDF, each cell within each cell-thread is called, acquiring the location coordinates of the cell centroids within a loop function. The linear distance of each cell centroid from the known cell-zone centre coordinates was then calculated by utilising vectorial

arithmetic. The acknowledgement of this linear distance (d_{cntrd}) was imperative as the tangential velocity function describing a forced vortex, $V_{tng-vrtx} = d_{cntrd} \cdot \Omega_{vrtx}$, utilises the variable to calculate the tangential velocity ($V_{tng-vrtx}$) at each cell centroid within the cell zone, where the tangential velocity varies linearly with radial distance, as illustrated in Appendix B.2.1 Figure B.3. The velocity was then adopted (hooked) as a fixed tangential velocity value in the cylindrical coordinate system library within the CFD solver, with the axial and radial cylindrical velocities set to null. As a result of the physical rotation and the induction of rotational velocity generation within the cell zone, a constant, steady-state vortex generation is induced within the simulation. Albeit the cell-zone is spatially static, the free-stream acts in a direction parallel to the rotor axis and perpendicular to the vortex zone axis, and therefore, the generated vortex is transported from the cell-zone towards the turbine structure as a constant barrage of vortices. The UDF code is detailed in Appendix B.2.2.

4.2.2 Structural Analysis

In analysing the structural response of the turbine rotor as a result of the hydrodynamic interaction, finite element method (FEM) models were created and resolved by means of the commercial solver ANSYS Mechanical APDL 19.2. The FEM solver was employed to implicitly compute the quasi-static structural mechanics of the blades within the linear-elastic Hooke's law relationship of the orthotropic and anisotropic fibre-composite materials.

4.2.2.1 Finite Element Mesh

Designed to explicitly incorporate all eight distinct rotor blades for the three internal blade designs, the physical models representing the solid and cored blade designs were imprinted with a hybrid hexahedral-tetrahedral mesh, and a hexahedral mesh for the reinforced blade design, all consisting of solid quadratic elements, illustrated in Figure 4.6, imposed with relevant boundary conditions. The implementation of solid elements was preferred to shell elements in representing the shell-segment of the blade as shell elements fall under the mathematical assumption that the structural outcomes

are largely consistent throughout the thickness of a structure, which was deemed to be untenable for the full-scale, high-solidity rotor due to the complex geometrical layout of the blade, together with the variable hydrodynamic pressure distribution upon its surface.

In addition to a solid element format, quadratic elements were utilised, hence introducing mid-nodes within each cell, in discretising the thickness of the shell & reinforcement structures, to increase the accuracy of the simulation. Further to this, a two-cell-thick layout was imposed along the thickness of the shell & reinforcement sections, as illustrated in Figures 4.6c & 4.6d, to attain a quadratic relationship between the structural outcomes and the thickness of the blade feature; hexahedral volumetric cells were imposed along the exposed surfaces for all blade designs.

To create the mesh upon the distinct structures, the solid and cored blades were instated as whole components for the mesh to be distributed along; the same mesh was utilised, yet allocating differing material properties, for both cases. The reinforced blade, however, was more complex to set up; to permit an equivalent distribution of hexahedral cells, the structure had to be discretised into blade sections, as illustrated in Figure 4.6b. Yet, due to the discretisation, the three-dimensional non-uniform rational basis spline (NURBS) sectioned structure was too complex to tessellate in a consistent manner. In consequence, the sections were meshed separately, and numerically linked by means of a face-to-face bonded contact merge when simulating. Overall, the solid/cored rotor mesh was comprised of a total of 635,672 elements and 2,680,248 nodes, whereas the reinforced rotor comprised of 571,392 elements and 3,362,160 nodes. A mesh independence procedure, elaborated in Appendix B.1 Table B.3, was carried out on all three internal structures by considering the parameter with the highest degree of dynamics; extreme free-stream at highest TSR condition.

4.2.2.2 One-Way Fluid-Structure Analysis

In an effort to constitute the one-way fluid-structure interaction framework, the boundary conditions inducing a loading distribution along the blade surfaces were instated from the distributions of pressure attained within, and imported directly from,

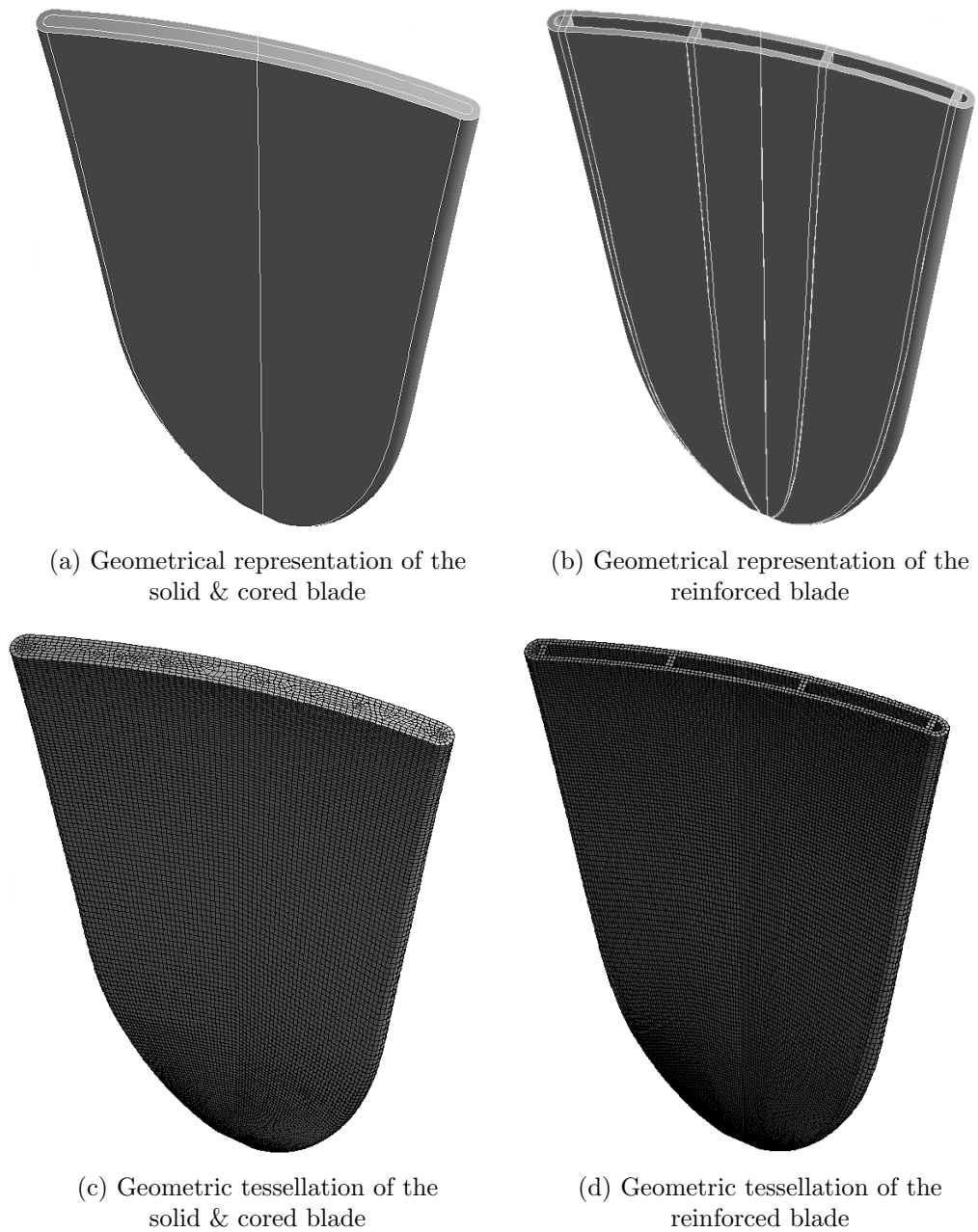


Figure 4.6: Implementation of the one-way fluid-structure interaction technique; importing pressure distribution along the blade surface

the CFD solver at distinct temporal points along the turbine rotation. Therefore, as each blade was modelled independent from the entire system, upon which unique loading conditions were imposed, the setup hence permitted an isolated blade-resolved fluid-structure interaction analysis, unique for the tidal turbine, within a wide range of

environmental conditions for the previously described blade designs.

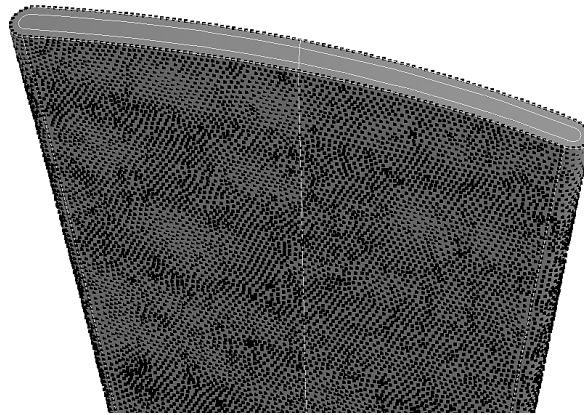
The blade surfaces utilised in the FEM analysis were a direct replication of those implemented within the CFD analysis, geometrically representing the fabricated blades protruding from the duct housing, as identified in Figure 2.7a. The importation of pressure from the hydrodynamic solver to the structural solver consisted of exporting data points comprising the Cartesian location and value of the parameters required. As the total force induced by a fluid flow is the summation of static pressure and shear stress upon a surface, as described in Equation 2.4, the two parameters were extracted from the CFD solver, the prior as a magnitude and the latter as a cartesian vector (x-,y-, and z-wall shear); on average, $\approx 55,000$ data points were transferred, with their implementation illustrated in Figure 4.7. The parameter distribution at the rotor surface was imported once every 45° along the rotation, for three periods, to attain a definitive representation of the dynamic load induced upon operation.

In addition to the hydrodynamic induction, hydrostatic pressure was introduced within the solution by estimating the rotor axis to be situated 20 m below sea-level due to the ducted tidal turbine design conditions of being installed at 35 m depth [44]. Furthermore, fixed boundary conditions were allocated to the root surface of the blade, together with Coriolis effect considered at constant rotational velocity, to acquire representative environmental conditions of the ducted, high-solidity rotor in operation.

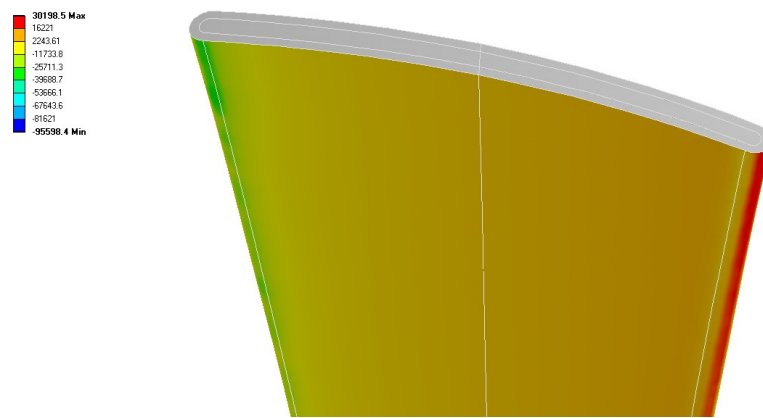
The finite-element computations were performed using the ARCHIE-WeSt cluster facility at the University of Strathclyde by running two Intel Xeon Gold 6138 2.00 GHz computational nodes, with 8 cores and up to 192 GB of RAM per node per simulation. One ducted rotor structural simulation was completed within roughly 20 wall-clock hours, equivalent to 160 core-hours.

4.3 Chapter Summary

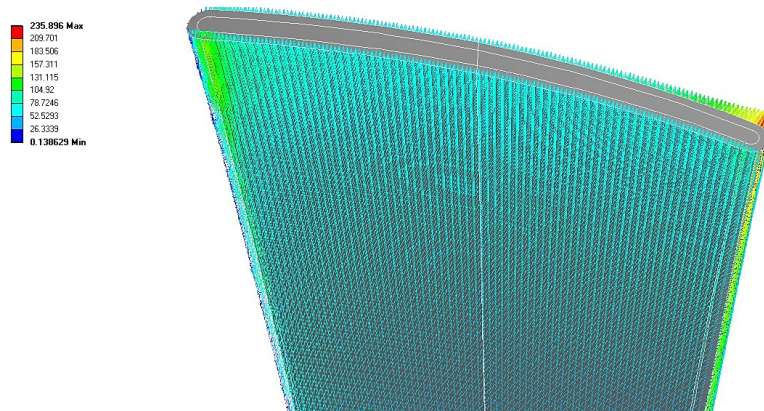
This chapter provided an elaboration on the procedures with which the one-way fluid-structure interaction analysis was performed. Primarily describing the geometrical models, hydrodynamic parameters, and structural properties utilised within the



(a) Distribution of input source points along the blade surface



(b) Static pressure input boundary condition



(c) Wall shear stress input boundary condition

Figure 4.7: Implementation of the one-way fluid-structure interaction technique; importing pressure distribution along the blade surface

turbine setup, a characterisation of the numerical setup framework, in reference to the computational fluid dynamic and finite element solvers, was presented.

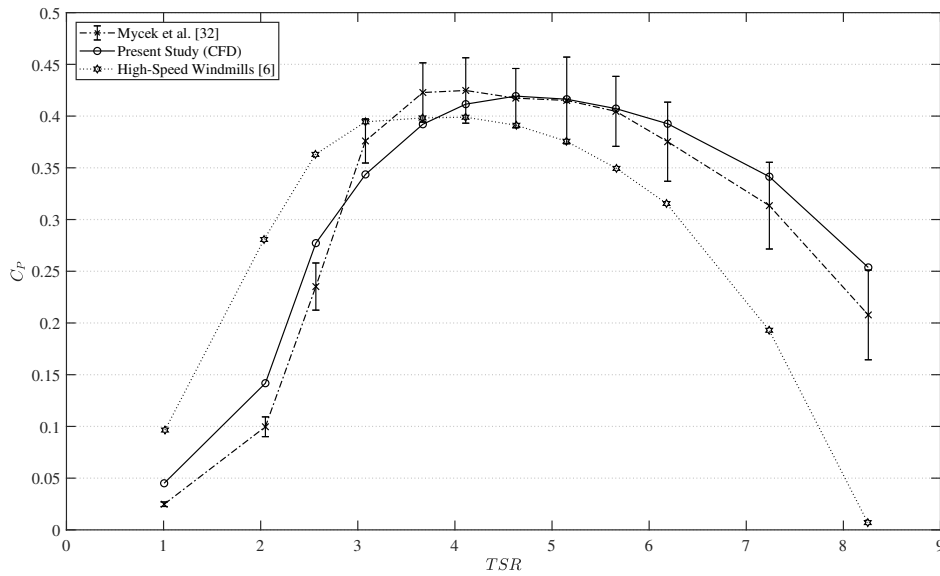
Chapter 5

Numerical Validation of a Three-Bladed Horizontal-Axis Tidal Turbine

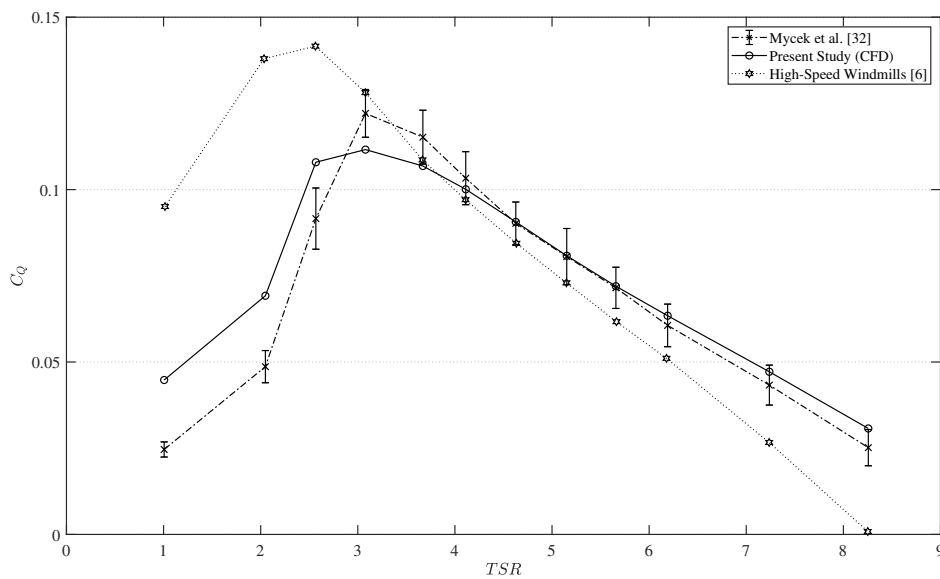
This chapter provides the validation requirement in ascertaining the computational fluid dynamic model for single-phase turbulent domain rotating-blade applications. Numerically replicating experimentation by Mycek et al. [140], utilising the STD τ - ω , the numerical results are attained within a TSR range of 1.00 - 8.26, in open-water conditions, in relation to the power coefficient, torque coefficient, thrust coefficient, and wake velocity profiles from near- to far-wake of a three-bladed HATT, equated utilising the coefficient of determination (R^2) statistical methodology.

5.1 Power Coefficient

Primarily, the power coefficient (C_P) curve established by numerical means, illustrated in Figure 5.1a, attained an R^2 of 0.955 as a degree of similarity with experimentation pertaining to the data points within the entire curve, and a 0.965 degree of similarity within the nominal TSR range (TSR 3.08 - 5.66). As the limits of the error bars in the graphs represent one standard deviation (σ), all CFD data points analysed



(a) Power coefficient (C_P) in relation to TSR



(b) Torque coefficient (C_Q) in relation to TSR

Figure 5.1: Comparative evaluation of the current horizontal-axis tidal turbine CFD model with experimentation [140], and high-speed windmills [143]

fell within $2\sigma_{C_P}$ of the experimentation points, hence within the 95th-percentile confidence range, except for low TSR values of 1.01 and 2.05. Furthermore, the torque coefficient (C_Q) curve established by numerical means, illustrated in Figure 5.1b, at-

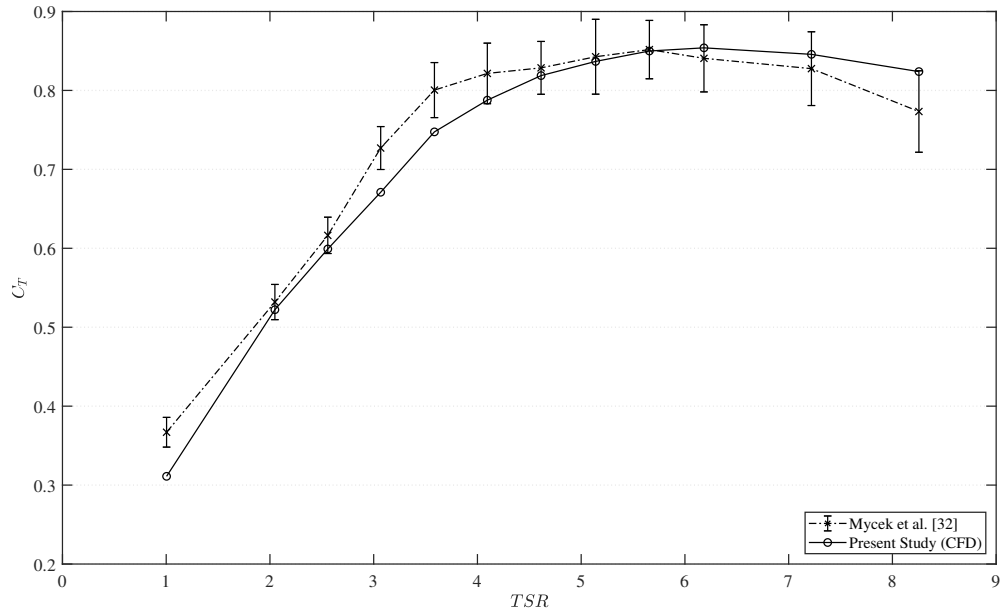


Figure 5.2: Comparative evaluation of the current horizontal-axis tidal turbine CFD model with experimentation [140] for thrust coefficient (C_T) in relation to TSR

tained an R^2 of 0.889 as a degree of similarity with experimentation pertaining to the data points within the entire curve, and a 0.965 degree of similarity within the nominal TSR range (TSR 3.08 - 5.66). All CFD data points analysed fell within $2\sigma_{C_Q}$ of the experimentation points, hence within the 95th-percentile confidence range, except for low TSR values of 1.01 and 2.05. Specifying the affiliated physics between the validation systems and large-scale systems, the numerical and experimentation data sets were compared to high-speed windmills presented in the Betz [143] technical memorandum, indicating good comparison specifically within the trends of the performance curves.

5.2 Thrust Coefficient

In continuation, the thrust coefficient (C_T) curve established by numerical means, in consideration of the rotor, nacelle, and mast, illustrated in Figure 5.2, attained an R^2 of 0.946 as a degree of similarity with experimentation pertaining to the data points within the entire curve, and a 0.841 degree of similarity within the nominal TSR range (TSR 3.08 - 5.66). All CFD data points analysed fell within $2\sigma_{C_T}$ of

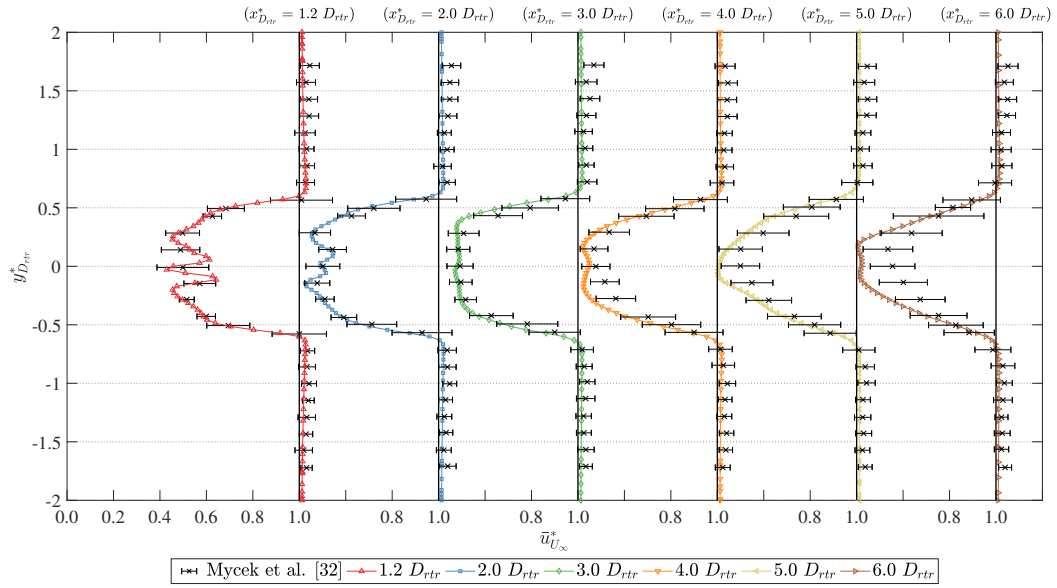


Figure 5.3: Comparative evaluation of the current horizontal-axis tidal turbine CFD model with experimentation [140] for the wake velocity profiles at distinct downstream displacements ($x_{D_{tr}}^*$) in relation to TSR

the experimentation points, hence within the 95th-percentile confidence range, except for the low TSR value of 1.01. The comparatively substantial discrepancy between the numerical and experimentation thrust coefficient may have come about due to the inaccuracy of the mast geometry implemented within the model. No data regarding the position and dimensions of the mast were noted in the literature, and hence, creating the complete geometry was executed with calculated estimations; in addition, fairings were utilised during the experimentation, whereas a bare mast was created in the numerical model, hence skewing the resultant data comparison.

5.3 Wake Velocity Profiles

In addition, the wake velocity profiles established by numerical means, illustrated in Figure 5.3, attained an R^2 of 0.999 and 0.852, as a degree of similarity with experimentation pertaining to the data points within the entire curve, at near-wake and far-wake respectively. All the CFD data points analysed fell within $2\sigma_{C_T}$ of the experimentation points, hence within the 95th-percentile confidence range. The comparatively

substantial discrepancy between the numerical and experimentation at the far-wake may be a result of the underestimation of the dissipation rate within the fluid, due to the implementation of the turbulence model, hence overestimating the resultant kinetic energy within the wake. It should be mentioned that the turbulence intensity of the flow was established within the experimentation as it has a substantial effect upon the velocity distribution. Yet, due to a study by Ahmed et al. [149], which acknowledged the inaptness of RANS turbulence modelling in resolving wake turbulence, its analysis in this work was abdicated.

As a result of the high degree of similarity between the four dynamic properties, it was ascertained that both the modelling characteristics, by means of the geometrical replication and mathematical interpretation, and the turbulence model implemented, were of applicable physical representation of a rotating bladed system.

5.4 Chapter Summary

This chapter provided a development of a numerical simulation in an attempt to achieve a validated hydrodynamic model, in relation to the numerical schemes and libraries implemented, for the physics induced by rotating blades. By replicating experimentation acquired through literature, undertaken upon a three-bladed tidal turbine, the critical outcomes defining the power, torque, and thrust coefficients, along with the velocity profiles of the wake, established by means of the numerical model was found to attain a high degree of similarity with the experimental values.

Chapter 6

Hydrodynamic Performance of a Ducted High-Solidity Tidal Turbine in Aligned Flow Conditions

In relation to studies that have endeavoured in modelling ducted tidal turbines [88, 105, 106], this present study produces a more coherent representation of the configuration, both due to the accurate geometrical representation, and in the numerical modelling of general conservation and turbulence, utilising the STD $\tau - \omega$, hence better analysing the hydrodynamic occurrence of the fluid-structure interaction.

6.1 Power Coefficient

Once the validated modelling techniques were implemented for the ducted turbine model, unique physical performance outcomes were displayed in representation of its high-solidity characteristics. Notably, the power coefficient TSR curve was relatively short spanning, with a TSR range of 1.00 - 2.50 to achieve a C_P decrease of 0.05 from the nominal TSR. Within this region, a maximum power coefficient range between 0.331

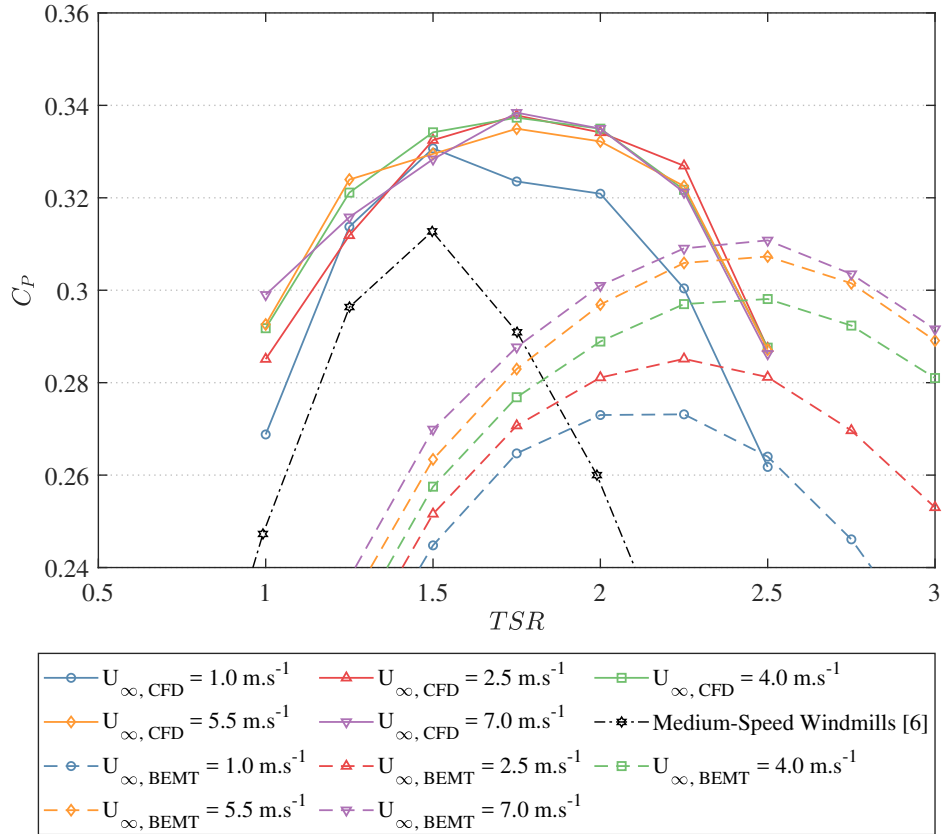


Figure 6.1: Evaluation of the mean ducted turbine power coefficient (C_P) in relation to TSR

and 0.338, at free-stream velocities of 1 m/s and 7 m/s respectively, was achieved, as illustrated in Figure 6.1. Throughout the free-stream velocity variation, the power coefficient decrease was largely consistent post-nominal TSR. The nominal TSR point, however, differs at distinctive velocities. At low free-stream velocities ($U_\infty = 1$ m/s), the nominal TSR lies at 1.50, whereas at higher velocities ($U_\infty = 2.5 - 7$ m/s), the nominal TSR was found to shift to 1.75. This variation in nominal TSR was found to be in consequence of the angle-of-attack (α_{AoA}) attained by the differing hydrofoils composing the blade.

As part of the work detailed in the thesis, Allsop [3] investigated the effect of the variation of chord-based Reynolds number on the hydrodynamic performance coefficients of the flat-plate hydrofoil sections comprising the high-solidity blade utilising CFD. By considering a Reynolds number range of $1 \cdot 10^6$ to $1 \cdot 10^7$, a transition in

the hydrofoil stall angle was depicted, increasing from an angle of 11° to that of 14° , respectively. As the distinct flat-plate hydrofoil sections constitute the full blade, the effect of this stall angle transition was depicted in the power coefficient curve. At low TSR, the angle-of-attack at distinct elements within the blade was considerably high, inducing flow separation due to boundary layer detachment along the downstream surface, resulting in a region of the blade to experience stall. With an increase in TSR, the angle-of-attack decreased to the stall threshold, where the highest lift coefficient value was attained. Within this flow range, the boundary layer sustained attachment to, and flows along, the section surface, resulting in the region to come out of stall. At this flow condition, optimal hydrodynamic parameters are induced, which characterises the criteria for peak power, occurring at optimal TSR. When this threshold was surpassed, a reduction in power was instigated in correlation to a steep linear decline in the lift parameter response of the flat-plate hydrofoil. The stall threshold was proportional to the chord-based Reynolds number, and hence, due to the shift in angle-of-attack, the optimal TSR correspondingly shifts to a higher TSR value at higher Reynolds numbers. Simulating more domain flow parameters would enable the identification of the definite TSR at which the blade is within the peak lift region, hence the point at which the degree of blade area within the stall region reaches tipping point. The physical value of this output, however, may be limited due to the sensitive nature of the rotating blade boundary layer, together with external influences from the turbulent and multi-directional nature of the tidal environment.

In accordance to the hydrodynamic performance characteristics, albeit a maximum power coefficient of 0.338 was attained, it may also be acknowledged that, due to the device area (A_{dvc}) being considered, hence rotor & duct, the power coefficient will increase once the power per rotor area (A_{rtr}), rather than system area, was acknowledged. In this respect, the rotor radius was 80% that of the system, hence increasing the maximum power coefficient by a magnitude of 1.5625 to a nominal peak value of 0.528. Due to the fact, however, that the power attained by the rotor was also disseminated from the fluid in contact with the duct, the entire system area was a more conservative approach to represent.

In comparison to BEMT modelling elaborated in Ref. [3], an areal discrepancy was acknowledged over the TSR range, and achieved moderately comparable figures at nominal TSR, with a discrepancy in evaluation of the maximum C_P , which ranged from 0.273 to 0.311, at the free-stream velocities considered. This discrepancy may be elucidated by the dissimilarities in the hydrodynamic modelling of the two numerical techniques. Notably, the BEMT method considers the turbine blade as an array of discrete hydrofoil sections, considerably reducing the computational expense, where the hydrodynamic parameters of the blades are attained by means of two-dimensional CFD analyses. This approach, however, neglects any span-wise flow interactions along the blade length, together with omitting complex flow separation at the open-centre blade tips, which are considered to be significant fluid dynamic features. The latter phenomenon is accounted for in BEMT by implementing the Prandtl tip loss factor, yet is better captured when utilising blade-resolved CFD. Albeit the drawbacks of the BEMT methodology, significantly accurate outputs were attained in consideration of the inputs provided within the numerical model contrived and the computational duration required.

Whilst presenting windmill findings in the technical memorandum, Betz [143] described a “medium-speed windmill” that attains maximum efficiency at a low TSR value within a short-spanning TSR curve. Potentially resembling the OpenHydro PS2 tidal turbine, a comparison was made between the reported findings and the CFD results, also illustrated in Figure 6.1. With a peak windmill power coefficient of 0.313 at a nominal TSR of 1.50, good agreement was acknowledged in the parameter trend when compared to the ducted high-solidity turbine system.

In continuation, to comprehend the physical representation of the power generated by the turbine, Figure 6.2 illustrates the variation in the power output with the velocity of the free-stream. In comparison to the theoretical representation of a power curve, the peak power coefficients at nominal TSR ($TSR = 1.75$) at varying velocities matched well with a mean power coefficient of 0.34. Further to the power curve, the variation in the torque coefficient (C_Q) induced on the turbine was illustrated in Figure 6.3. Similar areal discrepancies were attained in comparison to BEMT and the Betz curve,

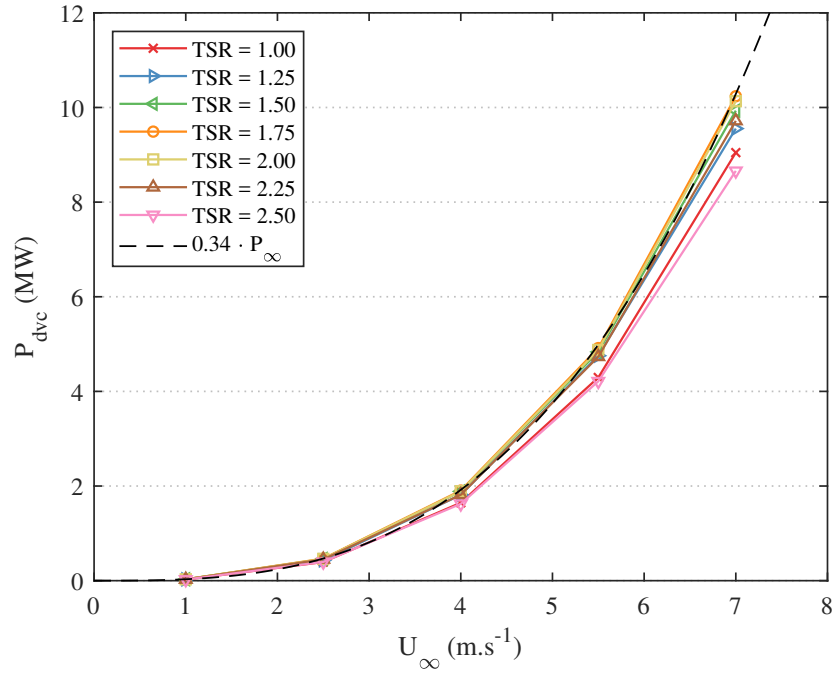


Figure 6.2: Evaluation of the ducted turbine mechanical power (P_{dvc}) in relation to free-stream velocity (U_∞) at distinct TSRs

yet, albeit the differences, the key similarity between the comparisons was the trend at which the torque varies.

In consideration of the correspondence between the power & torque coefficient performance curves displayed within the CFD results, BEMT outputs, and windmill (experimentation) findings, the applicability of full-scale analysis by means of the methodology implemented was acknowledged. The total discrepancy, however, both in comparison to windmill findings and BEMT outputs, may be a result of the over-sensitivity of the implemented turbulence model physics. This, ultimately, may overestimate the pressure distribution on the wall-bounded conditions, and hence, mechanical power transition due to the shear flow induced at the surfaces of the blades; further analyses utilising differing turbulence models may be required to ascertain this outcome. In definition of the parametric outcomes, the imperative of executing both CFD and BEMT methodologies when analysing turbine performance was exemplified. A denomination of the induced physical effects were more appropriately identified by means of a simplified model, and may be of assistance in understanding the fluid dynamic outcomes

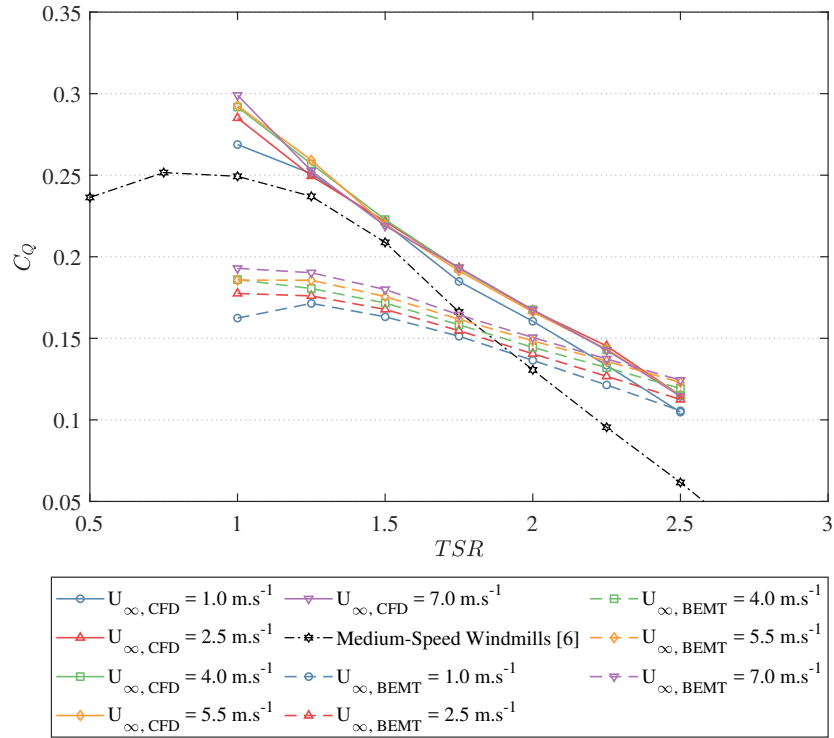


Figure 6.3: Evaluation of the ducted turbine torque coefficient (C_Q) in relation to TSR

of higher complexity analyses, such as that described within this work, due to the model capacity in capturing multiple coupled effects, such as lateral flow interactions down the blade length and temporal fluctuations in the rotor performance, as depicted in Figure 6.4, where the individual physical phenomena inducing the hydrodynamic behaviour are less obvious.

6.2 Thrust Coefficient

The implementation of a duct along the perimeter of a turbine subsequently increases the area onto which an external force may be induced, potentially bringing about an intensification in physical blunt-body conditions. In effect, the combined drag induced upon the system becomes of particular interest. Illustrated in Figure 6.5, the variation in thrust coefficient (C_T) with TSR and free-stream velocity is presented both in terms of the entire system, and in terms of the physical components: rotor

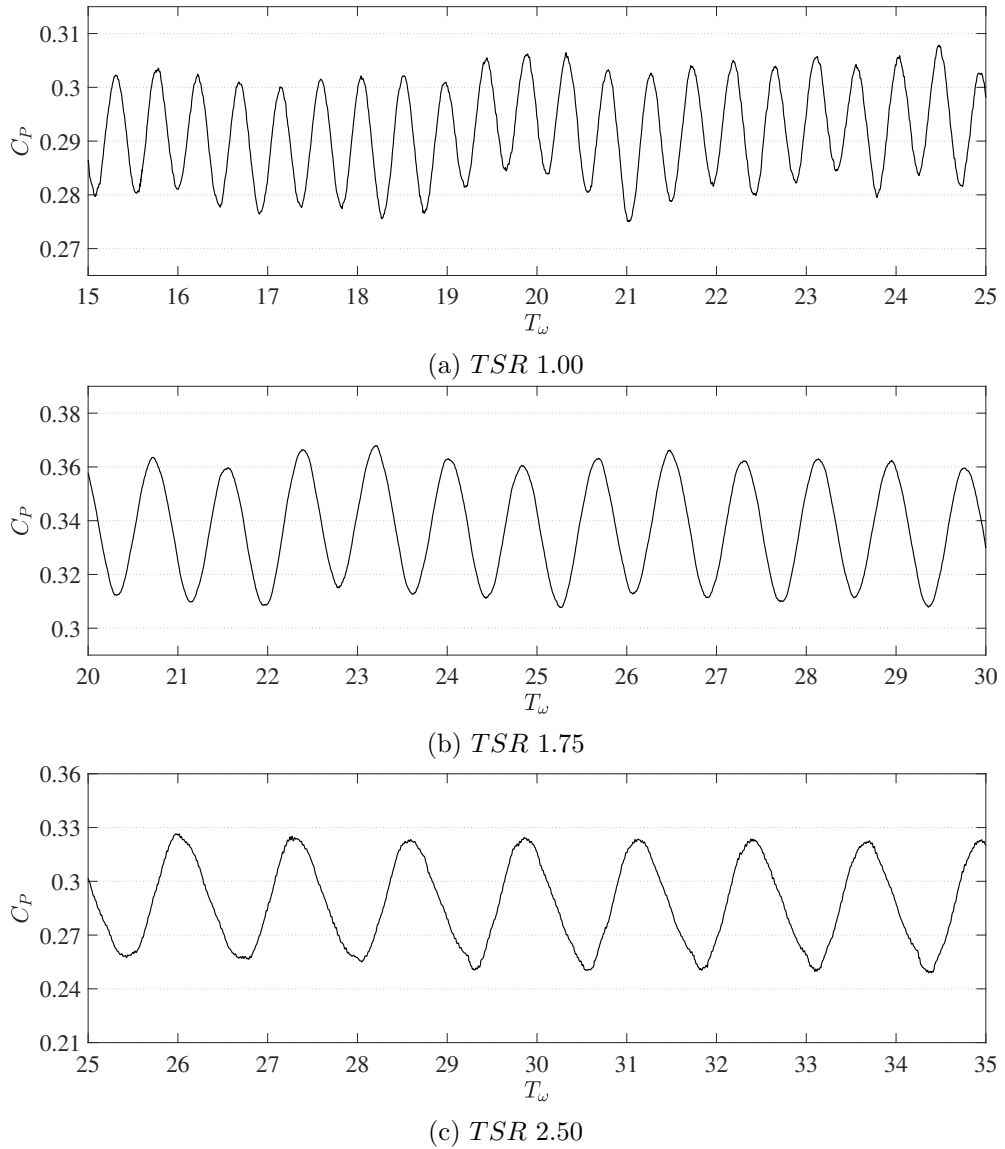


Figure 6.4: Representation of the transient power coefficient output at $U_\infty = 4.0\ m/s$ through turbine rotatory periods (T_ω)

and duct. As an entire system, a substantially high thrust coefficient was attained at low TSR, a mean value of 1.08, which decreased to a mean of 0.77 at high TSR in a polynomial manner; the mean thrust coefficient at nominal TSR is 0.97. Observed from the component curves, this considerable discrepancy in drag was largely consistent upon both the duct and the rotor, with a mean allocation of the global drag of approximately 33% and 67%, respectively. The rotor hence was succumb to two-thirds of the

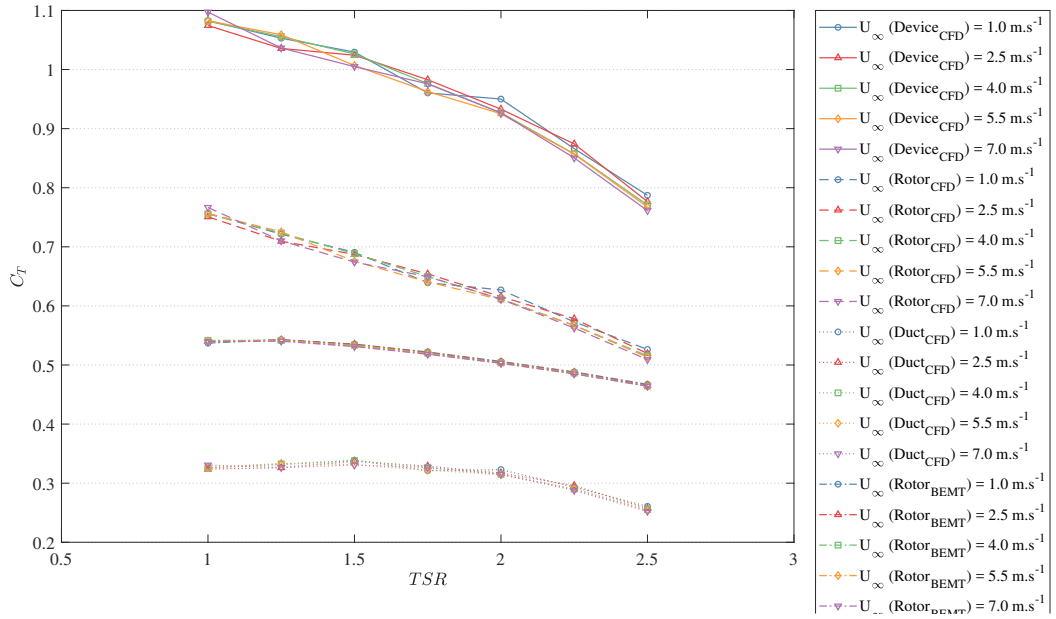


Figure 6.5: Evaluation of the ducted turbine thrust coefficient (C_T) in relation to TSR

global drag, whilst the duct was succumb to one-third; this allocation was somewhat relative to the areas of the duct and rotor, being 36% and 60% of the system area, respectively. In comparison to BEMT, which solely considered the drag on the rotor, a significant discrepancy was attained between the two methodologies, albeit exhibiting a moderately similar diminishing C_T trend.

In effort of establishing the source of the substantial drag on the rotor, the static pressure coefficient ($C_{Pr} = \frac{P_s}{\frac{1}{2}\rho U_\infty^2}$) distributions within the domain at the vicinity of the rotor were qualitatively analysed. Principally, the induction of axial drag upon a structure is a straightforward concept; pressure upstream and suction downstream of the structure induces this outcome. Illustrated in Figure 6.6, at low TSR , the static pressure difference through the rotor was substantial, inducing highly-loaded conditions. Acknowledging the flow-rate through the duct, at low TSR , the flux was comparatively low, as illustrated in Figure 6.7. As a result, as the free-stream was in constant contact with the structure, fluid accumulated at the inlet of the duct, upstream of the rotor, increasing the static pressure within this region. In continuation, due to the high-solidity of the rotor, insufficient fluid was permitted to flow through the duct, hence creating a region of low pressure. The duct sustained this variation in pressure as the upstream

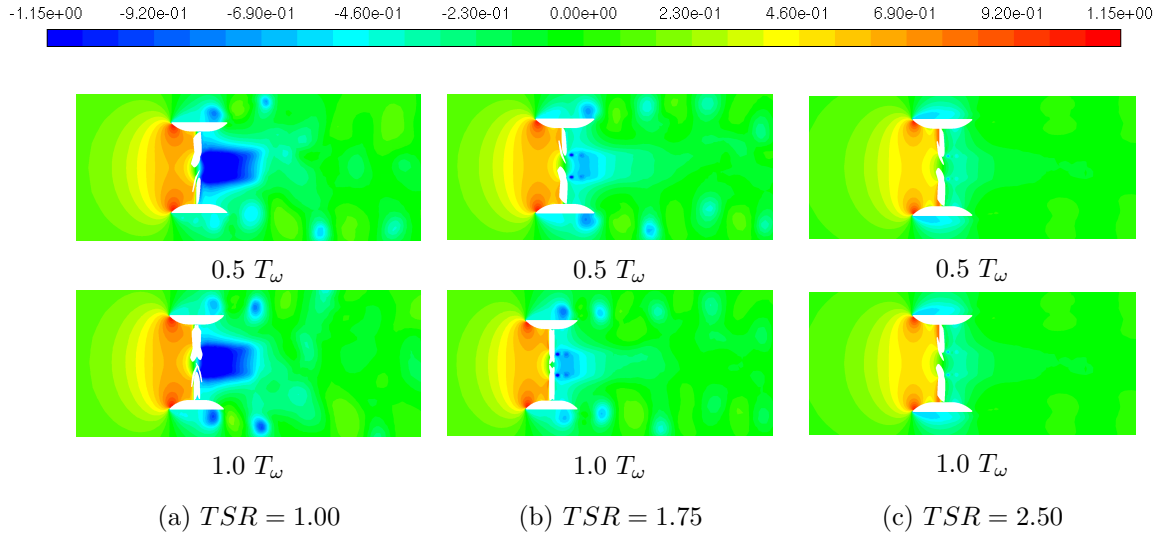


Figure 6.6: Illustrative top-view representation of the pressure coefficient (C_{Pr}) within the turbine domain at low, nominal, and high TSR at mean-average output; $U_\infty = 4 \text{ m/s}$

duct section confined the flow in the vicinity of the rotor, disallowing its leakage, hence inducing a pressure build-up, whilst, directly downstream of the rotor, disallowing the free-stream from re-energising the wake, hence sustaining the low pressure zone. As TSR increases, the flow-rate through the duct proportionally increases, hence decreasing the static pressure difference fore and aft of the rotor, subsequently reducing thrust on both the rotor and the duct; BEMT does not incorporate this fluid dynamic induction within its methodology, hence expounding the discrepancy observed. The variation in mass flow-rate through the turbine, attaining a mean coefficient of 0.71 at low TSR , which increases to a mean of 0.74 and 0.83 at nominal and high TSR , respectively, being inversely proportional to the resultant thrust, indicated the substantial influence upon the total drag induced on the entire structure. In consequence to the extensive capacity in mass-flow rate development, due to its high-solidity properties, as TSR was further increased, a negative pressure difference was eventually induced, resulting in the turbine to act as a propeller.

In addition to the system drag principally comprising of the rotor drag, the force on the duct, apart from being effected by the sustained pressure at the rotor, was

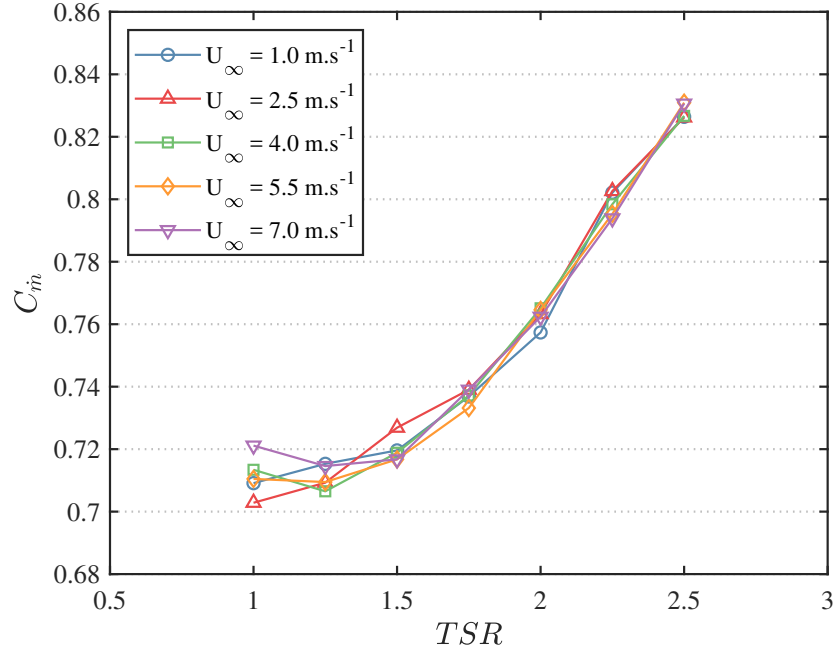
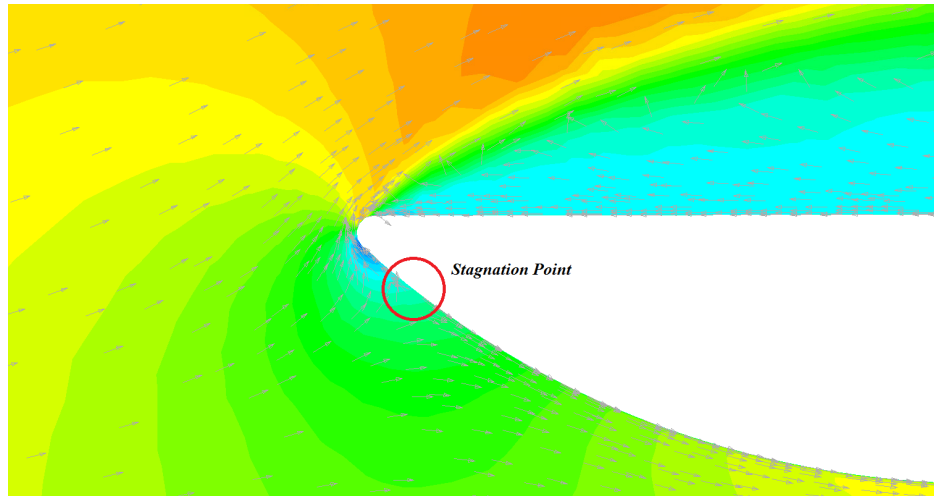
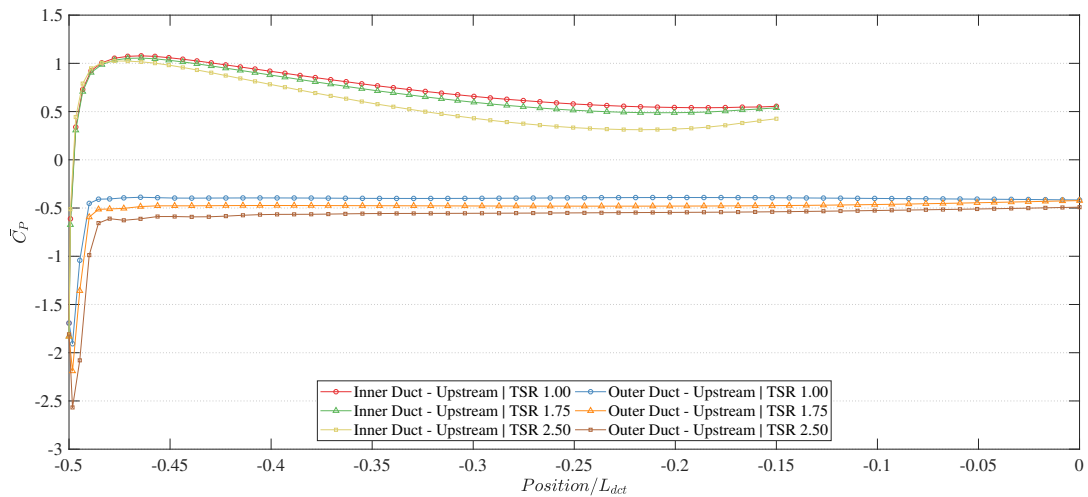


Figure 6.7: Evaluation of the ducted turbine mass-flow rate coefficient (C_m) in relation to TSR

dependent on the fluid-structure interaction at the profile of the duct structure. As the external fluid flow was in contact with the entire structure, a significant degree of static pressure built up at the walls of the duct inlet. This consequently affected the incoming flow as the far-flow in the direction of the system takes the path of least resistance, hence bypassing the duct inlet, flowing along the duct outer surface without any interaction with the internal structure. Fluid in the vicinity of the inner duct ridges, however, had impacted the internal structure, and interacted with the duct by flowing along the inner duct curvature, either against the free-stream, in an upstream direction away from the rotor, or with the free-stream, towards the rotor, illustrated in Figure 6.8a, both of which towards regions of lower pressure. Physically, along the perimeter of the duct, the point at which this occurred was the point of pressure stagnation, where static pressure is the highest, as velocity is nullified, and hence, induced significant drag; in this system, the stagnation point was induced, on average, at $\sim 0.94R_{dct}$.



(a) Axial velocity coefficient (\bar{u}_z^*) illustration of stagnation point on inner curved duct surface, and re-circulation zone on outer straight duct surface; $TSR = 1.75$



(b) Pressure coefficient (C_{Pr}) values at the inner curved and outer straight duct sections upstream of the rotor ($-0.5 \leq \frac{z}{L_{det}} \leq 0$)

Figure 6.8: Representation of the dynamics at the inner curved and outer straight geometry of the duct inlet; $U_\infty = 4 \text{ m/s}$

6.3 Static Pressure on Duct Ridges

The fluid flowing upstream of the stagnation point induced a unique phenomenon due to the flow being forced back up the duct, rather than through the turbine. Once

the flow surpassed the duct ridges, it interacted with the free-stream; due to the distinct velocities of the two flows, this induced a resultant, deflected flow misaligned to the free-stream, and hence, misaligned to the surface of the duct, resembling flow spillage. Similar to flow around a geometrical bend, substantial flow separation was induced, resulting in a region of re-circulating fluid, known as a separation bubble, within which rotational flow and turbulent mixing occur upon the duct surface, creating a low pressure zone. This concept is illustrated in Figure 6.8b, where the static pressure along the inner upstream duct surface was pressurised due to the inlet flux. Flux escaped upstream of the stagnation point, which resulted in a consistent measure of negative static pressure induced along the entire length of the outer duct, at all TSRs, implementing a degree of suction, induced by the re-circulating zone.

This phenomenon occurred at all TSRs modelled, yet the physical size of the re-circulation zone was seen to vary in an inversely proportional manner to the TSR of the rotor. As a result of the substantial static pressure within the duct at low TSRs, due to the lower mass-flow rate through the rotor, the flux of the fluid diverted upstream of the rotor was higher than that at higher TSRs. For this reason, the velocity resultant at the interaction with the free-stream was at a more obtuse angle to the surface of the duct than that at higher TSRs, creating a larger vortex zone. In addition, along the surface of the outer duct, the skin friction coefficient was minute, hence depicting that the re-circulation zone was incapable of completely reattaching. In consequence, the re-circulation zone was physically unstable, ensuing in its shedding; therefore, the external flow interacting with the duct instigated vortical rotational motion via the region of re-circulating fluid along the length of the duct, which was then shed at the duct outlet in the form of a ring vortex.

6.4 Vortex Shedding

Aft of the rotor, within the duct, the downstream turbine wake did not expand concomitant to the variation in the duct outlet geometrical profile, yet expanded at an angle more acute than the gradient of the inner duct contour. This signified that the

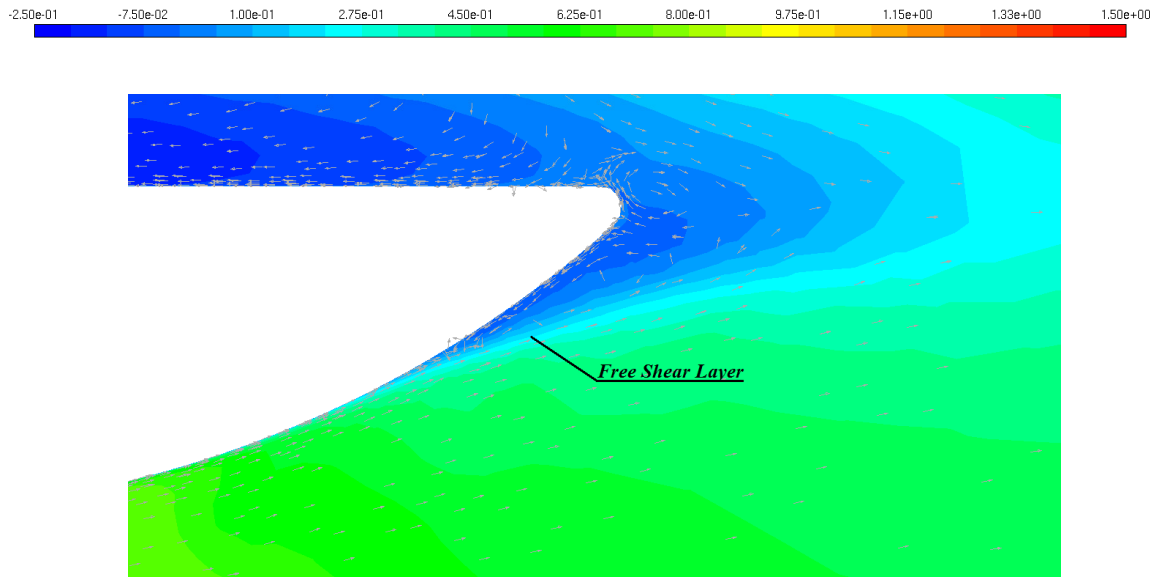


Figure 6.9: Axial velocity coefficient (\bar{u}_z^*) illustration of the free shear layer at the duct outlet; $U_\infty = 4 \text{ m/s}$, $TSR = 1.75$

flow refrains from attachment when flowing towards the outlet rim, hence providing evidence of boundary layer separation due to the adverse pressure gradient, decreasing duct efficiency. In addition, slight flow separation was induced within the fluid region between the wake and the duct due to the free shear layer at the boundaries of the wake, as illustrated in Figure 6.9. The distinct vortices, formed by the re-circulating fluid region along the circumference of the duct, and shed at the duct outlet as ring vortices, as illustrated in Figure 10.8, were transported within the turbine wake from this location. At low TSRs, the wake demonstrated a highly disorganised flow structure with turbulent intermixing, as illustrated in Figure 6.10. The large volume of the re-circulating zone induced substantial rotational motion within the created vortices, resulting in vortex shedding at comparatively high rotational kinetic energy; the high-energy vortices commingled with the low-energy wake, creating a chaotic wake. With an increase in TSR to nominal TSR, a consistent ring vortex stream was identified in the wake. The vortex effect diminished with an increase in TSR, due to the reduction of the re-circulating fluid zone and, hence, rotational kinetic energy. As the wake contains a higher degree of energy, this resulted in a more streamline wake at high TSRs; flow irregularity was nonetheless present in the wake, yet was comparatively minute, and

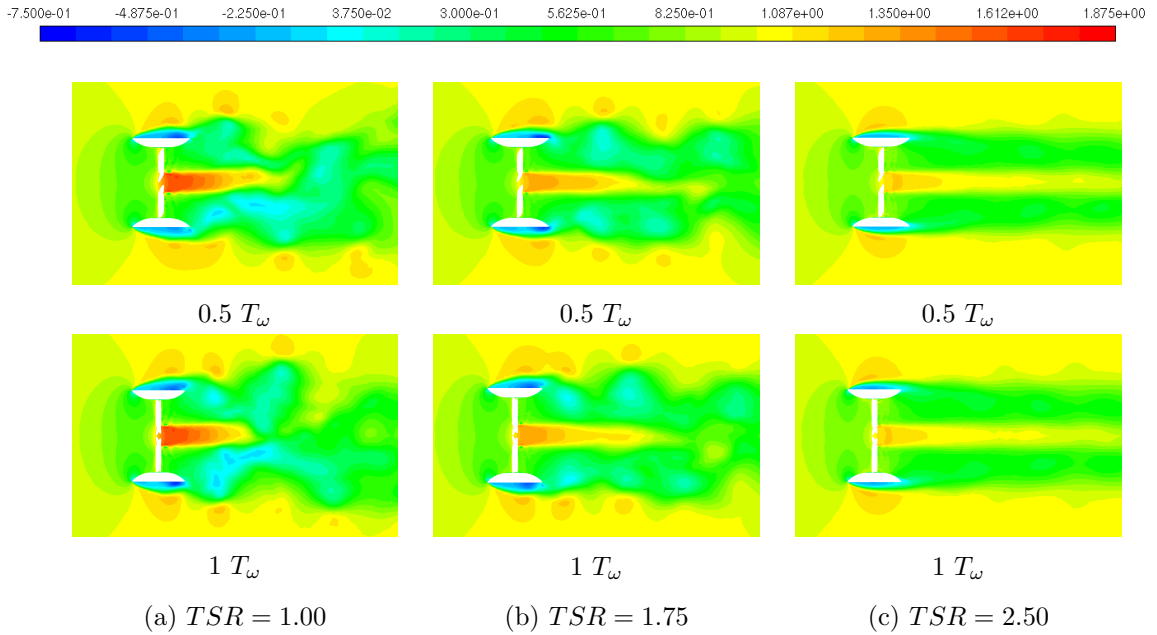


Figure 6.10: Illustrative top-view representation of the axial velocity coefficient (\bar{u}_z^*) within the turbine domain at low, nominal, and high TSR ; $U_\infty = 4 \text{ m/s}$

was solely transported within until dissipation. At the rotor, as the extremity (root) of the rotor blades were fixed to the duct, helical vortices were not present, permitting the ring vortices outside of the duct to be shed consistently, commingling with the turbulent vortex sheet wake. The vortex sheet sustained small scale vortices inducing viscous dissipation downstream of the turbine. At the open-centre, a helical vortex was shed from the rotor blade tips, where the flow structure was dissipated by the turbulent vortex sheet wake.

Correspondent to the vortex shedding, an analysis regarding the vortex effect on the axial drag force developed was considered by superimposing a sinusoidal function upon the global drag of the system in an effort to attain the frequency of the fluctuation. As a result, the vortex shedding frequency was found to be linearly proportional to the free-stream velocity, and, hence, Reynolds number (Re_L), as illustrated in Figure 6.11, in agreement with Strouhal's law; the shedding frequency is, therefore, solely dependent on the free-stream velocity of the domain. The quantity of the vortices shed per rotor rotation, however, act in an opposite manner, being independent of the free-stream

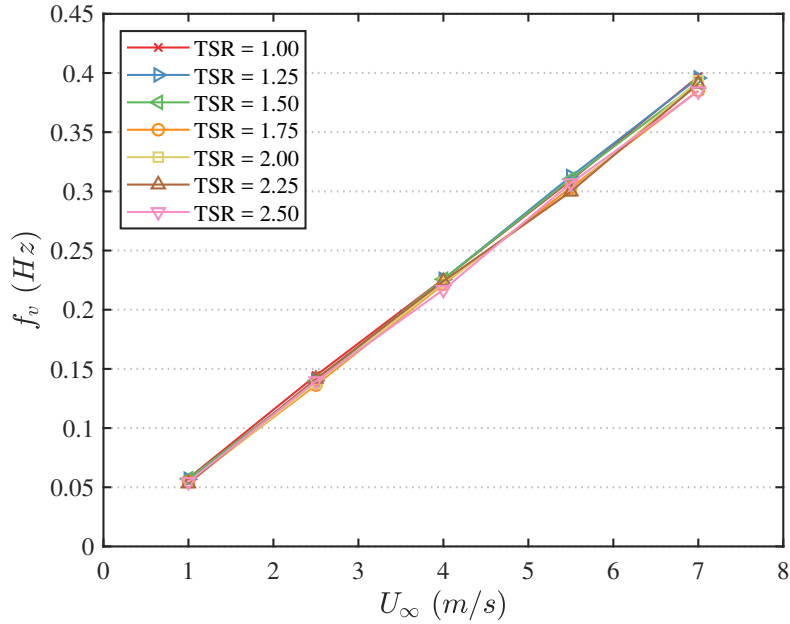


Figure 6.11: Evaluation of the vortex shedding frequency (f_v) in relation to free-stream velocity (U_∞) at distinct TSRs

velocity, yet dependent on the tip-speed ratio. Within that attribute, a mean of 2.15 and 0.83 vortices per rotation are shed at low TSR and high TSR, respectively. In attaining a Strouhal number (St) for the system, the duct length (L_{dct}) was utilised as the Strouhal characteristic length (L_{St}), hence resulting in a constant mean global Strouhal number of 0.558 for the ducted turbine system. For this reason, vortex shedding may have a significant influence on the system, where the potential presence of fatigue-inducing structural phenomena, such as vortex-induced vibrations (VIVs) on its foundation, together with fluttering at the blades, become a consequential factor to the dynamics of the system.

6.5 Blade Analysis

Further to analysing the static pressure on the duct, in effort of acknowledging the hydrodynamic impact on the blades, the static pressure on distinct sections along the radius of the rotor was considered. Figure 6.12 illustrates the variation in pres-

sure coefficient at nominal TSR in five physical iterations on the blade, from near-tip ($r_{rtr}/R_{rtr} = 0.3633$) to near-duct ($r_{rtr}/R_{rtr} = 0.9300$), to quantitatively extract the static pressure distribution along the rotor radius.

The distribution of static pressure along each section of the blades was found to be largely consistent. Induced with a pressurised side on the upstream surface of the blade, the stagnation point, at higher radii, was precisely at the leading edge of the blade, which shifts inwards along the pressurised surface at lower radii due to the variation in angle-of-attack. Attributable to the profile of the blade, a flat-plate with rounded edges, a separation point was induced along the downstream (suction) surface as a result of flow acceleration around the leading edge; the separation occurs at the location where the rounded edge joins the flat edges. Along the upstream (pressurised) surface, a pressure depression was similarly induced, yet attachment was sustained as a result of the external flow from the inlet of the duct.

Suction is dominant throughout the surfaces of the blades, withal at the upstream pressurised surface, where pressure decreases along the chord length, accentuating the inefficacy of the blade profile. A secondary pair of separation points are induced at the locations where the trailing rounded edge joins the flat plate, due to the sudden change in geometry. Precisely at the trailing edge, the suction is substantial enough to influence the post-separation low-pressure flow towards the wall, increasing the static pressure at this location. This description is consistent at differing radii, yet the extremities decrease proportionally to the radius-position of the blade, primarily due to the comparatively diminished dynamics towards the central axis of the rotor.

In addition to the quantitative measure of static pressure, in an effort to further contemplate the flow dynamics at the blade surfaces, pressure contours along the downstream suction side, illustrated in Figures 6.13 and 6.14, were qualitatively attained at low and nominal TSRs at quarterly positions of rotational period (T_ω) for low and mid free-streams. Regions of stall are elucidated at low rotational velocities, which recede with an increase in TSR; this accompanies well the analysis and speculations put forward as a result of the variation in angle of attack and resultant induced lift. By means of these contours, distinct aspects of the flow are established, specifically the spanwise

Chapter 6. Hydrodynamic Performance of a Ducted High-Solidity Tidal Turbine in Aligned Flow Conditions

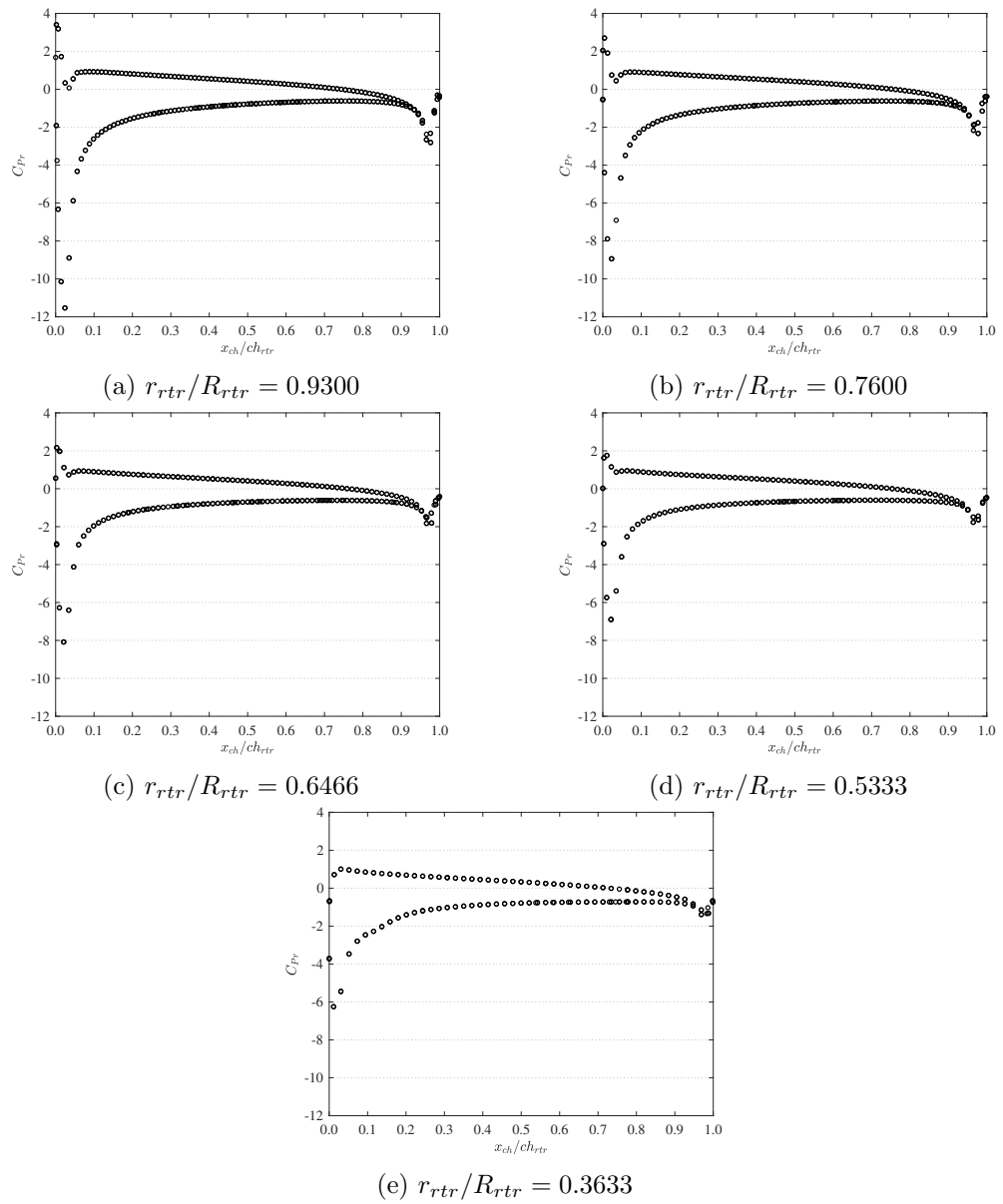


Figure 6.12: Plots of pressure coefficient (C_{Pr}) along the blade chord ratio (x_{ch}/ch_{rtr}) at distinct rotor radius ratios (r_{rtr}/R_{rtr}) at $U_{\infty} = 4.0 \text{ m/s}$, $TSR = 1.75$

flow acting along the blade, ascertaining the requirement of three-dimensionality when analysing rotating flows.

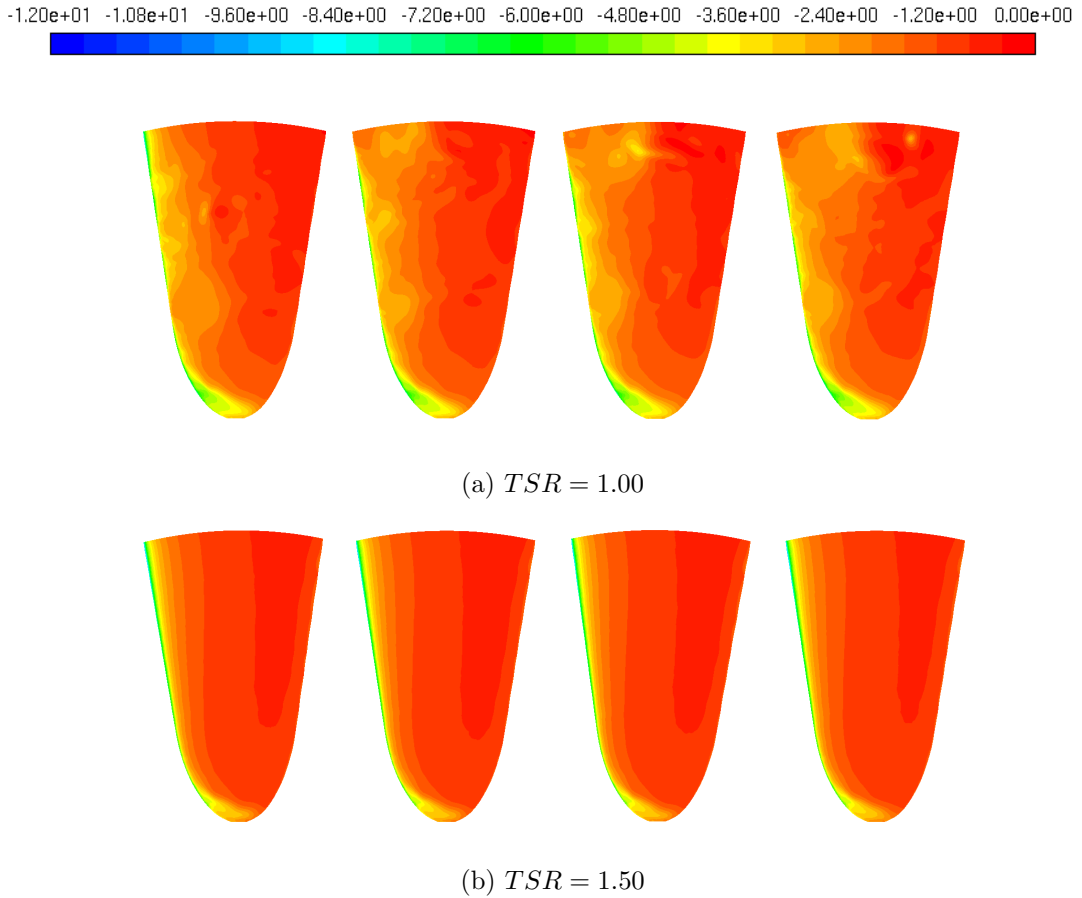


Figure 6.13: Pressure coefficient (C_{Pr}) contour representation along the suction edge of the blade at rotation period $\frac{1}{4} T_\omega$ (left), $\frac{2}{4} T_\omega$ (mid-left), $\frac{3}{4} T_\omega$ (mid-right), and $\frac{4}{4} T_\omega$ (right) at $U_\infty = 1.00$ m/s at low (top) and nominal (bottom) TSR

6.6 Wake Velocity Profiles

A potential aspect of the installation of ducts is the constraintment of the downstream wake; an advantage in the effort to limit wake interaction with subsequent rotors within a turbine farm. The axial velocity profiles of the wake of the rotor, from $0.5D_{rtr}$ to $6D_{rtr}$ downstream, are uniquely compound as a result of this installation. Illustrated in Figure 6.15, the dimensionless axial velocity ($\bar{u}_z^* = \frac{\bar{u}_z}{U_\infty}$) profiles at the distinct free-stream velocities considered are largely identical.

Within the near-wake, at $0.5 D_{rtr}$, the maximum axial wake velocity was identified to be at the centre; a result of the open-centre of the turbine. This velocity surpasses

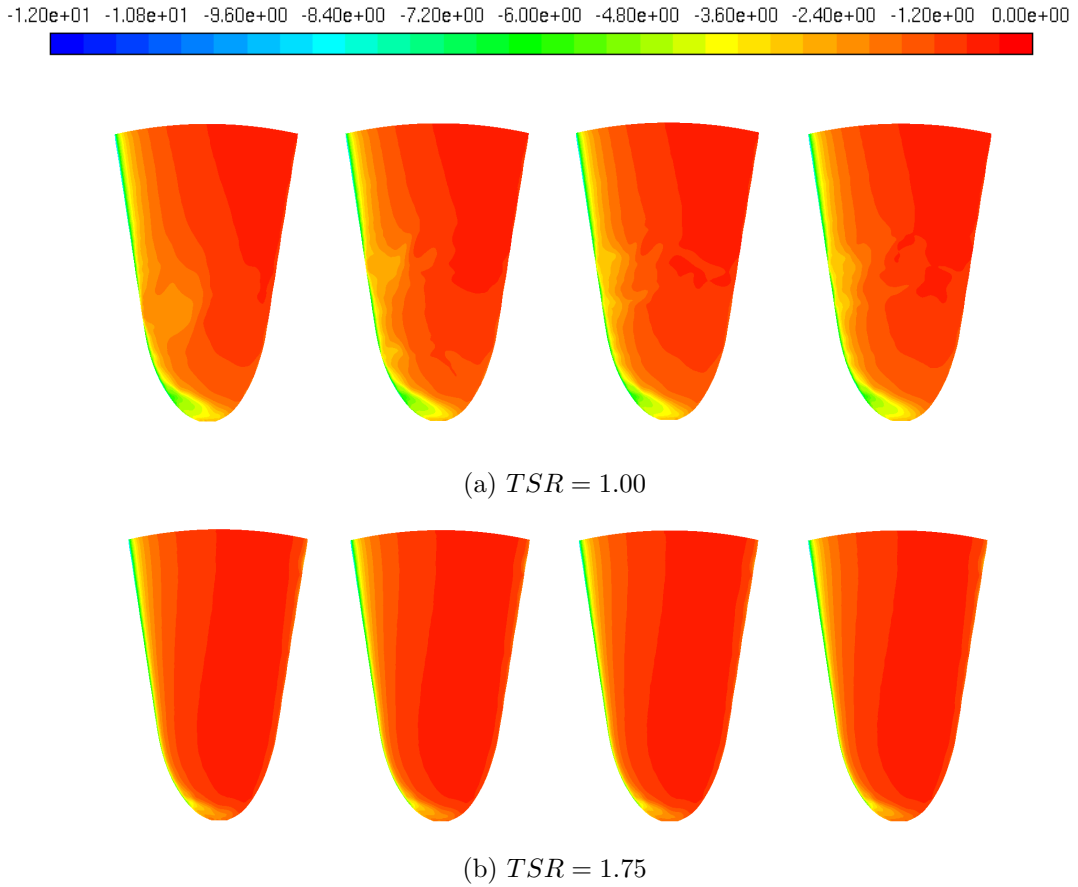


Figure 6.14: Pressure coefficient (C_{Pr}) contour representation along the suction edge of the blade at rotation period $\frac{1}{4} T_\omega$ (left), $\frac{2}{4} T_\omega$ (mid-left), $\frac{3}{4} T_\omega$ (mid-right), and $\frac{4}{4} T_\omega$ (right) at $U_\infty = 4.00$ m/s at low (top) and nominal (bottom) TSR

the value of the free-stream magnitude, acknowledging a phenomenon typically established in flow through an orifice: an induction of flow acceleration. This acceleration comes about in consequence of the substantial static pressure retained within the duct immediately upstream of the rotor, forcing fluid out through the open-centre. This outcome sacrifices torque on the blades, as a degree of fluid at the wall flows in a radial direction towards the orifice at the blade tip, rather than in a tangential orientation along the blades. In continuation, the axial velocity diminishes along the radius of the turbine ($y_{R_{tr}}^* = \frac{y}{R_{tr}}$) due to the presence of the blades and duct, where the point of minima axial velocity is situated at the ridge of the duct. The axial velocity then increases rapidly to a magnitude above the free-stream, an effect from the flow accel-

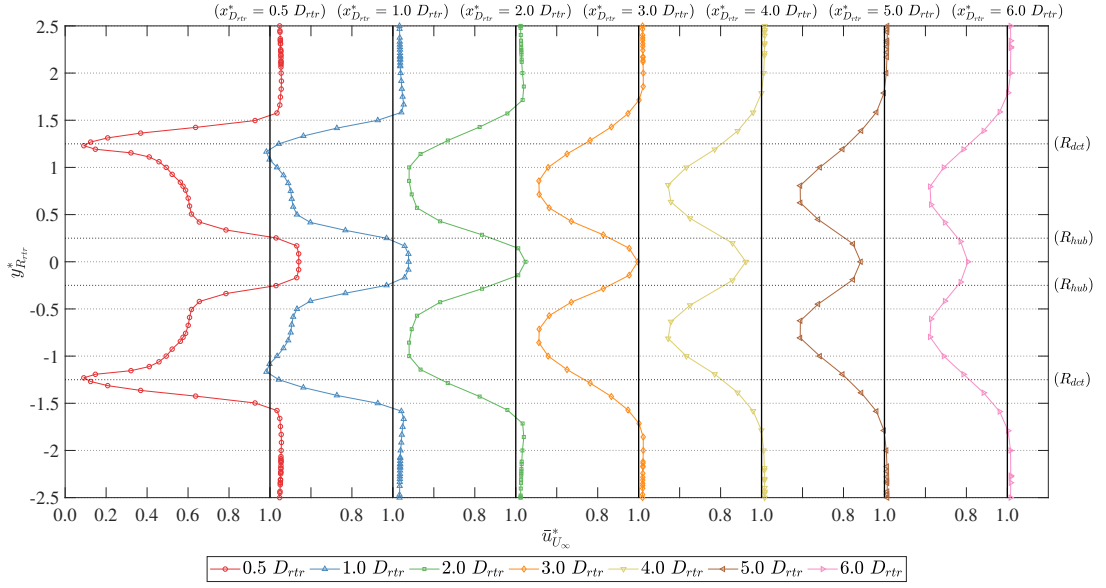


Figure 6.15: Dimensionless axial velocity (\bar{u}_z^*) profiles within the ducted turbine wake at different rotor diameter displacements downstream – $U_\infty = 4$ m/s, $TSR = 1.75$

eration at the upstream ridge, within a displacement of $1.5 R_{rtr}$ (or $1.2 R_{dct}$) from the central axis of the turbine, portraying the capacity of a duct in restricting the extent of the wake growth. The velocity then decreases gradually to the free-stream magnitude.

As the wake flows further downstream, regions of higher kinetic energy dissipate to regions of lower kinetic energy, hence axial velocity decreases within the region in the vicinity of the orifice to supplement the regions in the vicinity of the duct. The velocity profiles become more rounded, signifying an efficient distribution of energy. Far wake, at $6 D_{rtr}$, the velocity profile has largely regained its energy and becomes more consistent along the turbine radius, albeit portraying its unique aspects, particularly at orifice and duct regions.

6.7 Chapter Summary

This study has put forward an investigation into the hydrodynamic performance concerning a ducted, high-solidity tidal turbine utilising blade-resolved computational fluid dynamics. The endeavour strived to overcome the limitations of actuator disc

and blade-element momentum theory methodologies by implementing a computational fluid dynamic analysis with blade-explicit actuality, coupled with general continuity at both the domain and turbine. This feature allowed the aspect of modelling flow three-dimensionality at the turbine, together with induced turbulence effects, in further effort of numerically replicating its true performance.

The numerical outcomes of the main performance factors of the full-scale ducted turbine portrayed a peak power coefficient of 0.34 with a thrust coefficient of 0.97 at a nominal tip-speed ratio of 1.75. Further fluid dynamic analysis, namely the hydrodynamic effects along the duct, mass-flow rate through the duct, vortex shedding within the domain, static pressure along the rotor blades, and velocity profiles within the rotor wake, were established.

Chapter 7

Hydrodynamic Performance of a Ducted High-Solidity Tidal Turbine in Yawed Flow Conditions

In relation to investigations that have endeavoured in modelling ducted turbines in yawed flow conditions [20,105,107], this present study produces a more coherent representation of the configuration, utilising the STD τ - ω , due to the accurate geometrical representation, the numerical modelling of general conservation and turbulence, and in acquiring the parametric causation of a performance variation, hence better analysing the hydrodynamic occurrence of the fluid-structure interaction.

7.1 Power Coefficient

The turbine efficiency in converting kinetic energy from the free-stream into mechanical power at the distinct bearing angles was primarily established; the prior chapter had acknowledged the power coefficient curve of the ducted, high-solidity tidal turbine in aligned flow, which described a relatively short spanning curve, attaining a peak

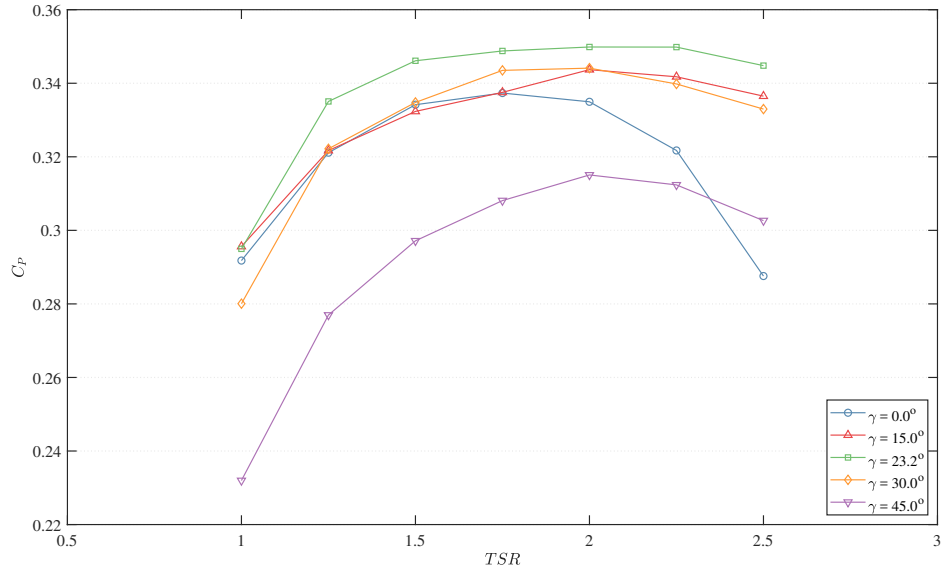


Figure 7.1: Evaluation of the mean ducted turbine power coefficient (C_P) at distinct flow bearings in relation to TSR

power coefficient of 0.338 at a nominal TSR of 1.75 within a range of 1.00 – 2.50. Once the validated modelling techniques were implemented for the turbine model in yawed flow, distinctive physical performance outcomes were displayed in representation of its ducted, high-solidity characteristics.

Illustrated in Figure 7.1, both the individual TSR output values and the general trend attained along the power curve at the yaw angles vary significantly in comparison to the parameters at aligned flow; the more notable, and favourable, outcome is the increase in peak power coefficient at the distinct bearings, surpassing that at aligned flow. In effect, the 23.2° bearing becomes the highest power generating condition, with maximum increases of 1.90%, 3.86%, and 1.90%, to values of 0.344, 0.350, and 0.344, at bearings of 15.0° , 23.2° , and 30.0° , respectively. This outcome comes about together with a shift in nominal TSR from a value of 1.75 at 0° to 2.00 at the bearings investigated, along with a broader power-generating region at higher TSRs (2.00 – 2.50), the most substantial increase being a 19.89% increase at high TSR. At a bearing of 45° , a general diminishment of power generated is perceived, apart from the power generated at high TSR, which is 5.22% higher than that at aligned flow.

In manipulation of the hydrodynamic performance characteristics, albeit a maxi-

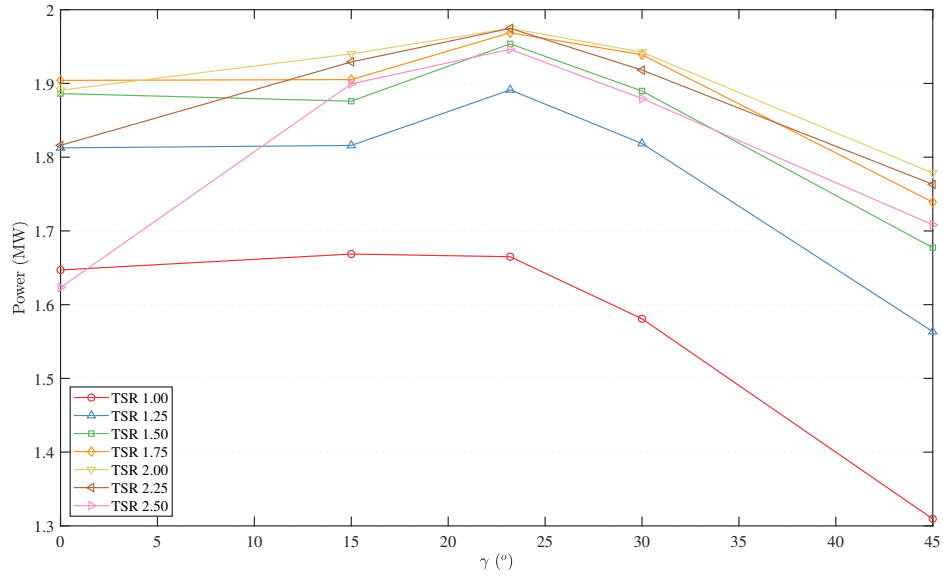


Figure 7.2: Evaluation of the true mean power at distinct TSRs in relation to flow bearing (γ)

imum power coefficient of 0.350 was attained, it may also be acknowledged that, due to the device area (A_{dvc}) being considered, hence rotor & duct, the power coefficient will increase once the power per rotor area (A_{rtt}), rather than system area, is implemented. In this respect, the rotor radius is 80% that of the system, hence increasing the maximum power coefficient by a magnitude of 1.5625 to a nominal peak value of 0.547. Furthermore, due to the flow bearing varying the output in a cubic proportion, the free-stream velocity component parallel to the rotor axis may be considered within the power coefficient equation, rather than the magnitude, increasing the power coefficient to 0.704. Due to the fact, however, that the power attained by the rotor is also disseminated from the fluid in contact with the duct, while the maximum energy in the flow is relative to the free-stream magnitude, applying the entire system area and global flow velocity is a more conservative approach to represent.

Due to the display in power coefficient, the variation in true power at the distinct yaw bearings was investigated, illustrated in Figure 7.2. As the flow angle increases to 15° , the power coefficient variation at lower TSRs (1.00 – 1.50) is arguably negligible, contrary to that at higher TSRs (2.00 – 2.50), which increases by a maximum of 17.28%. A bearing of 23.2° attains the highest performance values for all TSRs, with a peak

mechanical power value of 1.975 MW; this angular bearing was instigated as it is equivalent to the mean curvature gradient of the duct inlet rim. Subsequent bearings pertain diminishing performance values.

In acknowledging the transient nature of the rotating numerical turbine, the variation in power generation at nominal TSR of each bearing angle within five cycles of the time-dependent analysis was investigated, as illustrated in Figure 7.3. When succumb to aligned flow, a significant variance in the mechanical power from the mean is recognised, with a diminishment in variance as the free-stream angle is introduced, inducing a more stable output. The variance in the aligned flow output had been acknowledged to be due to the fluctuations in pressure and velocity [119] as a result of vortex ring shedding. Observing a considerable diminishment in fluctuation therefore signified a reduction in vortex shedding effects, due to the ungeneration of ring vortices, within the limited flow bearing range. The most stable output was attained at a bearing of 23.2° ; hence not only was the mean output highest at this bearing, yet it also attained the least deviation. Outcome fluctuations were evident at a bearing of 45° , yet were largely synchronised, with eight fluctuations per cycle, equivalent to the number of rotor blades.

Due to the fluctuations within a rotation cycle, the mean response of a rotor blade during its rotation was analysed by means of cycle-averaging, azimuth angle-synchronising, and, subsequently, blade-averaging the data attained, as illustrated in Figure 7.4; this output was multiplied by the number of blades for comparison purposes. At axial flow, the mean performance per blade per cycle was largely consistent along the turbine rotation. Upon an increase in flow bearing, the resultant performance is skewed, with a decrease in generation at top dead centre and an increase at bottom dead centre. This discrepancy was deemed to be a result of the variation in induced angle-of-attack along the rotation of the blade due to the angular flow. This resulted in the lowest lift-generating angle-of-attack to occur at the beginning/end of the cycle, with the highest lift-generating angle-of-attack occurring midway through the cycle; intermediary angles-of-attacks are attained between the two extremities.

A notable outcome was attributed to the 45° yaw free-stream due to a significant dip

Chapter 7. Hydrodynamic Performance of a Ducted High-Solidity Tidal Turbine in Yawed Flow Conditions

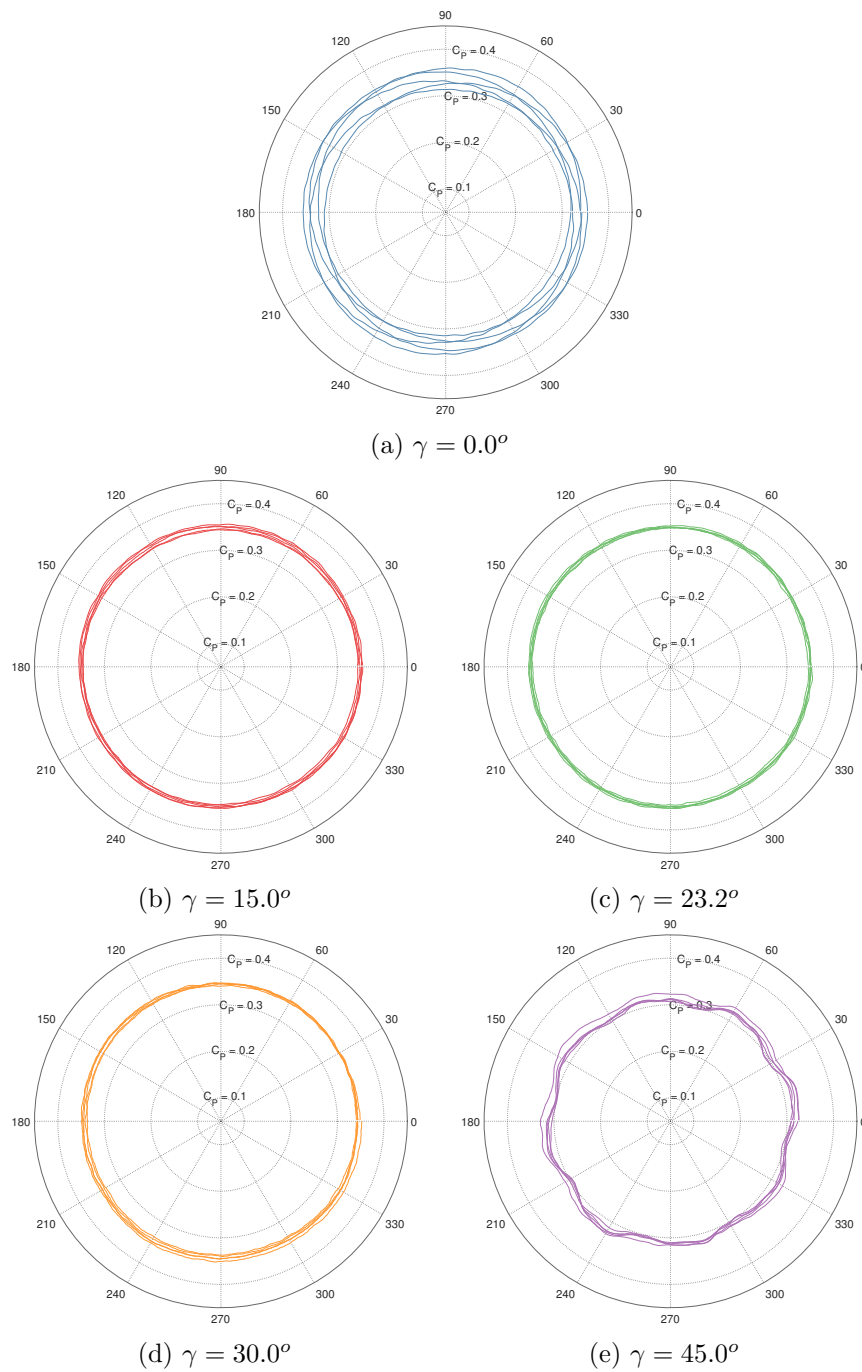


Figure 7.3: Evaluation of the instantaneous ducted turbine power coefficient (C_P) in relation to blade azimuth angle

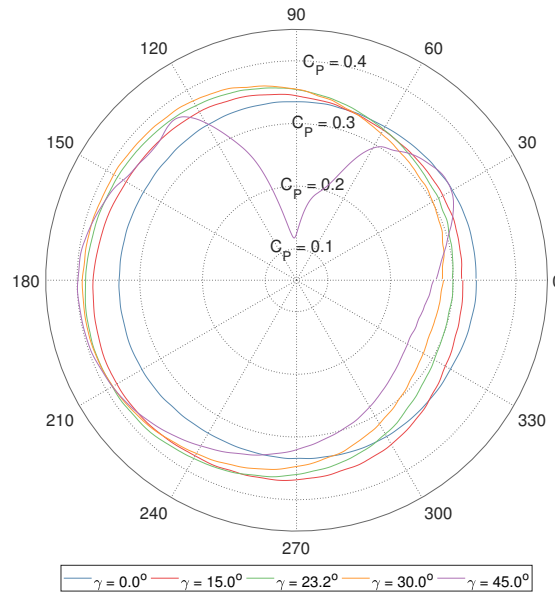


Figure 7.4: Evaluation of the mean single-blade response (C_P) in relation to azimuth angle

in efficiency at quarter-cycle. As the flow was incoming from portside, at an incoming angle distinctively higher than the inlet shroud angle, flow separation in the form of a re-circulation zone was induced within the duct, upstream of the rotor, instigating a low-pressure zone. This low-pressure zone diminished the pressure induced upon the blade surface at interaction, providing lower power generation; as the re-circulation zone was present solely within an acute segment of the turbine, this was acknowledged to be the causation of the sudden depreciation in power.

In continuation to the power generation, the variation in torque induced, illustrated in Figure 7.5, was analysed. Within aligned flows, the curve portrays a peak value of 0.292 at low TSR, which decreases in a steep quasi-linear manner to 0.115 at high TSR. A minutely higher torque is generated along the trend at yawed conditions, where, similar to the power curve, the most substantial variation occurred at high TSR with a 17.1%, 19.9%, and 15.8% increase at bearings of 15.0° , 23.2° , and 30.0° , respectively; a general decrease in torque is attained at a yaw angle of 45° .

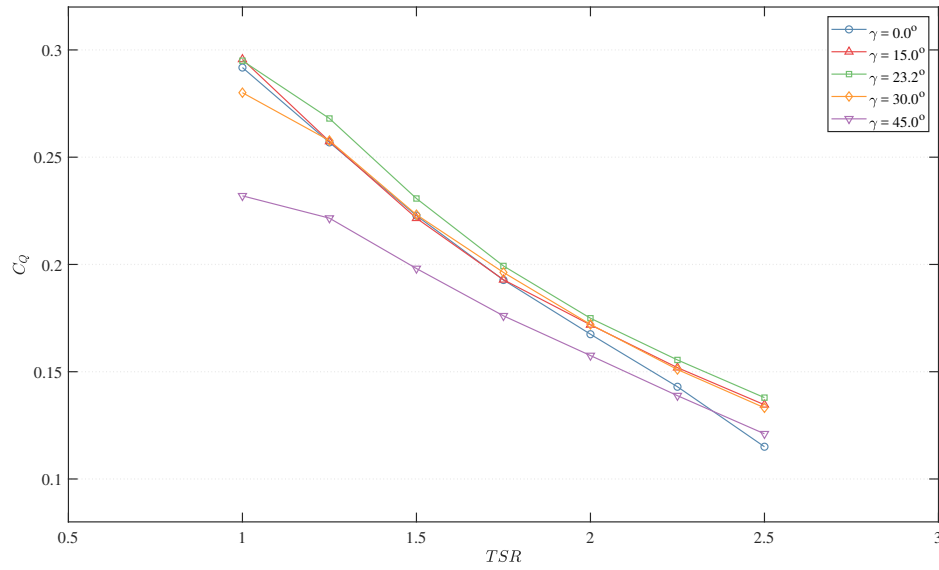


Figure 7.5: Evaluation of the mean ducted turbine torque coefficient (C_Q) at distinct flow bearings in relation to TSR

7.2 Thrust Coefficient

Owing to the fact that torque was enhanced within a limited range, it was apparent that the loading upon the blades had increased; to ascertain this, the thrust coefficient of the system, together with duct and rotor discretisation, illustrated in Figure 7.6, was investigated. Within aligned flows, the curve portrayed a peak value of 1.08 at low TSR, decreasing in a polynomial manner to 0.77 at high TSR. Similar to the power and torque curve, a parametric increase is presented at higher TSRs; the 23.2° bearing sustained the highest degree of both trend and individual thrust magnitude of 1.10 at low TSR, with the blades having been succumb to $\approx 69\%$ of the axial load. At this bearing, the most substantial increase occurred at high TSR to a coefficient of 0.9074, a 17.7% increase; the thrust then decreased at a 45° flow bearing. It was therefore acknowledged, due to the increase in thrust and torque at higher TSRs, that a higher degree of axial force loading was induced within the flow bearing variation.

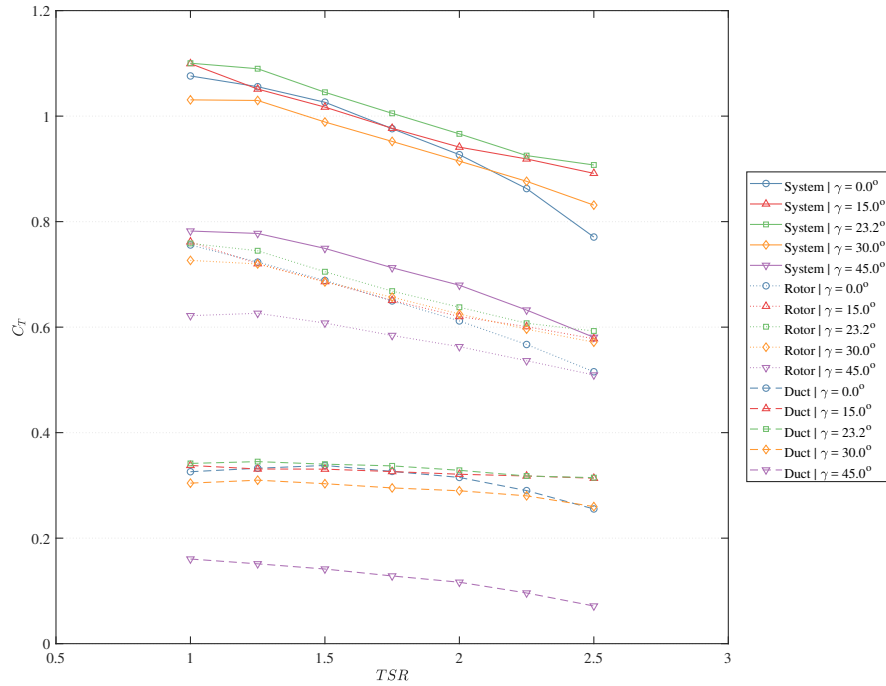


Figure 7.6: Evaluation of the mean ducted turbine thrust coefficient (C_T) at distinct flow bearings in relation to TSR

7.3 Linear Momentum Analysis

Albeit an increase in power, torque, and thrust had previously been pointed out when a ducted turbine has been succumb to yawed flows [17, 105], a definitive rationale for its occurrence had not been acknowledged. For this reason, linear momentum analysis was utilised within this investigation to pinpoint the hydrodynamic characteristics behind the substantial degree of loading induced at higher TSRs.

7.3.1 Axial Velocity & Volumetric Flow-Rate Coefficients

In ensuring that the numerical surfaces for data acquisition were introduced at a suitable location in relation to the rotor, the area-averaged axial velocity was analysed at the planes, and their equivalence at both was confirmed. Illustrated in Figure 7.7, the axial velocity through the duct was found to be largely consistent at all TSRs for the entire bearing range; the highest axial flow velocity values were attained at nominal bearing ($\gamma = 23.2^\circ$), acting proportionally to the rotational velocity of the rotor. Post-

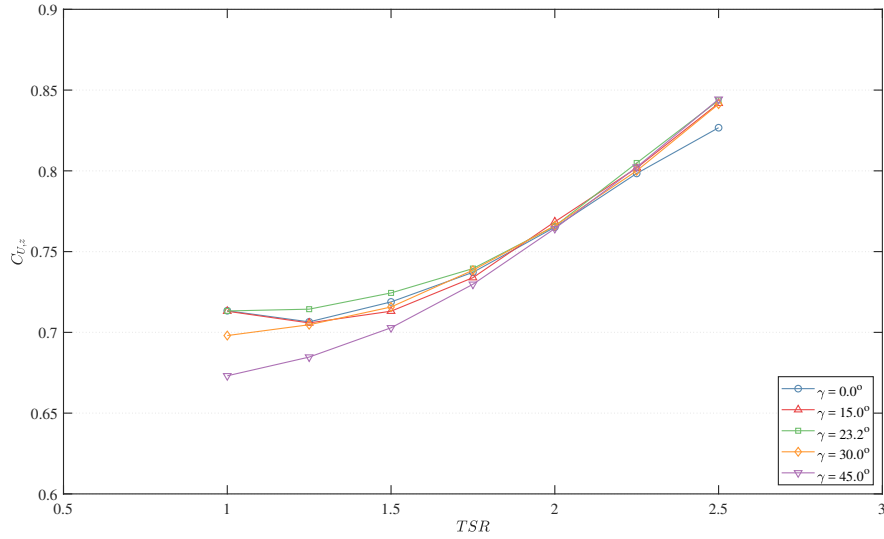


Figure 7.7: Evaluation of the mean axial velocity coefficient ($C_{U,z}$) at distinct flow bearings in relation to TSR

nominal angles depicted a similar trend, yet attained diminished values at pre-nominal TSRs, with pre-nominal bearings depicting a dip in flow at pre-nominal TSR. Higher TSRs attained largely equivalent axial velocity values at all bearings ($\approx 84\%$ of the free-stream at high TSR), notably higher than that in aligned flow. This outcome hence puts forward the unique capacity of the shroud installation in sustaining axial velocity through a rotor, albeit succumb to an angular velocity component variation with the rotor axis within the free-stream.

Further to the axial velocity, the volumetric flow rate was detailed, illustrated in Figure 7.8. This was established to acknowledge the true flow through the duct, as the axial velocity through the duct may have solely been a component of the flow rather than the entire flow vector, moreover at high free-stream bearings. Albeit this premise, the axial velocity coefficient was found to be, on average, $\approx 98\%$ of the volumetric flow rate, further portraying the capacity of the shroud installation.

7.3.2 Static Pressure Coefficient

In continuation to the implementation of linear momentum analysis, the static pressure values were extracted from the planar surfaces. Primarily plotting the pressure

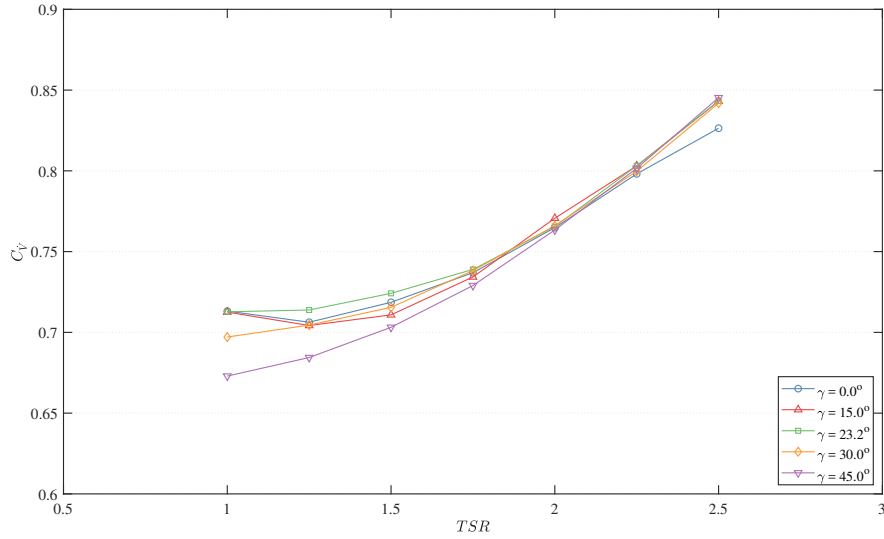


Figure 7.8: Evaluation of the mean volumetric flow-rate coefficient (C_{V_r}) at distinct flow bearings in relation to TSR

drop, fore and aft of the rotor, illustrated in Figure 7.9, a quasi-linear trend was apparent throughout the bearing range, with the highest pressure difference along the curve attained at the nominal bearing of 23.2° . The most significant variation in comparison to the response at aligned flow was the increase in pressure drop at high TSR, with 12.1%, 14.8%, and 10.2% increments at bearings of 15.0° , 23.2° , and 30.0° , respectively; a general decrease in pressure difference was attained at a yaw angle of 45° . This increase in static pressure difference along the higher TSR regions elucidates the increased loading, hence identifying the enhancement in power and thrust generated as described by the formulae constituting axial momentum theory.

Discretising the variation in static pressure difference by flow bearing, a more consistent distribution was acquired. Illustrated in Figure 7.10, the pressure difference values increased with a variation in bearing from aligned flow to nominal bearing, attaining the highest values of pressure difference for all TSRs, then decreasing at post-nominal angles. In an effort to establish the variation in pressure difference, the pressure upstream and downstream of the rotor were distinctively analysed, illustrated in Figures 7.11 and 7.12. The pressure induced upstream of the rotor acted proportional to the yaw angle as the exposed frontal area of the duct inlet, normal to the

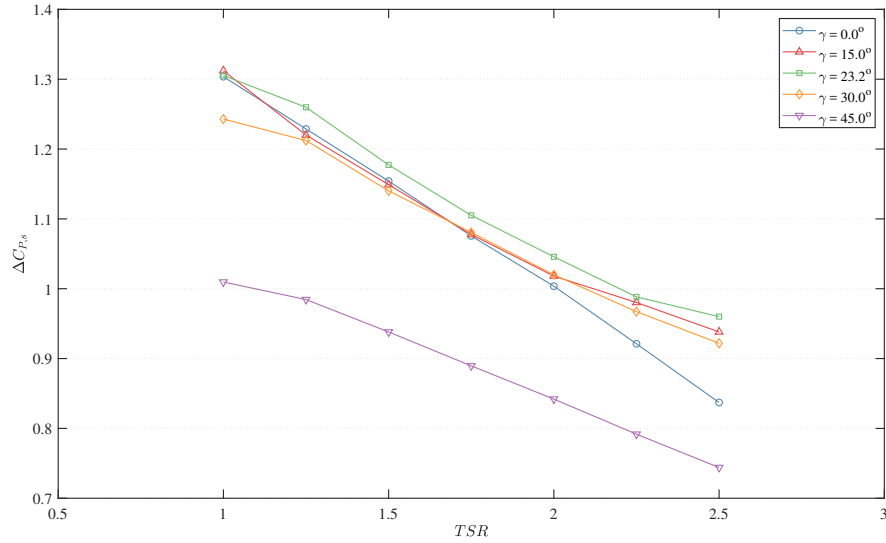


Figure 7.9: Evaluation of the mean static pressure difference coefficient ($C_{\Delta P,s}$) at distinct flow bearings in relation to TSR

flow, diminished. In relation to the rotational velocity, a slight increase was exhibited at lower TSRs and pre-nominal bearing, giving evidence to the dip in axial velocity, decreasing at post-nominal TSR, proportional to an increase in flow rate.

Further to this, the downstream pressure at the outlet of the duct was acknowledged to be more unique in response. When succumb to aligned flow, the static pressure increased in a polynomial manner with an increase in rotational velocity. At a free-stream bearing, the pressure similarly increased at lower TSRs, yet, at higher TSRs, a decrease was contrarily initiated, elaborating the condition of the increase in static pressure drop. Physically, within aligned flow, the wake flow exited the duct in a mean direction normal to the rotor plane, inducing back pressure at the duct outlet. Upon a yawed flow-stream, the wake profile was swept towards the general direction of the free-stream, a direction unequivalent to the rotor plane normal, and, as a result of the physical displacement of the resultant wake, the back pressure into the duct outlet diminished, acknowledging the causation of the reduced downstream rotor pressure and increased pressure difference.

This decrease in downstream pressure gives reason for the shift in nominal TSR at yawed bearings. A similar shift in nominal TSR had been acknowledged in prior aligned

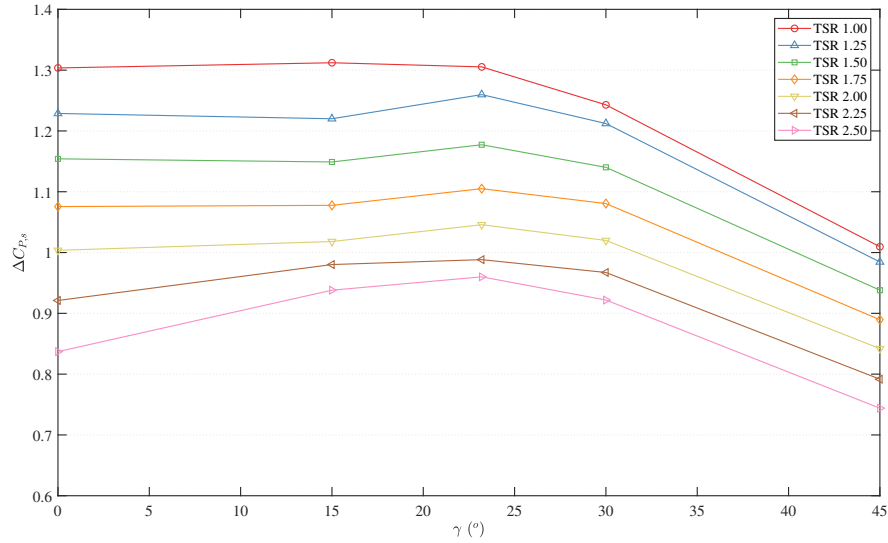


Figure 7.10: Evaluation of the mean static pressure difference coefficient ($C_{\Delta P,s}$) at distinct TSRs in relation to flow bearing (γ)

flow analyses [89,119], deduced to be a result of a variation in the stall angle in relation to an enhancement in chord-based Reynolds number due to an increase in free-stream velocity. This distinct elaboration, however, was deemed to be improbable as the mass-flow through the duct at high TSRs was retained, or very minutely enhanced, at all bearings, hence constraining the chord-based Reynolds number to be largely consistent.

In this regard, it may be conceptualised that the stall angle varied in relation to the decrease in downstream pressure. For this reason, it may be pertained that, due to the lower pressure within the duct, downstream of the rotor, the suction surface of the blade acquired lower degrees of pressure at a sustained flow-rate and chord-based Reynolds number. Hence, as the fluid flowed along the blade section, the laminar viscous sublayer over the upper blade surface was subjected to a lesser adverse pressure gradient at the leading edge of the section, when compared to aligned flows, sustaining boundary layer attachment to the under-surface of the blade section, rather than separating. As attachment was sustained, the stall angle, at which flow separation occurs, shifted to a slightly higher angle-of-attack, generating higher lift and producing a higher degree of power.

Within post-nominal bearings ($\gamma > 23.2^\circ$) at lower TSRs, the downstream pressure

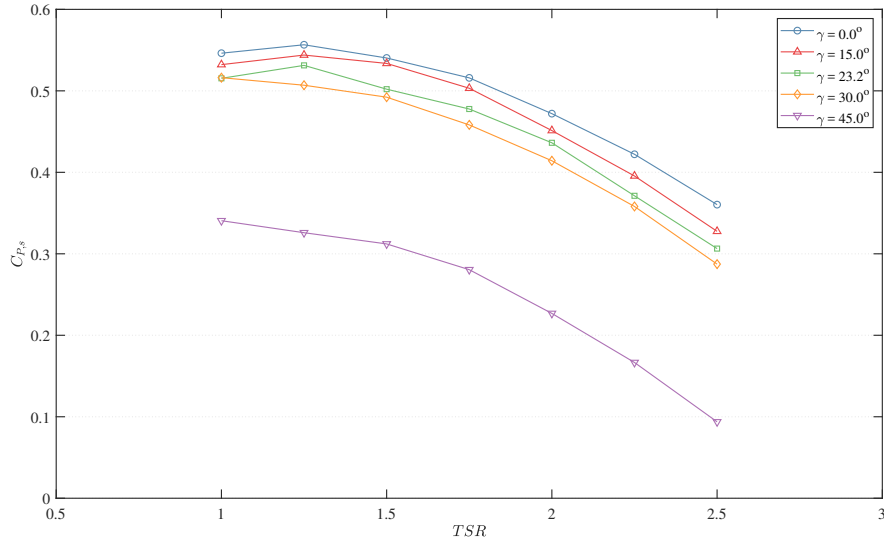


Figure 7.11: Evaluation of the mean static pressure coefficient ($C_{P,s}$) upstream at distinct flow bearings in relation to TSR

at the duct outlet was acknowledged to be higher than that at pre-nominal bearings. This variation was induced due to external flow entering the duct through the outlet; as the static pressure at 30° and 45° bearings along the duct outlet was substantially lower in comparison to the pressure at the external duct surfaces, this variation in pressure induced a degree of reverse flow, energising the region. The pressure decreased post-nominal TSR, similar to prior bearings.

7.3.3 Total Pressure Coefficient

In continuation to the implementation of the disc analysis, the total pressure difference was extracted from the planar surfaces. As total pressure is known to be the summation of static pressure and dynamic pressure, it may be correlated to the summation of the pressure potential energy and kinetic energy within the flow. The total pressure difference fore and aft of the rotor, illustrated in Figure 7.13, therefore depicts the highest energy extraction to occur at the nominal bearing of 23.2° , with comparable trends to the supplementary bearings, acknowledging the superior energy extraction.

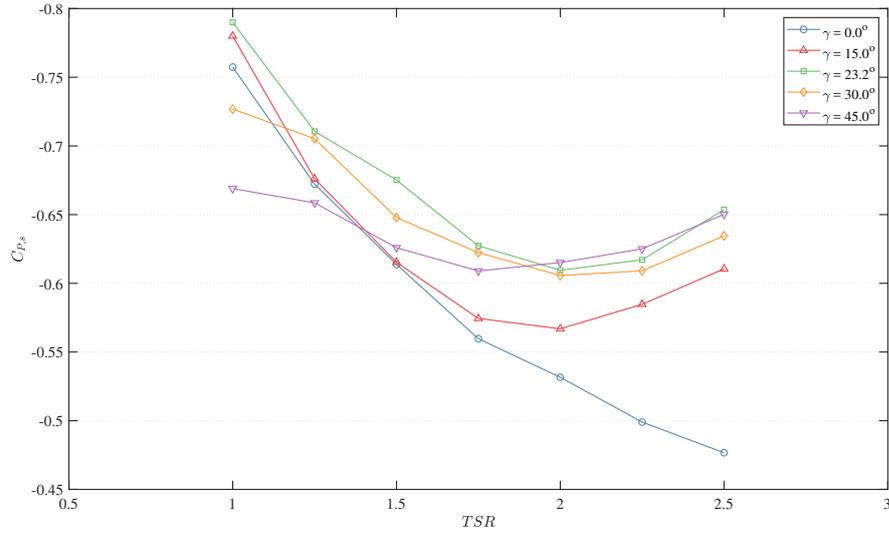


Figure 7.12: Evaluation of the mean static pressure coefficient ($C_{P,s}$) downstream at distinct flow bearings in relation to TSR

7.3.4 Linear Momentum Thrust Coefficient

Linear momentum theory states that the thrust induced upon the rotor by the free-stream is a factor of the static pressure drop and the structure frontal area. For this reason, the annular surfaces, in representation of the open-centre rotor, were utilised in extracting the static pressure by an identical manner as the circular plane. The product of the pressure coefficients and area coefficient, relating the rotor frontal area to the duct frontal area, were attained; the resultant actuator disc thrust outcomes were then compared to the blade-integrated thrust, illustrated in Figure 7.14, attaining good comparison. The actuator disc outcomes were found to underestimate the actual result, where, having utilised the coefficient of determination (R^2), the relation between the two methodologies were 0.942, 0.915, 0.901, 0.862, and -0.770 for the bearings 0.0° , 15.0° , 23.2° , 30.0° , and 45.0° , respectively. The coefficient of determination decreased proportional to the bearing angle, and negating at the highest bearing, largely due to the inapplicability of an area-averaged assumption at large yaws, as dynamic property inconsistencies, such as flow separation regions, are brought about along the rotor area. Corresponding to this outcome, due to the sufficient comparison between the two methodologies, the analysis and premise put forward regarding the variations in

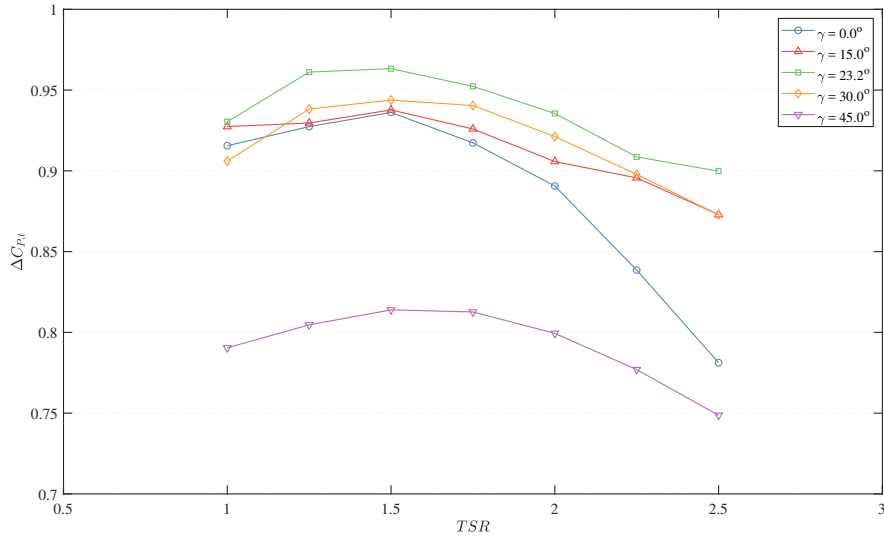


Figure 7.13: Evaluation of the mean total pressure coefficient difference ($\Delta C_{P,t}$) at distinct flow bearings in relation to TSR

pressure and velocity were therefore justified, within the limit of a bearing angle of 30° .

7.4 Lateral Load Coefficient

As the free-stream bearing diverged from the axis of the turbine, normal to the rotor plane, the resultant force acting perpendicular to the rotor axis, establishing a sway force, was evaluated. Illustrated in Figure 7.15, the force coefficient was acknowledged to increase with bearing, as the free-stream velocity vector component perpendicular to the turbine axis increased, hence augmenting the force induced upon the side of the duct. Albeit the vast majority of the force was instigated upon the duct ($\approx 98\%$), a measure of the resultant force was upon the rotor. At aligned flow, negligible lateral forces were present upon the structure, yet as the turbine was set at nominal bearing, to extract most power, a mean force coefficient of ≈ 0.411 was present, hence establishing the requirement for the installed supports to sustain significant lateral loads in addition to the axial loads induced.

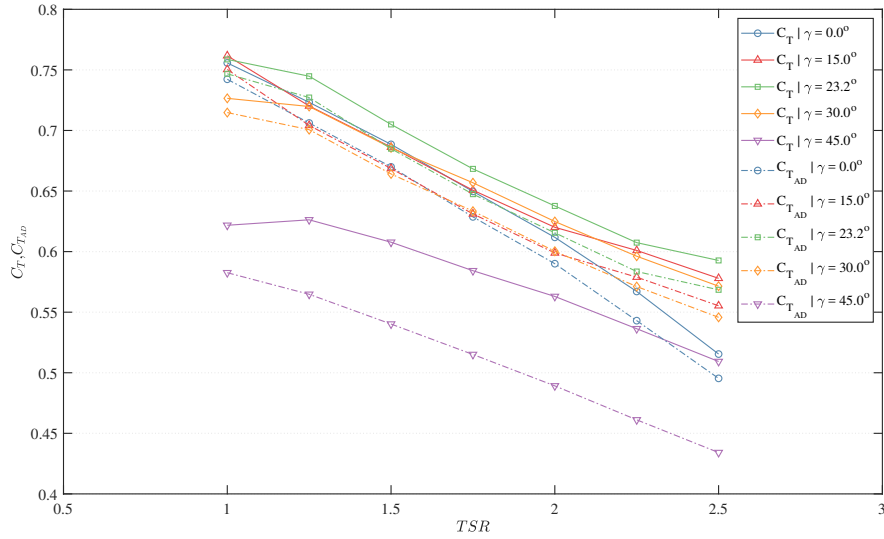


Figure 7.14: Evaluation of the mean blade thrust coefficient (C_T) with the mean linear momentum thrust (C_{TAD}) at distinct flow bearings in relation to TSR

7.5 Static Pressure Coefficient on Duct

In consideration of the geometrical profile of the duct inlet, upon a variation in flow bearing, the resultant angle-of-attack with the shroud may reach the stall limit, inducing flow separation along the inner duct surface, and hence resulting in the production of low-pressure vortices immediately upstream of the rotor. In an effort to establish the effects of an angular flow-stream upon the inlet, the static pressure distribution along the upstream section of the duct was analysed, depicted in Figure 7.16, where the surfaces were discretised by their internal and external positions, in starboard and port directions to the turbine.

Along the internal surfaces, the stagnation point at starboard was acknowledged to shift further into the duct, closer to the rotor, with an increase in yaw angle; the pressure distribution remained largely consistent, increasing immediately upstream of the rotor due to the build-up of fluid. At port, the pressure distribution diminished in accordance to yaw angle due to lesser flow interaction at a normal to the surface. The stagnation point along the inner surface was sustained solely at a yaw of 15° , with that at 23.2° being precisely at the inlet edge. A slight dip in pressure, inducing a degree of suction and a laminar bubble, was present along the inlet contour, which recovered,

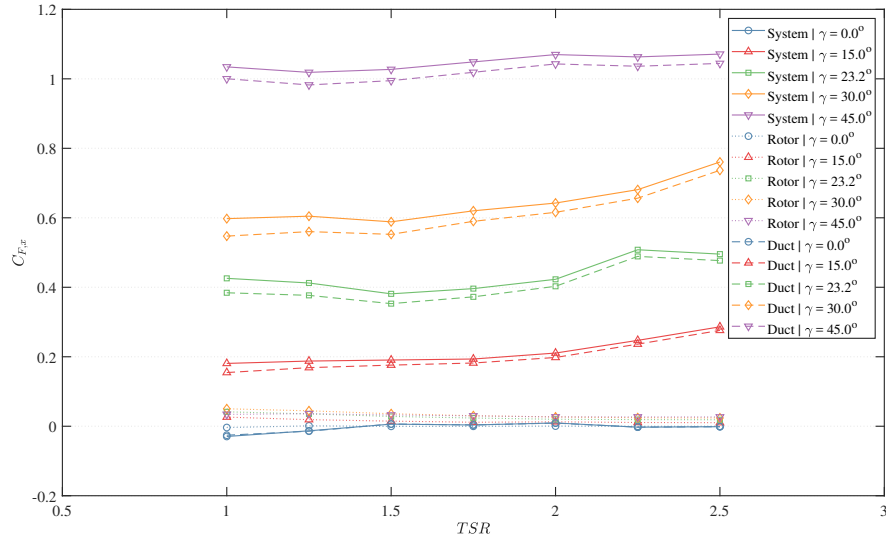


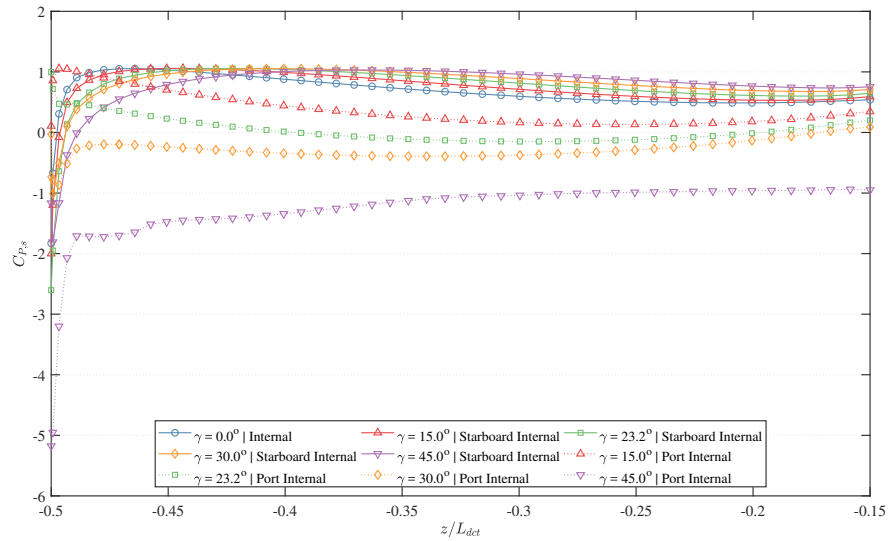
Figure 7.15: Evaluation of the mean lateral load coefficient ($C_{F,x}$) at distinct flow bearings in relation to TSR

increasing in pressure towards the rotor at nominal bearing. A substantial region of low pressure was present at 30° , yet also recovered at the rotor. At 45° , the yaw angle was beyond the stall angle of the duct inlet, resulting in high degrees of flow separation. The suction zone hence did not recover, developing into a re-circulation zone immediately upstream of the rotor, establishing a region of low pressure interacting with the blades at port; this phenomenon induced the sudden dip in torque at an azimuth angle of 90° from top-dead.

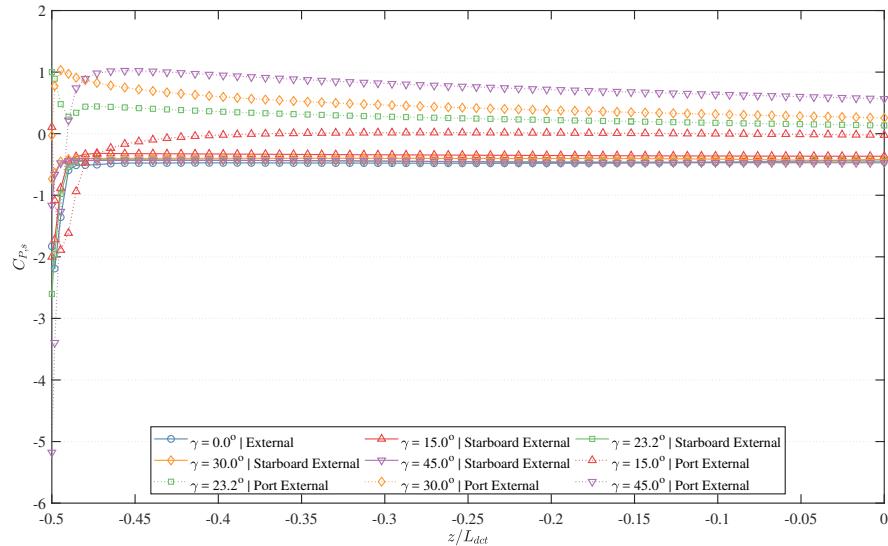
Along the external surfaces, re-circulation zones were formed at starboard, where the pressure sustained was largely consistent with yaw bearing. At port, the pressure distribution increased in accordance to flow bearing, with stagnation points being present at 30° and 45° flows; a slight laminar bubble was formed, yet attained re-attachment at 23.2° . Figure 7.17 puts forward a qualitative illustration of the upstream stream-tube boundaries, acknowledging the points of stagnation flow.

7.6 Wake Profiles

In visualising the velocity flow contours along the wake for the purpose of positioning further turbine installations, a qualitative analysis of the velocity distribution was



(a) Pressure coefficient along the internal duct surfaces



(b) Pressure coefficient along the external duct surfaces

Figure 7.16: Evaluations of static pressure coefficient ($C_{P,s}$) distribution along the duct inlet surfaces

undertaken. Illustrated in Figure 7.18, the wake varied in orientation with an increase in bearing; due to the shift, the duct attained the properties of a blunt body, and generated vortices downstream of the structure. At 15° and 23.2° , two symmetrical re-circulation zones, or Föppl vortices, were produced, with no shedding, yet with an increase in yaw to 30° and 45° , the energy within the static vortices was substantial,

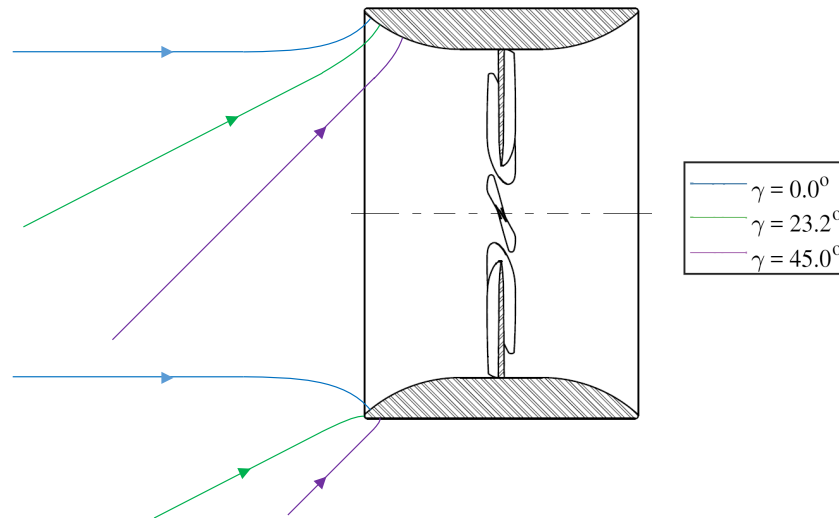


Figure 7.17: Illustrative representation of the upstream stream-tube boundaries at the duct inlet

resulting in large degrees of vortex shedding. Within the confines of a turbine farm, this aspect would hence potentially negatively effect the performance of neighbouring turbines. In addition, at 45° , a minute re-circulation zone was visualised immediately upstream of the rotor, illustrated in Figure 7.19, as elaborated in the quantitative analysis of the pressure distribution along the duct; the relative size, together with its location at the blade extremity rotation trajectory was the causation of the dip in loading.

7.7 Chapter Summary

This study has put forward an investigation into the hydrodynamic performance concerning a ducted, high-solidity tidal turbine in yawed flow utilising blade-resolved, unsteady computational fluid dynamics coupled with the 7-equation τ - ω RSM turbulence model. The research strived to overcome the limitations of prior analyses by acknowledging the explicit physicality of the rotor blades in establishing a coherent representation of the dynamic performance of the turbine in yawed flow. Having acknowledged the variation in the physical outcomes, linear momentum theory was utilised by extracting area-averaged outcomes of axial velocity and static pressure from

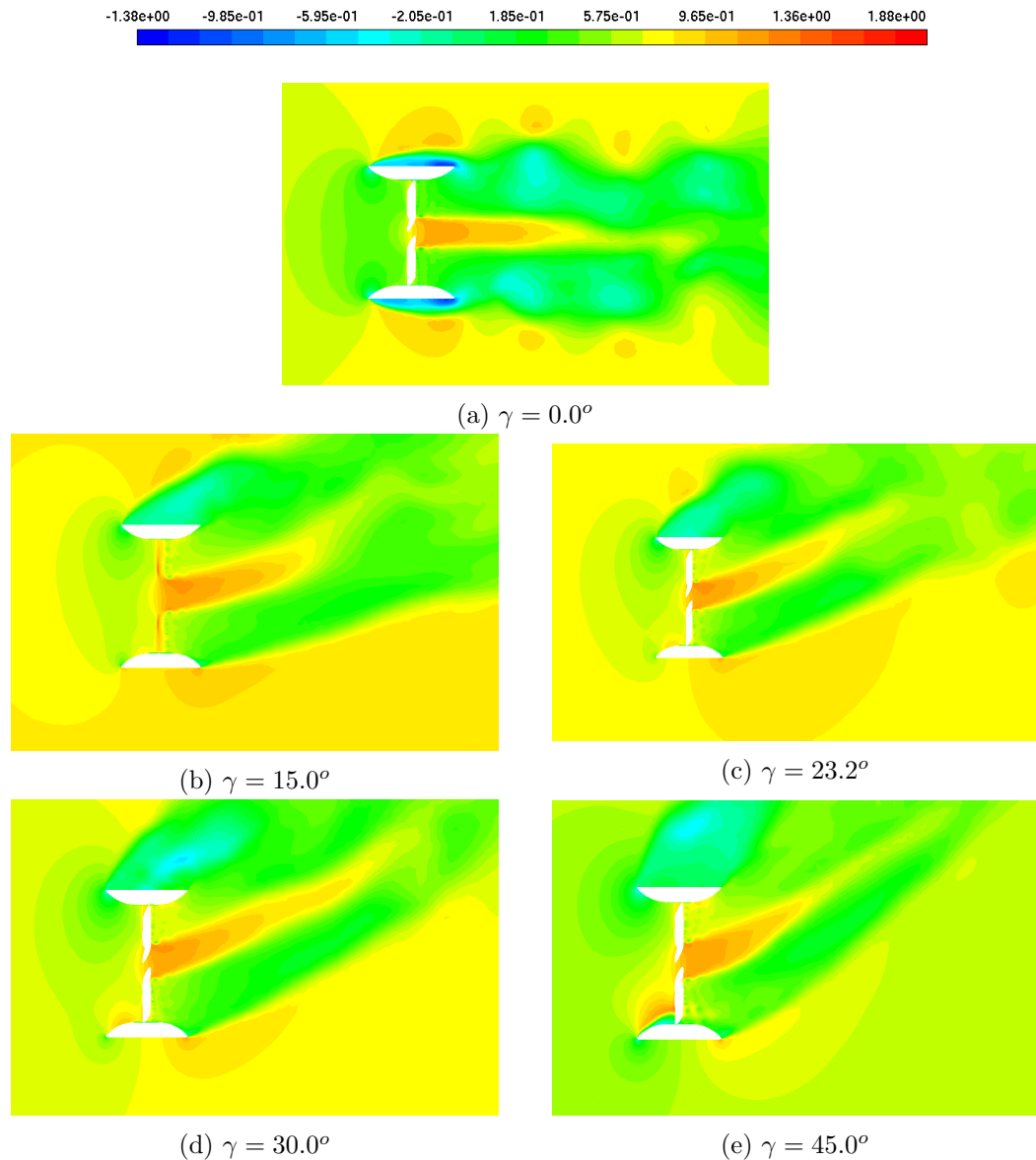


Figure 7.18: Illustrative top-view representation of the axial velocity coefficient ($C_{U,z}$) within the turbine domain at distinct flow bearings

implemented numerical surfaces created fore and aft of the rotor within the CFD model, in an effort to verify the portrayed characteristics.

Through blade-integrated pressure results, the peak power coefficient was found to increase at higher rotational velocities within the $15^\circ - 30^\circ$ angular range. At these conditions, the maximum power coefficient was found to reach a value of 0.35 at a bearing of 23.2° , equivalent to the geometrical gradient of the inner duct curvature,

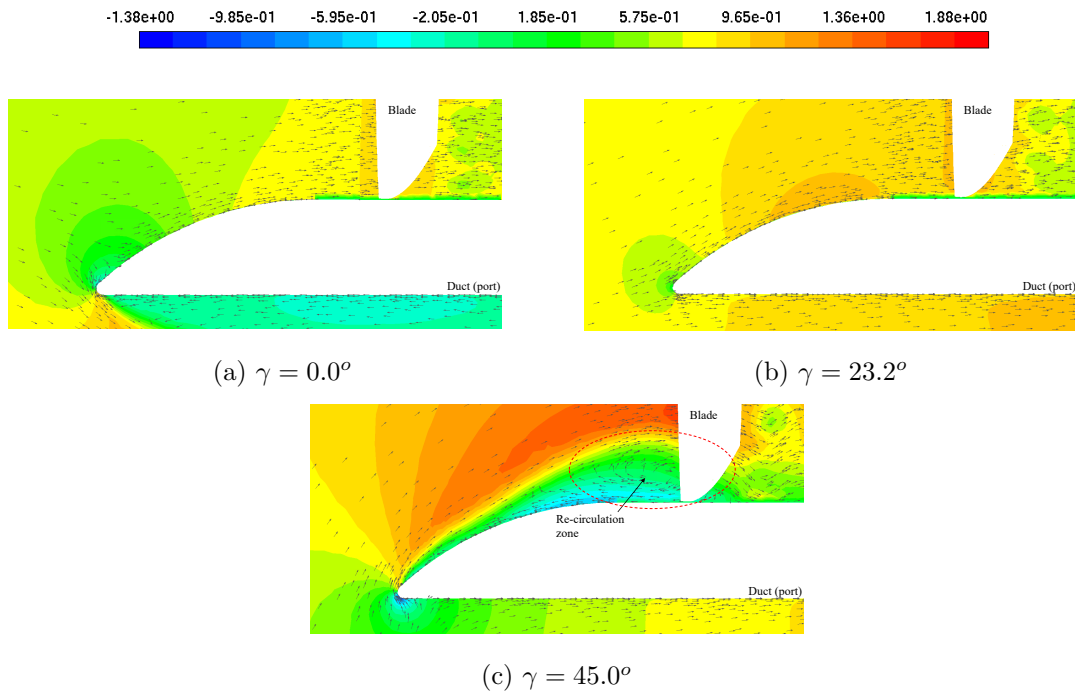


Figure 7.19: Illustrative top-view representation of the axial velocity coefficient ($C_{U,z}$) at port-side duct, focusing on the induced re-circulation zone region

together with a shift in nominal tip-speed ratio to 2.00. Due to this result, the induced torque and thrust were analysed, likewise increasing within the considered parameters due to the additional loading.

For this reason, actuator disc theory was utilised within the analysis to pinpoint the causation of the variation in performance. It was acknowledged that, due to the presence of the duct, the axial velocity was largely sustained through the rotor, with slight deviation at low TSR, yet essential equivalence at high TSR. Further to this, the pressure drop across the rotor increased with an introduction of a bearing, peaking at 23.2° , followed by a decline. The increase was due to the decrease of back-pressure at the outlet of the duct at higher TSRs, as the wake is shifted by the free-stream. The nominal bearing for this occurrence was deemed to be equivalent to the angle of duct inlet profile, as sufficient pressure is sustained upstream, yet simultaneously reduced downstream; post-nominal bearings portray a diminished pressure drop due to flow separation induced upstream of the rotor. As a result, power augmentation was acknowledged to be restricted by the stall limit of the shroud inlet profile.

Having derived the product of the coefficients of static pressure and axial velocity, a substantial correlation was established between the blade-integrated and the area-averaged values of thrust, hence verifying the attained area-averaged results to be applicable. For this reason, it was concluded that, due to the capacity of the turbine to sustain axial velocity, the decrease in pressure downstream of the rotor provided an augmented pressure drop to further improve the performance of a ducted turbine.

Chapter 8

Structural Analysis of Fibre-Reinforced High-Solidity Tidal Turbine Blades in Aligned and Yawed Flow Conditions

In analysing the structural response of the high-solidity tidal turbine rotor, a one-way fluid-structure interaction (FSI) methodology is utilised, undertaking distinct quantitative evaluations: a geometric analysis, attaining the physical properties of the rotor; hydrostatic analysis, evaluating the structural integrity upon non-operational procedures; hydrodynamic fracture analysis, attaining the attributes that lead to catastrophic failure upon operation; material cost analysis, attaining the financial expenditure of the structure; and fatigue analysis, attaining the characteristics that lead to temporal failure.

8.1 Geometric Analysis

Primarily acknowledging the variations in geometric characteristics between the blade designs, three distinct, relative properties were investigated: the moment of in-

Table 8.1: Geometric Properties of the High-Solidity Tidal Turbine Rotor

Blade Property	Solid Design	Cored Design	Reinforced Design
Moment of Inertia (kg.m^2)	4.587×10^5	2.422×10^5	3.640×10^5
Specific Mass (kg.m^{-3})	1850	982	1472
Specific Gravity	1.853	0.984	1.475

ertia, specific mass, and specific gravity of the high-solidity blades. By means of the analysis, the solid blade was found to attain the highest values in all parameters, as specified in Table 8.1; the rotor is hence the heaviest, and requires the highest degree of torque to induce a unit rotational acceleration. In contrast, the cored blade is the lightest as half of the dense GFRP volume is substituted for a light Corecell material; the specific gravity is, however, lighter than the domain fluid, which may present detrimental aspects in installation and maintenance scenarios, in addition to sustaining rotational momentum. The reinforced design, consisting of two GFRP materials for the shell and webs, whilst flooded with water, presented an intermediate value between the two prior designs.

8.2 Hydrostatic Analysis

Solely implementing hydrostatic pressure along the surfaces of the blade in simulation of the subsea depth, the suitability of the structures was acknowledged throughout non-operational procedures, such as installation and maintenance processes. By means of the analysis, all blade designs were found to successfully sustain their structural integrity; the solid and reinforced blade sustained no structural deviation whatsoever, whereas the cored blade was succumb to very minute yielding, due to the malleable foam-core, which induced a region of low strain at the root, as illustrated in Figure 8.1.

8.3 Hydrodynamic Fracture Analysis

Concerning the conditions leading to fracture along the fibre-composite blade structure upon operation, the blade deflection, normal elastic strain, equivalent elastic strain,

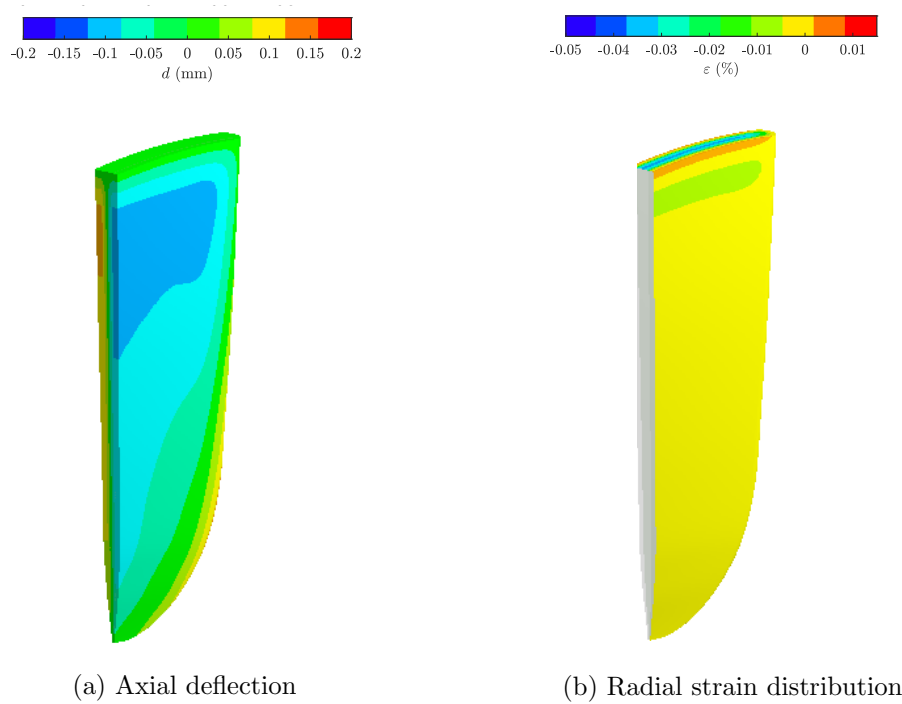


Figure 8.1: Structural response cross-section of the cored blade design under hydrostatic load

and shear elastic strain at the blade root were investigated.

8.3.1 Blade Deflection

Primarily analysing the blade deflection in the axial direction relative to the rotor axis, its correlation to the free-stream magnitude and turbine rotational velocity, for all three blade designs, was investigated. Albeit the deflection magnitudes varied dependent on the blade structure, the correlation factor of the deflections with flow properties was found to be independent, attaining a quadratic and quasi-linear quadratic proportion, respectively, as a result of the induced thrust force discussed in prior chapters; no explicit correlation was established with flow bearing.

By comparing the three blade designs, the solid blade was found to attain the least mean deflection, as illustrated in Figure 8.2, with the cored blade attaining the highest, albeit minutely, due to the implementation of the foam core, which constitutes 50% of the blade volume, diminishing the global Young's modulus, and hence, rigidity;

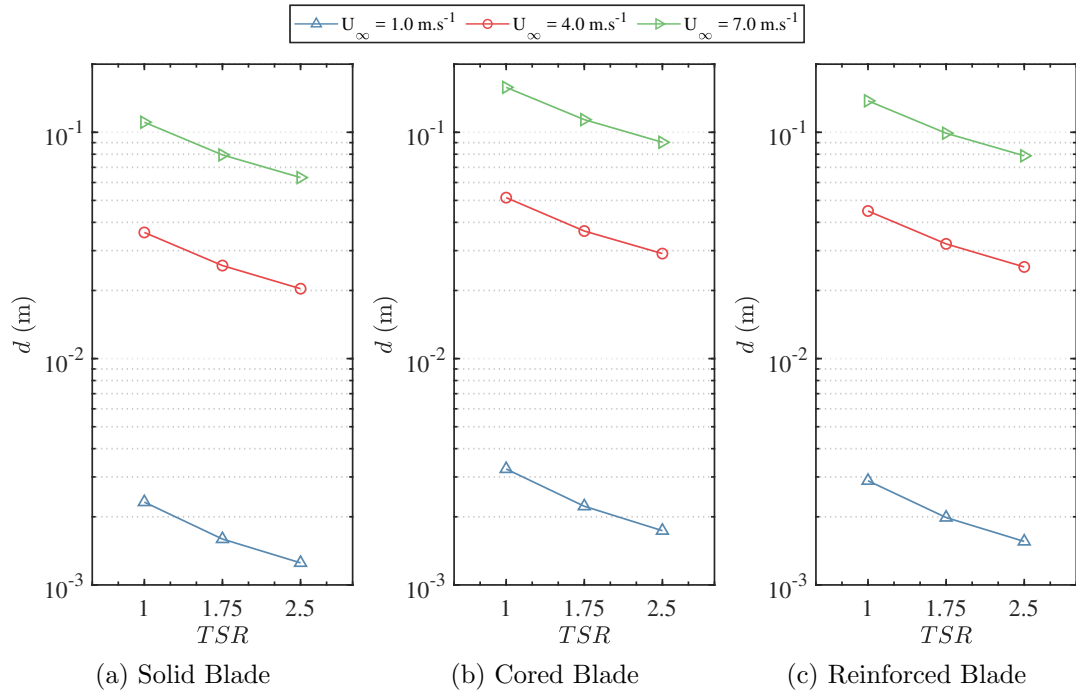


Figure 8.2: Axial deflection of the distinct blade designs within aligned flow conditions

the reinforced blade attains a mean deflection intermediate to the two supplementary designs. Albeit the outcomes, the axial deflection was acknowledged to be relatively insubstantial for all three designs, with a maximum deflection equivalent to $\approx 4\%$ of the blade length and a linear deflection angle of $\approx 2.4^\circ$; this minute deflection came about as the blade had been constrained at its tip, where the higher dynamics are induced, rather than at the hub. When comparing aligned flow deflections to those under yawed flow conditions, illustrated in Figure 8.3, the deflections of the blade at higher TSRs were more substantial under the latter condition, analogous to the variation in thrust when succumb to the hydrodynamic flow.

The behaviour of the deflection along the entire blade profile was investigated, attaining its maximum value at the trailing edge towards the rotor hub, as illustrated in Figure 8.5; the highest deflection was induced away from the hub extremity as a result of the comparatively high pitch in the cross-sectional profile of the blade at this location, inducing significant torsion upon the structure. Further to this, inspecting the deflection as a one-dimensional beam displacement down the mid-plane section of

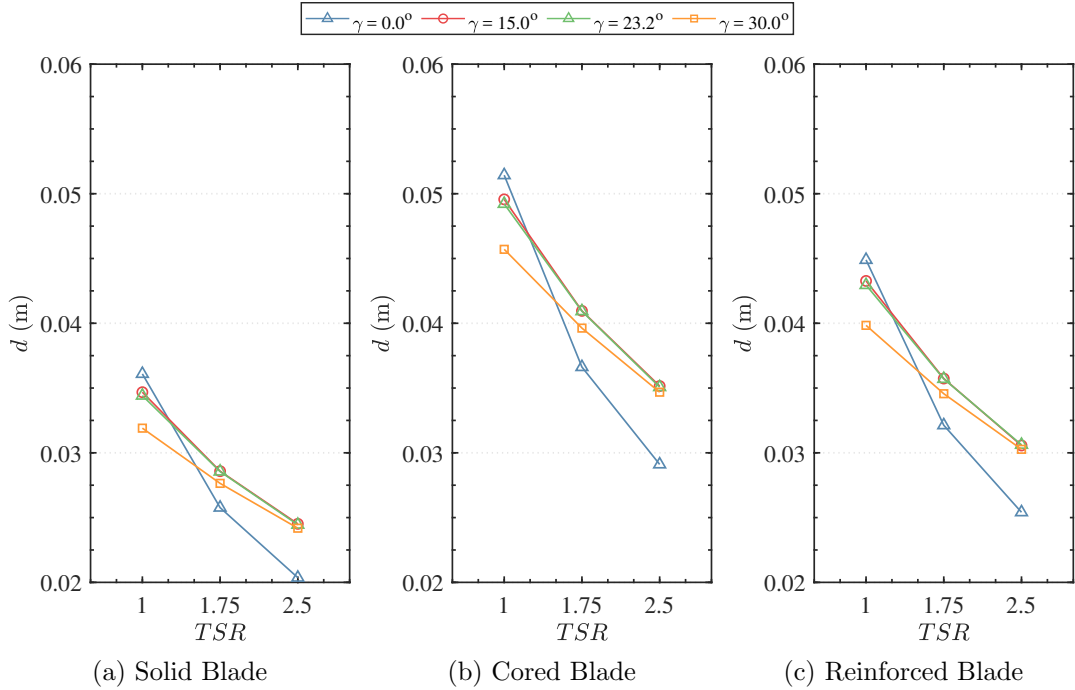


Figure 8.3: Axial deflection of the distinct blade designs within yawed flow conditions

the blade, depicted in Appendix F Figure F.1, the theoretical response of a cantilever beam was replicated, reflecting the first mode of vibration.

To acknowledge the proportion of the axial deflection upon the full physical response, the three-dimensional global deflection of the blades was acquired, illustrated in Figure 8.4. On average, for both aligned and yawed flow conditions, the axial deflection was found to be $\approx 94\%$ of the total deflection, hence acknowledging the majority of the dynamics induced to be acting within the axial direction of the rotor.

8.3.2 Normal Elastic Strain

In establishing the structural responses, the orientation of the strain distributions were acknowledged within a cylindrical coordinate system.

8.3.2.1 Radial Strain

Primarily identifying the radial response, hence acknowledging the strains acting in a direction parallel to the blade position upon rotation, illustrated in Figure 8.6, the

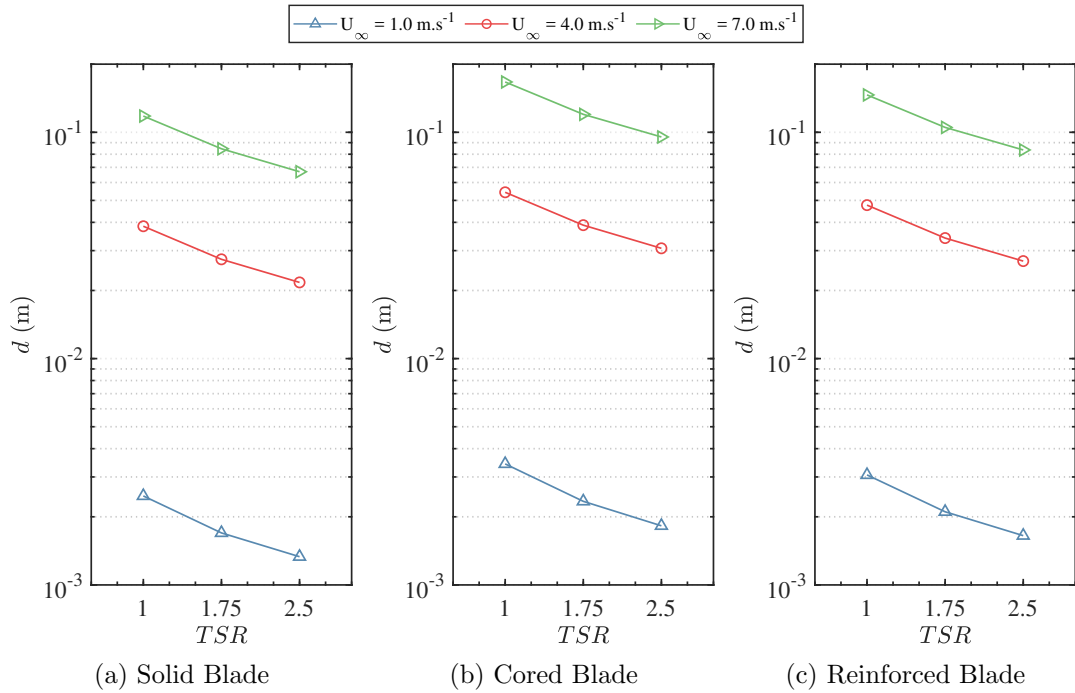


Figure 8.4: Global deflection of the distinct blade designs within aligned flow conditions

lowest values of radial strain were attained by the solid blade structure, whereas the highest values were displayed by the cored blade, due to the comparably lesser rigidity, with an intermediate value by the reinforced blade. The maximum radial strain along the blade was found to diminish with rotational velocity, whilst increasing with free-stream velocity, identical to the thrust induced upon the blade. The cored blade response at low free-stream conditions was acknowledged to be distinct from the supplementary two blade designs as a result of the strain induced by the hydrostatic pressure. In addition, the strain induced at yawed flow conditions was attained, specifying the maximum response at nominal and high rotational velocities to occur at nominal flow bearing ($\gamma = 23.2^\circ$), as depicted in Figure 8.7.

Albeit the strain, the maximum tensile value at extreme free-stream conditions and low rotational velocity upon the cored blade was solely 22.1% of the DB GFRP yield strength, hence not exceeding its ultimate strain-to-failure value; operation at the specified conditions is, therefore, inconsequential to the structural integrity of the

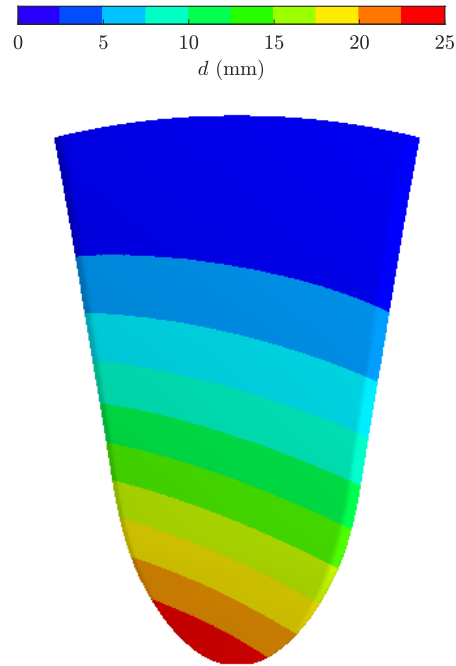


Figure 8.5: Axial deflection distribution along the ‘solid’ blade structural design at nominal flow (4 m.s^{-1}) and nominal rotational velocity (TSR 1.75)

rotor, and within the limits of reliable operation. Nonetheless, to ascertain its structural integrity, the maximum strain experienced by the blade should be significantly lower than its ultimate strain value; in recognition, an engineering safety factor of 2 was implemented, increasing the normal strain to 44.2% of the permissible strain.

Furthermore, in recognising the radial strain distribution along the surfaces of the three blade designs, illustrative representations of the structures at nominal free-stream and nominal rotational velocity, depicted in Figure 8.8, were attained. By means of the analysis, two concentrations of strain, in tension and compression, were acknowledged to be present towards the leading edge, at the root, of the high-solidity blade for all three structural designs in both aligned and yawed flows. Consequent to the presence of the strain localisation, if a structural defect were to therefore transpire, such as a crack, propagation of that defect may ensue, resulting in the structural failure of the high-solidity blade. This concentration was brought about due to the simultaneous bending and torsion instigated by the fluid-structure interaction upon the wide blade.

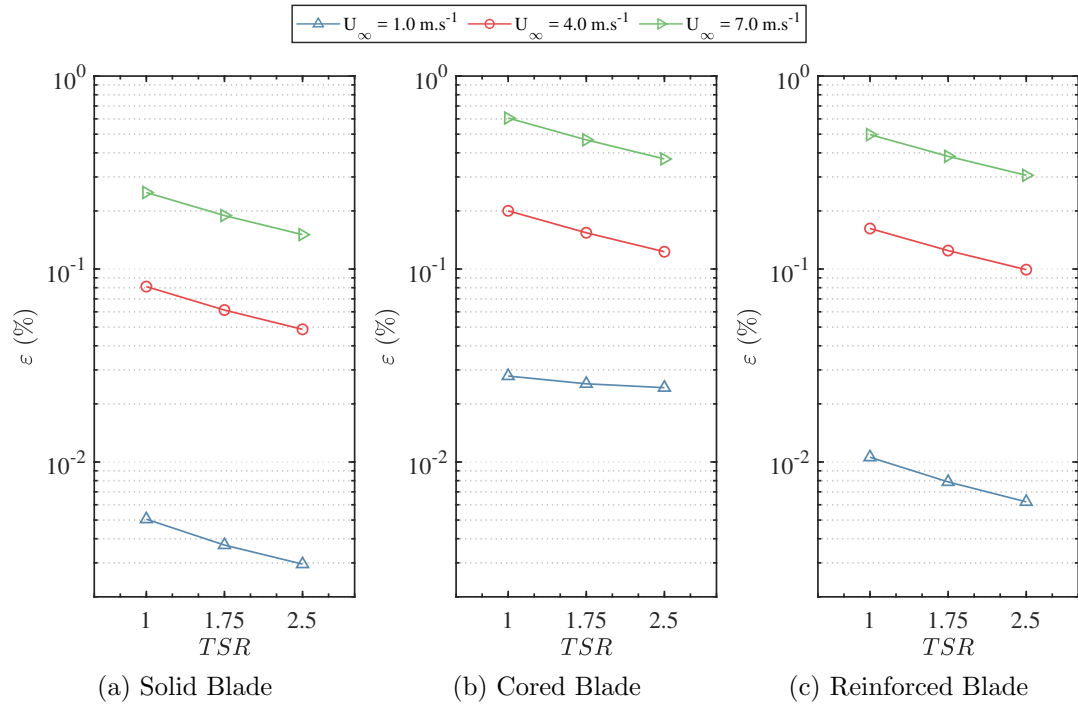


Figure 8.6: Mean values of the maximum normal radial strain of the distinct blade designs within aligned flow conditions

Additionally, the surface strain distribution of the three blades are distinct in relation to the internal layout. The solid blade attained a comparatively large concentration zone, which dissipated evenly throughout the structure. The cored blade sustained higher strain along the root of the rotor, due to the hydrostatic effect, inducing a minute concentration zone. The reinforced blade permitted global strain reduction, yet induced local strain increases at the locations of the reinforcement webs.

8.3.2.2 Tangential & Axial Strain

In identifying the response acting in a direction perpendicular to the blade position upon rotation, illustrated in Figure 8.9, the values of tangential strain were found to be, on average, a magnitude of 3 for solid blades, and a magnitude of 15 for cored and reinforced blades, lower than the radial strains. The lowest values of tangential strain were attained by the reinforced blade structure, whereas the highest values were displayed by the solid blade; due to the orthotropic material consistency, both in relation

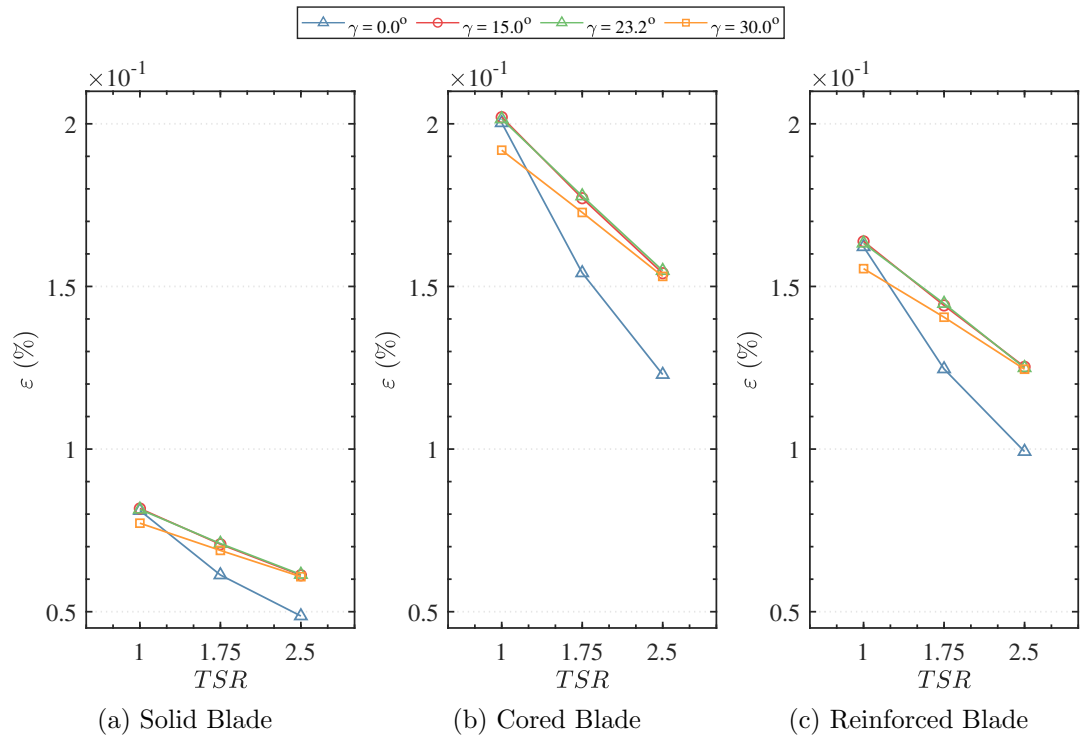


Figure 8.7: Mean values of the maximum normal radial strain of the distinct blade designs within yawed flow conditions

to properties and layout of the blade setup, its higher rigidity permitted diminished stress dissipation in comparison to the variant designs. Similarly to the proportion of hydrodynamic thrust induced upon the blade, the tangential strain along the blade was found to diminish with rotational velocity, whilst increasing with free-stream velocity.

In identifying the response acting in a direction parallel to the rotor axis, illustrated in Figure 8.10, the values of axial strains were found to be, on average, a magnitude of 3, for solid blades, and 13, for cored and reinforced blades, lower than the radial strains. The variations in structural outcomes display similarities with those of tangential strain.

8.3.3 Equivalent Elastic Strain

As acknowledged in prior sections, the structural response of the high-solidity rotor pertained multi-directional strain states, and, as a result, multiple strain components will act upon the blade material during operation. For this reason, the von Mises equivalent elastic strain was acquired from the finite-element analysis to recognise a

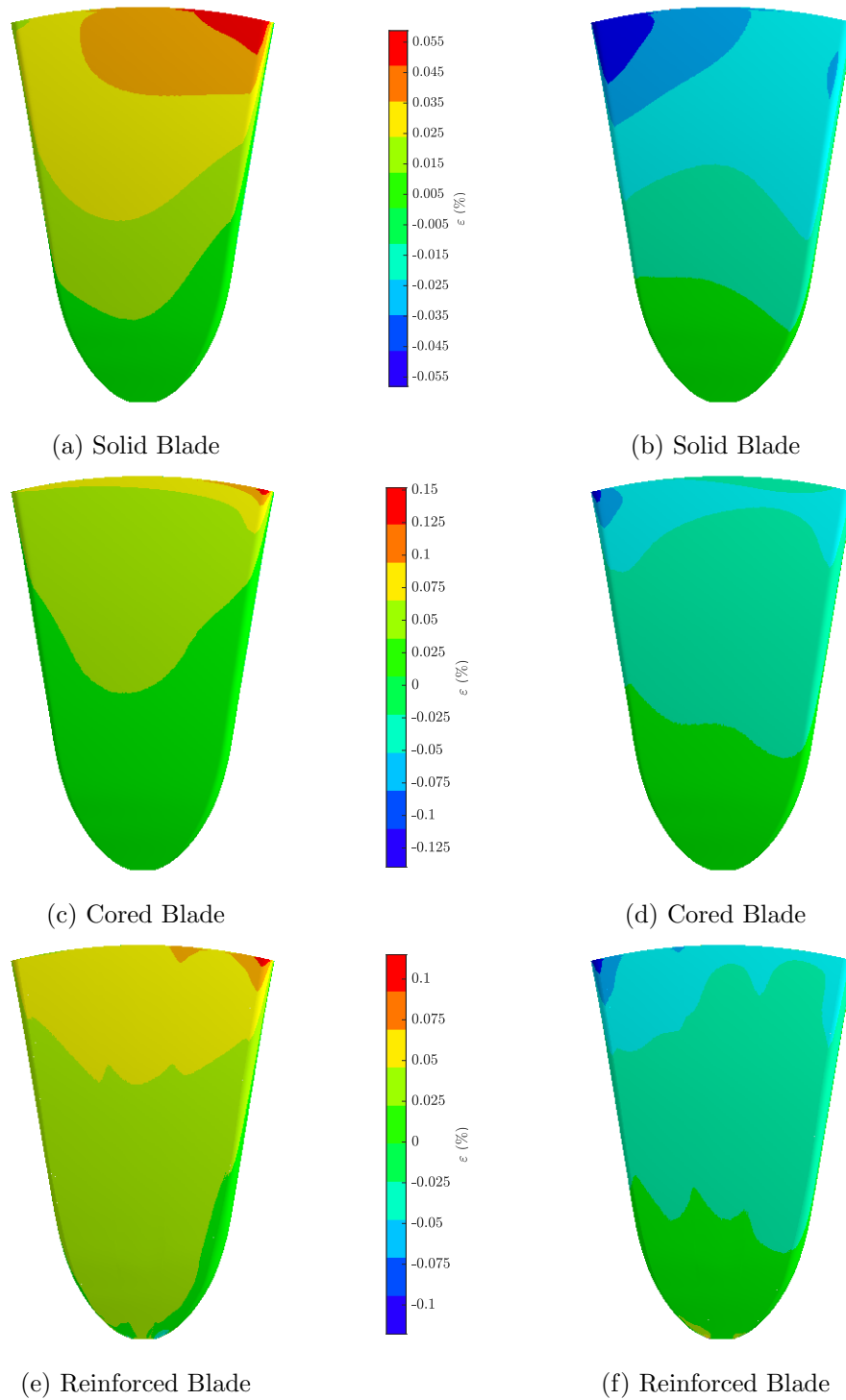


Figure 8.8: Radial strain distribution along the blade structural designs at nominal flow (4 m.s^{-1}) and nominal rotational velocity (TSR 1.75)

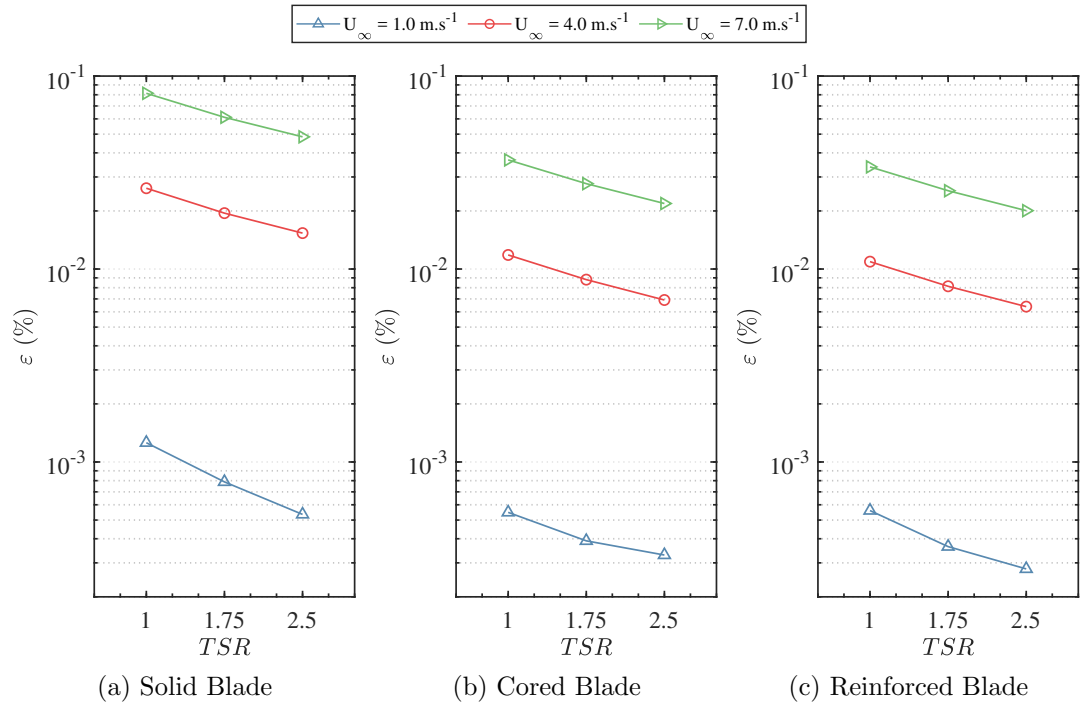


Figure 8.9: Mean values of the maximum normal tangential strain of the distinct blade designs within aligned flow conditions

strain component that depicts a scalar equivalence of the strain tensor.

Identical to the radial strain analysis, the lowest values of equivalent strain were attained by the solid blade structure, whereas the highest values were displayed by the cored blade due to decreased rigidity, with the reinforced design attaining an intermediate response, as illustrated in Figure 8.11. As a result of the degree of strain, the maximum tensile value at extreme free-stream conditions and low rotational velocity, upon the cored blade, increases to 33.9% of the DB GFRP yield strength, hence not exceeding its ultimate strain-to-failure value; operation at the specified conditions is, therefore, inconsequential to the structural integrity of the rotor, and within the limits of reliable operation. To ascertain its structural integrity, an engineering safety factor of 2 was implemented, increasing the normal strain to 67.8% of the permissible strain. In addition, the equivalent strain distribution along the surfaces of the three blade designs was largely identical to that of the radial strain.

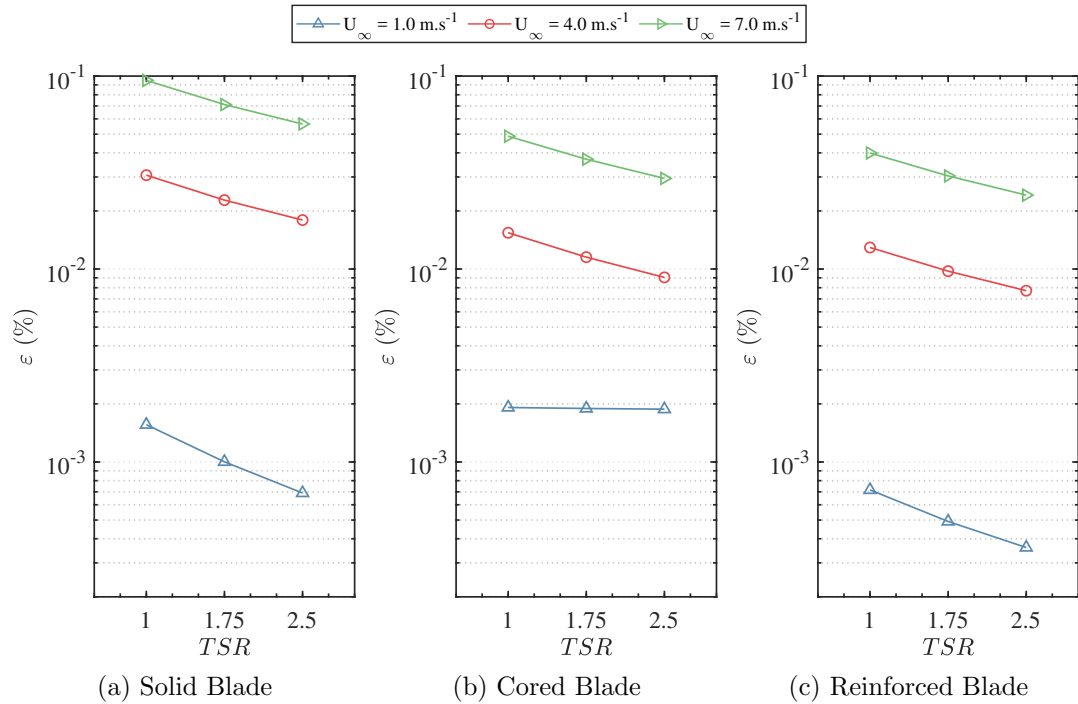


Figure 8.10: Mean values of the maximum normal axial strain of the distinct blade designs within aligned flow conditions

8.3.4 Shear Elastic Strain

As the design of the ducted tidal turbine consisted of rotor blades sharply extruding from the duct housing at the tip of the structure, where the dynamics are highest, the mean induced shear strain at the interfacing plane between the blade and the duct, hence at the root, was investigated. Illustrated in Figure 8.12, the value of the shear response was found to be equivalent in magnitude to the radial and equivalent strain, largely due to the strain concentrations being present within the vicinity of the blade root; the relationship with free-stream magnitude and rotational velocity was also equivalent. The shear distribution along the root plane at mean aligned velocity and nominal rotational velocity was investigated for the three blade designs, illustrated in Figure 8.13. As both torsion and bending motions were known to be induced, the strain concentrations along the plane were acknowledged. Along the three blade profiles, four particular concentration zones were developed at the rounded vertices of the plane; it was therefore established that the strain due to the induced torsion was

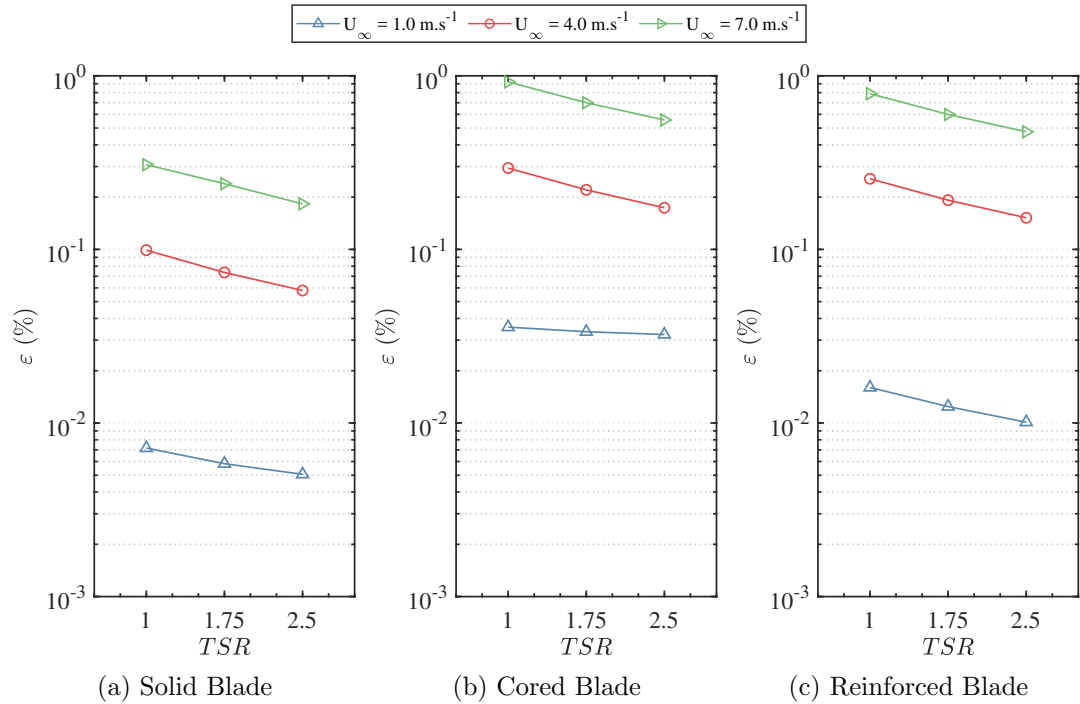


Figure 8.11: Von Mises analysis of the distinct blade designs within aligned flow conditions

more substantial than that induced by bending, as the strains were concentrated, not spread along the edges of the blade, hence identifying the blade profile susceptibility to a torque by the fluid-structure interaction.

8.4 Material Cost Analysis

In result of the outcomes attained via the prior investigations, the structural integrity of the three internal blade designs proposed was found to be largely sustained within the analysed conditions. To establish a distinction between the designs, a material cost analysis was put forward, acknowledging the most cost-effective composition, in exclusion of the costs of manufacturing and fabrication.

Implementing material costs for the uni-directional fibre sheet, bi-directional fibre sheet, epoxy resin, and structural foam materials from literature [150], whilst attaining the volume of the blade components from the established structural model, the most

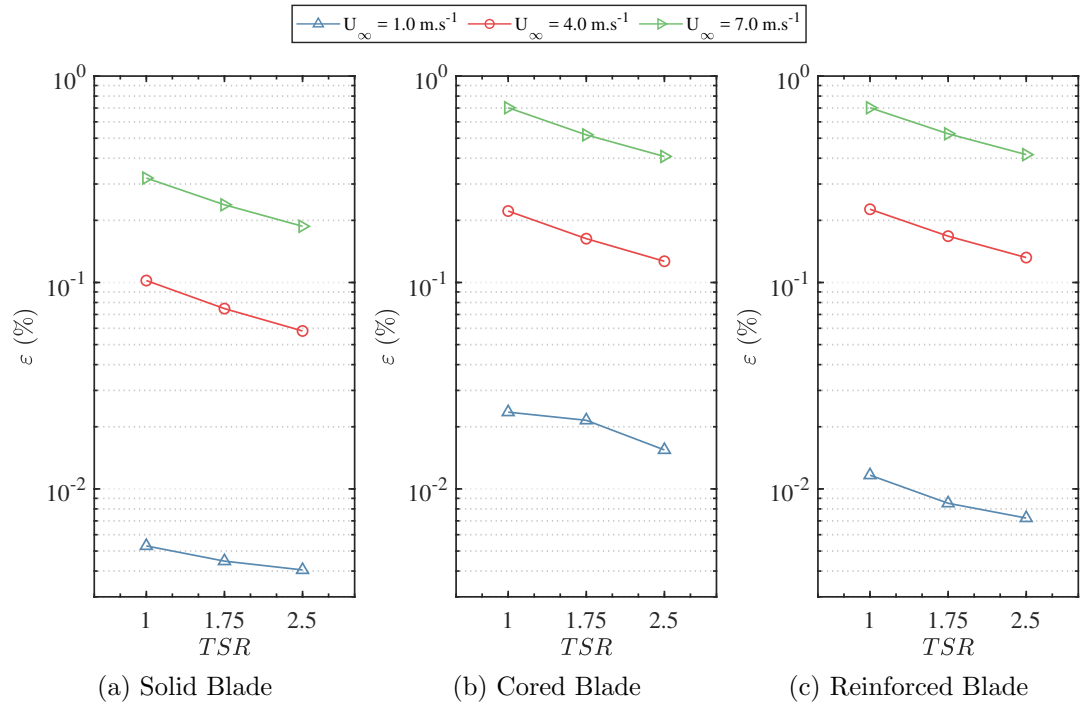


Figure 8.12: Shear strain of the distinct blade designs within aligned flow conditions

cost-effective arrangement, in terms of materials implemented, was found to be the reinforced design, being $\approx 50\%$ and $\approx 6.5\%$ cheaper than the solid and cored blades, respectively; the ratio of filler-to-matrix materials within the GFRPs was acquired by relating the densities of the matrix [151] and e-glass to the global density of the fibreglass material. The final costing estimations of the blade materials, for the entire rotor, are depicted in Table 8.2, with further details in Appendix F.

Table 8.2: Total Material Costs (rounded to the nearest thousand) for the High-Solidity Tidal Turbine Rotor Designs

Blade Structure	Solid Design	Cored Design	Reinforced Design
Cost (\$)	596,000	321,000	300,000

Chapter 8. Structural Analysis of Fibre-Reinforced High-Solidity Tidal Turbine Blades in Aligned and Yawed Flow Conditions

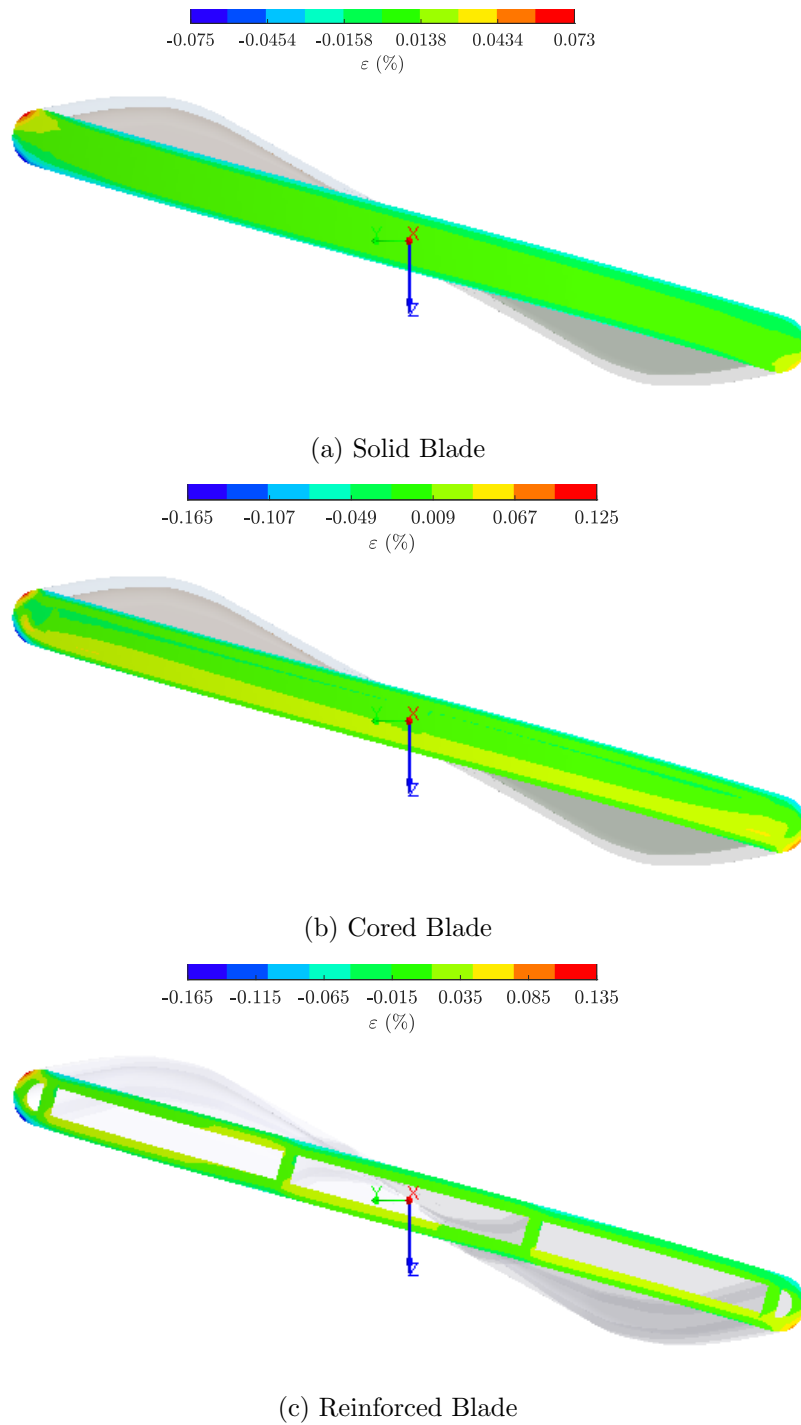


Figure 8.13: Shear strain distribution at the blade root at nominal flow (4 m.s^{-1}) and nominal rotational velocity (TSR 1.75)

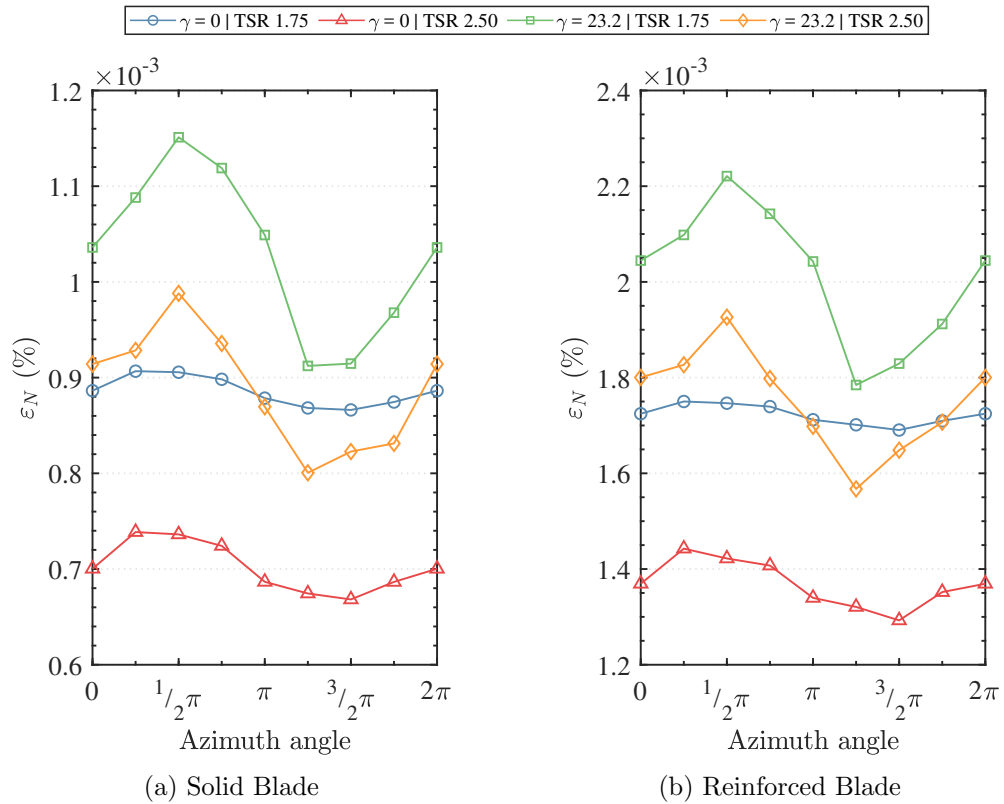


Figure 8.14: Cyclic representation of maximum equivalent strain of the distinct blade designs within aligned and yawed flow conditions

8.5 Fatigue Analysis

8.5.1 Principal Elastic Strain

In establishing the characteristics that lead to temporal failure as a result of fatigue due to crack propagation, the maximum principal strain along the blade was investigated. Analysed at the considered positions within the rotational operation at nominal free-stream magnitude (4 m.s^{-1}) within aligned (0°) and nominal bearing (23.2°) at nominal and high rotational velocities, the mean response at every 45° angle of motion was attained. By means of the investigation, a cyclic response was established, as illustrated in Figure 8.14, giving evidence of the likelihood of failure by fatigue.

8.5.2 Strain-Life Analysis

As a cyclic load was recognised to be induced within a period along the rotational motion of the power-generating operation, an investigation into the fatigue performance of the fibre-composite rotor blade was carried out. Due to the prior structural evaluation being contrived by strain analyses, the strain-life ($\varepsilon_E - N$) methodology was implemented in analysing the system whilst succumb to high-cycle fatigue to establish the fatigue response of the ducted turbine rotor within a 10- to 25-year design-life.

In accordance to the pursued technique, however, a major detriment was identified; the strain-life approximation requires specifications related to the failure properties of the material utilised, namely the fatigue strength exponent (or Basquin's exponent) (b) and fatigue strength parameter (σ'_f), to acquire the strain fluctuation that induces failure by fatigue within a number of cycles. These two values are typically established by means of experimentation in relation to destructive testing, which were not known for the adopted composite material. In this regard, as the supplementary terms within the strain-life equation were successfully acquired throughout the prior investigations, the methodology was therefore utilised to establish a definitive range that the material properties should fall within to avoid failure by fatigue. The equation was satisfied by implementing the mean variation in principal elastic strain per cycle ($\Delta\varepsilon_E$), acquired via the finite-element analysis, with the Young's modulus (E) adopted from literature, where the number of cycles to failure (N) was assumed to vary between 10 to 25 years of constant operation.

Primarily investigating the fatigue response of the reinforced design when succumb to aligned and nominal-yawed flow conditions at nominal and high rotational velocities, the fatigue strength exponent was computed in relation to a range of fatigue strength parameter values acquired through literature [152–154]. By means of the range comparison, illustrated in Figure 8.15, the maximum fatigue strength exponent was acknowledged to occur at nominal rotational velocities within nominal free-stream bearings.

Further to this analysis, an investigation into the fatigue response of the solid blades, illustrated in Figure 8.16, was undertaken due to its higher stiffness. As the solid struc-

Chapter 8. Structural Analysis of Fibre-Reinforced High-Solidity Tidal Turbine Blades in Aligned and Yawed Flow Conditions

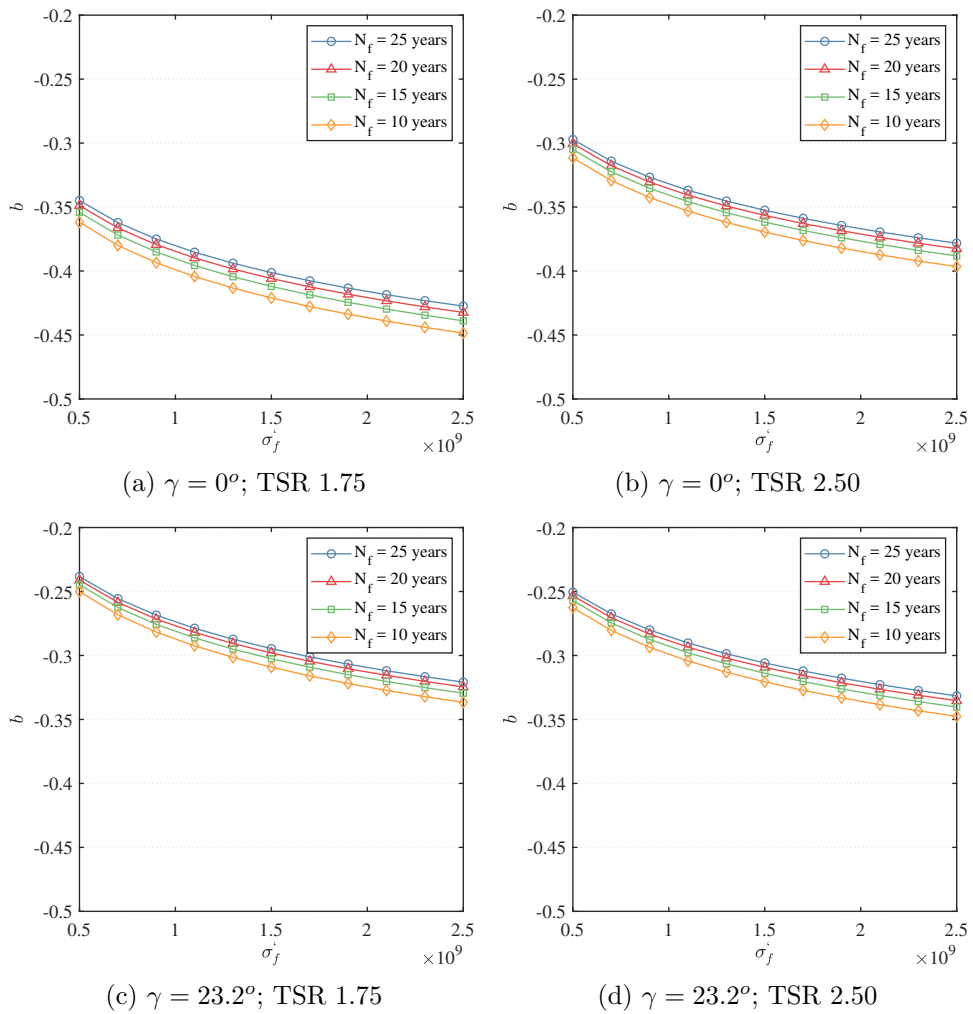


Figure 8.15: Fatigue response of a ‘reinforced’ high-solidity tidal turbine rotor blade

ture was deduced to be more rigid than the reinforced design, the response throughout the analyses was found to be lower than that attained by the reinforced design, with the maximum fatigue strength exponent also occurring at nominal rotational velocities within nominal free-stream bearings. In addition, material properties acknowledged for both designs were quasi-equivalent at nominal and high rotational velocity. Therefore, albeit a diminished degree of force is induced upon the blades at the latter condition, the load cycles are more frequent than the prior, hence equally contributing to the fatigue response.

In recognition of the fatigue analyses, the variation in the fatigue strength exponent

Chapter 8. Structural Analysis of Fibre-Reinforced High-Solidity Tidal Turbine Blades in Aligned and Yawed Flow Conditions

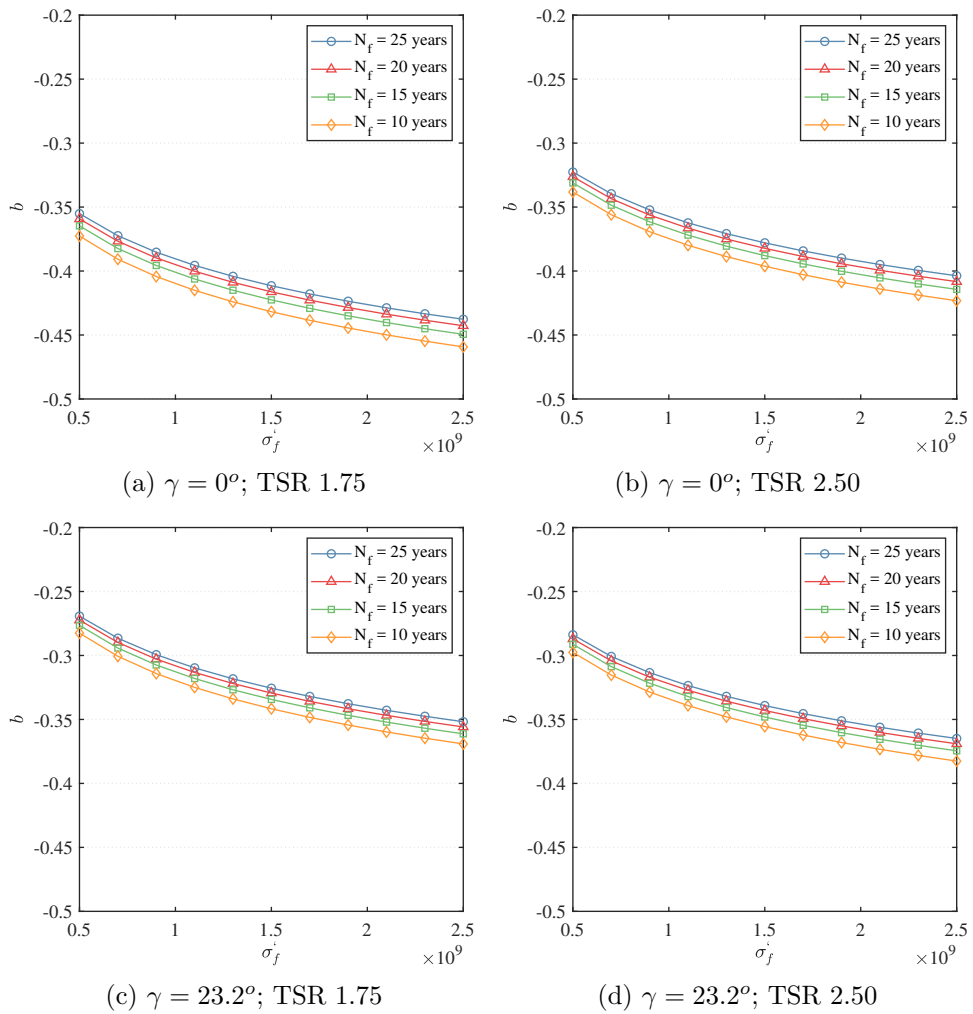


Figure 8.16: Fatigue response of a 'solid' high-solidity tidal turbine rotor blade

within the investigations, by considering the solid and reinforced blade designs, through a 25-year design life within nominal and aligned flow bearings at nominal and high rotational velocities, ranged from -0.24 to -0.46. In accordance, under the assumption that the structural response is consistent, the shell section of the high-solidity tidal turbine blade was deemed to be appropriate in application for double-biased glass-fibre reinforced composites with a fatigue strength exponent to fatigue strength parameter property correlation higher than the range specified in Figure F.3b. In consideration that a fatigue strength exponent of -0.119 had been attained at a fatigue strength parameter of 557 MPa for a GFRP [152], the modelled outcomes were acknowledged

to fall within a rational arrangement.

8.6 Evaluation of the Structural Designs

In consideration of the structural outcomes derived, the geometrical properties of the three rotor designs were primarily established; the moment of inertia of the cored and reinforced blade were found to constitute 53.1% and 79.6% that of the solid blade, respectively, with comparable values established for specific mass and specific density. The favourable structural design, solely through this analysis, was therefore the cored design due to its diminished weight, which facilitates the rotational acceleration of the blades at operational start-up.

Subsequently, hydrostatic analysis was implemented to prove the structural integrity of all three blades at the installation water depth; all designs were acknowledged to be appropriate, with slight yielding apparent, albeit negligible, upon the cored design. In continuation, hydrodynamic analysis from the computational fluid dynamic models was undertaken, where, via the attained normal strain response, the highest response was induced by the cored design, hence portraying least rigidity, and the solid blade attaining the least response, with the reinforced blade providing an intermediate value. The investigated conditions were found to not exceed the ultimate strain value of the double-biased glass-fibre reinforced polymer for all blade designs, and, hence, was within the limits of reliable operation. A notable outcome, however, was the concentration of strain present at the leading edge of the rotor blades, within the immediate vicinity of the root, occurring upon all three structural blade designs, in both aligned and yawed flows. Due to these outcomes, all three designs were deemed to be largely equivalent in sustaining structural integrity at the operational conditions.

Ancillary to the fracture analysis, a blade material cost analysis was undertaken to establish an estimation on the most cost-effective assortment of component materials implemented within the three blade designs. By means of this financial elaboration, the reinforced blade was established to be the least costly, with the solid blade attaining the highest expenditure.

Through the prior analyses, the reinforced blade design was identified to be the logical arrangement to adopt as a result of its adequate geometric properties, resistance against hydrodynamic yield, and low cost. In culmination, a fatigue analysis was undertaken to acknowledge an appropriate range of GFRP fatigue properties in its implementation within the considered conditions. Solely comparing the reinforced and solid blade designs, the values attained were found to be largely equivalent. Therefore, as a result of the responses attained and elaborated, the reinforced internal blade structure was considered to procure a favourable combination of high rigidity and comparatively lower weight, in addition to comparably lower material costs, deeming it to be the more efficacious design. Albeit the outcome, further investigations are required to pursue a more appropriate design, specifically in establishing the optimised shell and webbing thickness, for the operational conditions analysed.

8.7 Chapter Summary

Within this chapter the structural response of the high-solidity tidal turbine rotor was analysed, by means of a one-way, partition-approach fluid-structure interaction (FSI) methodology, undertaking distinct quantitative evaluations: a geometric analysis, attaining the physical properties of the rotor; hydrostatic analysis, evaluating the structural integrity upon non-operational procedures; hydrodynamic fracture analysis, attaining the attributes that lead to catastrophic failure upon operation; material cost analysis, attaining the financial expenditure of the structure; and fatigue analysis, attaining the characteristics that lead to temporal failure. In culmination, a selection of the most efficacious design, in relation to the quantitative analyses, was established.

Chapter 9

Turbulence Modelling for a Ducted High-Solidity Tidal Turbine

In recognition of the complex fluid dynamic phenomena induced within the ducted tidal turbine domain, this chapter puts forward an evaluation of the implementation of distinct turbulence models coupled to the momentum continuity equation. Carried out in an effort to acquire the most accurate simulation representation of the physics of rotating bladed structures within the Reynolds Averaged Navier-Stokes approach, the ducted turbine was analysed utilising distinct ‘specific dissipation rate’ (ω) turbulence models most utilised in literature. By distinguishing the performance outcomes, an evaluation of the most effective numerical Reynolds stress terminology-variation is established between: the Menter assumption (BSL τ - ω), the Wilcox assumption (STD τ - ω), or the Boussinesq-Menter assumption (SST k - ω). Through the most accurate scheme arrangement, the linear momentum equations for highly-loaded conditions are then solved to put forward a numerical calibration effort for analytical models.

9.1 Blade-Resolved CFD Analysis

Albeit the three related turbulence models contain theoretical variations, the mathematical foundation of the models are holistically identical; their use was therefore deemed to hold based on the agreement achieved between the experimentation and numerical results for the Standard τ - ω . This endeavour was hence developed to analyse the ducted tidal turbine in aligned flow at low (1 m.s^{-1}), mean (4 m.s^{-1}), and extreme (7 m.s^{-1}) free-stream velocities, and recognise discrepancies within the coupled schemes.

9.1.1 Power & Torque Coefficient

Primarily comparing the induced power output, the shape of the curve was acknowledged to retain general similarity, with a short spanning TSR range, through all the turbulence models implemented, as illustrated in Figure 9.1. A distinction, however, was present in the peak power coefficient attained. Acknowledging the variation in output, the Standard τ - ω (Wilcox assumption) was recognised to produce the highest outcome, establishing a peak C_P of 0.338, with the BSL τ - ω (Menter assumption) and SST k - ω (Boussinesq-Menter assumption) attaining quasi-equivalent results, establishing C_P maxima of 0.313 and 0.311, respectively, displaying a 6.8% and 7.7% discrepancy in peak power from the prior model. Furthermore, the nominal TSR represented by the turbulence models varied. The Wilcox assumption deduced a value of 1.50 at low velocities, which shifted to 1.75 at higher free-streams, the Menter assumption portrayed a constant TSR value of 1.50, whereas the Boussinesq-Menter assumption attained a nominal TSR value between 1.50 and 1.75 due to their equivalence.

Notable to the peak power coefficient attained by the Menter assumption turbulence models was the very good comparison with outcomes from the Betz windmill technical report, displaying a peak C_P discrepancy of 0.02% and 0.07%, respectively, at nominal TSR. In relation to the general trend of the curve, however, discrepancies in the rated power was acknowledged at both pre-nominal and post-nominal TSR values. In comparison to the BEMT results, a nominal C_P equivalence was depicted at

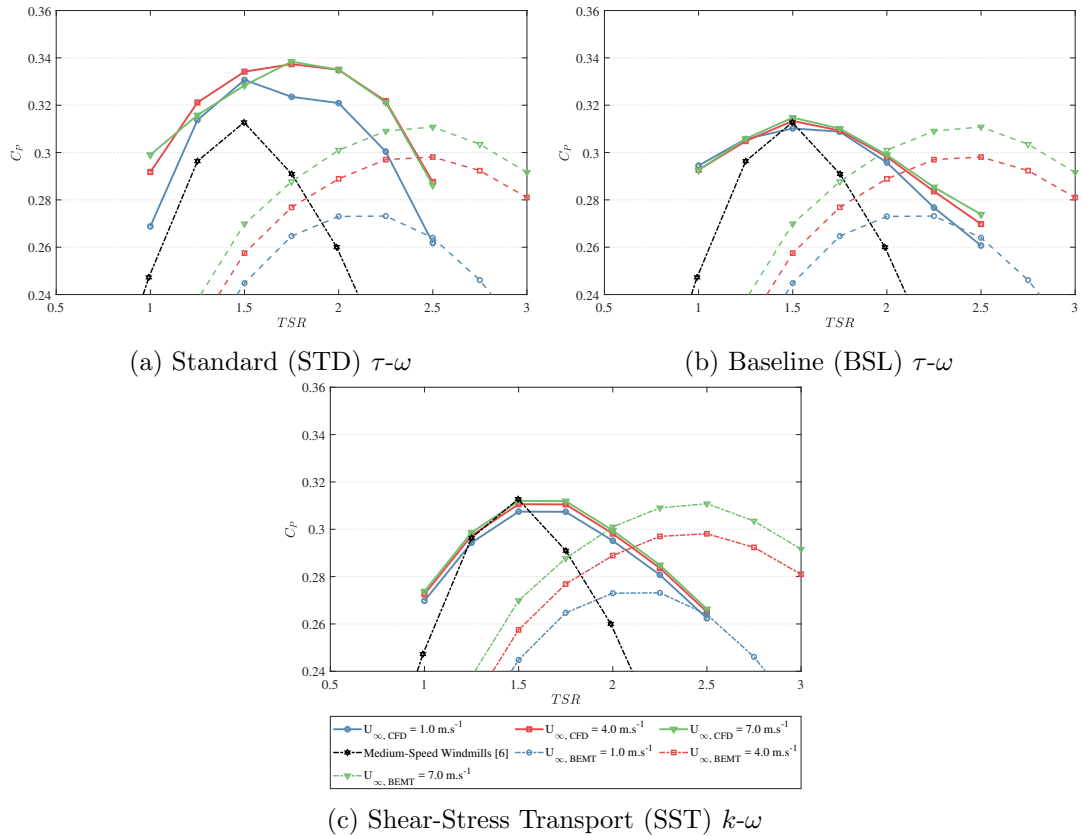


Figure 9.1: Comparison of the ducted turbine power coefficient (C_P) utilising different turbulence models

extreme conditions, yet a significant distinction in nominal TSR value was noted; the width of the curve was found to be comparable. As a result, the curve attained by the Menter assumption put forward a peak power coefficient equivalent to experimentation by Betz, yet with a curve width equivalent to BEMT by Allsop.

Further to the power curve, the variation in torque coefficient (C_Q) induced on the turbine is illustrated in Figure 9.2. Similar discrepancies between the outputs from the three turbulence models were attained in comparison to the Betz curve and BEMT outputs; notably, the trend at which the torque varied attained very good agreement.

9.1.2 Thrust Coefficient

The variation in thrust coefficient (C_T) dependent on the coupled turbulence model, as elaborated in prior chapters, was presented both in terms of the entire system,

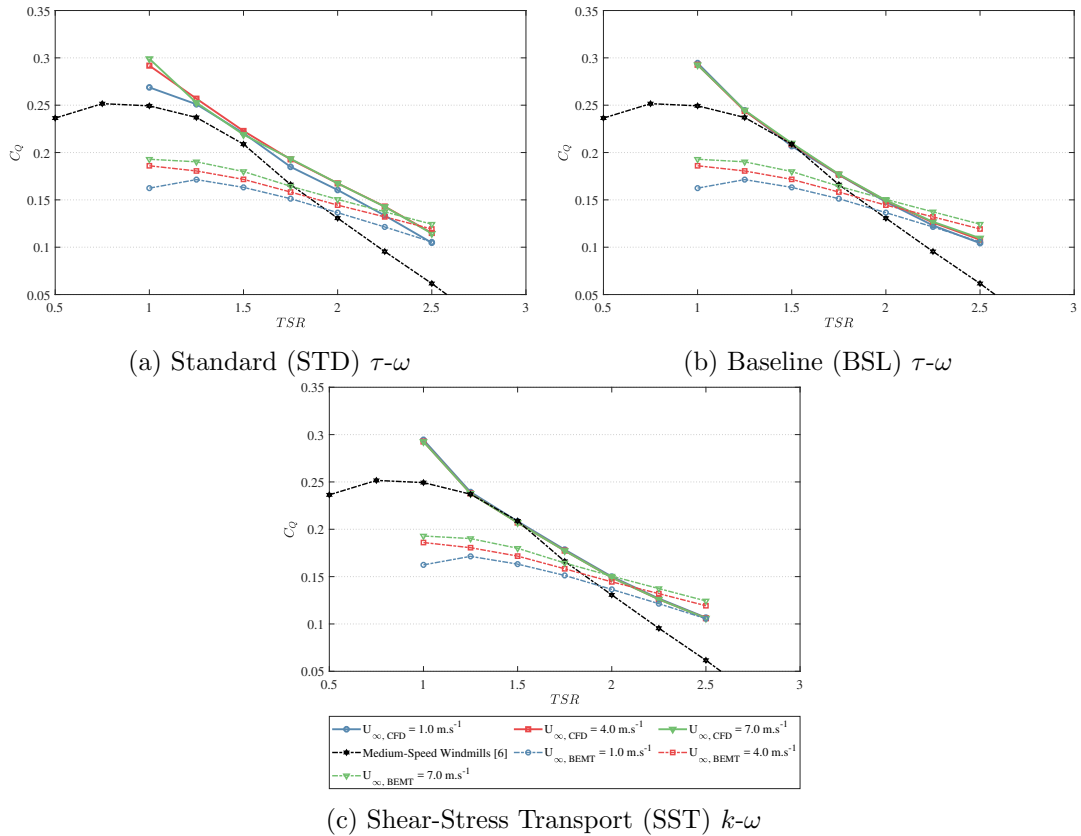


Figure 9.2: Comparison of the ducted turbine torque coefficient (C_Q) utilising different turbulence models

illustrated in Figure 9.3. Similar to the power and torque coefficient derivations, the thrust curve trend was acknowledged to retain general similarity, with a quasi-linear inversely proportional gradient, through all the turbulence models implemented. In distinction between the outputs, the Wilcox assumption attained a more polynomial variation, with the rate-of-change differing along the rotational range, in comparison to the Menter and Boussinesq-Menter assumption. Acknowledging the variation in output, the three turbulence models deduced a thrust coefficient of 1.05 - 1.10 at low TSR, whereas, at high TSR, the Wilcox assumption was recognised to produce the highest outcome, a C_T of 0.77, with the Menter and Boussinesq-Menter assumptions attaining quasi-equivalent results, a C_T of 0.69, displaying a 8.6% mean discrepancy.

Further to the system analysis, the denomination into the thrust induced upon the separate components was attained, illustrated in Figure 9.4. Distinctively, the thrust

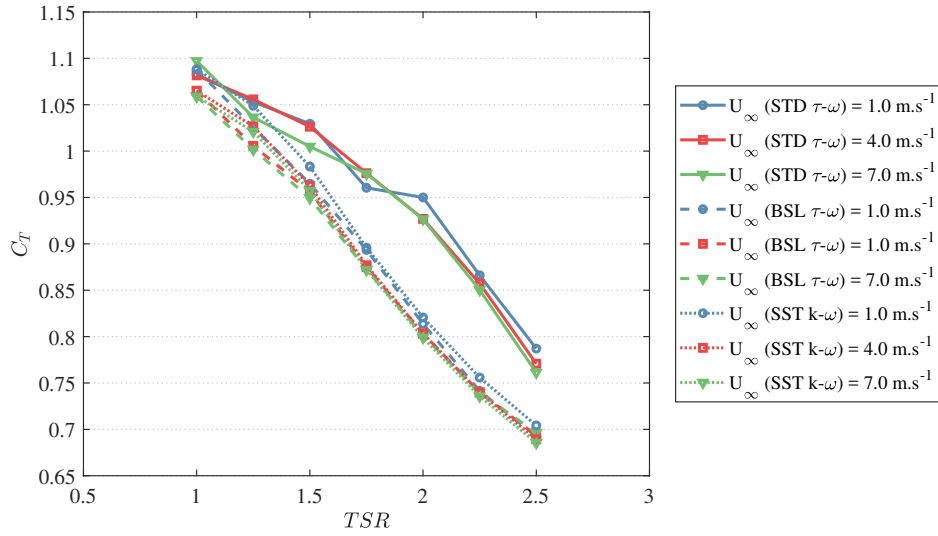
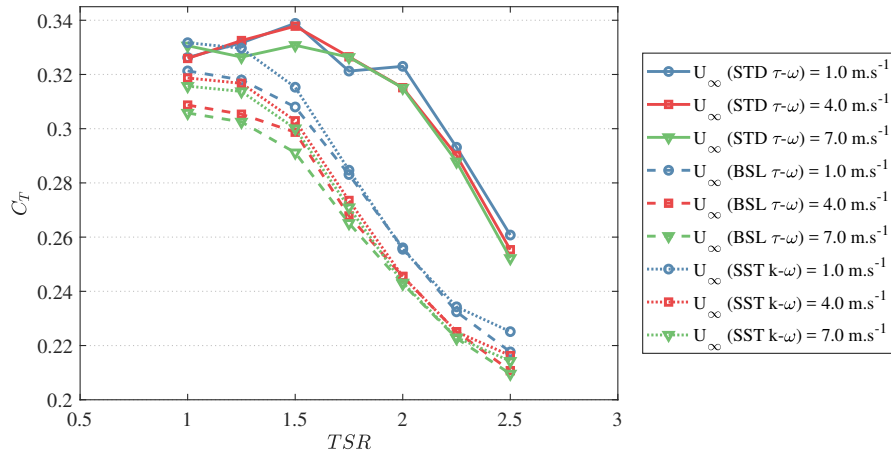


Figure 9.3: Comparison of the ducted turbine thrust coefficient (C_T) upon the system area utilising different turbulence models

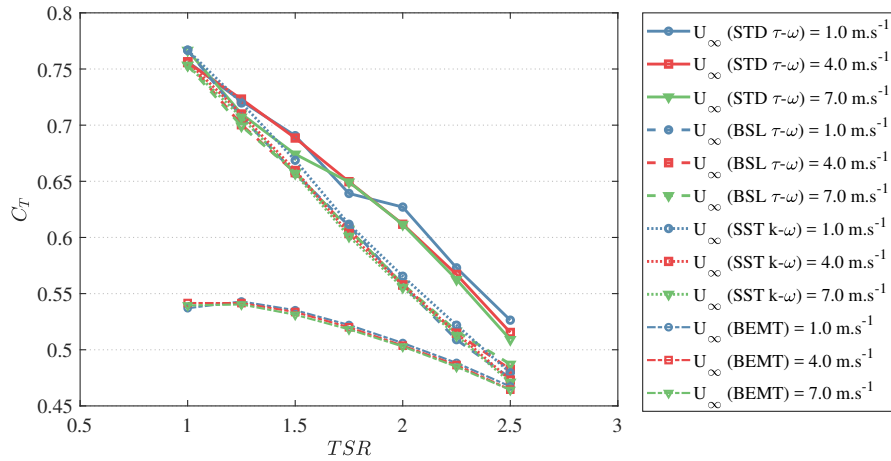
variation upon the duct differed significantly between the Wilcox assumption and the Menter assumptions. Albeit a similar value was attained at low TSR, 0.31 - 0.33, the output produced by the Menter assumptions decreased at a higher rate-of-change, due to the diminishing fluid accumulation, than that by the Wilcox assumption, resulting in a thrust coefficient of 0.21 and 0.26, respectively. On average, the results attained a 15.0% discrepancy. In reference to the rotor, the outputs attained by the three assumptions similarly attained equivalent values at low TSR, 0.76, which diminished at a linear rate-of-change, yet at a variant magnitude, resulting in a thrust coefficient of 0.49 and 0.52, respectively. On average, the results attained a 5.5% discrepancy. In comparison to BEMT, which solely considered the drag on the rotor, a significant discrepancy was attained between the two methodologies, albeit exhibiting a moderately similar diminishing C_T trend.

9.1.3 Axial Velocity & Static Pressure Difference

To acknowledge if the variation in the results solely occurred upon shear flow at the wall, or influenced the fluid parameters within the immediate region of the structure, the resultant axial velocity and static pressure difference attained by the turbulence



(a) Thrust coefficient upon the Duct



(b) Thrust coefficient upon the Rotor

Figure 9.4: Comparison of the ducted turbine thrust coefficient (C_T) upon the component areas utilising different turbulence models

models implementation was analysed, as illustrated in Figure 9.5. For both parameters, the Wilcox assumption attained higher values, albeit minutely, with a 3.7% and 5.3% mean discrepancy from the Menter assumption, respectively.

9.1.4 Wake Velocity Profiles

In analysis of the turbine wake profiles, the distribution of velocity through the domain cross-section was established qualitatively. In Chapter 6, the wake velocity profiles were established solely for the Wilcox assumption (STD $\tau\text{-}\omega$), where it was acknowledged that, due to the re-circulation zone induced along the length of the duct,

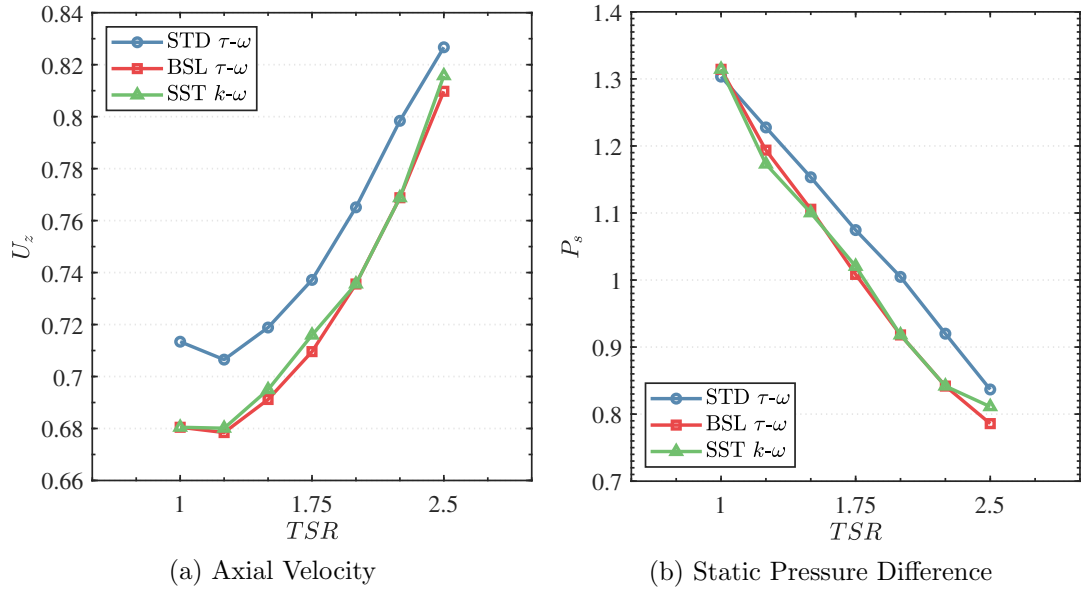


Figure 9.5: Comparison of the ducted turbine parameters utilising different turbulence models within a mean free-stream of $4 \text{ m}\cdot\text{s}^{-1}$

ring vortices were shed at the outlet of the duct, which commingled within the wake. Distinctively acknowledging the wake at nominal TSR, the implementation of the three distinct assumptions put forward three different occurrences.

Albeit the re-circulation zone was produced equivalently through the adoption of the turbulence models, by means of a stagnation zone along the inner segment of the duct, the interaction within the wake, however, varied. As elaborated prior, the Wilcox assumption induced ring vortices with a significant degree of kinetic energy, resulting in a chaotic wake, a highly disorganised flow structure with turbulent intermixing, in which the vortices resided until dissipation, as illustrated in Figure 9.6a. Implementing the Menter assumption, the re-circulation zone was also found to shed at the duct outlet as ring vortices. However, throughout the TSR range, the shed vortices did not induce a chaotic wake, but rather a comparatively more streamline wake, symmetrical down the turbine axis, with vortices explicitly present within the wake until dissipation, as illustrated in Figure 9.6b. Considering the Boussinesq-Menter assumption, a re-circulation zone was successfully formed, however no explicit fluid dynamic phenomena were induced. Explicit vortex formations were, therefore, not present within the wake,

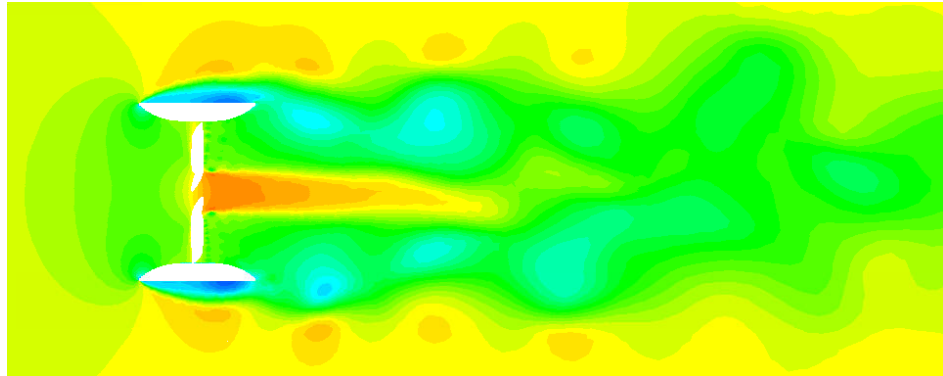
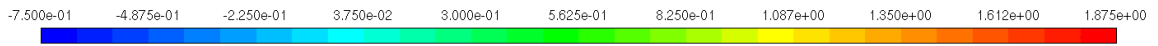
yet a rather homogenous distribution of low velocity, and low rotational kinetic energy, from the region, as illustrated in Figure 9.6c, in replacement of the ring vortices induced by means of the supplementary turbulence models.

9.2 Turbulence Modelling Review

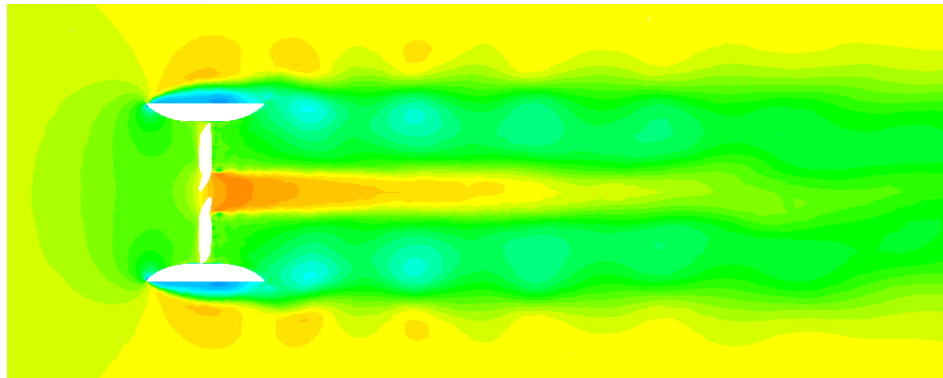
In analysis of the variation in accurately predicting the turbine performance due to the implementation of distinct turbulence models, the Standard τ - ω (Wilcox assumption) was acknowledged to overestimate the power and torque output parameters, throughout the curve, by a mean of 7% in comparison to the Baseline τ - ω (Menter assumption), whilst overestimating the global thrust coefficient by 8.6%. Furthermore, the velocity and pressure parameters induced within the immediate vicinity of the rotor were similarly found to be overestimated by the Wilcox assumption by 3.7% and 5.3%, respectively. The Baseline τ - ω (Menter assumption) and the Shear-Stress Transport k - ω (Boussinesq-Menter assumption) were acknowledged to attain similar results; the Wilcox assumption therefore depicted higher outcomes than that established by both Menter models.

Through these results, it was put forward that the Baseline τ - ω (Menter assumption) shall be the more accurate RANS turbulence model to implement for a ducted tidal turbine domain. This was due to both the attainment of a peak power coefficient equivalent to that established by Betz [143], and resolving of ring vortices within the wake, as a result of the theoretical foundation of explicitly characterising the Reynolds Stresses in three-dimensions whilst implementing a mathematical blending function to shift the closure coefficient values from that of an ω -model in the viscous sublayer (near a solid boundary) to that of a ε -model at the defect layer-region of the turbulent boundary layer (near the edge of the shear layer), attaining independence from the specific dissipation rate of the free-stream.

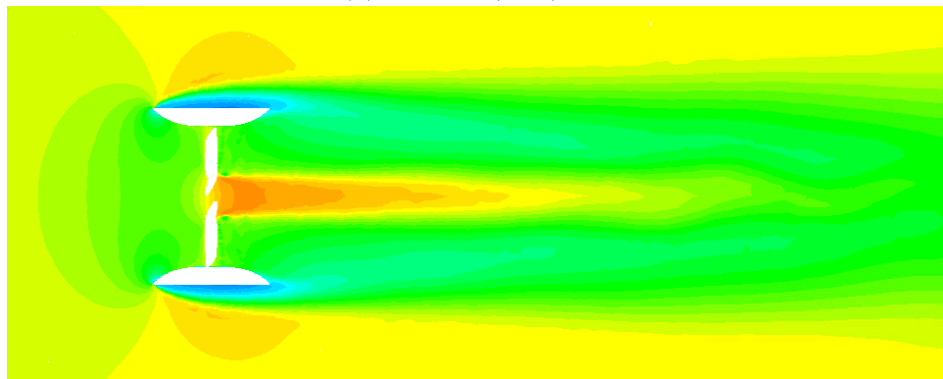
As elaborated in Wilcox [137], the Standard τ - ω will be sensitive to the free-stream value of ω , having a non-trivial effect on the solution, yet argued that once the free-stream value of ω is less than 1% of the maximum value in a turbulent shear layer, the



(a) Standard (STD) $\tau\text{-}\omega$



(b) Baseline (BSL) $\tau\text{-}\omega$



(c) Shear-Stress Transport (SST) $k\text{-}\omega$

Figure 9.6: Illustrative top-view representation of the axial velocity coefficient (\bar{u}_z^*) within the turbine domain at nominal TSR ; $U_\infty = 4 \text{ m/s}$

sensitivity will be of little consequence. This explanation was put forward in relation to a comparatively-simplistic setup of a flat-plate, whereas the concept put forward

throughout this study was a true-scale ducted tidal turbine, with more complex fluid dynamic phenomena induced. Due to the complex geometry, the numerical model was therefore sensitive to the flow adjacent to the boundary layer, which sustained distinctive values, arguably higher, of ω to the actual free-stream, specifically downstream of the rotor and along the duct perimeter as a result of the substantial flow separation and vortex effects. As a result, artificially-higher turbulence eddy viscosity was induced within the numerical boundary layer [155]. It was for these reasons that the values attained by the Wilcox assumption were higher than those by the Menter assumption. Yet, as a result of the discretisation of Reynolds stresses, the explicit ring vortices were successfully elucidated, albeit with excessive kinetic energy within the re-circulation zone, and hence the results and flow development put forward from prior sections were held, as the ring vortex shedding circumstance was deemed to be unique to the turbine.

The Shear-Stress Transport k - ω model (Boussinesq-Menter assumption) attained very similar outputs to the more accurate BSL τ - ω turbulence model, albeit considering a modified eddy viscosity to account for the transport of the principal turbulent shear stress, rather than their distinct characterisation. A key distinction between the outputs of the two-equation model to the seven-equation models, however, was the absence of ring vortices being shed within the wake. This was due to comparatively under-developed re-circulation zone along the turbine duct, a result of the isotropic representation of the Reynolds stresses, which was represented within the wake as a variant, homogenous region of low velocity, indicating the inferior physical representation of the SST k - ω model. Evidently, implementing the Boussinesq assumption to the turbulence model failed to capture the explicit phenomenon. Yet, if the wake discretisation had not been required, the increased computational expense of the seven-equation turbulence model would have been unjustifiable, hence resulting in the two-equation SST k - ω model to be the more advantageous.

9.3 Linear Momentum Rotor Properties under Highly-Loaded Conditions

As the BSL τ - ω RANS turbulence model coupled to the Reynolds-averaged representation of the momentum conservation equation to acquire the numerical hydrodynamic analysis of a ducted, high-solidity tidal turbine was verified to attain the most accurate representation, the CFD results were utilised to solve the theoretical linear momentum equations elaborated in Section 3.1.4. This was put forward both due to an absence of accurate theoretical representations of ducted, high-solidity rotors in literature, and for calibration of actuator disc (AD) and blade-element momentum theory (BEMT) models under highly-loaded conditions.

9.3.1 Axial Induction Factor

Primarily, as a result of the variation in the thrust induced upon the turbine rotor with rotational velocity, the relative variation in axial induction factor was distinguished, where the evaluated thrust coefficient was solely that upon the rotor, utilising the annular swept area of the rotor. Established to be portrayed within the highly-loaded turbine dynamic category, Equation 3.60 was utilised to acquire the disc-representative coefficient within nominal free-stream conditions ($U_\infty = 4 \text{ m.s}^{-1}$) at a range of tip/hub-loss factors. Illustrated in Figure 9.7, the thrust induced upon the rotor varied between conventional conditions and highly-loaded conditions dependent on the loss factor. In consideration of a loss factor lower than 0.90, the axial induction factor sustained an output solely within highly-loaded conditions. At loss factors higher or equivalent to 0.90, the induction factor varied from conventional to highly-loaded conditions, dependent on the rotor parameters, acknowledging the highly-loaded state of power-generation operation.

9.3.2 Tangential Induction Factor

In correspondence, as a result of the variation in the torque coefficient induced upon the turbine rotor with rotational velocity, the relative variation in tangential induction

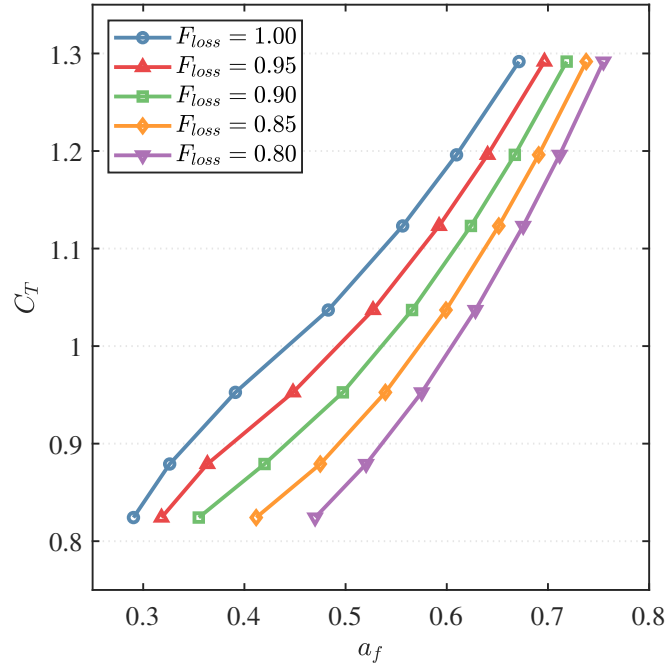


Figure 9.7: Evaluation of the ducted turbine rotor thrust coefficient (C_T) in relation to the axial induction factor (a_f)

factor was distinguished, utilising the annular swept area of the rotor. Established in relation to the axial induction factor range derived, Equation 3.24 was implemented to acquire the disc-representative coefficient within nominal free-stream conditions ($U_\infty = 4 \text{ m.s}^{-1}$) at a range of tip/hub-loss factors. Illustrated in Figure 9.8, the gradient variation of the torque induced upon the rotor altered dependent on the loss factor, hence resulting in a higher tangential induction factor range to attain an equivalent degree of torque.

It should be noted that the power coefficient must be derived via the torque coefficient, rather than via the thrust coefficient established prior. The power coefficient attained will therefore be solely that considering the annular area of the rotor, hence attaining a nominal peak value of 0.535; considering the analytical ideal turbine power coefficient at a TSR of 1.50 is equivalent to 0.452 [156], the ducted rotor setup therefore outperformed this theoretical limit.

Further to the analysis, the variation in tangential induction factor with that of the axial induction factor was distinguished in terms of tip & hub losses, as illustrated

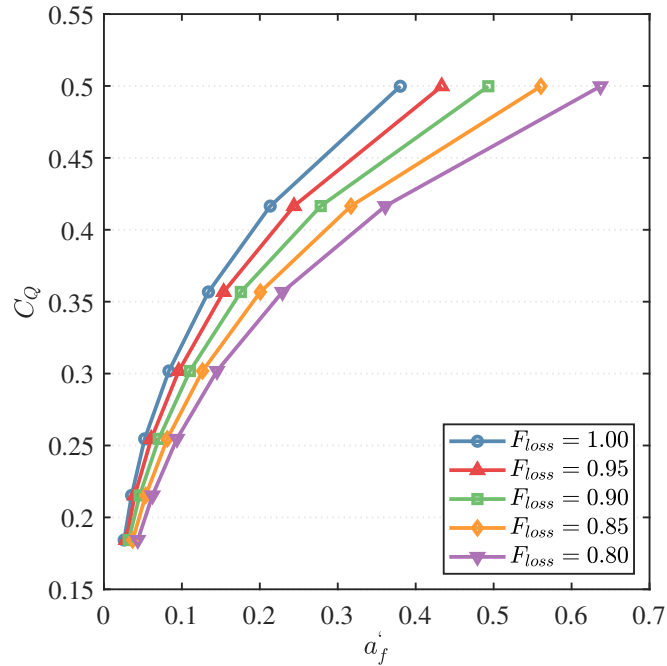


Figure 9.8: Evaluation of the ducted turbine rotor torque coefficient (C_Q) in relation to the tangential induction factor (a'_f)

in Figure 9.9. By means of this evaluation, the two induction factors were established to be directly proportional to each other, as acknowledged through the blade-explicit results.

9.3.3 Ducted Turbine Properties

In continuation to the induction factors established via the highly-loaded conditions analyses, the turbine properties in relation to the duct-embedded rotor, elaborated in Section 3.1.4, were solved.

9.3.3.1 Axial Velocity, Mass Flow-Rate, & Static Pressure at Rotor

The axial velocity through the duct, at the numerical annular surfaces introduced fore and aft of the rotor, was acknowledged to be equivalent, and therefore applicable for this analysis. Specifically, the axial velocity was established to vary in proportion to the turbine rotational velocity, as illustrated in Figure 9.10a; the mass-flow rate was confirmed to be identical to the axial velocity. This value may be implemented in

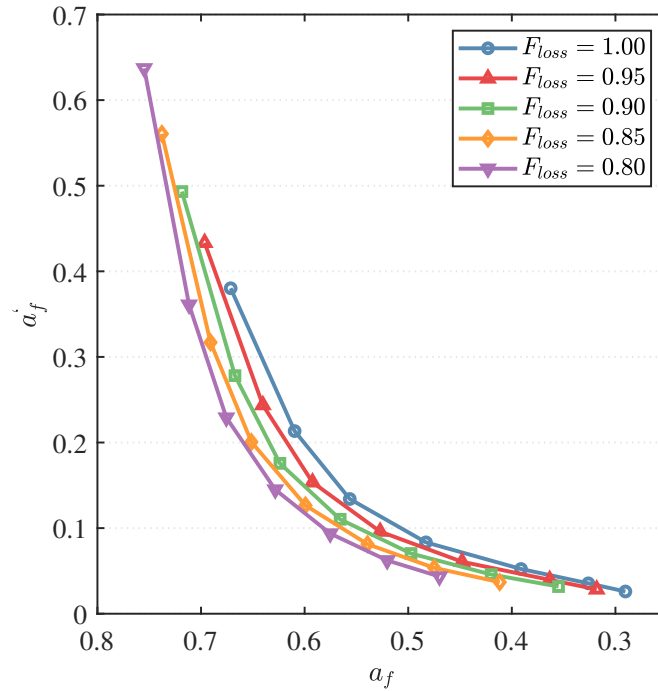


Figure 9.9: Evaluation of the tangential induction factor (a'_f) in relation to the axial induction factor (a_f)

Equations 3.33, 3.35, and 3.37.

In proportion to the turbine rotational velocity, the static pressure upstream of the rotor diminished in value, as illustrated in Figure 9.10b, whereas the pressure downstream of the rotor increased, as illustrated in Figure 9.10c. Acknowledging the difference in static pressure fore and aft of the rotor, illustrated in Figure 9.10d, the result is equivalent to the thrust coefficient attained through blade-explicit results, with an R^2 of 0.979 between the two outputs. These values may be implemented in Equations 3.18, 3.32, and 3.34.

9.3.3.2 Axial Velocity & Static Pressure at the Duct Outlet

Further to the acquisition of pressures and velocities at the disc, the pressure and velocity at the outlet of the duct was required to be deduced. Therefore, Equations 3.34, 3.35, 3.36, and 3.37 were implemented in relation to different duct outlet efficiencies (η_{34}). In relation to the analytical theory implemented, however, it is the opinion

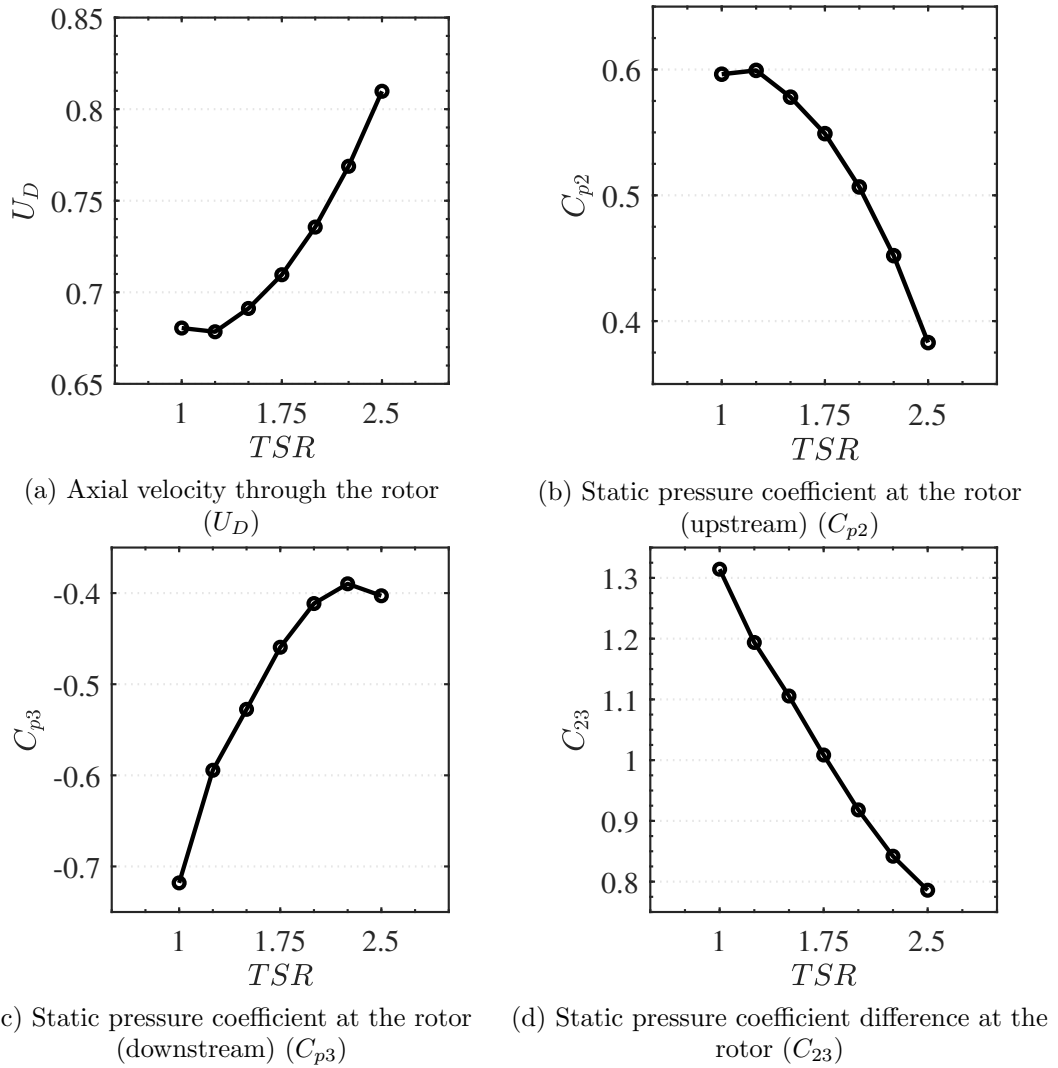


Figure 9.10: Linear momentum properties of the ducted turbine at a nominal free-stream velocity (U_∞) of 4 m.s^{-1}

of the author that Equation 3.35, and its substitution in the related equations, is inapplicable. Theoretically, Bernoulli's theorem is coupled from Equation 3.34 to produce Equation 3.35 to establish the pressure and velocity relationship with the expansion of the flow at the downstream segment of the ducted turbine [76]. Yet, between region 3 (downstream rotor) and region 4 (duct outlet) of the ducted turbine, the flow shall mix turbulently. As the mechanical energy of turbulent eddies decays through viscous dissipation, Bernoulli's theorem is deemed to be largely inapplicable due to its inviscid property assumption, and, therefore, Equation 3.35 is incorrect in capturing the

physical circumstances for ducted turbine theory.

For this reason, the author has derived a different equation for use of acquiring the pressure and velocity at the duct outlet from the parameters at the downstream rotor location. Alternate to utilising Bernoulli's theorem, a control volume was considered between the annular area at region 3 to the annular area at region 4. Equation 3.37 was coupled with a one-dimensional steady-state momentum conservation equation, described in Equation 9.1.

$$A_3 p_3 + \dot{m}_3 U_3 = A_4 p_4 + \dot{m}_4 U_4 \quad (9.1)$$

To accomplish the derivation, Equation 3.37 was incorporated with Equations 3.18, 3.32, 3.34, and 3.36 to attain Equations 9.2.

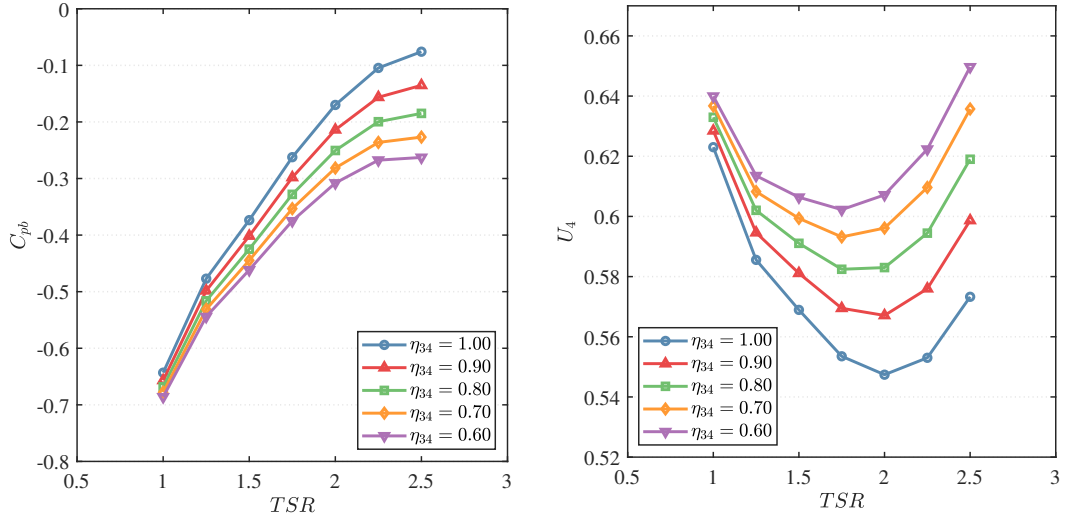
$$\frac{p_4}{\frac{1}{2}\rho U_\infty^2} - \frac{p_3}{\frac{1}{2}\rho U_\infty^2} - \eta_{34} \cdot \frac{U_D^2}{U_\infty^2} \cdot \left(1 - \frac{U_4^2}{U_D^2}\right) = 0 \quad (9.2)$$

Equation 9.1 was utilised within Equation 9.2, to attain Equation 9.3.

$$p_4 = p_3 \cdot \frac{1 - \frac{1}{2}\eta_{34}\frac{A_3}{A_4}}{1 - \frac{1}{2}\eta_{34}} + \frac{1}{2}\rho U_3^2 \cdot \frac{\eta_{34} \cdot \left(1 - \frac{A_3}{A_4}\right)}{1 - \frac{1}{2}\eta_{34}} \quad (9.3)$$

This equation has not been seen in literature, as Equation 3.35 is typically utilised. In compilation, the equation describes the static pressure at the duct outlet as a function of the static and dynamic pressure at the downstream region of the disc, establishing coefficients in relation to the variation of annular area and duct efficiency. This therefore puts forward a very convenient analytical equation to incorporate into an Actuator Disc or Blade-Element Momentum code. The full derivation may be found in Appendix H .

By means of the pressure output, illustrated in Figure 9.11a, it was observed that the outlet pressure was higher than that at the disc, hence putting forward an adverse pressure gradient through the downstream duct segment. In addition, a higher duct efficiency was required to attain the highest possible outlet pressure, where it was evident that the variation in outlet pressure was negligible at low TSRs, yet substantial at high TSRs. Through the outlet velocity, a similar concept had taken place, where



(a) Evaluation of the static pressure at the duct outlet (C_{pb}) in relation to TSR (b) Evaluation of the axial velocity at the duct outlet (U_4) in relation to TSR

Figure 9.11: Evaluation of the static pressure & axial velocity at the duct outlet with duct efficiency (η_{34})

the higher the duct efficiency attained, the lower the axial velocity induced due to the adverse pressure gradient. Additionally, the velocity variance at low $TSRs$ was negligible, yet substantial at high $TSRs$.

In closing the analytical coefficients, in Equation 3.33, η_{02} was found to vary between 1.104 and 1.112, with a mean average value of 1.108. By means of Equation 3.39, the analytical duct outlet efficiency was found to be equivalent to 1.011.

9.4 Chapter Summary

This chapter provided a direct comparison of the variant performance outputs of a ducted, high-solidity tidal turbine numerical model by utilising three high-end 'specific dissipation rate' turbulence models when coupling the mass and momentum conservation equations. Through the contrast between the quantitative results attained for power, torque, thrust, axial velocity, and static pressure difference, it was acknowledged that the Menter assumption implemented in the Baseline τ - ω and the Shear-Stress Transport k - ω produced the most accurate results, with the Wilcox assumption attaining a discrepancy of 4 - 8%. It was therefore evident that utilising a blending function

to vary the model closure coefficients instating insensitivity to the specific dissipation rate in the free-stream was imperative to attain accurate results from a full-scale ducted turbine model.

Through the contrast between the qualitative results attained for the turbine wake profiles, it was acknowledged that the Menter assumption implemented in the Baseline τ - ω and the Wilcox assumption implemented in the Standard τ - ω established ring vortices, with the Boussinesq-Menter assumption failing to develop the explicit phenomenon. It was therefore evident that discretising the Reynolds stresses within the domain was imperative to attain accurate results from a full-scale ducted turbine model. As a result, in ranking the turbulence models for the use of analysing a full-scale ducted turbine, the BSL τ - ω is most recommended, followed by the SST k - ω and the STD τ - ω .

As the BSL τ - ω was acknowledged to be the most accurate scheme arrangement, the linear momentum equations for highly-loaded conditions elaborated in Section 3.1.4 were solved in relation to the ducted turbine described in Section 4.1 to put forward a numerical calibration effort for analytical models. In extension, the equation established in literature solving for the duct outlet pressure was deemed to be inapplicable due to the implementation of Bernoulli's theorem within a zone of turbulent mixing, downstream of the rotor. As a result, a unique formula was derived utilising one-dimensional momentum conservation, hence constituting an appropriate physical representation of the pressure and velocity at the duct outlet.

Chapter 10

Vortex-Interaction Analysis of a Ducted High-Solidity Tidal Turbine

In effort of analysing the performance variation of a ducted high-solidity turbine, utilising the BSL τ - ω model, when succumb to explicit fluid dynamic phenomena induced by means of bathymetric interaction, the computational domain was numerically manipulated to generate vortices of three distinct length scales, in a trajectory towards the structure, to acknowledge the influence upon the outputs brought about.

10.1 Power Coefficient

Primarily acknowledging the discrepancy in power generation when explicit vortices are present within the free-stream, and interact with the rotor blades, a significant variation in the resultant efficiency was found to be induced in relation to the vortex length scale, as illustrated in Figure 10.1. With regard to the rotor output within a free-stream precluded from vortices, the power curve sustains its shape throughout the analysis once the flow phenomenon was introduced. The power coefficient TSR curve, at all vortex length scales, therefore maintained its short spanning features due to the

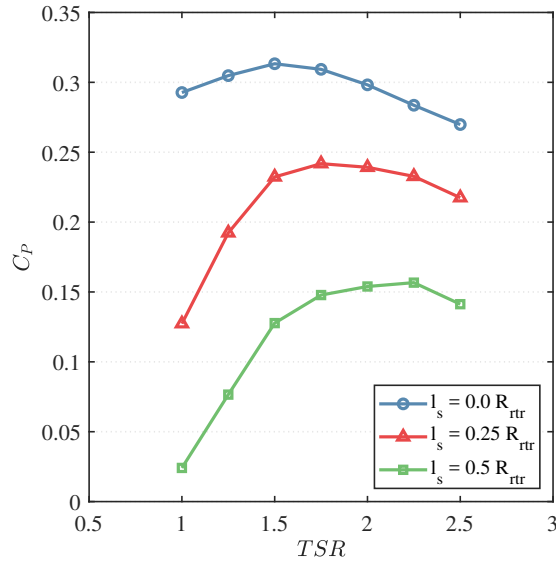


Figure 10.1: Evaluation of the mean ducted turbine power coefficient (C_P) in relation to TSR

high-solidity characteristics, attaining peak power coefficient within a TSR range of 1.00 - 2.50, albeit at a diminished magnitude.

By means of the investigation, the highest power coefficient efficiency achieved by the turbine was acknowledged to be attained when the length scale value of the incoming vortices was negligible, therefore describing an absence of vortices present within the free-stream, peaking at a power coefficient of 0.31. Contrarily, the lowest values of power efficiency were attained when the rotor was succumb to the highest length scale value, $0.5 \cdot R_{rtr}$, peaking at a power coefficient of 0.16. In relation to the depiction elaborated in Clark [30], the power coefficient relationships at low, nominal, and high TSRs were found to vary in a polynomial manner with length scale, attaining a maximum peak coefficient discrepancy of 50.5%.

In continuation, to acknowledge the transient nature of the induced forces upon the rotating bladed structure, the variation in power generation in time at nominal TSR, whilst succumb to the array of vortices at all three length scales, was investigated within five cycles, as illustrated in Figure 10.2. Operating within a vortex stream of differing length scales, a substantial variation in the energy extraction was recognised upon the introduction of the phenomenon. At all length scales, a degree of variance about the

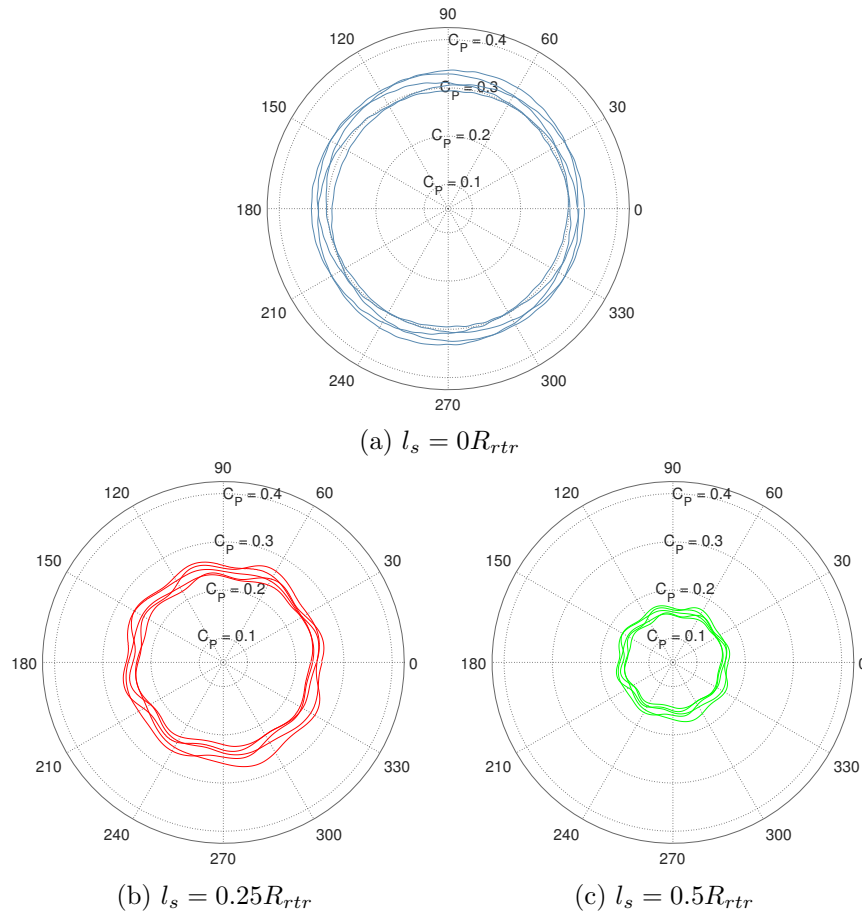


Figure 10.2: Evaluation of the instantaneous ducted turbine power coefficient (C_p) in relation to blade azimuth angle under distinct vortex length-scales at nominal TSR.

mean was acknowledged; at negligible length scales, the variance in turbine output had been acknowledged to be due to the fluctuations in pressure and velocity [119] as a result of vortex ring shedding. Upon the presence of, and increases in, length scale, distinct fluctuations were established within the instantaneous output; in particular, eight distinct depressions per cycle were recognised throughout the output of the turbine operation.

In an effort to establish the causation of the variance within a rotation cycle, the mean response of a rotor blade output during its rotation was attained at nominal TSR at all three length scales, as illustrated in Figure 10.3, by means of cycle-averaging, azimuth angle-synchronising, and, subsequently, blade-averaging the data attained; this

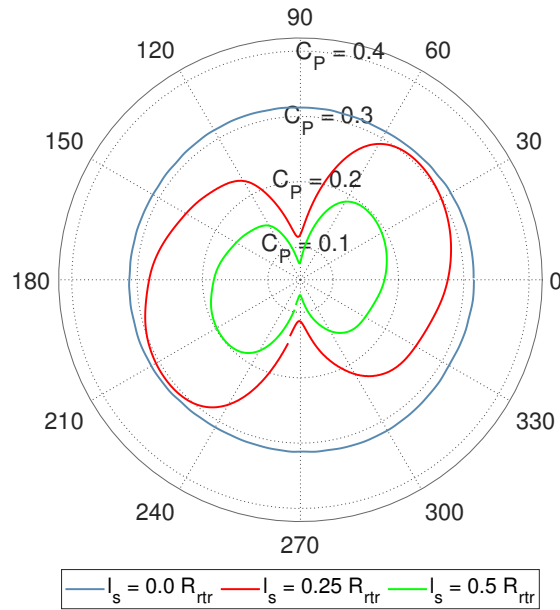


Figure 10.3: Evaluation of the mean single-blade response (C_P) in relation to azimuth angle under distinct vortex length-scales at nominal TSR

output was multiplied by the number of blades for comparison purposes. At negligible length scale, the mean performance per blade per cycle was largely consistent along the turbine rotation; upon an introduction in length scale, a notable outcome was recognised by a significant drop in efficiency at each mid-cycle. Given that the vortex stream was introduced within a physical range as a phenomenon strip throughout the domain, a depression of velocity and pressure was induced in concordance to the modification of the free-stream flow. The sudden drop of generated power, therefore, was considered to be evidence of a successful implementation of the vortex stream.

In analysis of the load drop, it was established that the output not only severely diminished, yet the reduction occurred at a rate-of-change that was initiated far from the location at which minimum power was attained. This aspect was deemed to be a result of the fluid dynamic property manipulation in the immediate vicinity of the induced vortex, which acted along the wide frontal profile of the high-solidity rotor blades, hence instigating a considerable region within which a load reduction took place due to the decrement in fluid pressure and velocity. The effect of this region upon both the rate-of-change and magnitude of the generated power was relative to

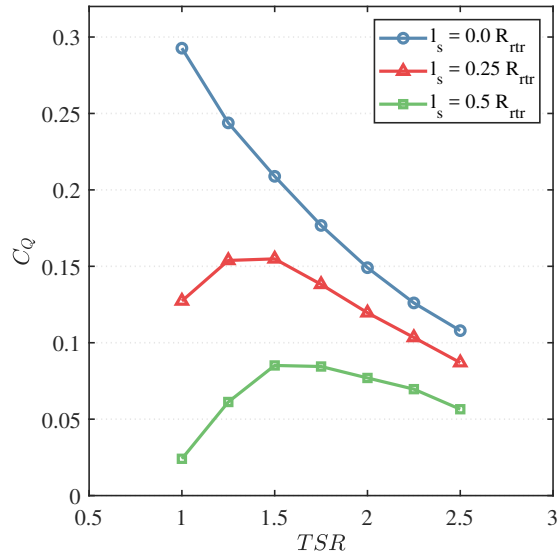


Figure 10.4: Evaluation of the ducted turbine torque coefficient (C_Q) in relation to TSR

the size of the vortex, which pinpointed the causation of the diminishment in the power coefficient curve.

Further to the power curve, the variation in the torque coefficient (C_Q) generated by the turbine rotor is illustrated in Figure 10.4. At a negligible length-scale, a quasi-linear inversely proportional trend relating the torque induced to the rotor angular velocity had been acknowledged. Yet, with the introduction of a vortex at the definitive length-scales, the torque curve was altered, establishing a severe diminishment in torque from low TSR to mid-range TSR, at which the torque acted in a similar trend to the sans-vortex curve. The largest discrepancy was that at low TSR, elaborating the effect of a diminishment in the pressure accumulation typically noted for the high-solidity, highly-loaded rotor conditions. This incurred as a result of the low pressure vortex zone interacting with the blade surface, inducing a snap-load reduction; as the high-torque characteristics of the high-solidity turbine are induced due to high pressure accumulation, the snap reduction in pressure, therefore, substantially diminished the torque generated. At higher TSRs, as the upstream pressure is inherently reduced under sans-vortex conditions, the discrepancy between the average pressure accumulation and the vortex pressure had reduced. As a result, the torque was acknowledged to

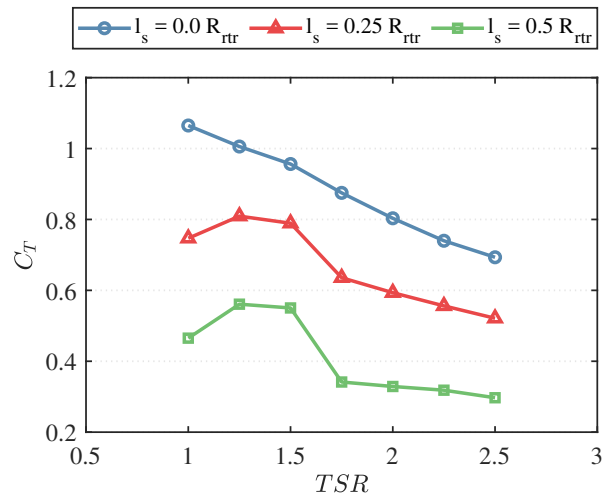
become resemblant of the torque curve at negligible length scale, albeit at a diminished magnitude. Due to arithmetic proportionality, the discrepancy in induced torque in relation to the vortex length scale was comparable to the power curve, with a maximum torque diminishment of 93.1% from negligible length scale to that at $0.5 \cdot R_{rtr}$.

10.2 Thrust Coefficient

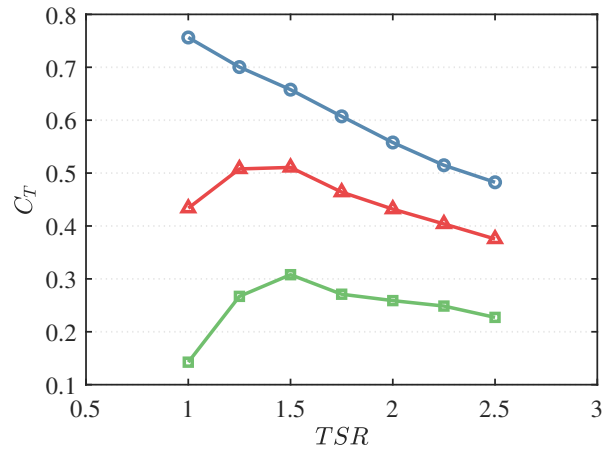
With the presence of vortices in the incoming hydrodynamic flow, the effect of the duct implementation along the perimeter of the high-solidity rotor upon the fluid dynamic phenomena was uncertain. From the torque response, it was made apparent that, at the rotor, variations in the induced loading were present to a substantial degree. Yet, at the boundaries of the turbine, where variant pressure gradients are induced along the uneven duct topology, the incoming vortices may undergo bursting (or breakage) due to impact at the rim, or yielding as a result of the adverse pressure gradient at the high-pressure duct inlet, in accordance to duct-vortex interaction. In effect, acknowledging the drag induced upon both components of the system was deemed to be of particular interest, giving insight to the resultant occurrence.

Illustrated in Figure 10.5, the variation in thrust coefficient (C_T) with TSR and length-scale is presented both in terms of the entire system, and in terms of the physical components: rotor and duct. As an entire system within a negligible length-scale ($l_s = 0 \cdot R_{rtr}$), a substantially high thrust coefficient was attained at low TSR, a mean value of 1.07, which decreased quasi-linearly to a mean of 0.70 at high TSR. With the introduction of a vortex stream, the global thrust decreased in a proportional manner relative to length scale, diminishing by 0.41 at peak thrust when succumb by that equivalent to $0.5 \cdot R_{rtr}$; in effect, the presence of vortices had a substantial influence upon the turbine axial loading.

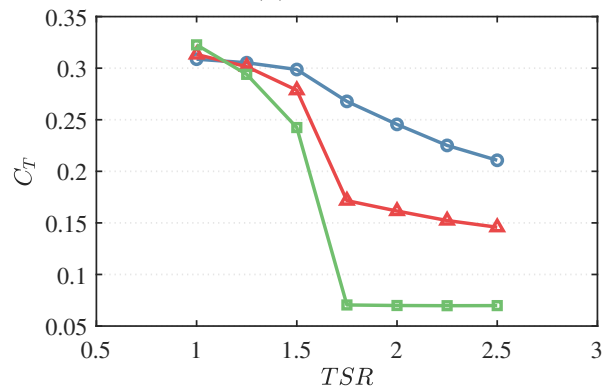
In an effort to establish the impact on the distinct turbine components, the thrust curve was discretised into the loads induced upon the duct and rotor in segregation. At negligible length scale, the drag was largely consistent upon both the duct and the rotor, with a mean allocation of the global drag of approximately 32% and 68%,



(a) Full Turbine



(b) Rotor



(c) Duct

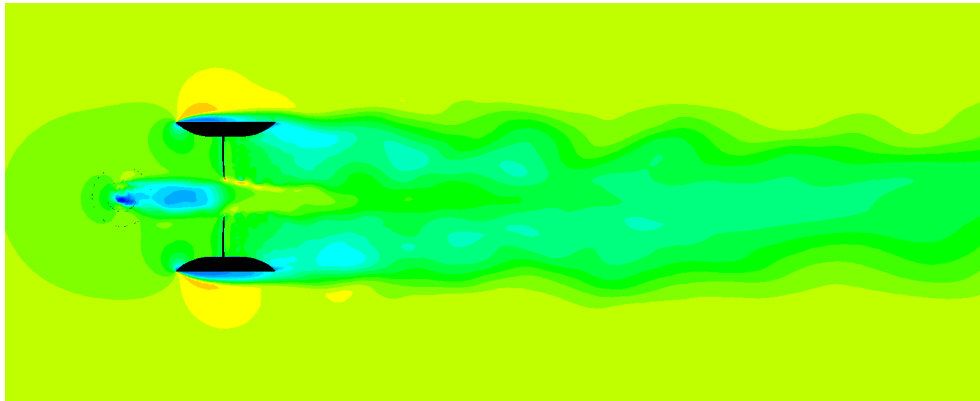
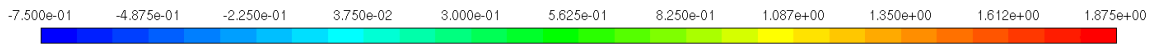
Figure 10.5: Evaluation of the mean single-blade response (C_P) in relation to azimuth angle under distinct vortex length-scales at nominal TSR

respectively. When succumb to a vortex stream, the load upon both the rotor and duct diminished substantially, as acknowledged from the torque derivation, yet the variation in drag upon the duct at low TSRs was comparably minute; quantitatively, the largest discrepancy in the rotor load was found to be 82%, whereas the load upon the duct diminished by 71%.

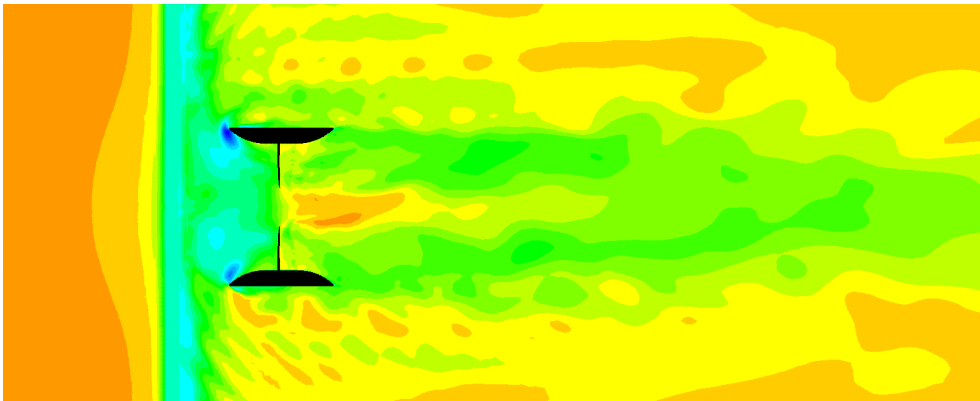
The load diminishment upon the duct varied substantially from lower to higher TSRs, arguably due to the diminutively-exposed area in comparison to its entire frontal area. The loads induced upon the duct were established to be a balance of pressure and viscous loading on its surfaces; along the outer perimeter of the duct, where viscous forces were deemed to be prevalent, vortical effects were negligible as the vortex dynamics largely acted in a planar manner, parallel to the surface. Pressure loads were prevalent along the inner duct curvature, where slight thrust variation was present at lower TSRs at all three length scales. Due to the sharp topology of the structure, together with the high pressure accumulation, the conditions put forward a means for the vortices to be broken, hence diminishing their effect within the immediate vicinity of the duct at low TSRs; at high TSRs, the pressure load dropped substantially due to the presence of the vortices. In result, the established load deficiency, in relation to the induced phenomenon, upon the duct was determined to be of slight influence at low angular velocities, but substantial at higher angular velocities.

10.3 Wake Profiles

In visualising the velocity flow contours along the wake for the purpose of positioning further turbine installations, a qualitative analysis of the velocity distribution was undertaken in the two orientation planes parallel to the turbine axis. Within the plane normal to the induced tube-vortex axis, illustrated in Figure 10.6a, the wake was not significantly affected directly by the presence of the vortex stream due to the minute length-scale in comparison to the turbine diameter. The general wake profile was largely identical to that of a domain without an integrated upstream vortex stream, where the induced flow structures described a wake width quasi-equivalent to the diameter of the



(a) Velocity contours along the plane normal to vortex axis

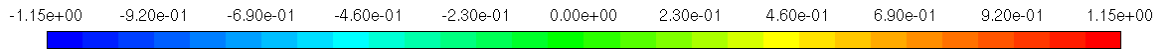


(b) Velocity contours along the plane parallel to vortex axis

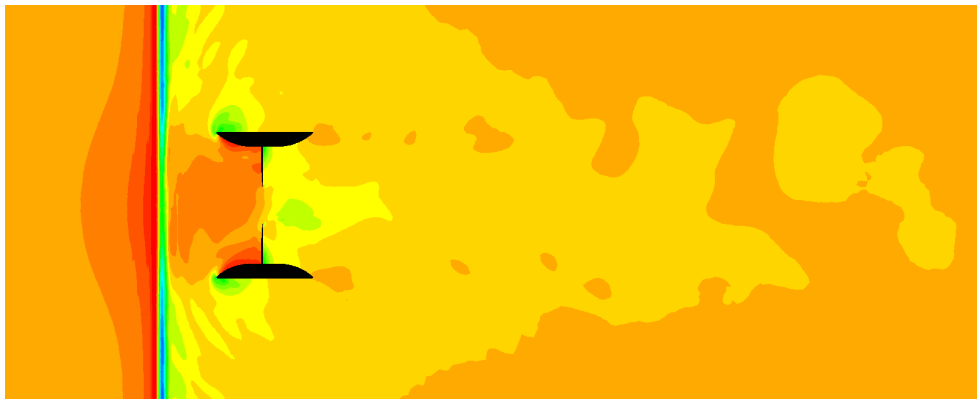
Figure 10.6: Illustrative top-view representation of the velocity coefficient within the turbine domain at nominal TSR and $l_s = 0.25 \cdot R_{tr}$; $U_\infty = 4 \text{ m/s}$

duct, commingled with ring vortices shed from its perimeter. The velocity of the flow passing through the rotor orifice hub, however, was seen to diminish due to the incoming vortex stream. Acknowledging the static pressure distribution throughout the domain, illustrated in Figure 10.7a, the location of the artificially-induced vortex was clearly recognised, where the cell-zone successfully produced the vortex stream without any residual phenomena, as established within the vortical distribution in Figure 10.8a, diminishing the pressure build-up at the inlet of the turbine, yet unaffected the wake structure along the Cartesian plane.

Contrarily, within the plane parallel to the induced tube vortex axis, the wake was



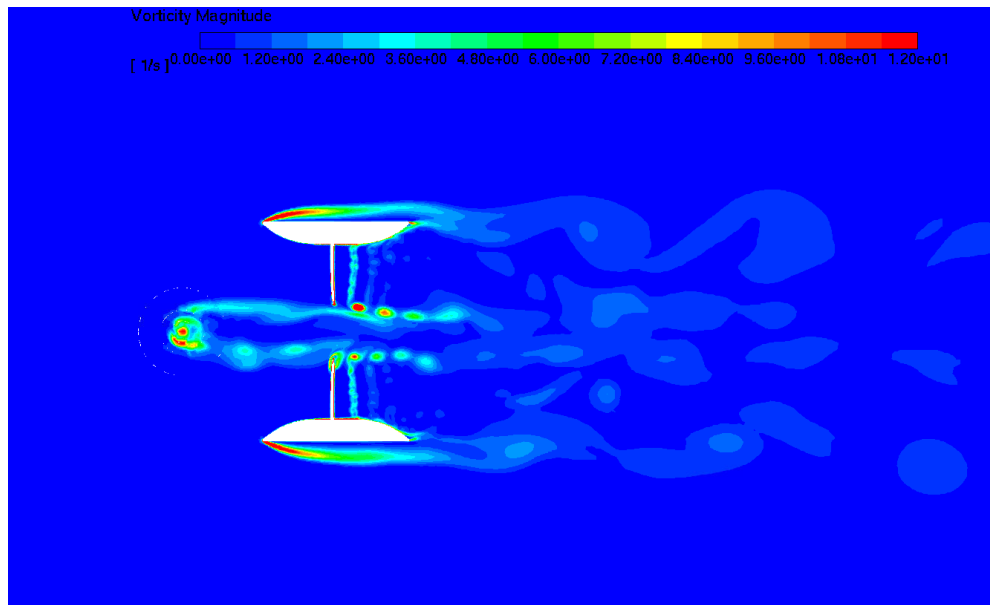
(a) Pressure contours along the plane normal to vortex axis



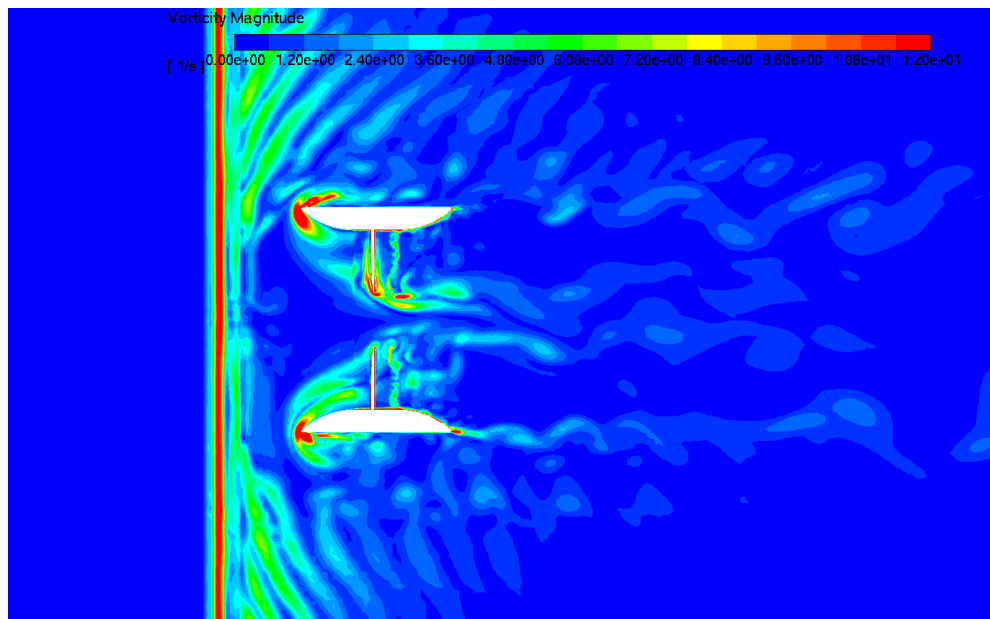
(b) Pressure contours along the plane parallel to vortex axis

Figure 10.7: Illustrative representation of the pressure coefficient (C_{Pr}) within the turbine domain at nominal TSR and $l_s = 0.25 \cdot R_{tr}$; $U_\infty = 4 \text{ m/s}$

directly affected by the presence of the shed vortices as a result of the diminishment in velocity along the plane; consequently, the general wake profile portrayed a disturbed, turbulent wake, with a significant discrepancy in the velocity distribution. Within the re-circulation zone, the accumulation of turbulent kinetic energy was inexistent due to the lesser degree of velocity along the plane; albeit the reverse flow was present at the duct inlet, it incorporated with the free-stream, rather than transforming into a static vortex. The flow phenomenon therefore refrained from developing a ring vortex, yet shifted into a horseshoe vortex. In addition, as the depreciation of velocity due to the



(a) Vorticity contours along the plane normal to vortex axis



(b) Vorticity contours along the plane parallel to vortex axis

Figure 10.8: Illustrative representation of the vorticity within the turbine domain at nominal TSR and $l_s = 0.25 \cdot R_{rtr}$; $U_\infty = 4 \text{ m/s}$

artificial vortex was consistent throughout the width of the domain, the turbine wake was entirely affected along the distinct plane. As a result, flow depreciation was induced at all locations within the domain: the rotor orifice hub, rotor, duct, and free-stream,

portraying the velocity variance illustrated in Figure 10.6b. This was also apparent in the pressure distribution in Figure 10.7b, where the accumulation of pressure at the duct inlet, together with the free-stream flow, were disrupted, as illustrated in the vortical distribution in Figure 10.8b.

10.4 Chapter Summary

This chapter has put forward an investigation into the hydrodynamic performance concerning a ducted, high-solidity tidal turbine in vortex flow utilising blade-resolved, unsteady computational fluid dynamics. Due to the comparatively minute clearance present between the seabed and the bottom-fixed tidal turbine structure, circumstances may arise that, due to the bathymetry of a project site, flow separation may be induced in the form of shed vortices. As the flow phenomena may interact with the turbine, potentially causing a local depression of pressure upon the blade surface, the resultant outcome discrepancy in relation to vortices of distinctive length-scales were analysed. The research acknowledged the explicit physicality of both the rotor blades and the vortices present within the fluid domain in establishing a coherent representation of the dynamic performance of the turbine when succumb to bathymetry-generated vortices in aligned flow. Three vortex length-scales, $0 \cdot R_{rtr}$, $0.25 \cdot R_{rtr}$, and $0.5 \cdot R_{rtr}$, were implemented to be generated directly upstream of, and shed in a trajectory towards, the ducted turbine.

Through blade-integrated pressure results, the peak power coefficient was found to decrease inversely proportional to the vortex length-scale; at these conditions, the maximum power coefficient was found to reach a value of 0.31, 0.24, and 0.16 at length scales of $0 \cdot R_{rtr}$, $0.25 \cdot R_{rtr}$, and $0.5 \cdot R_{rtr}$, respectively. Particularly, the general curve shape was sustained, yet diminished in its definite integral in relation to the length scale of the interacting vortex. Due to this result, the induced torque and thrust were analysed, likewise diminishing within the considered parameters. For this reason, a blade-averaged representation of the load induced upon the rotor throughout its rotation was established, acknowledging a sudden dip in performance at bearings where

the vortex-interaction zone was present. This elaboration was coherent with literature describing the snap (un)loading of static pressure generated along the surface, hence diminishing the forces induced upon the blades.

In accordance, it was concluded that, as a variation in the resultant rotor output had occurred, the numerical methodology implemented was successful in generating a zonal range of discrete vortices within the domain that interact with the ducted turbine. Furthermore, the turbine response was found to be highly susceptible to the presence of vortices, diminishing the response in relation to the length-scale. The vortices were found to sustain composition albeit the adverse pressure gradient at the turbine inlet, inducing an effect upon the pressure accumulation at the surface of the rotor blades.

These outcomes, however, were circumstantial as the vortex stream was artificially generated in close vicinity of the turbine, and would solely be valid if a barrage of vortices, moderately longer than the diameter of the turbine, would impact the structure. Albeit this trait, the results acquired have justified the implementation of the methodology. In consideration of the fact that commercial CFD codes do not have a built-in numerical methodology to introduce explicit vortices within a domain, this chapter has substantiated a framework that is implementable. This chapter has therefore put forward a novel approach into analysing rotors (and other structures) within extreme conditions to attain a value of the turbine performance attenuation due to vortices within a free-stream to further improve the ducted turbine.

Chapter 11

Conclusion

Efforts to increase the efficiency of energy-generating turbines will persevere with pushing the technological boundaries of offshore engineering structures. This thesis has put forward the concept of a partitioned-approach fluid-structure interaction analysis of a ducted high-solidity open-centre tidal turbine in an effort to establish its hydrodynamic properties and blade structural response in aligned, yawed, and vortex flows. In specification to the analyses, the rotor performance was established in regard to the power and torque output, thrust induction, axial velocity, and static pressure difference across the rotor to determine the numerical and theoretical representation of the turbine. Additionally, the structural performance of the rotor blades was investigated in terms of axial deflection and strains induced upon the fibre-composite material structure.

From a numerical hydrodynamic perspective, this body of research strived to overcome the limitations of actuator disc and blade-element momentum theory methodologies by implementing a computational fluid dynamic analysis with blade-explicit actuality, coupled with general continuity at both the domain and turbine. This feature allowed the aspect of modelling flow three-dimensionality at the turbine, together with induced turbulence effects, in further effort of numerically replicating its true performance.

11.1 Summary of the Fluid-Structure Interaction Analysis

In regard to the fluid-structure interaction methodology, numerical validation was primarily attained via an explicit experimentation replication of a three-bladed tidal turbine under steady hydrodynamic flow undertaken to simulate the physics of rotating blades. The numerical outcomes of the performance factors, notably power coefficient, torque coefficient, thrust coefficient, and wake velocity profiles attained a coefficient of determination of 0.965, 0.965, 0.84, and 0.99, respectively, with the performance output curves acquired via experimentation.

11.1.1 Aligned Flow Analysis

In application of the validated modelling schemes, the full-scale high-solidity ducted tidal turbine in operation was simulated, portraying a peak power coefficient of 0.34 with a thrust coefficient of 0.97 at a nominal tip-speed ratio of 1.75. The values were assimilated to calculations undertaken by means of blade-element momentum theory, together with experimentation results representing medium-speed windmills to justify the applicability of the full-scale analysis and condone further fluid dynamic analysis, namely the hydrodynamic effects along the duct, mass-flow rate through the duct, vortex shedding within the domain, static pressure along the rotor blades, and velocity profiles within the rotor wake.

In summary of the numerical analysis of a ducted high-solidity tidal turbine, it had been observed that, due to the incorporation of a duct with a high number of blades, and hence blade area, the phenomena induced by the fluid-structure interaction were substantial. In effect of the force equilibrium between the magnitude of the flow interaction at the upstream surfaces of the blades with that at the downstream blade surfaces, the resultant torque was substantial at low TSRs, yet decreased rapidly with an increase in TSR. This short-spanning range in TSR was, hence, a direct attribute of the high-solidity properties of the turbine, and was, therefore, the primal reason of its incapability to acquire high values of mechanical power, albeit the high torque attained.

This outcome agreed well with Betz's projections for medium-speed windmills".

The thrust on the rotor was found to decrease significantly with TSR, mainly due to the diminishing static pressure difference at higher rotational to free-stream velocity ratios, in consequence of higher mass-flow rates. The most significant phenomena, however, was induced as a result of the introduction of the duct. A stagnant pressure point was developed along the duct inlet, where fluid upstream of this point was forced out of the inlet to flow along the outer flat surface of the duct. Due to its interaction with the free-stream at the duct ridge, a region of low pressure was created, inducing a re-circulating fluid zone. In effect, along the length of the duct, the static pressure at the flat outer surface of the duct was significantly low, inducing suction. Ring vortices were generated as a result of the re-circulating zone, which were shed at the duct outlet. The vortices commingled with the rotor wake, prompting chaotic flow at low TSRs, which streamlined at higher TSRs.

11.1.2 Yawed Flow Analysis

Upon a vectorial discrepancy in the mean free-stream with the turbine axis, the turbine performance outcomes depicted a variation in relation to the yaw angle. Through blade-integrated pressure results, the peak power coefficient was found to increase at higher rotational velocities within the 15° - 30° angular range. At these conditions, the maximum power coefficient was found to reach a value of 0.35 at a bearing of 23.2° , equivalent to the geometrical gradient of the inner duct curvature, together with a shift in nominal tip-speed ratio to 2.00. Due to this result, the induced torque and thrust were analysed, likewise increasing within the considered parameters.

For this reason, actuator disc theory was utilised within the analysis to pinpoint the causation of the variation in performance. It was acknowledged that, due to the presence of the duct, the axial velocity was largely sustained through the rotor, with slight deviation at low TSR, yet essential equivalence at high TSR. Further to this, the pressure drop across the rotor increased with an introduction of a bearing, peaking at 23.2° , followed by a decline. The increase was acknowledged to be due to the decrease of back-pressure at the outlet of the duct at higher TSRs, as the wake was shifted by

the free-stream. The nominal bearing for this occurrence was the angle of duct profile variation, as sufficient pressure was sustained upstream, yet simultaneously reduced downstream; post-nominal bearings portrayed a decreased drop due to flow separation induced upstream of the rotor, hence power augmentation was restricted by the stall limit of the shroud inlet profile. Therefore, it was recognised that the performance enhancement was largely common for ducted turbine setups, yet the degree of the enhancement was solely dependent on the profile of the duct cross-section.

Having derived the product of the coefficients of static pressure and axial velocity, a substantial correlation was acknowledged between the blade-integrated and the area-averaged values of thrust, hence verifying the attained area-averaged results to be relevant. For this reason, it was concluded that, due to the capacity of the turbine to sustain axial velocity, the decrease in pressure downstream of the rotor provided an augmented pressure drop to further improve the performance of a ducted turbine.

11.1.3 Structural Analysis

In completing the fluid-structure interaction analysis, a structural evaluation of the turbine rotor, when succumb to the hydrodynamic conditions, was established in an effort to acquire a composite-material selection, together with an appropriate internal structural formation, for a quantitative-based design of the rotor blades. The endeavour strived to overcome the limitations of prior analyses by acknowledging the explicit three-dimensional physicality of the rotor blades, both in the hydrodynamic and structural models, to establish a coherent representation of the dynamic turbine blade response in aligned and yawed current flows; as a result, high-accuracy loading conditions were adopted within the structural model by means of the hydrodynamic model. In recognition of the accurate mapping of static pressure and wall shear stress along the surface of the structural blade model, together with a solid element structure layout, three distinct internal blade designs were put forward and analysed to establish the more appropriate configuration for high-solidity ducted rotor blades: a solid, cored, and reinforced setup.

In consideration of the structural outcomes derived, the geometrical properties of

the three rotor designs were primarily established; the moment of inertia of the cored and reinforced blade were found to constitute 53.1% and 79.6% that of the solid blade, respectively, with comparable values established for specific mass and specific density. Subsequently, hydrostatic analysis was undertaken to prove the structural integrity of the three blade designs at the installation water-depth; all designs were acknowledged to be appropriate, with slight yielding apparent, albeit negligible, upon the cored design. In continuation, hydrodynamic analysis was undertaken, where, via the attained maximum normal strain response, the highest response was induced by the cored design, hence portraying least rigidity, with the solid blade attaining the least response; the reinforced blade provided an intermediate value. The investigated conditions were found to not exceed the ultimate strain value of the double-biased glass-fibre reinforced polymer for all blade designs, and, hence, was within the limits of reliable operation. Due to these outcomes, all three designs were deemed to be largely equivalent in sustaining structural integrity at the operational conditions. Albeit the deduced, a notable outcome was the concentrations of strain present at the leading edge of the blade, within the immediate vicinity of the root, occurring upon all three structural blade designs in both aligned and yawed flows; this structural aspect may present a detrimental feature within the design. Ancillary to the fracture analysis, a blade material cost analysis was undertaken to establish an estimation on the most cost-effective assortment of materials implementable within the three blade designs. By means of this financial elaboration, the reinforced blade was established to be the least costly, with the solid blade attaining the highest expenditure.

In culmination, a fatigue analysis was undertaken to acknowledge an appropriate range of GFRP material fatigue properties in its implementation within the considered flow conditions; solely comparing the reinforced and solid blade designs, the values attained were found to be largely equivalent. Therefore, as a result of the responses attained and discussed, the reinforced internal blade structure was considered to procure a favourable combination of high rigidity and comparatively lower weight, in addition to comparably lower material capital expenditure, deeming it to be the more efficacious design.

It should be acknowledged that, as linear and rotational deflections had been established to occur, both the position and the angle-of-attack of the blade segments shall vary in relation to the free-stream. As a result, the static pressure and wall shear stress shall, in relation, vary dependent on the physical orientation of the blade, hence requiring a monolithic-approach (two-way) fluid-structure interaction analysis. This endeavour, however, had been deemed to be effective in putting forward an accurate, computationally-efficient methodology with which design-selection and material-selection may be undertaken. From the outcomes, further investigations are required to pursue a more appropriate design, specifically in establishing the optimised shell and webbing thickness, for the operational conditions analysed, to further improve the performance of the ducted, high-solidity tidal turbine.

11.1.4 Turbulence Modelling Analysis

As distinct turbulence models have been derived through literature in analysing the fluid dynamics of structures, a direct comparison of the variant performance outputs of a ducted, high-solidity tidal turbine numerical model was undertaken by utilising three high-end 'specific dissipation rate' turbulence models when coupling with the momentum conservation equation. Through the contrast between the quantitative results attained for power, torque, thrust, axial velocity, and static pressure difference, it was acknowledged that the Menter assumption implemented in the Baseline τ - ω and the Shear-Stress Transport k - ω produced the most accurate results, in comparison to literature, with the Wilcox assumption attaining a discrepancy of 4 - 8%. It was therefore evident that utilising a blending function to vary the model closure coefficients instating insensitivity to the specific dissipation rate in the free-stream was imperative to attain accurate results from a full-scale ducted turbine numerical model.

Through the contrast between the qualitative results attained for the turbine wake profiles, it was acknowledged that the Menter assumption implemented in the Baseline τ - ω and the Wilcox assumption implemented in the Standard τ - ω established ring vortices, with the Boussinesq-Menter assumption failing to develop the explicit phenomenon. It was therefore evident that discretising the Reynolds stresses within the

domain was imperative to attain accurate results from a full-scale ducted turbine model. As a result, in ranking the turbulence models for the use of analysing a full-scale ducted turbine, the BSL τ - ω is most recommended, followed by the SST k - ω and the STD τ - ω .

In extension, the formula established in literature solving for the duct outlet pressure was deemed to be inapplicable due to the implementation of Bernoulli's theorem within a zone of turbulent mixing, downstream of the rotor. As a result, a unique formula was derived utilising one-dimensional momentum conservation, hence constituting an appropriate physical representation of the pressure and velocity at the duct outlet.

11.1.5 Vortex Flow Analysis

An investigation was put forward into the hydrodynamic performance concerning a ducted, high-solidity tidal turbine in vortex flow, acknowledging the explicit physicality of both the rotor blades and the vortices present within the fluid domain. Three vortex length-scales were implemented to be generated directly upstream of, and shed in a trajectory towards, the ducted turbine.

Through blade-integrated pressure results, the peak power coefficient was found to decrease inversely proportional to the vortex length-scale; likewise, the induced torque and thrust were acknowledged to diminish within the considered parameters. For this reason, a blade-averaged representation of the load induced upon the rotor throughout its rotation was established, acknowledging a sudden dip in performance at bearings where the vortex-interaction zone was present. This elaboration was coherent with literature describing the snap (un)loading of static pressure generated along the surface, hence diminishing the forces induced upon the blades.

In accordance, it was concluded that, as a variation in the resultant rotor output had occurred, the numerical methodology implemented was successful in generating a zonal range of discrete vortices within the domain that interact with the ducted turbine. Furthermore, the turbine response was found to be highly susceptible to the presence of vortices, diminishing the response in relation to the length-scale.

The resultant outcomes acquired had justified the implementation of the methodology. In consideration of the fact that commercial CFD codes do not have a built-in

numerical methodology to introduce explicit vortices within a domain, this had substantiated a framework that would be implementable. A novel approach was therefore put forward to analyse the ducted tidal turbine within extreme conditions to attain a value of the turbine performance attenuation due to vortices within a free-stream.

11.2 Evaluation of the Ducted High-Solidity Tidal Turbine

Having attained a validated numerical model for simulating rotating bladed physics by means of a direct comparison to experimentation in literature analysing a small-scale, three-bladed tidal turbine within three distinct parameters, notably power (& torque) coefficient, thrust coefficient, and velocity profiles in the near and far wake, the numerical schemes and libraries implemented were considered for a full-scale analysis. In investigating the performance of the full-scale, high-solidity, ducted tidal turbine, the outcomes were further compared to the parameters defined in Betz’s “medium-speed windmill” curve in literature, and via a secondary numerical methodology, blade-element momentum theory; due to the degree of similarity between the three methodologies, the concluded outcomes were considered to hold.

In accordance, this work provided analyses in evidence to the notion that ducted turbines generate higher power per rotor unit area as a result of the flow convergence towards the rotor when interacting with the inner duct. In elaboration of these claims, the power generated by a ducted rotor would be approximately equivalent to the power generated by an unducted rotor ($P_{rtr_{duct}} \approx P_{rtr_{unductd}}$), given that the radius of the duct is equal to the radius of the unducted rotor ($R_{duct} = R_{rtr_{unductd}}$), where the true cut-off area is the circular region of stagnant pressure on the duct inlet geometry, whose location is dependent on the cross-sectional formation. Under this prospect, the power per unit rotor area of a ducted rotor would be higher in comparison to the power per unit rotor area of an unducted turbine, as the area of the ducted rotor is significantly lesser than that of the unducted rotor ($A_{rtr_{duct}} \ll A_{rtr_{unductd}}$). Yet, albeit the potential increase in power per rotor unit area, the thrust coefficient induced as a result of the

implementation of the duct was found to be physically substantial as the degree of static pressure increased as a result of fluid accumulation at the inlet. In addition, the complementary flow phenomena, specifically the shedding of vortex rings, potentially negates any related advantageous aspects of the installation. Yet some phenomena may be suppressed by design variations, such as instating tubercles or increasing the roughness of the duct rim to transition the laminar boundary layer into a turbulent one efficiently, or decreasing the gradient of the inner duct rim to mitigate trailing edge boundary layer separation.

This outcome varies once succumb to yawed flow; an increase in power and thrust was acknowledged to occur within a limited flow bearing, speculated to be induced as a result of a comparatively significant diminishment in static pressure at the duct outlet. Due to the variation in the flow vector, the exposed profile of the duct differs, altering the developed wake into a more chaotic flow structure.

In essence, therefore, as a result of the induced hydrodynamic effects, it may be speculated that if the areal annulus in which the duct coincides is lower in both capital and operation cost than the blades present in an identical areal annulus of an unducted turbine, then potentially-sustainable advantages, in relation to an implementation of a duct, may be present. Albeit this indication, this study solely considers a single geometrical design of a duct within a flow in open-water conditions, which brings about a degree of assumptions in comparison to real-world implementations. Therefore, the combination of variations in flow direction, external inlet shear flow, and differences in free-stream turbulence intensities/turbulent length scales is required to be analysed within a coupled model approach to establish a holistic evaluation of the ducted, high-solidity tidal turbine.

11.3 Future Work

Further research in establishing the performance of turbine rotors within a duct installation, and its enhancement, may be pursued by undertaking distinct tasks:

- In tackling the numerical methodologies with which the turbine performance may be analysed, the libraries implemented could be substituted for numerical schemes that introduce higher computational accuracy. In accordance, the turbulence-incorporating Reynolds-Averaged Navier Stokes (RANS) models may be substituted by Large-Eddy Simulation (LES) models, together with supplementary pressure-velocity coupling schemes. Additionally, multi-phase flow modelling schemes, such as the Volume-of-Fluid (VOF) method, may be useful to acknowledge any wave-interaction and cavitation effects.
- Further to numerical schemes, the physical properties of the simulated hydrodynamic flow may be varied. To replicate the flow at the site, the shear flow profile, acknowledging the variation in flow velocity, together with the present turbulence intensity, is required to be introduced within the model; time-variant velocity profiles would also be required.
- In relation to the physical geometry of the turbine structure, this study analyses a single duct profile. Variant profiles may be analysed, where the more imperative characteristic of the duct feature to alter is the induction of the re-circulation zones upon the outer perimeter of the turbine, which are imposed by the free-stream, inducing ring vortices within the wake. The generation of the re-circulation zone may be suppressed by altering the revolved duct profile by adding a hump at the leading edge and trailing edge of the duct; this will limit the acceleration of the fluid at those locations, diminishing the turbulent kinetic energy of the static vortex. Resultant drag may be increased, yet, as re-circulation zones inherently increase drag upon a structure, this notion may require a comparative analysis. In addition, the inner duct variation profile from the duct inner radius to the outer radius may be varied from the current convex profile to a Sigmoid function (or an analogous probability density function), to vary the location of the stagnation flow ring-zone along the duct inlet; the most effective location would be at the inlet rim, however, this would effect the yawed flow properties of the turbine.

- In reference to the rotor, the primary aspect is the number of blades; due to its high-solidity, the power coefficient may solely reach a limited value. In recognition of this, the blade number may require a reduction to attain higher torque values at higher tip-speed ratios. Yet, as the notion of the high-solidity turbine was to generate power at low rotational velocities to avoid impact with subsea life, the number of blades should not be reduced to less than four with an identical hydrofoil profile spectrum; five (or six) blades may put forward a sweet-spot. In relation to the actual blade structure, it was acknowledged that a region of the blade upstream surface was succumb to negative pressure, which, in effect, reduces the resultant thrust upon the rotor. The general dimensions of the hydrofoils that constitute the blade were attained by means of BEMT, however, due to assumptions when considering the influence of the duct upon the fluid in the vicinity of the rotor, this methodology may not produce the most applicable geometry. For this reason, a limitation on the blade cross-sectional chord length is recommended. Additionally, the rounded-edge flat plate blade profile should be varied to an elliptical-edge flat plate to diminish localised regions of flow separation. Furthermore, tubercles may be implemented along the leading edge of the blade to transition a turbulent boundary layer in an effort to sustain attachment along a larger surface area of the turbine blade.
- As the composite structural analysis in selecting an appropriate blade material and formation solely considered a consistent material within the setup, a high-fidelity structural analysis of the rotor blades implementing sandwich composite materials is required.
- The foundational structure of the turbine, in addition to the turbine itself, is to be simulated under the hydrodynamic conditions to ascertain no effects are induced upon the rotor. Further, a holistic structural analysis is required.
- Lastly, the wake-interaction with other turbines within a farm must be analysed to acknowledge variations in the outcomes.

11.4 Chapter Summary

This chapter consisted of a conclusion to the thesis, putting forward the resultant hydrodynamic and structural mechanic outcomes of the methodologies implemented for the analyses, together with a general evaluation of the ducted, high-solidity tidal turbine.

References

- [1] F. O Rourke, F. Boyle, and A. Reynolds, “Tidal energy update 2009,” *Applied Energy*, vol. 87, no. 2, pp. 398–409, 2010.
- [2] F. M. White, “Fluid Mechanics,” in *Fluid Mechanics*, ch. 6, pp. 325–426, New York: McGraw Hill, 8th ed., 2015.
- [3] S. C. Allsop, *Hydrodynamic Modelling for Structural Analysis of Tidal Stream Turbine Blades*. PhD thesis, University of Edinburgh, 6 2018.
- [4] C. Belloni, *Hydrodynamics of Ducted and Open-Centre Tidal Turbines*. PhD thesis, Oxford University, UK, 2013.
- [5] H. Glauert, “Airplane propellers,” in *Aerodynamic Theory: A General Review of Progress Under a Grant of the Guggenheim Fund for the Promotion of Aeronautics*, pp. 169–360, Berlin, Heidelberg: Springer Berlin Heidelberg, 1935.
- [6] A. Betz, “Das maximum der theoretisch möglichen ausnutzung des windes durch windmotoren,” *Zeitschrift fur das gesamte Turbinenwesen*, vol. 20, 1920.
- [7] B. Newman, “Actuator-disc theory for vertical-axis wind turbines,” *Journal of Wind Engineering and Industrial Aerodynamics*, vol. 15, no. 1, pp. 347 – 355, 1983.
- [8] G. Riegler, “Principles of energy extraction from a free stream by means of wind turbines,” *Wind Engineering*, vol. 7, no. 2, pp. 115–126, 1983.

- [9] B. L. Gilbert and K. M. Foreman, “Experiments With a Diffuser-Augmented Model Wind Turbine,” *Journal of Energy Resources Technology*, vol. 105, pp. 46–53, 03 1983.
- [10] R. A. Oman, K. M. Foreman, and B. L. Gilbert, “Investigation of diffuser-augmented wind turbines: Part i,” Tech. Rep. COO/2616-2 (Pt.1), Research Department, Grumman Aerospace Corporation, Bethpage, New York, January 1977.
- [11] D. G. J. W. van Bussel, “The science of making more torque from wind: Diffuser experiments and theory revisited.,” *Journal of Physics: Conference Series*, vol. 75, p. 012010, jul 2007.
- [12] Y. Ohya, T. Karasudani, A. Sakurai, K. Abe, and M. Inoue, “Development of a shrouded wind turbine with a flanged diffuser,” *Journal of Wind Engineering and Industrial Aerodynamics*, vol. 96, pp. 524–539, 6 2008.
- [13] G. M. Lilley and W. J. Rainbird, “A preliminary report on the design and performance of ducted windmills,” Tech. Rep. 102, College of Aeronautics, Cranfield, Bedfordshire, United Kingdom, 04 1956.
- [14] K. Abe, M. Nishida, A. Sakurai, Y. Ohya, H. Kihara, E. Wada, and K. Sato, “Experimental and numerical investigations of flow fields behind a small wind turbine with a flanged diffuser,” *Journal of Industrial Aerodynamics*, vol. 93, pp. 951–970, 12 2005.
- [15] Verdant Power, “Verdant Power.” <http://www.verdantpower.com/what-initiative>, 2012. [Online; accessed 28-April-2013].
- [16] Tidal Energy Pty Ltd., “What is hydro kinetic energy.” <http://tidalenergy.net.au/index-subpage-2.html>, 2012. [Online; accessed 02-February-2014].
- [17] N. W. Cresswell, G. Ingram, and R. Dominy, “The impact of diffuser augmentation on a tidal stream turbine,” *Ocean Engineering*, vol. 108, pp. 155–163, 10 2015.

- [18] B. R. Clayton and P. Filby, “Measured effects of oblique flows and change in blade pitch angle on performance and wake development of model wind turbines,” in *Wind Energy Workshop*, (Bedfordshire, England), pp. 24–26, Cranfield Institute of Technology, 1982.
- [19] D. N. Khatri, P. Chatterjee, R. Metoyer, A. P. Mazzoleni, M. Bryant, and K. O. Granlund, “Dual-actuator disc theory for turbines in yaw,” *AIAA Journal*, vol. 57, no. 5, pp. 2204–2208, 2019.
- [20] M. Anderson, “Horizontal axis wind turbines in yaw,” in *Wind Energy Workshop*, (Bedfordshire England), pp. 57–67, Cranfield Institute of Technology, 1979.
- [21] I. Grant, P. Parkin, and X. Wang, “Optical vortex tracking studies of a horizontal axis wind turbine in yaw using laser-sheet, flow visualisation,” *Experiments in Fluids*, vol. 23, pp. 513–519, December 1997.
- [22] M. Lewis, S. Neill, P. Robins, and M. Hashemi, “Resource assessment for future generations of tidal-stream energy arrays,” *Energy*, vol. 83, pp. 403 – 415, 2015.
- [23] J. Clarke, G. Connor, A. Grant, and C. Johnstone, “Regulating the output characteristics of tidal current power stations to facilitate better base load matching over the lunar cycle,” *Renewable Energy*, vol. 31, no. 2, pp. 173 – 180, 2006. Marine Energy.
- [24] T. Zhang, A. E. Yankovsky, A. R. Piola, and D. Valla, “Observations of semidiurnal internal tides on the patagonian shelf,” *Continental Shelf Research*, vol. 167, pp. 46 – 54, 2018.
- [25] C.-T. Pham and V. A. Martin, “Tidal current turbine demonstration farm in paimpol-brehat (brittany): tidal characterisation and energy yield evaluation with telemac,” in *Proceedings of the 8th European Wave and Tidal Energy Conference, Uppsala, Sweden*, vol. 710, 2009.

- [26] C. Pham and K. Pinte, “Paimpol brehat tidal turbine demonstration farm (brittany): optimisation of the layout, wake effects and energy yield evaluation using telemac,” in *3rd International Conference on Ocean Energy*, 2010.
- [27] SIMEC Atlantis Energy, “Atlantis Unveils the Worlds Largest Tidal Turbine The AK1000.” <https://simecatlantis.com/2010/08/11/atlantis-unveils-the-worlds-largest-tidal-turbine-the-ak1000/>, 2010. [Online; accessed 30-September-2019].
- [28] Orbital Marine Power, “Orbital O2 2MW.” <https://orbitalmarine.com/technology-development/orbital-o2/>, 2018. [Online; accessed 30-September-2019].
- [29] R. Barthelmie, S. Frandsen, O. Rathmann, K. Hansen, E. Politis, J. Prospathopoulos, J. Schepers, K. Rados, D. Cabezon, W. Schlez, A. Neubert, and M. Heath, “Flow and wakes in large wind farms: Final report for upwind wp8,” Tech. Rep. Risø-R-1765(EN), Risø DTU, National Laboratory for Sustainable Energy, Potsdam, NY, 1 2011.
- [30] T. H. Clark, “Turbulence in Marine Environments (TiME): A framework for understanding turbulence and its effects on tidal devices,” in *European Wave and Tidal Energy Conference*, vol. 11th, (Nantes, France), EWTEC, September 2015.
- [31] European Marine Energy Centre (EMEC) Ltd., “Tidal Clients.” <http://tidalenergy.net.au/index-subpage-2.html>, 2012. [Online; accessed 02-February-2014].
- [32] P. Gipe, “WIND-WORKS: Ducted Wind Turbines,” 2018.
- [33] A. Roberts, B. Thomas, P. Sewell, Z. Khan, S. Balmain, and J. Gillman, “Current tidal power technologies and their suitability for applications in coastal and marine areas,” *Journal of Ocean Engineering and Marine Energy*, vol. 2, pp. 227–245, May 2016.

- [34] H. Boye, E. Caquot, P. Clement, L. de La Cochetiere, J. Nataf, and P. Sergent, “Rapport de la mission d’étude sur les énergies marines renouvelables,” *Paris: Ministère de l’écologie, du développement durable et de l’énergie*, 2013.
- [35] Renewable Energy UK, “Lunar Energy Tidal Power.” <http://www.reuk.co.uk/wordpress/tidal/lunar-energy-tidal-power>, 2012. [Online; accessed 04-November-2019].
- [36] Pacific Northwest National Laboratory (PNNL), “Race Rocks Tidal Energy Project.” <https://tethys.pnnl.gov/annex-iv-sites/race-rocks-tidal-energy-project>, 2016. [Online; accessed 04-November-2019].
- [37] SIMEC Atlantis Energy, “Tidal Turbines.” <https://simecatlantis.com/services/turbines>, 2010. [Online; accessed 04-November-2019].
- [38] J. Hardisty, “Tidal power technologies,” in *The Analysis of Tidal Stream Power*, ch. 4, pp. 89–119, John Wiley & Sons, Ltd, 2009.
- [39] The Canadian Press, “Cape Sharp Tidal turbine in Bay of Fundy now being monitored remotely,” 2018.
- [40] E. Benezet, “La grande vague des hydroliennes,” 2018.
- [41] N. Mehmood, Z. Liang, and J. Khan, “Harnessing ocean energy by tidal current technologies,” *Research Journal of Applied Sciences, Engineering and Technology*, vol. 4, pp. 3476–3487, 09 2012.
- [42] Bloomberg L.P., “OpenHydro Group Limited: Private Company Information - Bloomberg,” 2018.
- [43] OpenHydro Group Ltd., “Projects,” 2016.
- [44] Z. Zhou, M. Benbouzid, J.-F. Charpentier, F. Sculler, and T. Tang, “Developments in large marine current turbine technologies – a review,” *Renewable and Sustainable Energy Reviews*, vol. 71, pp. 852 – 858, 2017.

- [45] Z. Zhou, F. Sculler, J. F. Charpentier, M. Benbouzid, and T. Tang, “An up-to-date review of large marine tidal current turbine technologies,” in *2014 International Power Electronics and Application Conference and Exposition*, pp. 480–484, Nov 2014.
- [46] Guinard Energies, “BluStream: Innovative second-generation high-output turbine.” <http://www.pole-mer-bretagne.com/blustreamr-innovative-second-generation-high-output-turbine.php>, 2013. [Online; Accessed 20-September-2013.].
- [47] Green-Tide Turbines Ltd., “Green-Tide Turbines: Technology.” <http://www.green-tide.com/technology>, 2013. [Online; Accessed 20-September-2013.].
- [48] UEK Corporation, “Underwater Electric Kite.” <http://uekus.com/>, 2013. [Online; Accessed 20-September-2013.].
- [49] A. Kogan and A. Seginer, “T.A.E. Rep. No. 32A: Final report on shroud design,” tech. rep., Department of Aeronautical Engineering, Technion Israel Institute of Technology, Haifa, Israel, 1963.
- [50] P. Masukume, G. Makaka, and D. Tinarwo, “Optimum Geometrical Shape Parameters for Conical Diffusers in Ducted Wind Turbines,” *International Journal of Energy and Power Engineering*, vol. 5, pp. 177–181, 12 2016.
- [51] P. Masukume, G. Makaka, and P. Mukumba, “Optimization of the Power Output of a Bare Wind Turbine by the Use of a Plain Conical Diffuser,” *Sustainability*, vol. 10, pp. 1–7, 7 2018.
- [52] T. Setoguchi, N. Shiomi, and K. Kaneko, “Development of two-way diffuser for fluid energy conversion system,” *Renewable Energy*, vol. 29, pp. 1757–1771, 8 2004.
- [53] F. Ponta and P. Jacovkis, “Marine-current power generation by diffuser-augmented floating hydro-turbines,” *Renewable Energy*, vol. 33, no. 4, pp. 665 – 673, 2008.

- [54] K. Foreman, B. Gilbert, and R. Oman, “Diffuser augmentation of wind turbines,” *Solar Energy*, vol. 20, no. 4, pp. 305 – 311, 1978.
- [55] B. Gilbert, R. Oman, and K. Foreman, “Fluid Dynamics of Diffuser-Augmented Wind Turbines,” *Journal of Energy*, vol. 2, pp. 368–374, 11 1978.
- [56] B. Gilbert and K. Foreman, “Experimental Demonstration of the DiffuserAugmented Wind Turbine Concept,” *Journal of Energy*, vol. 3, pp. 235–240, 11 1979.
- [57] O. Igra, “Compact shrouds for wind turbines,” *Energy Conversion*, vol. 16, pp. 149–157, 1 1977.
- [58] R. Luquet, D. Bellevre, D. Fréchet, P. Perdon, and P. Guinard, “Design and model testing of an optimized ducted marine current turbine,” *International Journal of Marine Energy*, vol. 2, pp. 61–80, 6 2013.
- [59] U. Goltenbott, Y. Ohya, S. Yoshida, and P. Jamieson, “Aerodynamic interaction of diffuser augmented wind turbines in multi-rotor systems,” *Renewable Energy*, vol. 112, pp. 25 – 34, 2017.
- [60] O. Igra, “Design and Performance of a Turbine Suitable for an Aerogenerator,” *Energy Conversion*, vol. 15, pp. 143–151, 1 1976.
- [61] Y. Ohya and T. Karasudani, “A shrouded wind turbine generating high output power with wind-lens technology,” *Energies*, vol. 3, no. 4, pp. 634–649, 2010.
- [62] H. Grassmann, F. Bet, G. Cabras, M. Ceschia, D. Cobai, and C. DelPapa, “A partially static turbine first experimental results,” *Renewable Energy*, vol. 28, pp. 1779–1785, 9 2003.
- [63] D. G. Phillips, *An Investigation on Diffuser Augmented Wind Turbine Design*. PhD thesis, University of Auckland, Auckland, Australia, 2003.
- [64] K. D. Visser, “Wind tamer turbine performance report,” Tech. Rep. 11, Clarkson University, Potsdam, NY, 11 2009.

- [65] M. M. Moeller and K. Visser, “Experimental and Numerical Studies of a High Solidity, Low Tip Speed Ratio DAWT,” in *48th AIAA Aerospace Sciences Meeting Including the New Horizons Forum and Aerospace Exposition*, vol. 48th, (Orlando, Florida), AIAA, January 2010.
- [66] J. Reinecke, T. W. von Backstrom, and J. L. Van Niekerk, “Effect of a diffuser on the power production of an ocean current turbine,” in *9th European Wave and Tidal Energy Conference*, (Brisbane, Australia), Sustainable Energy Research Group, 2011.
- [67] H. Sun and Y. Kyojuka, “Experimental Validation and Numerical Simulation Evaluation of a Shrouded Tidal Current Turbine,” *Journal of the Japan Society of Naval Architects and Ocean Engineers*, vol. 16, pp. 25–32, 1 2012.
- [68] T. A. Lokocz, “Testing of a Ducted Axial Flow Tidal Turbine,” Master’s thesis, University of Maine, Maine, United States of America, 2012.
- [69] W. Shi, D. Wang, M. Atlar, B. Guo, and K.-c. Seo, “Optimal design of a thin-wall diffuser for performance improvement of a tidal energy system for an AUV,” *Ocean Engineering*, vol. 108, pp. 1–9, 10 2015.
- [70] M. M. Nunes, R. C. Mendes, T. F. Oliveira, and A. C. B. Junior, “An experimental study on the diffuser-enhanced propeller hydrokinetic turbines,” *Renewable Energy*, vol. 133, pp. 840–848, 4 2019.
- [71] O. Igra, “The shrouded aerogenerator,” *Energy*, vol. 2, pp. 429–439, 2 1977.
- [72] B. Kosasih and A. Tondelli, “Experimental Study of Shrouded Micro-Wind Turbine,” *Procedia Engineering*, vol. 49, pp. 92–98, 11 2012.
- [73] O. Igra, “Research and development for shrouded wind turbines,” *Energy Conversion and Management*, vol. 21, no. 1, pp. 13–48, 1981.
- [74] M. Shives and C. Crawford, “Developing an empirical model for ducted tidal turbine performance using numerical simulation results,” *Proceedings of the In-*

- stitution of Mechanical Engineers, Part A: Journal of Power and Energy*, vol. 226, pp. 112–125, 2 2012.
- [75] R. Lewis, J. Williams, and M. Abdelghaffar, “A theory and experimental investigation of ducted wind turbines,” *Wind Engineering*, vol. 1, no. 2, pp. 104–125, 1977.
- [76] C. J. Lawn, “Optimization of the power output from ducted turbines,” *Proceedings of the Institution of Mechanical Engineers, Part A: Journal of Power and Energy*, vol. 217, no. 1, pp. 107–117, 2003.
- [77] P. M. Jamieson, “Beating Betz: Energy Extraction Limits in a Constrained Flow Field,” *Journal of Solar Energy Engineering*, vol. 131, 07 2009. 031008.
- [78] M. J. Werle and W. M. Presz, “Ducted wind/water turbines and propellers revisited,” *Journal of Propulsion and Power*, vol. 24, no. 5, pp. 1146–1150, 2008.
- [79] R. Bontempo and M. Manna, “Solution of the flow over a non-uniform heavily loaded ducted actuator disk,” *Journal of Fluid Mechanics*, vol. 728, p. 163195, 2013.
- [80] R. Bontempo and M. Manna, “Performance analysis of open and ducted wind turbines,” *Applied Energy*, vol. 136, pp. 405–416, 2014.
- [81] R. Bontempo and M. Manna, “Effects of the duct thrust on the performance of ducted wind turbines,” *Energy*, vol. 99, pp. 274–287, 3 2016.
- [82] R. Bontempo and M. Manna, “The axial momentum theory as applied to wind turbines: some exact solutions of the flow through a rotor with radially variable load,” *Energy Conversion and Management*, vol. 143, pp. 33–48, 7 2017.
- [83] C. Fletcher, “Diffuser-Augmented Wind Turbine Analysis,” in *Australasian Conference on Hydraulics and Fluid Mechanics*, vol. 7th, (Brisbane, Australia), pp. 435–438, Institution of Engineers, Australia, August 1980.

- [84] C. A. Fletcher, “Computational analysis of diffuser-augmented wind turbines,” *Energy Conversion and Management*, vol. 21, no. 3, pp. 175 – 183, 1981.
- [85] D. A. T. D. do Rio Vaz, A. L. A. Mesquita, J. R. P. Vaz, C. J. C. Blanco, and J. T. Pinho, “An extension of the blade element momentum method applied to diffuser augmented wind turbines,” *Energy Conversion and Management*, vol. 87, pp. 1116–1123, 2014.
- [86] J.-M. Laurens, M. Ait-Mohammed, and M. Tarfaoui, “Design of bare and ducted axial marine current turbines,” *Renewable Energy*, vol. 89, pp. 181–187, 2016.
- [87] M. Nachtane, M. Tarfaoui, D. Saifaoui, A. E. Moumen, O. Hassoon, and H. Benyahia, “Evaluation of durability of composite materials applied to renewable marine energy: Case of ducted tidal turbine,” *Energy Reports*, vol. 4, pp. 31 – 40, 2018.
- [88] S. Allsop, C. Peyrard, P. R. Thies, E. Boulougouris, and G. P. Harrison, “Hydrodynamic analysis of a ducted, open centre tidal stream turbine using blade element momentum theory,” *Ocean Engineering*, vol. 141, pp. 531–542, 9 2017.
- [89] S. Allsop, C. Peyrard, P. Bousseau, and P. Thies, “Adapting conventional tools to analyse ducted and open centre tidal stream turbines,” *International Marine Energy Journal*, vol. 1, no. 2, pp. 91–99, 2018.
- [90] M. Kardous, R. Chaker, F. Aloui, and S. B. Nasrallah, “On the dependence of an empty flanged diffuser performance on flange height: Numerical simulations and piv visualizations,” *Renewable Energy*, vol. 56, pp. 123–128, 2013. The International Conference on Renewable Energy: Generation and Applications.
- [91] T. S. Kannan, S. A. Mutasher, and Y. K. Lau, “Design and flow velocity simulation of diffuser augmented wind turbine using cfd,” *Journal of Engineering Science and Technology*, vol. 8, no. 4, pp. 372–384, 2013.

- [92] K. Mansour and P. Meskinkhoda, “Computational analysis of flow fields around flanged diffusers,” *Journal of Wind Engineering and Industrial Aerodynamics*, vol. 124, pp. 109 – 120, 2014.
- [93] T. A. Khamlaj and M. P. Rumpfkeil, “Analysis and optimization of ducted wind turbines,” *Energy*, vol. 162, pp. 1234–1252, 11 2018.
- [94] J. E. Kesby, D. R. Bradney, and P. D. Clausen, “Determining diffuser augmented wind turbine performance using a combined cfd/bem method,” *Journal of Physics: Conference Series*, vol. 753, pp. 10736–10774, 2016.
- [95] A. M. El-Zahaby, A. Kabeel, S. Elsayed, and M. Obiaa, “Cfd analysis of flow fields for shrouded wind turbines diffuser model with different flange angles,” *Alexandria Engineering Journal*, vol. 56, no. 1, pp. 171–179, 2017.
- [96] G. Tampier, C. Troncoso, and F. Zilic, “Numerical analysis of a diffuser-augmented hydrokinetic turbine,” *Ocean Engineering*, vol. 145, pp. 138–147, 11 2017.
- [97] C. F. Fleming and R. H. Willden, “Analysis of bi-directional ducted tidal turbine performance,” *International Journal of Marine Energy*, vol. 16, pp. 162–173, 2016.
- [98] R. Venters, B. T. Helenbrook, and K. D. Visser, “Ducted Wind Turbine Optimization,” *Journal of Solar Energy Engineering*, vol. 140, 11 2017.
- [99] R. Bontempo and M. Manna, “A ring-vortex actuator disk method for wind turbines including hub effects,” *Energy Conversion and Management*, vol. 195, pp. 672 – 681, 2019.
- [100] D. G. Phillips, P. J. Richards, G. D. Mallinson, and R. G. J. Flay, “Computational Modelling of Diffuser Designs for a Diffuser Augmented Wind Turbine,” in *Australasian Fluid Mechanics Conference*, 13th, (Melbourne, Australia), pp. 207–210, Australasian Fluid Mechanics Society (AFMS), December 1998.

- [101] M. O. L. Hansen, N. N. Sørensen, and R. G. J. Flay, “Effect of Placing a Diffuser around a Wind Turbine,” *Wind Energy*, vol. 3, pp. 207–213, 10 2000.
- [102] V. Dighe, D. Suri, F. Avallone, and G. van Bussel, “Ducted wind turbines in yawed flow: A numerical study,” *Wind Energy Science Discussions*, vol. 2019, pp. 1–13, 2019.
- [103] D. L. Gaden and E. L. Bibeau, “A numerical investigation into the effect of diffusers on the performance of hydro kinetic turbines using a validated momentum source turbine model,” *Renewable Energy*, vol. 35, no. 6, pp. 1152 – 1158, 2010.
- [104] S. Hjort and H. Larsen, “Rotor design for diffuser augmented wind turbines,” *Energies*, vol. 8, pp. 10736–10774, 2015.
- [105] C. Belloni, R. Willden, and G. Houlby, “An investigation of ducted and open-centre tidal turbines employing CFD-embedded BEM,” *Renewable Energy*, vol. 108, pp. 622–634, 8 2017.
- [106] C. S. Belloni, R. H. Willden, and G. T. Houlby, “A Numerical Analysis of Bidirectional Ducted Tidal Turbines in Yawed Flow,” *Marine Technology Society Journal*, vol. 47, pp. 23–35, 7 2013.
- [107] A. C. Aranake, V. K. Lakshminarayan, and K. Duraisamy, “Computational analysis of shrouded wind turbine configurations using a 3-dimensional rans solver,” *Renewable Energy*, vol. 75, pp. 818–832, 2015.
- [108] H. Ghassemi, H. Ghafari, and E. Homayoun, “Hydrodynamic performance of the horizontal axis tidal stream turbine using rans solver,” *Scientific Journals of the Maritime University of Szczecin*, vol. 55, pp. 23–33, September 2018.
- [109] S.-H. Wang and S.-H. Chen, “Blade number effect for a ducted wind turbine,” *Journal of Mechanical Science and Technology*, vol. 22, pp. 1984–1992, Oct 2008.
- [110] B. Hadya and J. Pailla, “Performance analysis of an omnidirectional intake duct wind turbine using cfd,” *International Journal of Latest Engineering and Management Research (IJLEMR)*, vol. 02, pp. 01–10, September 2017.

- [111] *Diffuser-Augmented Composite Material Wind Turbine Design Using CFD*, vol. Volume 4: Energy Systems Analysis, Thermodynamics and Sustainability; Combustion Science and Engineering; Nanoengineering for Energy, Parts A and B of *ASME International Mechanical Engineering Congress and Exposition*, 08 2012.
- [112] K. Prakash, R. Sreeju, S. Vijaychandran, and A. R. Sridharan, “Optimisation of wind turbine with diffuser using cfd tool,” *International Journal of Engineering Sciences & Research Technology*, vol. 06, pp. 292–296, January 2017.
- [113] S. P. Venkatesan, J. Kumarsoni, and A. Burugpalli, “Increasing efficiency of a wind turbine using a convergent nozzle in combination with a flanged diffuser,” *International Journal of Applied Engineering Research*, vol. 10, pp. 10234–10240, July 2015.
- [114] E. Alpman, “Multiobjective aerodynamic optimization of a microscale ducted wind turbine using a genetic algorithm,” *Turkish Journal of Electrical Engineering & Computer Sciences*, vol. 26, pp. 618–629, January 2018.
- [115] W. Han, P. Yan, W. Han, and Y. He, “Design of wind turbines with shroud and lobed ejectors for efficient utilization of low-grade wind energy,” *Energy*, vol. 89, pp. 687–701, 2015.
- [116] S. Takahashi, Y. Hata, Y. Ohya, T. Karasudani, and T. Uchida, “Behavior of the blade tip vortices of a wind turbine equipped with a brimmed-diffuser shroud,” *Energies*, vol. 5, pp. 5229–5242, December 2012.
- [117] M. A. Zefreh, “Design and cfd analysis of airborne wind turbine for boats and ships,” *International Journal of Aerospace Sciences*, vol. 4, no. 1, pp. 14–24, 2016.
- [118] M. G. Borg, Q. Xiao, S. Allsop, A. Incecik, and C. Peyrard, “Numerical analysis of a ducted high-solidity tidal turbine,” in *2018 OCEANS - MTS/IEEE Kobe Techno-Oceans (OTO)*, pp. 1–5, May 2018.

- [119] M. G. Borg, Q. Xiao, S. Allsop, A. Incecik, and C. Peyrard, “A numerical performance analysis of a ducted, high-solidity tidal turbine,” *Renewable Energy*, vol. 159, pp. 663 – 682, 2020.
- [120] M. G. Borg, Q. Xiao, S. Allsop, A. Incecik, and C. Peyrard, “An actuator disc analysis of a ducted high-solidity tidal turbine in yawed flow,” in *ASME 2019 38th International Conference on Ocean, Offshore, and Arctic Engineering, OMAE 2019*, pp. 1–5, June 2019.
- [121] M. G. Borg, Q. Xiao, S. Allsop, A. Incecik, and C. Peyrard, “A blade-resolved numerical analysis of a ducted, high-solidity tidal turbine in yawed flow,” *Applied Energy*, 2019.
- [122] M. G. Borg, Q. Xiao, S. Allsop, A. Incecik, and C. Peyrard, “Analysing fibre composite designs for high-solidity ducted tidal turbine blades,” in *OCEANS 2019 - Marseille*, pp. 1–8, June 2019.
- [123] M. G. Borg, Q. Xiao, S. Allsop, A. Incecik, and C. Peyrard, “A numerical fluid-structure interaction analysis of a fibre-composite, ducted, high-solidity tidal turbine rotor in aligned and yawed flow conditions,” *Ocean Engineering*, 2020.
- [124] K. D. Visser, “Wind Tamer Turbine Performance Report 1kW-15 kW Performance Predictions,” tech. rep., Clarkson University, Potsdam, 2009.
- [125] J. F. Manwell, J. G. McGowan, and A. L. Rogers, “Aerodynamics of wind turbines,” in *Wind Energy Explained*, ch. 3, pp. 91–155, John Wiley & Sons, Ltd, 2010.
- [126] M. Shives, C. Crawford, and S. Grovue, “A tuned actuator cylinder approach for predicting cross-flow turbine performance with wake interaction and channel blockage effects,” *International Journal of Marine Energy*, vol. 18, pp. 30–56, 6 2017.

- [127] T. Burton, N. Jenkins, D. Sharpe, and E. Bossanyi, “Aerodynamics of horizontal axis wind turbines,” in *Wind Energy Handbook*, ch. 3, pp. 39–136, John Wiley & Sons, Ltd, 2011.
- [128] R. P. Coleman, A. M. Feingold, and C. W. Stempin, “Evaluation of the induced-velocity field of an idealized helicopter rotor,” tech. rep., NATIONAL AERONAUTICS AND SPACE ADMINISTRATION HAMPTON VA LANGLEY RESEARCH CENTER, 1945.
- [129] F. White and B. B. Blake, “Improved method predicting helicopter control response and gust sensitivity,” in *Proceedings of the 35th Annual Forum of the American Helicopter Soc.*, 1979.
- [130] D. Pitt and D. Peters, “Theoretical prediction of dynamic-inflow derivatives,” *Vertica*, vol. 5, pp. 21–34, 1981.
- [131] J. J. Howlett, “UH-60A Black Hawk engineering simulation program. Volume 1: Mathematical model,” tech. rep., National Aeronautics and Space Administration, Washington, DC, December 1981.
- [132] H. Glauert and G. B. A. R. Committee, *The Analysis of Experimental Results in the Windmill Brake and Vortex Ring States of an Airscrew*. ARC/R&M-1026, H.M. Stationery Office, 1926.
- [133] M. L. Buhl Jr, “New empirical relationship between thrust coefficient and induction factor for the turbulent windmill state,” tech. rep., National Renewable Energy Lab.(NREL), Golden, CO (United States), 2005.
- [134] R. E. Wilson and P. B. S. Lissaman, “Applied aerodynamics of wind power machines,” tech. rep., Oregon State Univ., Corvallis (USA), 1974.
- [135] ANSYS Inc., *FLUENT User’s Guide*. Lebanon, NH: ANSYS Inc., 5 ed., 1998.
- [136] T. Kajishima and K. Taira, *Computational Fluid Dynamics: Incompressible Turbulent Flows*. Cham: Springer International Publishing, 2017.

- [137] D. C. Wilcox, *Turbulence Modeling for CFD, Third Edition*. San Diego: DCW Industries, Inc, third ed., 2006.
- [138] K. A. Hoffmann and S. T. Chiang, “Turbulence and turbulent flows,” in *Computational Fluid Dynamics Volume III*, ch. 1, pp. 1 – 19, Engineering Education System, August 2000.
- [139] H. K. Versteeg and W. Malalasekera, “Turbulence and its modelling,” in *An Introduction to Computational Fluid Dynamics: The Finite-Volume Method*, ch. 3, pp. 40 – 114, Longman Group Ltd., 2007.
- [140] P. Mycek, B. Gaurier, G. Germain, G. Pinon, and E. Rivoalen, “Renewable Energy Experimental study of the turbulence intensity effects on marine current turbines behaviour. Part I: One single turbine,” *Renewable Energy*, vol. 66, pp. 729–746, 2014.
- [141] S. P. Neill, J. R. Jordan, and S. J. Couch, “Impact of tidal energy converter (TEC) arrays on the dynamics of headland sand banks,” *Renewable Energy*, vol. 37, pp. 387–397, 1 2012.
- [142] A. Bahaj and L. Myers, “Analytical estimates of the energy yield potential from the Alderney Race (Channel Islands) using marine current energy converters,” *Renewable Energy*, vol. 29, pp. 1931–1945, 10 2004.
- [143] A. Betz, “Windmills in the light of modern research,” tech. rep., National Advisory Committee for Aeronautics, Washington, DC, 8 1928.
- [144] A. Bourgoïn, *Bathymetry induced turbulence modelling the Alderney Race site: regional approach with TELEMAC-LES*. PhD thesis, Normandie Université, March 2019.
- [145] L. Krstulovic-Opara, B. Klarin, and Z. Domazet, “A non-destructive wind turbine blade analysis based on the Thermal Stress Analysis,” (Split, Hrvatska), 2009.
- [146] D. Grogan, S. Leen, C. Kennedy, and C. Bradaigh, “Design of composite tidal turbine blades,” *Renewable Energy*, vol. 57, pp. 151–162, 9 2013.

- [147] A. Mason-Jones, D. M. O’Doherty, C. E. Morris, T. O’Doherty, C. B. Byrne, P. W. Prickett, R. I. Grosvenor, I. Owen, S. Tedds, and R. J. Poole, “Non-Dimensional Scaling of Tidal Stream Turbines,” *Energy*, vol. 44, pp. 820–829, 2012.
- [148] N. D. Katopodes, “Chapter 7 - vorticity dynamics,” in *Free-Surface Flow* (N. D. Katopodes, ed.), pp. 516 – 565, Butterworth-Heinemann, 2019.
- [149] U. Ahmed, D. Apsley, I. Afgan, T. Stallard, and P. Stansby, “Fluctuating loads on a tidal turbine due to velocity shear and turbulence: Comparison of CFD with field data,” *Renewable Energy*, vol. 112, pp. 235–246, 11 2017.
- [150] P. Bortolotti, D. Berry, R. Murray, E. Gaertner, D. Jenne, R. Damiani, G. Barter, and K. Dykes, “A Detailed Wind Turbine Blade Cost Model,” Tech. Rep. NREL/TP-5000-73585, National Renewable Energy Laboratory, Golden, Colorado, June 2019.
- [151] Solvay S.A., “MTM 28 SERIES.” <https://www.solvay.com/en/product/mtm-28>, 2013. [Online; accessed 22-November-2019].
- [152] C. Manjunatha, A. Taylor, A. Kinloch, and S. Sprenger, “The tensile fatigue behaviour of a silica nanoparticle-modified glass fibre reinforced epoxy composite,” *Composites Science and Technology*, vol. 70, no. 1, pp. 193–199, 2010.
- [153] A. Bhanage and P. Krishnan, “Design for fatigue and simulation of glass fibre/epoxy composite automobile leaf spring,” *Journal of Engineering and Applied Sciences*, vol. 9, p. 196, 03 2014.
- [154] J. Mandell, R. Reed, and D. Samborsky, “Fatigue of fiberglass wind turbine blade materials,” tech. rep., 1992.
- [155] F. R. Menter, “Two-equation eddy-viscosity turbulence models for engineering applications,” *AIAA Journal*, vol. 32, no. 8, pp. 1598–1605, 1994.
- [156] H. Jiang, Y. Li, and Z. Cheng, “Performances of ideal wind turbine,” *Renewable Energy*, vol. 83, pp. 658–662, 2015.

- [157] R. C. of the 25th ITTC, “Uncertainty analysis in cfd verification and validation methodology and procedures,” tech. rep., 2008.
- [158] T. Leroux, N. Osbourne, and D. Groulx, “Numerical study into horizontal tidal turbine wake velocity deficit: Quasi-steady state and transient approaches,” *Ocean Engineering*, vol. 181, pp. 240 – 251, 2019.

Appendix A

Characterisation Modelling of a Ducted Tidal Turbine

A.1 Law of the Wall

In defining the terminologies within the law of the wall theorem:

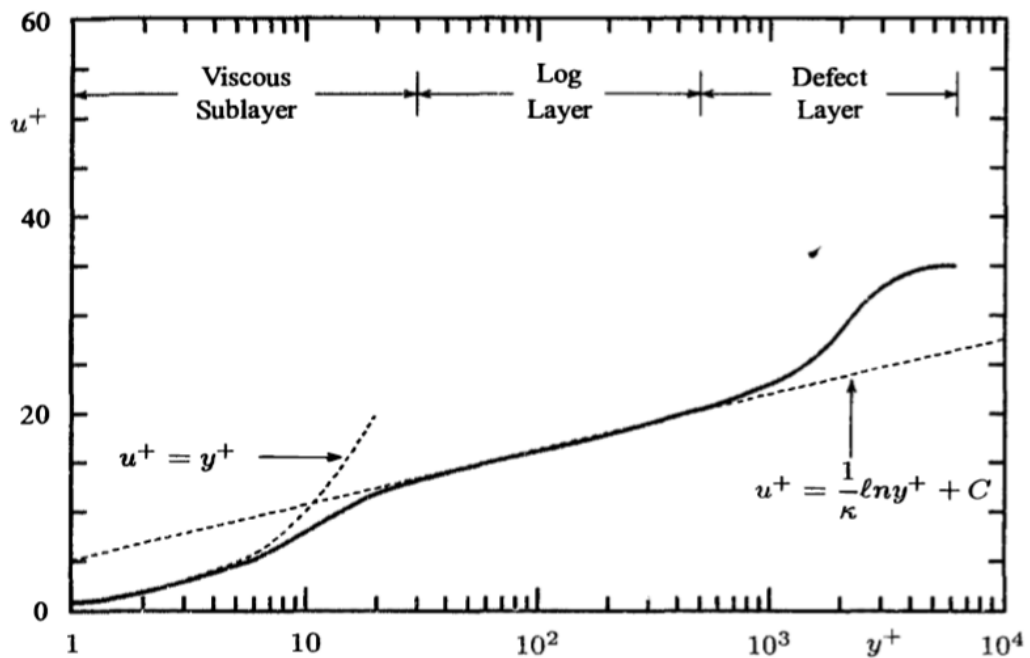


Figure A.1: Typical velocity profile for a turbulent boundary layer [137]

Appendix B

Methodology of the Fluid-Structure Interaction

B.1 Mesh Independence Analysis

In establishing the mesh independent parameters for the fluid-structure interaction, recommended meshing procedures and guidelines [157] were followed. Defining the mesh independent verification of the three-bladed numerical model in relation to torque:

Table B.1: Mesh Independence analysis for the Validation Three-Bladed Tidal Turbine

Cell Number	r_i	S_i	ε_i	R_i
13,485,062	1.397	0.03135	-0.001140	0.2517
9,652,138	1.480	0.03021	-0.004530	
6,522,223		0.02568		

Appendix B. Methodology of the Fluid-Structure Interaction

Defining the mesh independent verification of the ducted turbine numerical model in relation to torque:

Table B.2: Mesh Independence analysis for the Ducted, High-Solidity Tidal Turbine

Cell Number	r_i	S_i	ε_i	R_i
18,621,356	1.440	0.1121	-0.00890	0.4113
12,932,325	1.270	0.1032	-0.02164	
10,185,673		0.08156		

Defining the mesh independent verification of the ducted turbine rotor blade numerical model in relation to radial strain:

Table B.3: Mesh Independence analysis for the Rotor Blade Structural Design

Cell Number	r_i	S_i	ε_i	R_i
635,672	1.242	0.002528	-0.000030	0.2451
511,834	1.340	0.002498	-0.000122	
382,167		0.002376		

B.2 Concentrated Vortex Generation

B.2.1 Domain Model

The course of thought behind this methodology was defined in an effort to introduce a discreet, explicit vortex upstream of the ducted, high-solidity tidal turbine. The analysis of vortex-interaction is an imperative concept to tackle upon the design of a turbine. Yet there exists a gap in the methodological availability of the various computational fluid dynamic schemes, particularly the concept of introducing such vortices within a numerical domain. For this reason, this chapter provided an innovative, yet limited, method with which CFD analysts may introduce explicit vortices within a turbine domain.

The UDF elaborated is utilised in the "Fixed Values" menu of the cell zone conditions within ANSYS Fluent. More specifically, this was implemented within the three-dimensional, cylindrical coordinate system fixed values of tangential, radial, and axial velocities within the distinct cell zone created for the generation of vortices. The reason of requiring the cell zone to be segregated from the rest of the domain was this manipulation.

Albeit the beneficial use, the problematic aspect of this implementation was that the fixed values were not superimposed properties upon the flow, but numerically overwritten properties within the cells. Therefore, the vorticial kinematic properties were not introduced coherently with the incoming stream, but overwritten upon the cell zone, as illustrated in Figure B.3. This domain region therefore solely contains the vorticial kinematic properties; this was acknowledged to be an unholistic representation of actuality. Yet, due to the fact that no other methodologies exist in commercial CFD solvers to induce explicit vortices, this unique and novel numerical setup was deemed to be the most representative of the concept, given the absence of any other numerical schemes/methods.

For the methodology to accurately represent reality, the vorticial properties are required to be superimposed upon the existent flow properties, rather than replacing the properties. This, however, cannot be done from the software graphical user-interface,

and hence, would require a development in the back-end source code of the software. Yet the current methodology succeeds in providing a proof-of-concept of the cell zone segregation and flow-property manipulation, which is what the chapter endeavours in putting forward.

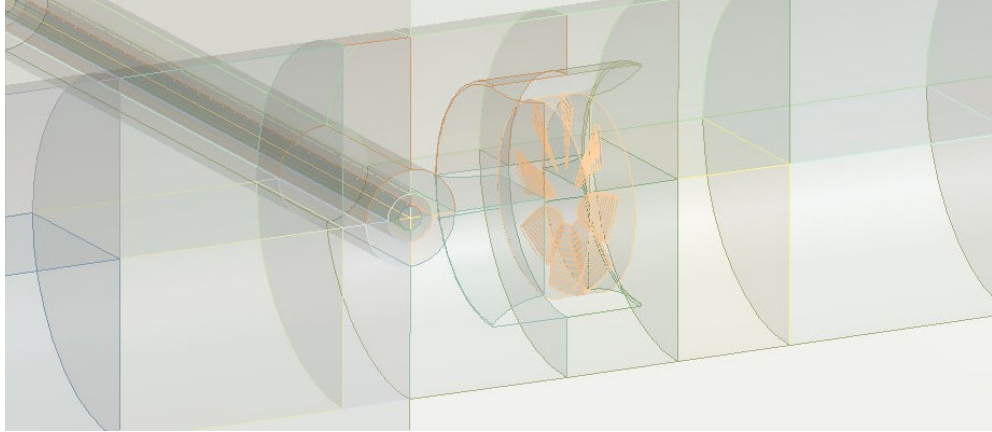


Figure B.1: Vortex Domain Layout

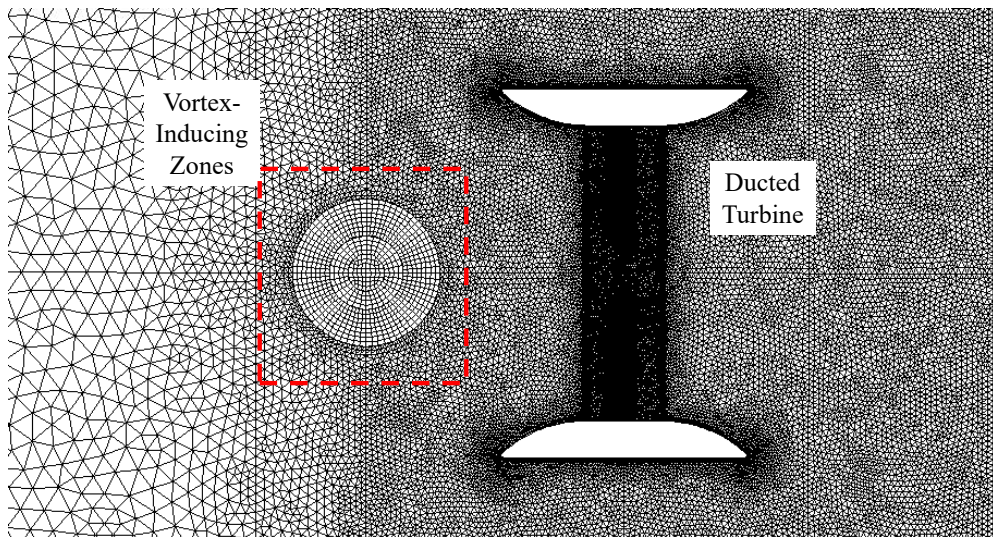


Figure B.2: Vortex Domain Mesh

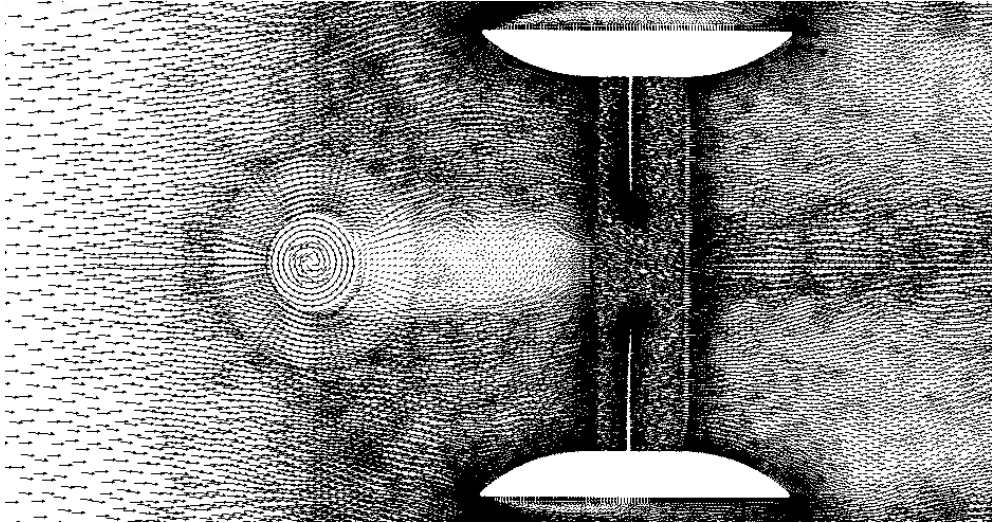


Figure B.3: Vortex Domain Example

B.2.2 User-Defined Function Macro

This method is a novel, untried, and unproven numerical scheme that introduces a disparity in the flow in an effort to replicate the presence of a vortex stream within the domain. To accomplish this, the mesh had to, therefore, be segregated, and the kinematics of the cell-zone had to be manipulated by means of a macro. This macro sustained a loop, where each of the cells within that cell-zone thread was manipulated by overwriting the kinematics within that cell. In this case, the velocities within a cylindrical coordinate system were varied; the radial and axial velocity were nulled, and the tangential velocity was calculated by means of the formula $v = \omega \cdot r$.

Additionally, the cell zone was induced with a moving mesh scheme to mimic both the kinematics and the physical motion of a static vortex; it is imperative to note that this artificially-induced vortex was static yet rotating on its own axis. Therefore, the free-stream interacted with this manipulated cell zone, acquired the vortex kinematics, which then interacted with the turbine rotor. It was acknowledged that this method was not a holistic representation of actual vortex occurrence. Yet, given that no other numerical scheme is available within commercial software to introduce explicit vortices, this methodological implementation was deemed to be the most valid compared to all other schemes. Additionally, the implementation was acknowledged to be of, at least,

Appendix B. Methodology of the Fluid-Structure Interaction

decent success given that established variations in the performance outputs was present, as required and predicted.

In defining the macro developed to induce an explicit vortex-zone within the domain.

```

/*****
/* Rotating Vortex Field in Cylindrical Coordinates          */
*****/

#include "udf.h"
#include "mem.h"

#define omega -2.0 /* defining the vorticial rotational velocity */

DEFINE_PROFILE(tangential_velocity,t,i)

{
cell_t c;          /* defining the cell name */

real radius;      /* defining the variable */
real pos[3];      /* defining a three-dimensional vector */
real zone[3];     /* defining a three-dimensional vector */
real cent[3];     /* defining a three-dimensional vector */

zone[0]=-12.5;    /* defining the vortex cell
zone centroid location */
zone[1]=0.0;
zone[2]=2.0;

#if !RP_HOST

begin_c_loop(c,t) /* defining the loop */
```

Appendix B. Methodology of the Fluid-Structure Interaction

```
{  
  
    C_CENTROID(pos,c,t);  
  
    cent[0]=pos[0]-zone[0];  
    cent[1]=pos[1]-zone[1];  
  
    radius=MAX(sqrt((cent[0]*cent[0])+(cent[1]*cent[1])),0);  
    /* finding the distance from the cell centroid to the  
    zone centroid */  
    F_PROFILE(c,t,i)=(omega*radius);  
    /* defining the equation */  
}  
end_c_loop(c,t)  
#endif  
}
```

Appendix C

Numerical Validation of a Three-Bladed Horizontal-Axis Tidal Turbine

In relation to the turbulence modelling variation work undertaken in Chapter 9, it should be stated that further analyses in Chapter 5, utilising all three turbulence models, may have been of aid. This, however, was omitted due to the study put forward by Leroux et al. [158] where an identical validation procedure was put forward, yet with the implementation of the SST $k-\omega$. The validation output from this study attained a very high similarity result, as high as the validation in this thesis with the STD $\tau-\omega$.

As Wilcox [137] stated in the book, the distinction between the Standard ' ω ' and the Baseline/SST ' ω ' models, implementing a numerical shift from an epsilon-based to an omega-based model, had been deemed to be solely significant at a high Reynolds number. This was evident when comparing the data from the implementation of the two turbulence models for the model-scale turbine simulation. As both models had accurately replicated the turbine dynamics, the distinction between the two models was insignificant for that case study. This, however, was deemed to be due to the comparatively low Reynolds number, as Wilcox had elaborated. Therefore, given that both the Standard and the SST ω -based models attained a largely identical validation

Appendix C. Numerical Validation of a Three-Bladed Horizontal-Axis Tidal Turbine

phase, further validation analyses within this work utilising the BSL and SST ω -based model was acknowledged to be superfluous. In relation to the full-scale ducted turbine, however, the utilisation of all three turbulence models was necessary as the Reynolds number increases significantly. In fact, the resultant outputs of that analysis varied substantially.

Appendix D

Hydrodynamic Performance of a Ducted High-Solidity Tidal Turbine in Aligned Flow Conditions

Appendix D. Hydrodynamic Performance of a Ducted High-Solidity Tidal Turbine in Aligned Flow Conditions

Defining the standard deviation of the temporal torque data:

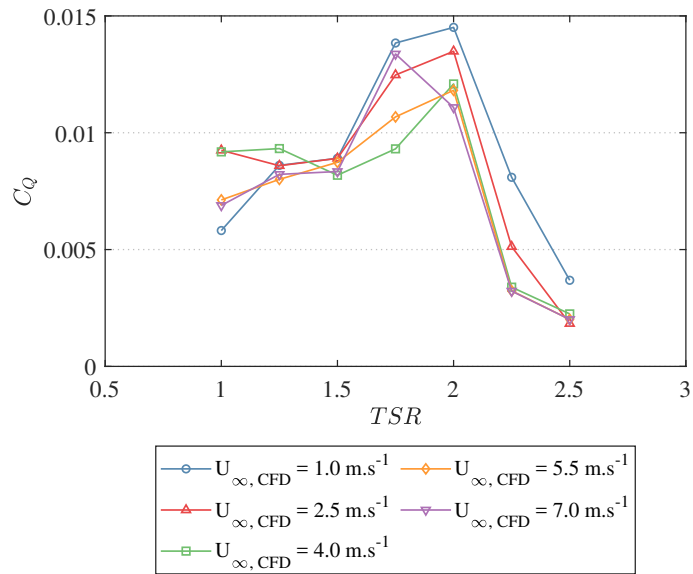


Figure D.1: Torque Coefficient Standard Deviation

Defining the standard deviation of the temporal thrust data:

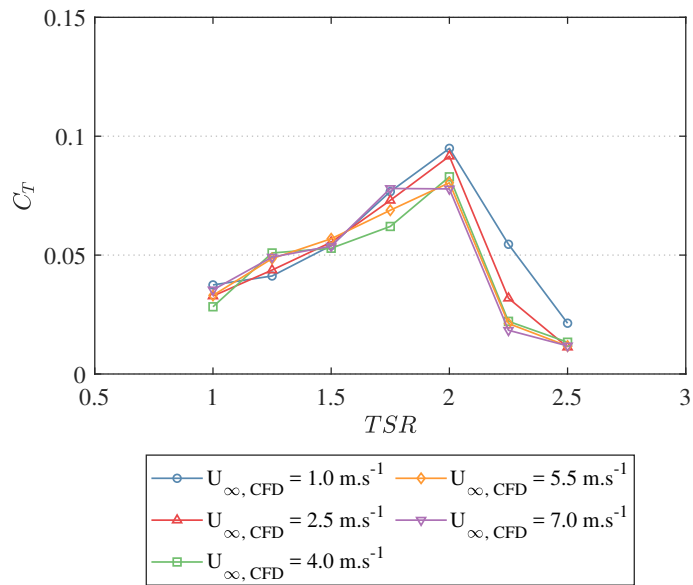


Figure D.2: Thrust Coefficient Standard Deviation

Appendix D. Hydrodynamic Performance of a Ducted High-Solidity Tidal Turbine in Aligned Flow Conditions

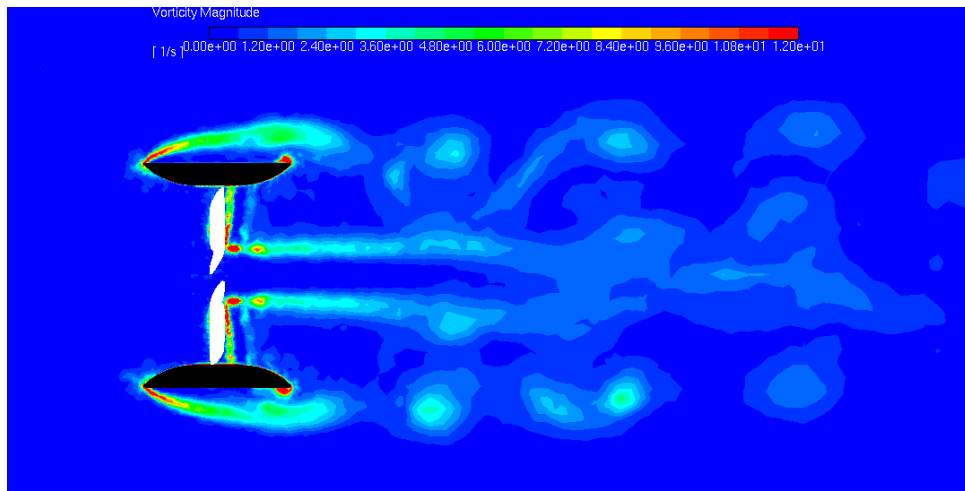


Figure D.3: Illustrative top-view representation of the vorticity within the turbine domain at nominal TSR; $U_\infty = 4 \text{ m.s}^{-1}$

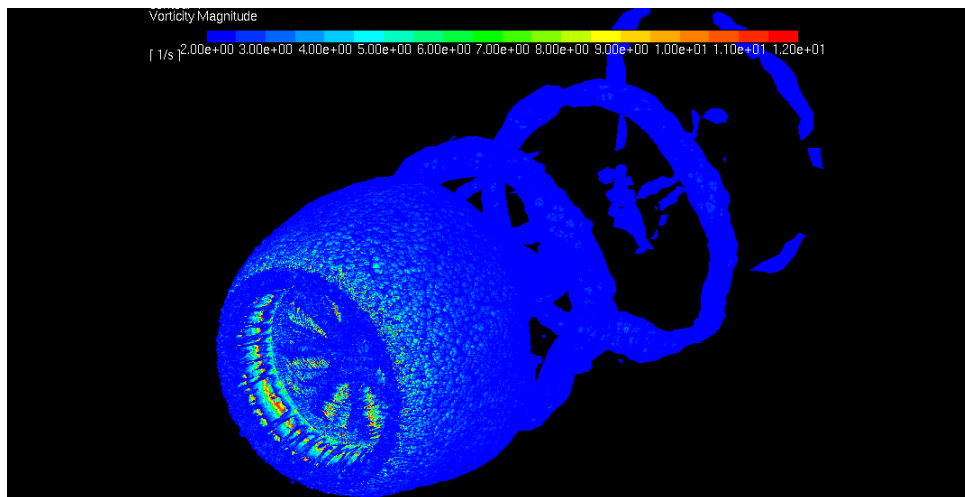


Figure D.4: Illustrative angular representation of the vorticity within the turbine domain at nominal TSR; $U_\infty = 4 \text{ m.s}^{-1}$

Appendix E

Hydrodynamic Performance of a Ducted High-Solidity Tidal Turbine in Yawed Flow Conditions

Appendix E. Hydrodynamic Performance of a Ducted High-Solidity Tidal Turbine in Yawed Flow Conditions

In defining the standard deviation of the temporal torque data:

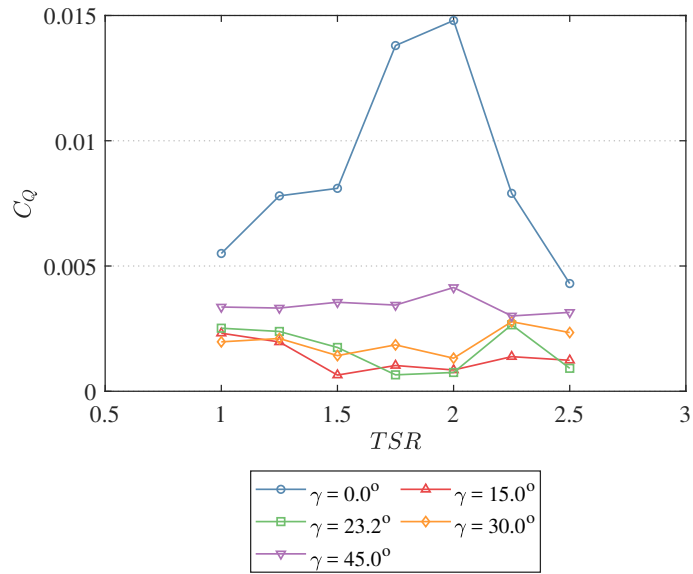


Figure E.1: Torque Coefficient Standard Deviation

In defining the standard deviation of the temporal thrust data:

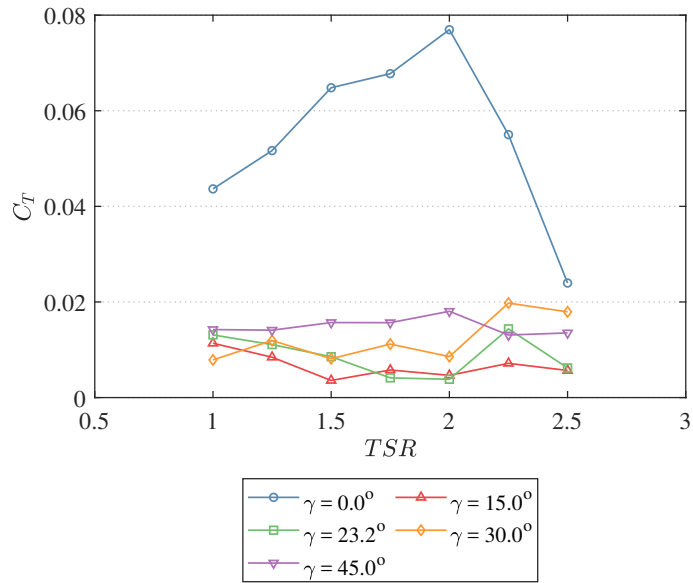


Figure E.2: Thrust Coefficient Standard Deviation

Appendix F

Structural Analysis of Fibre-Reinforced High-Solidity Tidal Turbine Blades

In defining the structural vibrational mode of the blade deflection:

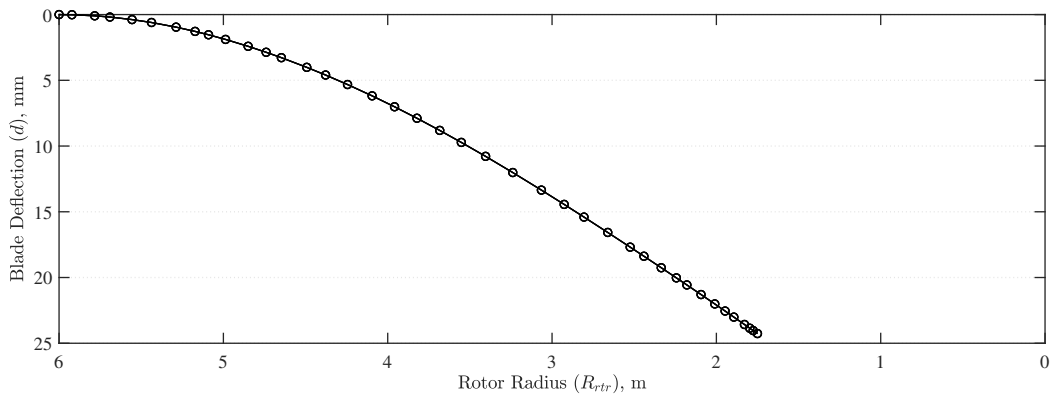


Figure F.1: Structural response cross-section of the ‘solid’ blade design at $4 \text{ m}\cdot\text{s}^{-1}$ TSR 1.75

In defining the standard deviation of the temporal radial strain in aligned flow:

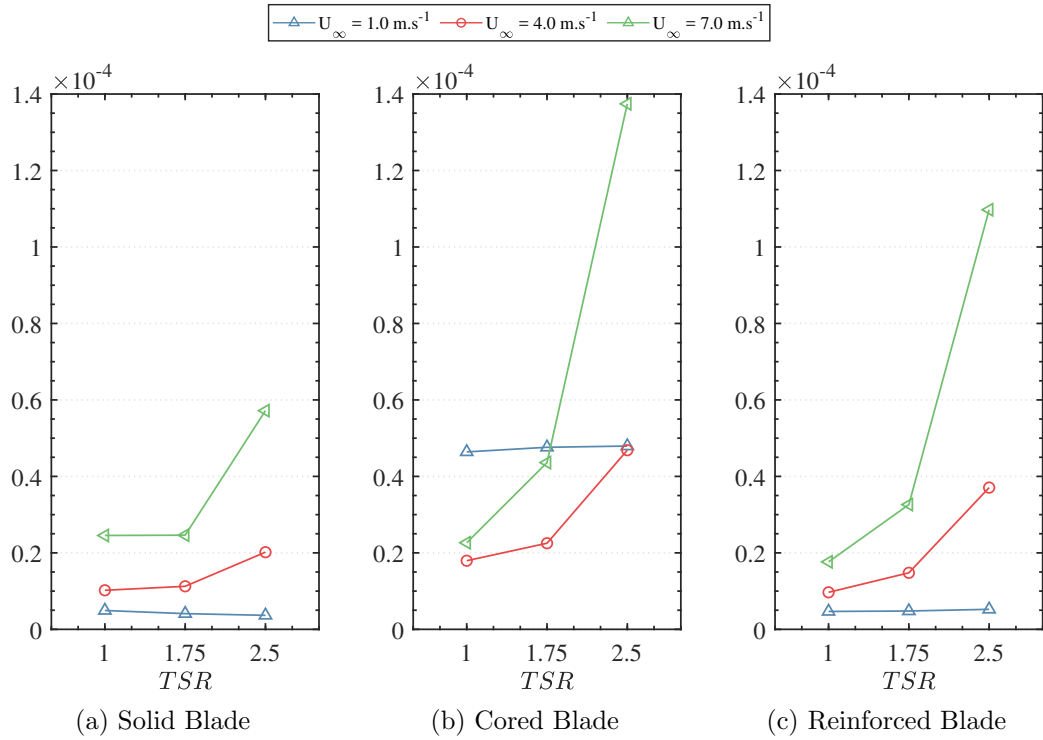


Figure F.2: Standard deviation of the maximum normal radial strain of the distinct blade designs within aligned flow conditions

In defining the standard deviation of the temporal radial strain in yawed flow:

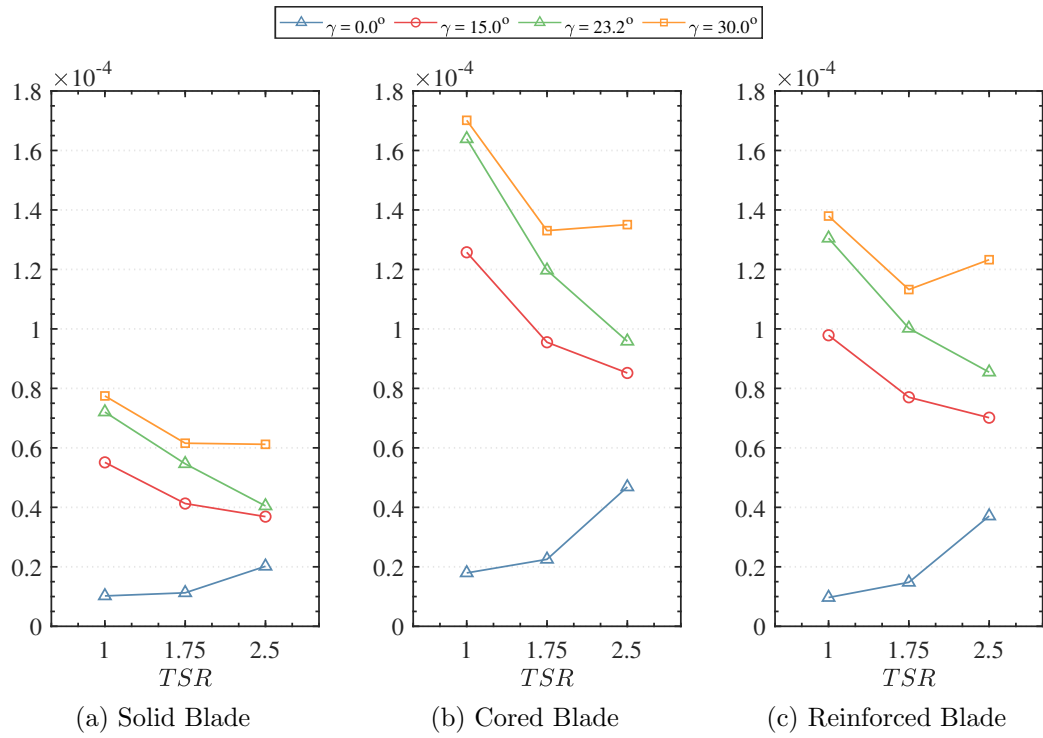


Figure F.3: Standard deviation of the maximum normal radial strain of the distinct blade designs within aligned flow conditions

Appendix G

Cost Analysis

In defining the price per kg of material utilised for the internal structural blade design:

Table G.1: Material Cost per unit mass for the High-Solidity Tidal Turbine Rotor Designs

Blade Material	Bi-Axial Fibre Sheet	Tri-Axial Fibre Sheet	Resin & Hardener	Structural Foam
Cost (\$ / kg)	3.00	2.86	3.63	7.23

In establishing the volume of material utilised for the internal structural blade design:

Table G.2: Required Material Volume for the High-Solidity Tidal Turbine Rotor Designs

Blade Volume	Blade Shell	Blade Core	Reinforcements
Volume (m³)	6.033	6.033	0.0518

In defining the equations utilised to acquire the volumetric percentage of glass fibres and matrix constituting the composite material utilised for the internal structural blade

design:

$$\rho_{cmpst} = x_{\%mtrx}\rho_{mtrx} + x_{\%fbr}\rho_{fbr} \quad (\text{G.1})$$

$$x_{\%mtrx} + x_{\%fbr} = 1 \quad (\text{G.2})$$

In defining the volumetric percentage of glass fibres and matrix constituting the composite material utilised for the internal structural blade design:

Table G.3: Total Material Costs (rounded to the nearest thousand) for the High-Solidity Tidal Turbine Rotor Designs

Blade Material	Uni-Directional Fibreglass	Double-Biased Fibreglass
Filler (fibre)	54%	47%
Matrix (resin)	46%	53%

Appendix H

Ducted Turbine Outlet Pressure Equation Derivation

Initiating the ducted turbine pressure outlet equation derivation by means of one-dimensional momentum conservation from the downstream rotor region to the duct outlet region:

$$A_3 p_3 + \dot{m}_3 U_3 = A_4 p_4 + \dot{m}_4 U_4 \quad (\text{H.1})$$

$$A_3 p_3 - A_4 p_4 = \rho A_4 U_4^2 - \rho A_3 U_3^2 \quad (\text{H.2})$$

$$U_4^2 = \frac{-A_4 p_4 + A_3 p_3 + \rho A_3 U_3^2}{\rho A_4} \quad (\text{H.3})$$

In continuation, the ducted turbine adaptation established in prior sections was then extended and incorporated with the one-dimensional momentum conservation equation:

$$0 = C_T - C_{p02} - C_{p34} \cdot \frac{U_D^2}{U_\infty^2} - C_{pb} \quad (\text{H.4})$$

$$0 = \frac{p_2 - p_3}{\frac{1}{2}\rho U_\infty^2} - \frac{p_2 - p_\infty}{\frac{1}{2}\rho U_\infty^2} - \eta_{34} \left(1 - \frac{U_4^2}{U_D^2}\right) \frac{U_D^2}{U_\infty^2} - \frac{p_\infty - p_4}{\frac{1}{2}\rho U_\infty^2} \quad (\text{H.5})$$

$$0 = \frac{p_4}{\frac{1}{2}\rho U_\infty^2} - \eta_{34} \left(1 - \frac{U_4^2}{U_D^2}\right) \frac{U_D^2}{U_\infty^2} - \frac{p_3}{\frac{1}{2}\rho U_\infty^2} \quad (\text{H.6})$$

Appendix H. Ducted Turbine Outlet Pressure Equation Derivation

$$0 = \frac{p_4}{\frac{1}{2}\rho} - \eta_{34}\left(1 - \frac{U_4^2}{U_D^2}\right)U_D^2 - \frac{p_3}{\frac{1}{2}\rho} \quad (\text{H.7})$$

$$0 = \frac{p_4}{\frac{1}{2}\rho} - \eta_{34}U_D^2 + \eta_{34}U_4^2 - \frac{p_3}{\frac{1}{2}\rho} \quad (\text{H.8})$$

$$\frac{p_4}{\frac{1}{2}\rho} = \frac{p_3}{\frac{1}{2}\rho} + \eta_{34}U_D^2 - \eta_{34}U_4^2 \quad (\text{H.9})$$

$$\frac{p_4}{\frac{1}{2}\rho} = \frac{p_3}{\frac{1}{2}\rho} + \eta_{34}U_D^2 - \eta_{34} \cdot \frac{-A_4p_4 + A_3p_3 + \rho A_3U_3^2}{\rho A_4} \quad (\text{H.10})$$

$$\frac{p_4}{\frac{1}{2}\rho} = \frac{p_3}{\frac{1}{2}\rho} + \eta_{34}U_D^2 + \frac{\eta_{34}p_4}{\rho} - \frac{\eta_{34}}{\rho A_4} \cdot A_3p_3 - \eta_{34} \frac{A_3}{A_4}U_D^2 \quad (\text{H.11})$$

$$\frac{p_4}{\frac{1}{2}\rho} - \frac{\eta_{34}p_4}{\rho} = \frac{p_3}{\frac{1}{2}\rho} + \eta_{34}U_D^2 - \frac{\eta_{34}}{\rho A_4} \cdot A_3p_3 - \eta_{34} \frac{A_3}{A_4}U_D^2 \quad (\text{H.12})$$

$$p_4 - \frac{1}{2}\eta_{34}p_4 = p_3 - \frac{1}{2}\eta_{34} \frac{A_3}{A_4}p_3 + \frac{1}{2}\eta_{34}\rho U_D^2 - \frac{1}{2}\eta_{34} \frac{A_3}{A_4}\rho U_D^2 \quad (\text{H.13})$$

$$p_4\left(1 - \frac{1}{2}\eta_{34}\right) = p_3\left(1 - \frac{1}{2}\eta_{34} \frac{A_3}{A_4}\right) + \frac{1}{2}\eta_{34}\rho U_D^2\left(1 - \frac{A_3}{A_4}\right) \quad (\text{H.14})$$

$$p_4 = p_3 \cdot \frac{\left(1 - \frac{1}{2}\eta_{34} \frac{A_3}{A_4}\right)}{1 - \frac{1}{2}\eta_{34}} + \frac{1}{2}\rho U_D^2 \cdot \frac{\eta_{34}\left(1 - \frac{A_3}{A_4}\right)}{1 - \frac{1}{2}\eta_{34}} \quad (\text{H.15})$$

This therefore defined a novel formula to more accurately equate the static pressure at the duct outlet downstream of the rotor in relation to the static and dynamic pressure at the immediate downstream segment of the turbine. In extrapolation, the velocity at the duct outlet may additionally be acquired.